Integrated adaptive optics for atmospheric turbulence effects mitigation on optical links

Yann Lucas

université PARIS-SACLAY

Integrated adaptive optics for atmospheric turbulence effects mitigation on optical links

Optique adaptative intégrée pour l'atténuation des effets de la turbulence atmosphérique sur les liaisons optiques

Thèse de doctorat de l'université Paris-Saclay

École doctorale n° 572, Ondes et matières, EDOM
Spécialité de doctorat : Physique
Graduate School : Physique. Référent : Faculté des sciences d'Orsay

Thèse préparée dans l'unité de recherche **DOTA (Université Paris-Saclay, ONERA)**, sous la direction de **Vincent MICHAU**, Directeur de recherche, la co-direction de, **Guillermo MARTIN**, Maître de conférence, et le co-encadrement de **Serge MEIMON**, Directeur de recherche

Thèse soutenue à Paris, le 10 décembre 2024, par

Yann LUCAS

Composition du Jury

Membres du jury avec voix délibérative

Julien FADE Professeur, Institut Fresnel	Président du jury
Sylvestre LACOUR Chargé de recherche HDR, Observatoire de Paris	Rapporteur & Examinateur
Mikhail VORONTSOV Professeur, Université de Dayton	Rapporteur & Examinateur
Antonella BOGONI Professeure, Ecole Supérieure Sant'Anna	Examinatrice

THESE DE DOCTORAT

NNT : 2024UPASP172

Remerciements

Je tiens tout d'abord à remercier les membres du jury, Julien Fade, Antonella Bogoni, Sylvestre Lacour et Mikhail Vorontsov pour l'intérêt qu'ils ont porté à cette thèse ainsi que le temps qu'ils ont consacré à son évaluation.

Un grand merci à Nadège Courjal pour les nombreuses discussions sur les PIC en Niobate de Lithium et l'accueil qui m'a été fait à Femto-st lors de mon séjour pour réparer le PIC Niobate.

Un grand merci à l'équipe de Pise : Giampiero Contestabile, Lorenzo De Marinis et Peter Seigo Kincaid pour l'accueil qui m'a été fait pour les caractérisations du PIC SOI.

Je tiens à remercier mon équipe d'encadrement: Mathieu Boutillier côté CNES pour ton implication dans le suivi de la thèse et le prêt de matériel de caractérisation que j'ai pu ramener de Toulouse ! Guillermo Martin côté IPAG pour ta bonne humeur et ton enthousiasme constant. Serge Meimon, mon encadrant ONERA, pour les nombreuses heures passées à discuter sur "les pages et les pages de calculs".

Et enfin la personne qui m'a le plus soutenu au cours de ces trois années, mon directeur de thèse Vincent Michau, tu as toujours été disponible lorsque j'en avais besoin. Merci pour toutes les discussions que l'on a eu et durant lesquelles tu as eu la patience non seulement de m'enseigner de nombreux savoirs mais surtout de me transmettre des méthodes de réflexions, de synthèses et un sens physique pour aborder les problèmes en se posant les bonnes questions pour tenter de les résoudre. Arrivé à la fin de ma thèse, c'est ce bagage là qui est le plus important alors merci pour tout.

Je tiens à remercier tous les permanants de l'équipe HRA. Vous m'avez tous apporté votre aide à un moment donné. Je tiens à remercier particulièrement Caroline qui m'a introduit au sujet, Laurie pour tout le temps que tu nous as consacré, à moi et aux autres "pioupiou", pour nous avoir pris sous ton aile afin de nous guider dans les méandres de la thèse et s'assurer de notre bonne santé ! Et enfin Joseph pour ton aide précieuse sans qui la manip n'aurait jamais abouti, et un grand merci à toi et à Domi pour toutes les fois où vous nous avez emmenés (et supportés !) à Thiais, au Viaduc, à Fontainebleau...

Je ne pourrais jamais remercier suffisament tous les doctorants, anciens et nouveaux, de la HRAteam qui ont rendu ces trois années géniales avec tous les jeux, les sorties, l'escalade et la voile ! Luca, Antoine C, Hiyam, Léa, Yann, Pyblo, Alix, Pepe, Valentina, Emile, Mehdi, Nicolas, Iva, Antoine A, Antoine G, Eve, Pierre, Mahawa, Elyes, Maxime, Hugo, Mathieu, Alberto, Kyliann, Théo, Florian, Noé, Inés la meilleur co-bureau imaginable et les marins Zoé et Timothée et tous ceux que j'ai pu rencontrer. Un merci spécial pour Luca dont j'ai été le stagiaire avant la thèse et qui m'a fait découvrir l'escalade les samedis avec Pablo Paolo et Carmen !

Un grand merci à mes amis Karim, Hugo, Thomas et Lénaïc qui m'ont soutenu pendant toute la thèse !

Pour finir je remercie mes parents mon frère et ma famille qui m'ont soutenu pendant toutes mes études et qui me supporte depuis toutes ces années !

Contents

Résumé de la thèse en français

Avec un besoin croissant de communication en espace libre, les transmissions radiofréquences deviennent saturées et les liaisons optiques représentent une solution prometteuse. A la réception, l'injection du signal optique dans une fibre optique monomode (FOM) permet un débit élevé en utilisant les composants déjà développés pour les communications fibrées. Cette injection peut être fortement perturbée par les effets de la turbulence pour des liens à travers l'atmosphère. Pour s'affranchir de ces effets, l'optique adaptative (OA) est couramment utilisée. Une approche alternative, appelée ici optique adaptative intégrée, a été récemment proposée. Cette solution repose sur la décomposition modale du champ par un démultiplexeur spatial suivi d'une recombinaison cohérente par un circuit photonique intégré (PIC) assurant l'injection dans la FOM. L'OA-intégrée pourrait représenter une solution compacte et robuste s'appliquant aussi aux fortes perturbations. Sa mise en œuvre nécessite toutefois la réalisation d'un PIC complexe, avec des pertes minimales et des déphaseurs rapides pour un contrôle en temps réel. Or les PIC actuels ne répondent pas à ces besoins. Les PIC en niobate de lithium autorisent des déphaseurs avec une bande passante élevée mais pas une architecture complexe, alors que la technologie Silicium permet des architectures complexes mais des déphaseurs relativement lents. Par ailleurs, les pertes sont encore élevées avec les deux technologies.

Cette thèse porte sur l'analyse des performances ultimes d'une OA-intégrée en présence de turbulence atmosphérique, basée sur le développement d'une méthode de contrôle originale pour des architectures de PIC dédiés à la combinaison cohérente.

Dans le chapitre 2, j'ai caractérisé les propriétés des signaux à combiner afin d'évaluer l'efficacité moyenne de recombinaison des architectures de PIC et l'évolution temporelle des signaux à recombiner.

Ainsi, une analyse des propriétés statistiques des amplitudes complexes en sortie du démultiplexeur spatial m'a conduit à proposer une architecture simplifiée basée sur une correction de phase seule suivie d'une combinaison cohérente statique présentant moins de pertes. Une telle architecture réduisant significativement les pertes dans le PIC, je l'ai retenue dans la suite de ma thèse.

J'ai ensuite établi une expression analytique du temps de décorrélation des amplitudes complexes en sortie du démultiplexeur spatial. En appliquant cette expression au cas d'une liaison satellite-sol, j'ai mis en évidence que la bande passante typique des déphaseurs des PIC en silicium est limitée pour permettre un contrôle classique par modulation dans le cas d'un grand nombre d'entrées.

Pour surmonter cette contrainte, j'ai proposé, dans le chapitre 3, une méthode de contrôle originale basée sur une modulation spatiale. Avec cette méthode, le PIC peut être vu comme un analyseur de surface d'onde ce qui permet d'estimer les phases résiduelles à corriger en une seule période de modulation spatiale. J'ai analysé le comportement de

cette méthode en présence de bruit de mesure et j'ai optimisé la forme de la modulation spatiale vis-à-vis de ce critère. Le codage optimal permet à cette méthode d'atteindre la limite fondamentale de la propagation du bruit de photons des analyseurs de surface d'onde.

Les expressions analytiques et les méthodes développées dans cette thèse permettent de dimentionner une OA-intégrée et d'évaluer analytiquemement ses performances.

Dansd le chapitre 4, sur la base des conclusions précédentes (correction phase seule, temps de décorrélation, codage spatial optimisé), j'ai défini les principaux paramètres d'une OA-intégrée dédiée à une liaison satellite-sol. J'ai évalué ses performances en établissant un budget d'erreur basée sur des expressions analytiques des différents termes d'erreur impactant l'OA-intégrée.

Pour valider le dimentionnement de l'OA-intégrée, j'ai réalisé une expérience numérique et démontré que la méthode de contrôle basée sur un codage spatial de la modulation permet la fermeture de la boucle et est stable en présence de bruit de mesure représentatif de conditions réalistes. J'ai également proposé une architecture légèrement modifiée pour simplifier la loi de contrôle.

Les développements du chapitre 4 reposent sur un PIC parfait. Or un PIC expérimental présente de nombreuses imperfections. Ainsi, pour analyser le comportement de la méthode de contrôle originale basée sur un codage spatial appliquée à un PIC réel présentant des imperfections, je l'ai mise en œuvre expérimentalement dans le chapitre 5 avec un PIC en Niobate de Lithium que j'ai préalablement caractérisé. J'ai mis en évidence son intérêt en comparant ses performances à celles de méthodes de modulation classique.

Enfin, j'ai utilisé la caractérisation d'un PIC experimental en silicium, à laquelle j'ai participé, pour définir l'architecture d'un futur PIC avec des performances optimales.

List of Figures

List of Tables

Acronyms

AO Adaptive Optics.

ASPGD Adaptive Stochastic Parallel Gradient Descent.

DL Deep Learning.

DM Deformable Mirror.

ESA European Space Agency.

FSO Free Space Optical.

GEO GEOstationary.

HG Hermite-Gaussian.

HydRON High-thRoughput Optical Network.

LEO Low Earth Orbit.

LG Laguerre-Gaussian.

LiNbO3 Lithium Niobate.

LNOI Lithium Niobate On Insulator.

MIMO Multiple-Inputs Multiple-Outputs.

MISO Multiple-Inputs Single-Output.

MMI Multimode Interference Splitters.

MPLC Multi-Plane Light Conversion.

MZI Mach-Zehnder Interferometer.

OGS Optical Ground Station.

PIC Photonic Integrated Circuit.

PL Photonic Lanterns.

PSD Power Spectral Density.

RF Radio Frequency.

RTC Real Time Computer.

RTF Rejection Transfer Function.

SiN Silicon Nitride.

SMF Single Mode Fibre.

SMID Single Mode Injection Device.

SOFA Small Optical Ground Stations Focal-Optics Assembly.

SOI Silicon On Insulator.

SPGD Stochastic Parallel Gradient Descent.

SVD Singular Value Decomposition.

TAOGS Transportable Adaptive Optical Ground Station.

TEC Thermoelectric Peltier Cooler.

TURANDOT TURbulence simulator for spAce-grouND Optical Telecommunication.

WFS WaveFront Sensor.

Introduction (English)

The use of satellites is growing steadily for applications such as communication networks or Earth observation, implying increasing needs in free-space communications, especially for satellite-to-ground downlinks. Free Space Optical (FSO) links appear as a promising solution to lighten saturated radio-frequency transmissions whose bandwidths become saturated and are no longer sufficient. Indeed, compared to radio frequency transmissions, FSO links are more directive, allowing for higher bandwidth up to THz with unlicensed spectrum channels. Furthermore, FSO links benefit from the mature technological components developed for guided optical communications. For this, the optical wave is usually injected into a Single Mode Fibre (SMF) at the receiver end. However, the propagation of the optical wave in the atmosphere induces distortions on the complex field due to atmospheric turbulent effects, severely degrading the optical wave coupling in the SMF. Thus, mitigating atmospheric turbulence effects is mandatory to reach FSO links with high data rates.
Various passive methods have been developed to overcome the loss of information induced by turbulent atmospheric effects. However, active methods are required to increase the optical wave coupling in a SMF at the receiver end. The classic active turbulent atmospheric effects mitigation method is Adaptive Optics (AO). Classic AO is used since the 90s in astronomy and is now used in FSO links. It uses wavefront sensors and deformable mirrors to correct distorted wavefronts. However, classic AO is a mechanically complex solution. Furthermore, at low satellite elevation, fluctuations of the amplitude of the optical wave induce measurement errors on the wavefront sensor, implying a degradation of the AO correction performances.

To overcome classic AO limitations, a new mitigation method has been proposed by N.Schwartz in his thesis [1]. This solution is based on two components: a spatial demultiplexer performing the modal decomposition of the distorted field into a finite set of guided waves that are coherently combined in a SMF using an active Photonic Integrated Circuit (PIC). This new mitigation method will be referred to here as integrated-AO. To deploy a wide range of FSO links receiver ends, integrated-AO appears as a promising solution more compact and robust than classic AO, also enabling correction in strong perturbation regimes.

Several laboratory proofs of concept have been carried out but without complete characterization of the system performances under real use case conditions [2, 3, 4, 5].

The first work of characterization of integrated-AO performances under real use case conditions have been carried out by L.Rinaldi in his thesis [6]. He studied the two components of integrated-AOs separately. He statistically characterized the coupling efficiency of a distorted field for different mode families. In other words, he characterized how well a spatial demultiplexer fits a distorted field given a specific modal decomposition on a finite set of modes-guided waves. Then, he numerically studied the guided waves coherent combination by the PIC assuming instantaneous and perfect correction. However, integrated-AO components may present high losses compared to classic AO. Thus, a

joint study of the coherent combination efficiency of PIC architectures with respect to the spatial demultiplexer choice is required to define an integrated-AO solution with optimal performances.
The spatial properties of integrated-AO have been studied by L.Rinaldi. However, the turbulent atmosphere is evolving dynamically, implying fluctuations in the complex amplitudes of the guided waves at the spatial demultiplexer output. Although the temporal evolution of the turbulent atmosphere is well known, the impact of spatial demultiplexers on the temporal evolution of the complex amplitudes of the guided waves at spatial demultiplexers output has not been studied yet. From the control point of view, classic AO allows a linear relation between measurements and corrections whereas with an integrated-AO the relation between measurements and corrections is non-linear. The control of an integrated-AO is similar to the control of a sensorless AO or the coherent combination of multiple laser beams. Thus, classic modulation-based control methods may be considered for the control of integrated-AO. However, with such classic modulation-based methods, the required modulation bandwidth depends on the number of guided waves to combine. Thus, depending on the integrated-AO sizing and temporal evolution of the complex amplitudes of the guided waves, performing the real-time control of the PIC with classic modulation-based control methods may require bandwidth higher than the active PIC reachable bandwidth. In this case, a specific control method must be developed for the real-time control of the PIC. In this way, a promising solution for the real-time control of PICs could be the modulation spatial coding method developed by L.Rinaldi to control a deformable mirror for sensorless AO [7].

This thesis focuses on the analysis of the ultimate performances of an integrated-AO in the presence of atmospheric turbulence, based on the development of an original control method for photonic integrated circuit architecture dedicated to coherent combination.

First of all, in Chapter 1, I summarize atmospheric turbulence effects on optical wave propagation and classic mitigation methods of these effects before introducing the concept of integrated-AO. I recall the classic control methods used for sensorless AO and laser beams coherent combination, as well as the technological platforms and spatial high specifications of PIC for coherent combination. I discuss the internal losses of integrated-AO with respect to PIC architecture choice and coherent combination strategy in terms of phase-only or phase and amplitude correction.

To develop an integrated-AO with optimal performances considering the important internal losses of PICs, the benefits of architectures allowing phase and amplitude correction compared to architectures allowing phase-only correction can be questioned. Compared to phase and amplitude correction, the coherent combination efficiency of phase-only correction PIC depends on the statistics of its input complex amplitudes. In Chapter 2, I start by jointly studying the coherent combination efficiency of phase-only correction PIC with respect to the statistical properties of the complex amplitudes of the guided waves at the PIC input depending on the spatial demultiplexer choice and turbulent atmospheric conditions.
Furthermore, the phase shifters required bandwidth depends on the temporal evolution of the complex amplitudes to be coherently combined in real-time. Although the temporal evolution of fields distorted by atmospheric effects is well known, the impact of the spatial demultiplexer is unknown. For this, I study the temporal evolution of the guided waves complex amplitudes at the PIC inputs by deriving an analytical expression of their temporal decorrelations in Chapter 2.

To overcome the modulation bandwidth constraints of classic sensorless control methods, in Chapter 3, I adapt the sensorless method of L.Rinaldi to control phase-only cor-

rection PIC with a spatial coding of the modulation. This method is referred to here as spatial modulation control method. In this chapter, considering perfect PIC, I study the linear regime of such a method and analyze its noise propagation. From this, I discuss the choice of the amplitude of the spatial coding. Finally, I study the choice of the spatial coding of the modulation with regard to noise propagation.

In Chapter 4, I give a general method for the sizing of integrated-AO and apply it to a specific satellite-to-ground downlink scenario with the sizing of a perfect phase-only correction PIC. Then, I use this scenario to validate the performances of the spatial modulation control method with a numerical experiment. For this, I perform an end-to-end simulation and implement the spatial modulation control method in a control loop, I evaluate its capacity to close the loop and analyze its closed-loop performances as well as its robustness to noises. I compare the performances of the spatial modulation control method to the classic sequential modulation control method. Finally, I study the usefulness of a slightly modified architecture to simplify the control law.

After evaluating the performances of the spatial modulation control method on perfect theoretical PIC, I study in Chapter 5 its implementation difficulties on an experimental PIC in Lithium Niobate that I characterize beforehand. Finally, I discuss the design and sizing of an experimental realistic PIC to reach optimal performances from the characterization of a Silicon On Insulator experimental PIC.

CHAPTER 1

Context

Contents

1.1 Introduction

With more and more growing needs in wireless communications, Radio Frequency (RF) transmissions become saturated, and an alternative transmission channel is required, such

as optical channel [8].
Indeed, with optical wavelength (700-1600 nm compared to 0.03-3 m for RF [9]), the beam is more directive allowing link bandwidth up to THz, a thousand times higher than RF bandwidth [9, 10]. Such links are referred to as Free Space Optical (FSO) communications.

FSO communications are deployed in a wide range of links such as ground-to-ground, ground-airborne, ship-to-ship, ground-to-satellite and inter-satellite [9, 8, 11, 12].
Terminals can be interlinked in global networks such as the High-thRoughput Optical Network (HydRON) project supported by the European Space Agency (ESA). HydRON aims at developing a FSO network with inter-satellite and ground-satellite [13], see Figure 1.1.

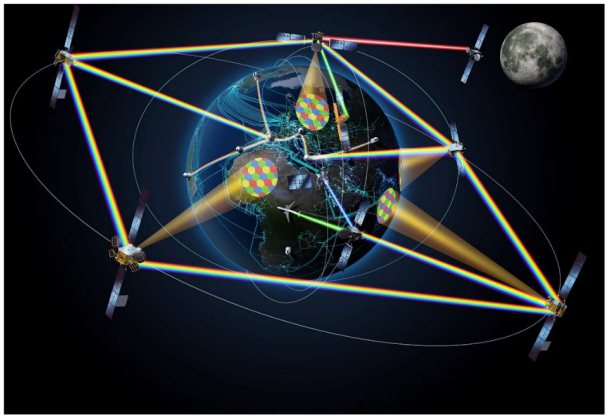

Figure 1.1: Artist view of HydRON project [14].

This thesis focuses on Low Earth Orbit (LEO) satellite-to-ground downlinks. Data are transmitted using a laser beam which propagates through the turbulent atmosphere before being collected by a ground telescope (part of an Optical Ground Station (OGS)). The window 1520-1600 nm allows low atmospheric absorption 0.01 dB/km and is compatible with optical emitter and detector technologies [9]. Furthermore, at 1.5 μm, optical links benefit from ground Single Mode Fibre (SMF) network technologies allowing to fully exploit optical channel bandwidth [15, 16, 17]. Figure 1.2 depicts a satellite-to-ground FSO link.

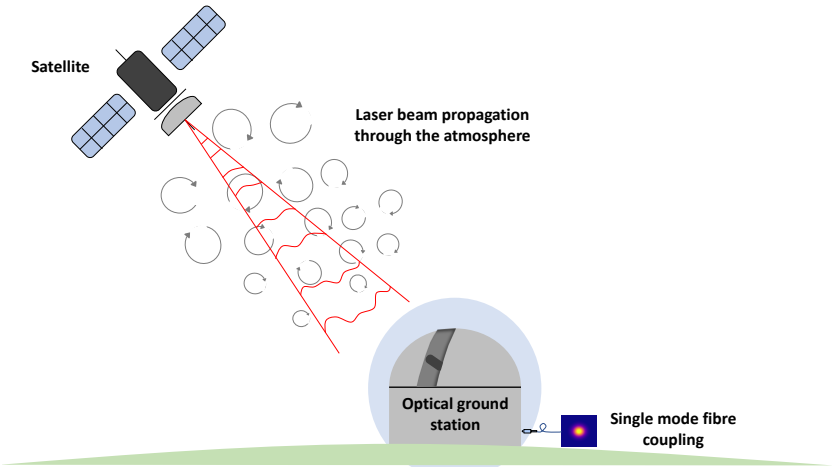

Figure 1.2: Schema of a satellite-to-ground FSO link.

In this thesis, we consider 1.5 μm links with SMF coupling at the receiver end. One of

the main issues comes from effects induced on the laser beam during propagation through the turbulent atmosphere, significantly impacting the coupling of the laser beam into the SMF and thus degrading link performances [18, 9, 8, 17].

This first chapter begins in Section 1.2 by describing the turbulent atmosphere and its effects induced on an optical wave propagating as well as the consequences on SMF coupling. Then, classic atmospheric turbulence effects mitigation methods are developed in Section 1.3 as well as their limitations. Afterwards, a new mitigation method, referred to here as integrated adaptive optics (integrated-AO), is presented in Section 1.4. This new mitigation method was first proposed by N.Schwartz [1] and is based on a spatial demultiplexer followed by an active Photonic Integrated Circuit (PIC) that ensures the SMF injection after coherent combination. Then, Section 1.5 gives a review of sensorless AO control methods applicable to PIC real-time control. Finally, high-level specifications of PIC for coherent combination are presented in Section 1.6.

1.2 Atmospheric turbulence effects

1.2.1 Turbulent atmosphere

Earth's atmosphere undergoes inhomogeneous heat transfer from ground to atmosphere and from direct heating by solar radiations. It results in the motion of large eddies of scale, L_0, named outer scale with sizes of tens of meters. In Kolmogorov's theory, the kinetic energy of such large eddies is transferred to smaller and smaller eddies up to a point where the energy is dissipated in heat by viscous frictions. Such eddies are named inner scale, l_0, with sizes of a few millimeters. This energy transfer, from the outer scale to the inner scale, is known as the Kolmogorov cascade energy and corresponds to the inertial domain in which the turbulence is fully developed.

1.2.1.1 Spatial statistical properties of the turbulent atmosphere at optical wavelengths

Inhomogeneous environments in temperature and humidity impact the refractive index, $n(\boldsymbol{r})$, which undergoes random fluctuations [19] such as:

$$n(\boldsymbol{r}) = \langle n \rangle + N(\boldsymbol{r})\,. \tag{1.1}$$

$\langle n \rangle$ is the constant average refractive index and $N(\boldsymbol{r})$ is the random fluctuating part with $\boldsymbol{r} = (x, y, z)$ the spatial coordinates.

Structure function of the refractive index: The structure function of the refractive index, $D_n(\rho)$, represents the average quadratic difference of the refractive index over a distance ρ, considering isotropic statistics. In the inertial domain $D_n(\rho)$ follows Obukhov's law [19]:

$$\begin{aligned} D_n(\rho) &= \left\langle \Big(n(r) - n(r+\rho) \Big)^2 \right\rangle . \\ &= C_n^2 \rho^{\frac{2}{3}} \end{aligned} \tag{1.2}$$

C_n^2 is the refractive index structure constant, and $\langle . \rangle$ denotes the ensemble average.

Power spectral density of the refractive index: In Kolmogorov's inertial domain, $\frac{1}{L_0} < f < \frac{1}{l_0}$, the power spectral density of the refractive index is given by:

$$W_n(f) = 0.033(2\pi)^{-2/3} C_n^2 f^{-11/3} . \tag{1.3}$$

Tatarski gives the expression for frequencies higher than the inner scale cutoff frequency, $1/l_0$ [20]:

$$W_n(f) = 0.033(2\pi)^{-2/3} C_n^2 f^{-11/3} exp\left(-l_0^2 f^2\right) . \tag{1.4}$$

When the turbulence is not fully developed, for lower frequencies than the outer scale cutoff frequency, $1/L_0$, the Von Kármán spectrum is proposed [21]:

$$W_n(f) = 0.033(2\pi)^{-2/3} C_n^2 \left(f^2 + \left(\frac{1}{L_0}\right)^2\right)^{-11/6} exp\left(-l_0^2 f^2\right) . \tag{1.5}$$

Figure 1.3 plots the power spectral density of the refractive index for $C_n^2 = 1$ and different examples of inner scale and outer scale.

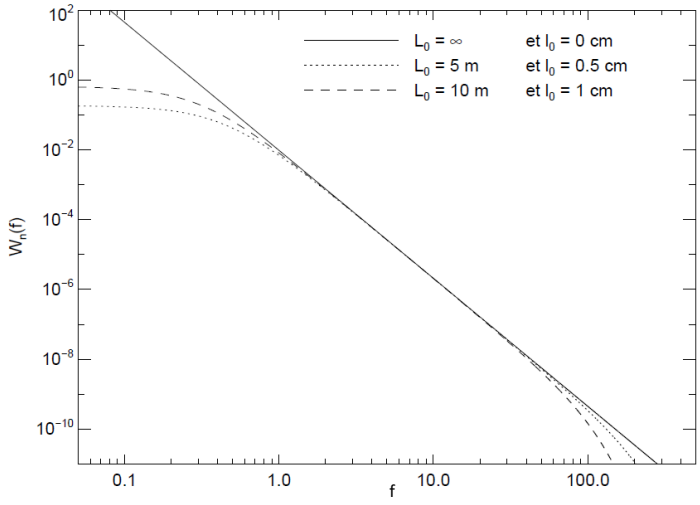

Figure 1.3: Kolmogorov's power spectral density of the refractive index for the inertial domain with Tatarski and Von Kármán spectrum modifications for outer inertial domain. Taken from [22] with $C_n^2 = 1$.

Structure constant of the refractive index: The atmospheric properties depend on the altitude, h, so it is possible to express the C_n^2 variation as a function of h. Several $C_n^2(h)$ models exist, in this thesis we use the Hufnagel-Valley profile [23, 24]:

$$\begin{aligned} C_n^2(h) =& 8.148 \times 10^{-56} v_{rms}^2 h^{10} exp\left(\frac{-h}{1000}\right) \\ &+ 2.7 \times 10^{-16} exp\left(\frac{-5}{1500}\right) + C_n^2(0) exp\left(\frac{-5}{100}\right) \end{aligned} . \tag{1.6}$$

v_{rms}^2 corresponds to the wind velocity fluctuations at the upper layers and $C_n^2(0)$ corresponds to the value of C_n^2 at ground level. This model describes averages of measured C_n^2 vertical profiles.

1.2.1.2 Atmospheric turbulence dynamics

Following Taylor hypothesis [25], the dynamic of turbulent layers is given by their overall displacement corresponding to the local wind. In this thesis, we use a Bufton profile [26] to model the natural wind velocity function of the altitude h:

$$\boldsymbol{v_{hw}}(h) = \boldsymbol{v_{ground}} + \boldsymbol{v_T} e^{-\left(\frac{h-h_T}{L_T}\right)^2} . \tag{1.7}$$

v_{ground} is the wind velocity near the ground, v_T is the velocity of the highest layer in the tropopause at altitude h_T and of scale L_T.

The transverse velocity displacement of a given layer is the sum of $\boldsymbol{v_{hw}}$ and of an equivalent wind speed, $\boldsymbol{v_{hsat}}$, induced by the displacement of the satellite. A flat Earth approximation gives:

$$\boldsymbol{v_{hsat}} = \boldsymbol{\mathring{\theta}_{sat}} \times \frac{h}{sin(\theta)} , \tag{1.8}$$

with $\boldsymbol{\mathring{\theta}_{sat}}$ the satellite angular velocity and θ the satellite elevation.

1.2.2 Optical propagation through the turbulent atmosphere

1.2.2.1 Helmholtz equation

Considering a monochromatic electromagnetic wave : $\boldsymbol{E}(\boldsymbol{r}, t) = \boldsymbol{E}(\boldsymbol{r})e^{-iwt}$, the equation of propagation is:

$$\nabla^2 \boldsymbol{E} + k_0^2 n^2 \boldsymbol{E} + 2\nabla\left(\boldsymbol{E}.\nabla ln(n)\right) = 0 , \tag{1.9}$$

obtained from Maxwell's equations, with $k_0 = w/c$ the wave vector and n the refractive index whose temporal fluctuation can be neglected. $\nabla = (\partial/\partial x, \partial/\partial y, \partial/\partial z)$ is the nabla operator. The right term, $2\nabla\left(\boldsymbol{E}.\nabla ln(n)\right)$ corresponds to a depolarization term. Since the inner scale is much larger than the wavelength, $l_0 >> \lambda$, this term is negligible [27, 28]. Thus, equation 1.9 can be restrained to the scalar Helmholtz Equation:

$$\nabla^2 E + k_0^2 n^2 E = 0 . \tag{1.10}$$

In the following, we suppose that the refractive index can be written as $n(\boldsymbol{r}) = 1+N(\boldsymbol{r})$. Considering a plane wave propagating in the z direction, the field is written $E(\boldsymbol{r}) = \Psi(\boldsymbol{r})e^{ik_0 z}$. $\Psi(\boldsymbol{r})$ is the complex amplitude of the field $E(\boldsymbol{r})$. The parabolic approximation considers that the diffraction of the wave due to the heterogeneity of the medium remains weak in the direction of propagation, and we have $\frac{\partial^2 E}{\partial z^2} << k_0 \frac{\partial E}{\partial z}$. Thus, the propagation equation becomes:

$$\frac{\partial^2 \Psi}{\partial x^2} + \frac{\partial^2 \Psi}{\partial y^2} + 2ik_0 \frac{\partial \Psi}{\partial z} + 2k_0^2 N \Psi = 0 \tag{1.11}$$

The solution of the propagation of Ψ in vacuum is given by the Fresnel propagator.

1.2.2.2 Spatial coherence function of the distorted field

We consider a turbulent atmospheric layer at altitude h, transverse to the laser beam propagation path and with a thickness δh small enough to neglect diffraction effects in it. The impact of such a turbulent layer can be characterized by the spatial coherence function, $B_{\Psi,h}(\boldsymbol{\rho})$ [29]. It corresponds to the covariance of the distorted field at the output of a thin atmospheric turbulent layer:

$$B_{\Psi,h}(\boldsymbol{\rho}) = \langle \Psi_h(\boldsymbol{r})\Psi_h^*(\boldsymbol{r}+\boldsymbol{\rho})\rangle \ . \tag{1.12}$$

$\langle\rangle$ is the ensemble average.

From Roddier [29] we have:

$$B_{\Psi,h}(\rho) = e^{-3.44\left(\frac{\rho}{r_{0,h}}\right)^{5/3}} , \tag{1.13}$$

with $r_{0,h}$ the Fried parameter of the thin layer defined as:

$$r_{0,h} = \left[0.423k_0^2 \int_h^{h+\delta h} C_n^2(z)dz\right]^{-3/5} . \tag{1.14}$$

The distorted field after propagation through the turbulent atmosphere can be determined by considering propagation through several phase screens using the Markov approximation [30]. This assumes the propagation equation can be integrated with discreet increment dz on the refractive index, large enough so that $< N(x,y,z)N(x,y,z+dz) >= 0$.

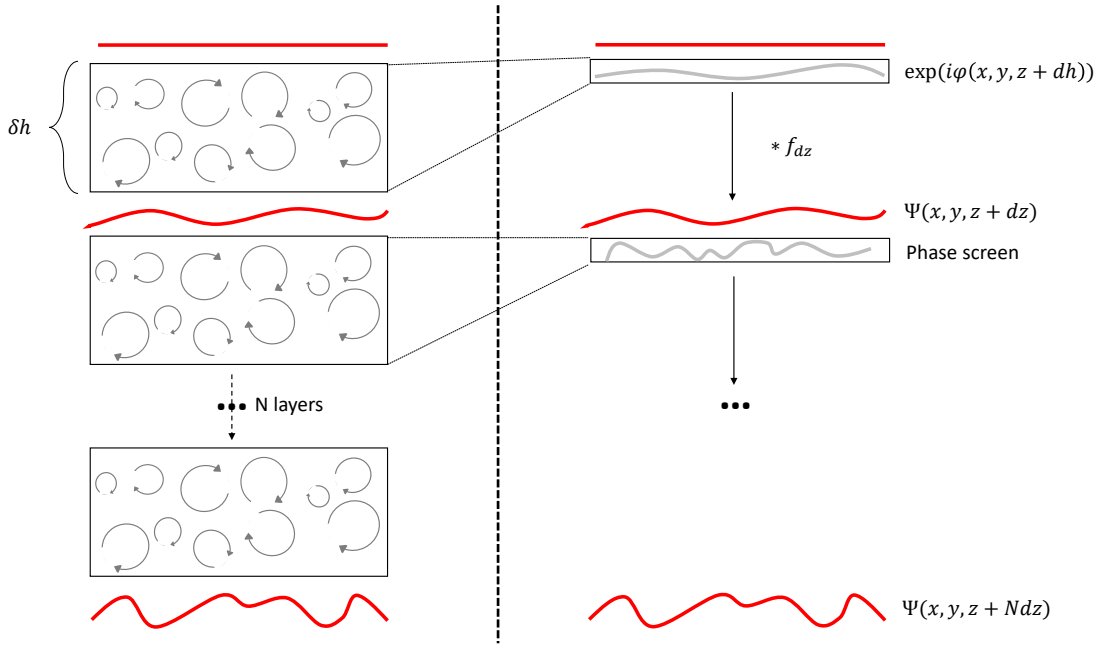

Figure 1.4: Field propagation through phase screens.

Figure 1.4, schematizes the propagation of a field, $\Psi(x,y,z)$, in the direction z through several phase screens applied as phase terms $\varphi(x,y)$. f_{dz} denotes the Fresnel propagator, the distorted field after propagation on a distance, dz, is:

$$\Psi(x,y,z+dz) = \Psi(x,y,z)e^{i\varphi(x,y)} * f_{dz} \, , \tag{1.15}$$

with $\varphi(x,y) = k_0 \int_z^{z+dh} N(x,y,z)dz$ and $*$ denoting the convolution operator.

Atmospheric turbulent effects on the propagated beam can be determined by considering propagation through multiple thin layers with Fresnel propagation between each turbulent layer [29]. The spatial coherence function is unchanged by Fresnel propagation. The spatial coherence function of the distorted field after propagation through the atmosphere is:

$$B_{\Psi^{turb}}(\rho) = \prod_h e^{-3.44\left(\frac{\rho}{r_{0,h}}\right)^{5/3}} = e^{-3.44\left(\frac{\rho}{r_0}\right)^{5/3}} , \tag{1.16}$$

with the Fried parameter:

$$r_0 = \left[0.423 k_0^2 \int_0^{Z_{max}} C_n^2(z) dz\right]^{-3/5} . \tag{1.17}$$

1.2.2.3 Temporal evolution

To take into account the temporal effects in the coherence function of the distorted field, the spatio-temporal covariance is derived for a given layer at altitude h from [29], such as:

$$B_{\Psi,h}(\boldsymbol{\rho}, \tau) = \langle \Psi_h(\boldsymbol{r}, t) \Psi_h^*(\boldsymbol{r} + \boldsymbol{\rho}, t + \tau) \rangle , \tag{1.18}$$

$\langle\rangle$ denotes the ensemble average. Using the Taylor's frozen flow hypothesis it comes:

$$B_{\Psi,h}(\boldsymbol{\rho}, \tau) = B_{\Psi,h}(\boldsymbol{\rho} - \tau \boldsymbol{v_h}, 0) , \tag{1.19}$$

with $\boldsymbol{v_h}$ the total velocity, transverse to the direction of propagation, undergoes by the layer at altitude h.
For a given layer at altitude h, the spatio-temporal covariance is given by [29]:

$$B_{\Psi,h}(\boldsymbol{\rho}, \tau) = e^{-3.44\left|\frac{\boldsymbol{\rho} - \tau \boldsymbol{v_h}}{r_{0,h}}\right|^{5/3}} , \tag{1.20}$$

with $r_{0,h}$ the equivalent Fried parameter of a layer at altitude h and $\boldsymbol{v_h} = \boldsymbol{v_{hw}} + \boldsymbol{v_{hsat}}$.
The total spatio-temporal covariance of the distorted field after atmospheric propagation considering a number of N layers is [29]:

$$B_{\Psi}(\boldsymbol{\rho}, \tau) = \prod_j^N e^{-3.44\left|\frac{\boldsymbol{\rho} - \tau \boldsymbol{v_j}}{r_{0,j}}\right|^{5/3}} . \tag{1.21}$$

As for the Fried parameter r_0, corresponding to a spatial coherence area of the distorted field, a coherence time τ_0 of the distorted field can be defined as [29]:

$$\tau_0 = \frac{r_0}{v_{moy}} , \tag{1.22}$$

corresponding to the time over which the spatio-temporal covariance converges to zero. $v_{moy} = 1/N \sum_j v_j$ corresponds to the average velocity of the layers along the propagation path.

1.2.2.4 Phase screens propagation

Using Equation 1.15, after propagation through the turbulent atmosphere, the distorted field can be computed by end-to-end (E2E) simulation [31]. In this thesis, we use the code TURbulence simulator for spAce-grouND Optical Telecommunication (TURANDOT) developed by ONERA and CNES [18] to simulate propagation through the turbulent atmosphere.

1.2.2.5 The Rytov approximation

The complex amplitude in the propagation equation 1.11 can be written as:

$$\Psi(\boldsymbol{r}) = e^{\psi(\boldsymbol{r})}\,, \tag{1.23}$$

with $\psi(\boldsymbol{r}) = \chi + i\varphi(\boldsymbol{r})$ considering the complex amplitude decomposed in phase and amplitude such as: $\Psi(\boldsymbol{r}) = A(\boldsymbol{r})e^{i\varphi(\boldsymbol{r})}$, with $\chi = ln(A(\boldsymbol{r}))$ the log-amplitude.

The Rytov approximation supposes that $\psi(\boldsymbol{r})$ can be decomposed in an unperturbed term ψ_0 and a small perturbation term ψ_1 induced by the first-order perturbation of the refractive index [21]. The substitution of 1.23 in 1.11 and solving the new propagation equation gives an analytical solution of the perturbation term ψ_1 [32]:

$$\psi_1(\boldsymbol{r}) = \frac{k_0^2}{2\pi e^{\psi_0}} \int_v N(\boldsymbol{r'}) e^{\psi_0(\boldsymbol{r'})} \frac{e^{ik_0|\boldsymbol{r}-\boldsymbol{r'}|}}{|\boldsymbol{r}-\boldsymbol{r'}|} d\boldsymbol{r'}\,. \tag{1.24}$$

v is the volume of propagation. In the Rytov approximation, the fluctuations of φ and χ are supposed to be Gaussian.

1.2.2.6 Intensity fluctuations

Let I be the intensity of the optical wave such as $I = \Psi\Psi^* = e^{2\chi}$. The fluctuations of the intensity are usually characterized by their normalized fluctuations:

$$\delta I = \frac{I - \langle I \rangle}{\langle I \rangle}\,. \tag{1.25}$$

The variance of the normalized intensity fluctuations are:

$$\begin{aligned} \sigma_{\delta I}^2 =& \frac{\langle I^2 \rangle}{\langle I \rangle^2} - 1 \\ =& e^{4\sigma_\chi^2} - 1 \end{aligned} \tag{1.26}$$

As the strength of the turbulence or the propagation path increases, the perturbation regimes become stronger, and the intensity fluctuations increase up to a saturation point.

1.2.2.7 Statistics of the modulus of the complex amplitude of the distorted field after propagation through the turbulent atmosphere

The statistic of the modulus of the complex amplitude of the distorted field collected by a telescope after propagation through the turbulent atmosphere depends on the turbulence strength. Two models are commonly used: a log-normal distribution in weak perturbation conditions given by the Rytov approximation [21], and a Rayleigh distribution when the variance of the amplitude of the distorted field is strong [33] and we can consider random phasor sums.

Rayleigh distribution: The Rayleigh's probability density function is:

$$f(x, \sigma) = \frac{x}{\sigma^2} e^{\frac{-x^2}{2\sigma^2}}\,, \tag{1.27}$$

with σ the scale parameter of the distribution. Let X be a random variable following a Rayleigh distribution of parameter σ, the first moment is:

$$\begin{aligned} \mu_1 &= \langle X \rangle \\ &= \sigma \sqrt{\frac{\pi}{2}} \,. \end{aligned} \tag{1.28}$$

The variance of X is given by:

$$\begin{aligned} var(X) &= \left\langle X^2 \right\rangle - \langle X \rangle^2 \\ &= \left(2 - \frac{\pi}{2}\right) \sigma^2 \,. \end{aligned} \tag{1.29}$$

Thus it comes:

$$\left\langle X^2 \right\rangle = 2\sigma^2 \,. \tag{1.30}$$

Finally we have the relation:

$$\langle X \rangle = \sqrt{\frac{\pi}{4}} \times \sqrt{\langle X^2 \rangle} \tag{1.31}$$

Log-normal distribution: The log-normal's probability density function is:

$$f(x, \sigma, \mu) = \frac{1}{x\sigma\sqrt{2\pi}} e^{\frac{-ln(x-\mu)^2}{2\sigma^2}} \,, \tag{1.32}$$

with μ and σ the parameters of the law. Let X be a random variable following a log-normal distribution of parameter σ and μ, we have:

$$\langle X \rangle = e^{\mu + \sigma^2/2} \,, \tag{1.33}$$

and

$$\begin{aligned} \left\langle X^2 \right\rangle &= e^{2\mu + 2\sigma^2} \\ &= \langle X \rangle^2 \, e^{\sigma^2} \,, \end{aligned} \tag{1.34}$$

Finally we have the relation:

$$\langle X \rangle = e^{-\sigma^2/2} \times \sqrt{\langle X^2 \rangle} \,. \tag{1.35}$$

1.2.3 SMF coupling

Let $\Psi^{turb}(\boldsymbol{r})$ be the complex amplitude of the field in the pupil plane of a telescope after turbulent atmospheric propagation. The power coupled in a SMF, calculated in the pupil plane, is [34]:

$$\eta = \left| \frac{\left\langle \Psi^{turb} P | M_0 \right\rangle}{\sqrt{\langle P\Psi^{turb} | P\Psi^{turb} \rangle \, \langle M_0 | M_0 \rangle}} \right|^2 \,, \tag{1.36}$$

with $\langle X(\boldsymbol{r}) | Y(\boldsymbol{r}) \rangle = \int X(\boldsymbol{r}) Y(\boldsymbol{r})^* d\boldsymbol{r}$ denoting the scalar product. M_0 the SMF mode can be approximated by a Gaussian mode in the pupil plane. P is the telescope pupil transmittance. Without turbulence, considering a circular pupil the maximum coupling rate η is ≈ 0.82 [34].

The power coupled in the SMF severely degrades in the presence of atmospheric turbulence as shown in [35, 17, 34] implying fadings (complete loss of signal) and strongly attenuating the average coupled power, which limits the link bandwidth. Thus, atmospheric turbulence effects mitigation methods are required.

1.3 Atmospheric turbulence effects mitigation methods for FSO communications

Atmospheric turbulence effects induce fading and average attenuation in the SMF coupling rate. For applications where the signal attenuation is limiting, active mitigation methods are required to increase the average coupled flux. For example, for GEO-ground links, the average coupled flux is critical due to geometrical losses. For applications where the average coupled flux is less limiting but fadings still need to be mitigated, passive or active mitigation methods can be used.

1.3.1 Passive mitigation methods

Increasing the telescope aperture allows to average the scintillation effects and to reduce the fadings [9]. However, increasing the telescope aperture degrades the seeing conditions and reduces the average coupling ratio. Thus, passive methods have been developed to overcome the loss of FSO link bandwidth due to atmospheric turbulence effects such as diversity methods in time, frequency or spatial [9, 8]. In spatial diversity, multiple receiver apertures are used to obtain multiple uncorrelated signals. On the other hand, the spatial aperture separation must be greater than the spatial coherence area, r_0, [36, 9], increasing the receiver system complexity. In wavelength diversity, the signal is transmitted on several wavelengths, and the receiver end is composed of several receiver apertures, each detecting a specific wavelength [37, 9]. In time diversity, temporal coding and interleaving are used to add redundant information in the link on time longer than the coherence time [38, 9]. However, time diversity implies latency delay and requires large memory at the receiver [38].

It is worth noting the Small Optical Ground Stations Focal-Optics Assembly (SOFA) of DLR, which is used on two OGS (LaBoT and FOGATA). The SOFA system provides direct signal detection with avalanche photodetectors. The idea behind SOFA is to provide a fully integrated and low-cost instrument to be mounted on existing telescopes to provide easy deployment and cost-effective OGSs [39]. Further deployments of SOFA are planned at the University of the Bundeswehr Munich's OGS, the University of Auckland's OGS, and DLR's OGSOP. On the other hand, the link bandwidth reachable with such a system is only 1 Gbs^{-1} [40].

In addition to passive methods, it is also possible to actively mitigate the effects of atmospheric turbulence. These active methods are known as adaptive optics.

1.3.2 Classic adaptive optics

Adaptive Optics (AO) was first conceptualized by Babcock in the early 50s [41]. The first public development of AO was demonstrated in the early 90s to mitigate atmospheric turbulence effects in astronomy with the COME-ON project [42]. As presented in Figure 1.5 an AO system is composed of three components.

1. The WaveFront Sensor (WFS) is a device giving indirect information on wavefront distortion using intensity measurements.

2. The RTC aims to estimate the shape of the distorted wavefront in real-time. The intensity measurements provided by the WFS are first used to compute the phase slopes. Then, a command matrix is used to compute the residual correction voltages of the Deformable Mirror (DM) from the phase slopes. The RTC apply the residual correction voltages in a feedback loop, an integrator control loop as an example, to compute the correction voltages to be sent to the DM.

3. The DM which is composed of actuators controlled by voltages applied by the RTC, so that the overall shape of the DM compensates for the distorted measured wavefront.

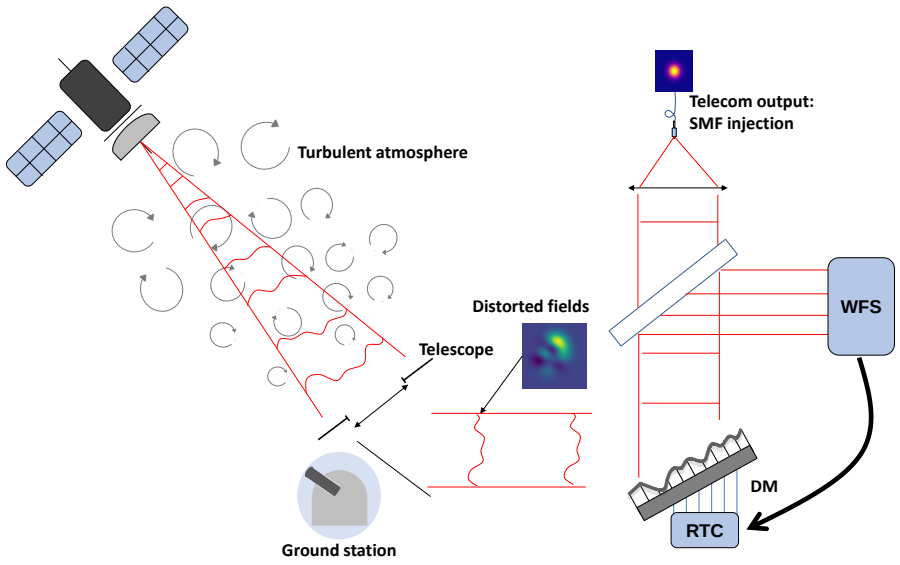

Figure 1.5: Satellite-to-ground link, the distorted field is collected by the telescope of the OGS and atmospheric turbulent effects are mitigated by the AO system. After correction, the laser beam is injected in a SMF.

1.3.2.1 WFS limitations

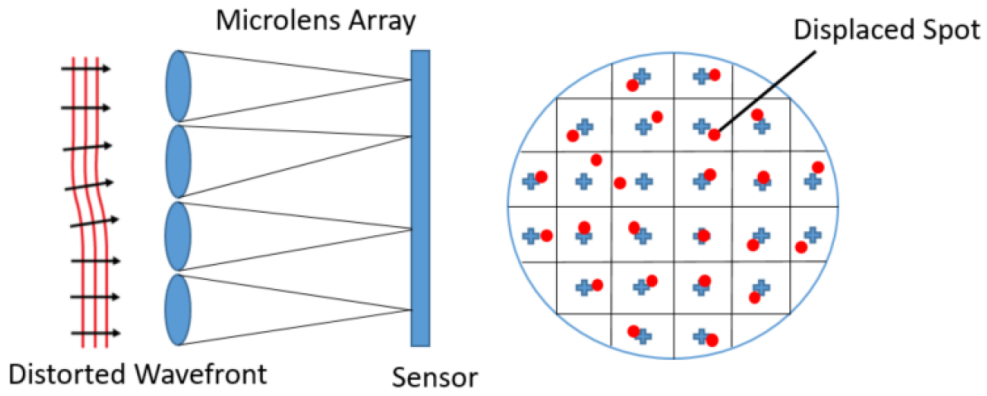

Figure 1.6: Shack-Hartmann WFS principle, taken from [6].

The most used WFS in AO is the Shack-Hartman WFS (SHWFS). It is composed of a microlens array followed by a matrix of sensors. Each sub-pupil aims at measuring the local wavefront slope. Other types of WFS are used, such as the pyramid WFS, the curvature WFS or the phase diversity method [43].

Figure 1.6 schematizes a SHWFS. The wavefront is estimated using the relative displacement between the intensity spots in the sensor. For low satellite elevation, the scintillation effects are predominant. Scintillation effects imply fluctuating intensity extinctions on the sensor, which degrades the WFS performances [44, 45].

1.3.2.2 DM limitations

A DM comprises several actuators, allowing it to modify its surface shape. The number of actuators gives the number of modes it can mitigate and, thus, how well the distorted wavefront can be compensated. This leads to the definition of the fitting error, which is defined as the residual phase variance after correction:

$$\sigma^2_{fitting} = a \left(\frac{d}{r_0} \right)^{5/3} . \tag{1.37}$$

d is the step between each actuator and, a, is a coefficient depending on the type of DM considered [43].
The DM surface can be segmented or continuous. Various technologies of actuators exist. Piezoelectric actuators allow 10 kHz of resonance frequency but are bulky DMs. Electromagnetic actuators are more compact but are limited in bandwidth to a few kHz [43]. Electrostatic actuators allow extreme miniaturisation DMs with large bandwidths but are fragile and allow only small amplitude corrections [43]. The main limitation comes from the limited bandwidth of the actuators.

1.3.2.3 Classic AO bench induced losses

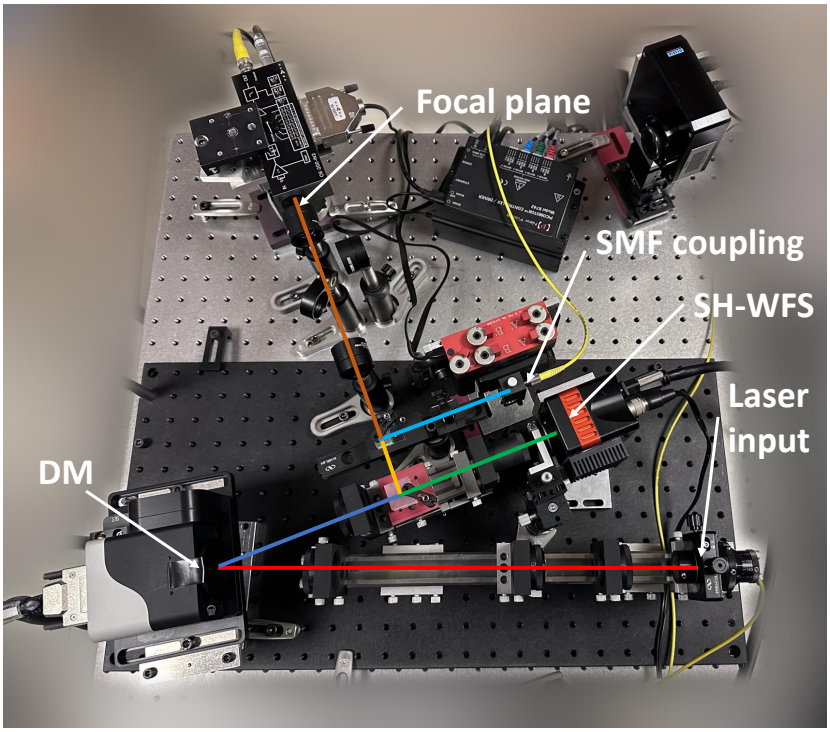

Figure 1.7: LISA, a compact AO bench for LEO-to-ground links at ONERA [46].

An AO bench possesses two main sources of losses: the losses induced by transmissions and reflections on imperfect optics and the losses induced by SMF coupling. With a SMF coupling of 0.82, considering 3% of loss per optical surface, and an AO bench possessing

about twenty optical surfaces, an order of magnitude for the total losses of an AO bench is:

$$\begin{aligned} L_{AO} &= 10 \times (log(0.82) + log(0.97) \times 20) \\ &= -3.5\ dB \end{aligned}.$$

Figure 1.7 presents a photo of LISA, a compact AO bench developed at ONERA for LEO-to-ground FSO links. Compared with the value calculated above, the LISA bench possesses 3.3 dB losses (including SMF coupling) [46].

In this thesis, we take 4 dB of total loss as the maximum target value to be reached by the atmospheric turbulence mitigation technique studied in this thesis.

1.3.3 Solutions implementing classic AO

Most existing OGS, or in development, integrates AO to mitigate atmospheric effects to performed SMF injection such as:

- The NASA OCTIL OGS [15] used with a CubeSat to perform 100 and 200 Gbps LEO links at 1.5 µm with a 1 m telescope equiped with AO [47]. It is part of the NASA Laser Communications Relay Demonstration (LCRD) [48] composed of a GEO-satellite and two OGS. It is a long-term experiment to evaluate atmospheric turbulence effects on link availability and performances for bidirectional FSO link between ground and GEO-satellite.
- The Tesat and DLR Transportable Adaptive Optical Ground Station (TAOGS), is a transportable OGS with a 27 cm receiver telescope equipped with AO for LEO and GEO link. Demonstration of 1.8 *Gbps* was performed [49, 50, 51].
- The ESA OGS with a 1 m telescope equipped with AO located in Tenerife [52], has performed FSO link with the GEO-satellite AlphaSat [53].
- The DLR's Oberpfaffenhofen OGS is equipped with a 80 cm telescope [54] with AO. Several links were performed with a GEO satellite, with AlphaSat, and with a CubeSat in Sun-synchronous orbit.
- The ONERA OGS FEELINGS equipped with AO is designed for GEO feeder links pre-compensation. It comprises a 60 cm telescope and a 20 cm decentered telescope. It is also designed to perform LEO downlinks [55].
- The FROG CNES OGS equipped with AO uses two 50 cm telescopes to perform LEO data repatriation and satellite feeder links [56].
- The Australian National University is developing the ANU OGS with a 70 cm telescope equipped with AO. It is being designed for LEO and GEO links [57].
- The University of Western Australia is developing three OGS (TeraNet) for LEO links. TeraNet-2 will be equipped with AO [39].

1.3.4 Sensorless adaptive optics

As developed above, for LEO satellite downlinks at low elevations, the WFS is limited by the scintillation effects, which can impair the AO correction. Furthermore, with developments of OGS networks and transportable OGSs, using more compact and easier-to-implement atmospheric effects mitigation methods could ease such developments.

Sensorless AO has been developed in this way. It uses the SMF injected power as a metric to be maximized to control the DM [58, 59, 60, 61, 62, 63]. Still, sensorless AO correction can be impaired by DMs limited bandwidth.

1.4 Integrated adaptive optics: a new mitigation method to overcome AO limitations

In his thesis [1], N. Schwartz proposed a new turbulent atmospheric effects mitigation method avoiding the use of WFS and DMs to obtain a compact and mechanically robust solution which comes as an integrated adaptive optics. Figure 1.8 depicts the integrated-AO atmospheric turbulence effects mitigation technique. It consists of decomposing the distorted field received in the telescope pupil plane in several guided waves using a spatial demultiplexer and coherently combining the demultiplexer outputs using a Photonic Integrated Circuit (PIC) in order to maximize the intensity injected in a SMF.

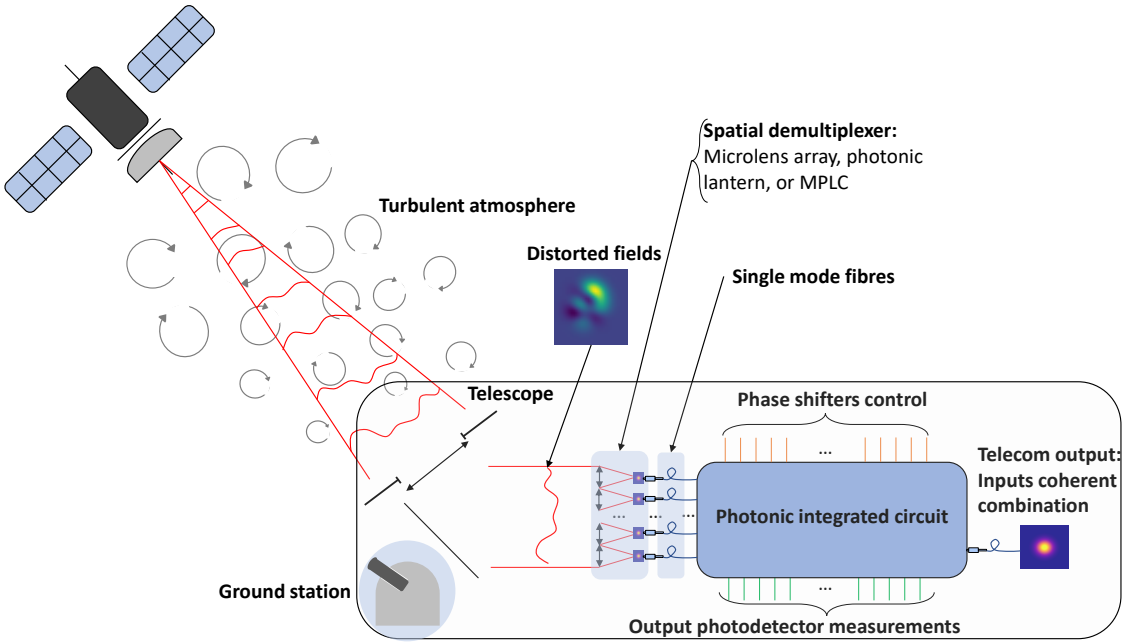

Figure 1.8: Principle of integrated adaptive optics.

1.4.1 Spatial demultiplexer

Let Ψ^{turb} be the complex amplitude of the distorted field received in the OGS telescope pupil plane after turbulent atmospheric propagation. $P\Psi^{turb}$, with P corresponding to the telescope pupil transmittance, is part of a Hermitian space and it can be decomposed in orthonormal bases of modes (M_j) such as:

$$P\Psi^{turb} = \sum_{j=0}^{N-1} \langle P\Psi^{turb} | M_j \rangle M_j + \underbrace{\sum_{j=N}^{\infty} \langle P\Psi^{turb} | M_j \rangle M_j}_{\Psi_\infty} . \tag{1.38}$$

$\langle | \rangle$ denotes the scalar product defined as $\langle X(\boldsymbol{r}) | Y(\boldsymbol{r}) \rangle = \int X(\boldsymbol{r}) Y^*(\boldsymbol{r}) d\boldsymbol{r}$, N is the number of modes on which the modal decomposition of $P\Psi^{turb}$ is performed and Ψ_∞ the fitting error term, equivalent to the fitting error in AO, corresponding to unseen modes.

A review of the various spatial demultiplexer devices available to perform the modal decomposition is given in L.Rinaldi's thesis [6] and in [64]. In this thesis we focus on the three main spatial demultiplexers: Microlens arrays, photonic lanterns and MPLC.

1.4.1.1 Microlens Arrays

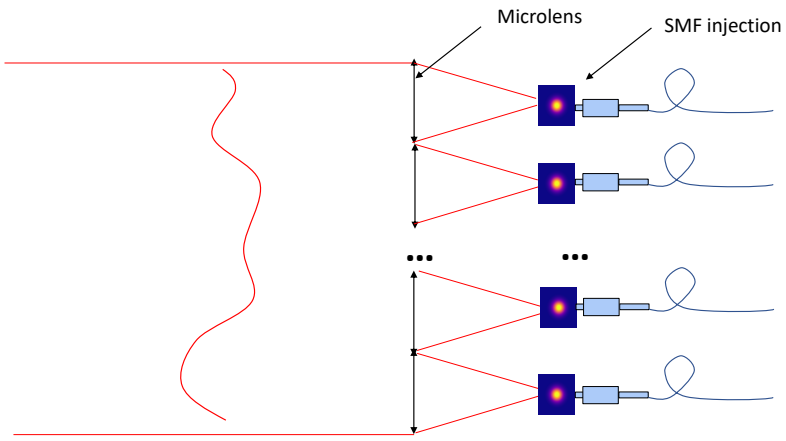

Figure 1.9: Microlens Array used as a spatial demultiplexer.

Microlens Arrays can be used as fibre collimator arrays [65]. As in a Shack-Hartmann WFS, each microlens sample a part of the incident distorted field. A 2D SMF array is placed behind the microlens array so that each microlens focal plane complex amplitude is injected in a SMF [35], see Figure 1.9. With a Microlens Array, it is possible to decompose the distorted fields over hundreds of modes [66]. However, with existing devices, positioning imprecision of the fibre array behind the microlens array generates losses [67]. A rough estimate of the positioning imprecision is of the order of the μm [68, 69], approximately the same order of magnitude as the spot size at the microlens focal plane. Thus, static tip-tilt correction devices, such as SLM or tip-tilt actuators, are used to compensate for the static positioning imprecision to reach an overall loss of around 3 dB [70].

1.4.1.2 Photonic Lantern (PL)

PL comprises one multimode end and another with multiple SMF outputs. With a PL, the distorted field is injected in the multimode end and decomposed in the SMFs at the output of the PL [71, 72]. Decomposition over a few tens of modes is possible with losses below 1 dB [64]. A schema from [73] is given Figure 1.10. PL are also used as wavefront sensors [73, 74]. However, this technology is still in development in laboratories, and the distorted field modal decomposition efficiency with PL modes is still to be evaluated.

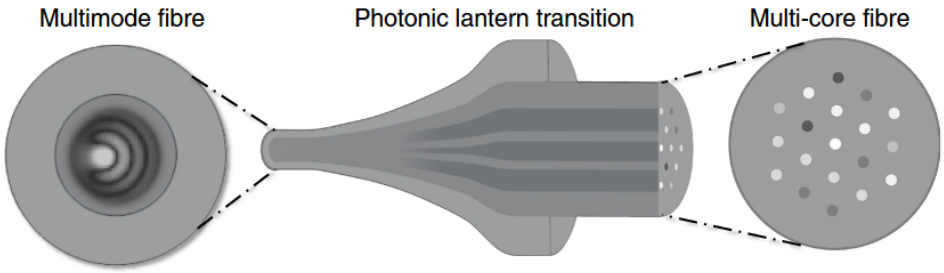

Figure 1.10: Photonic lantern schema from [73] with its multimode fibre end on the left and the multiple SMF end on the right.

1.4.1.3 Multi-Plane Light Conversion (MPLC)

A MPLC is a device allowing to perform unitary transform between two bases of modes using multiple reflections on phase plates [75, 76], see Figure 1.11. A MPLC allows a decomposition over a few tens of modes with between 3-5 dB losses [64, 75].

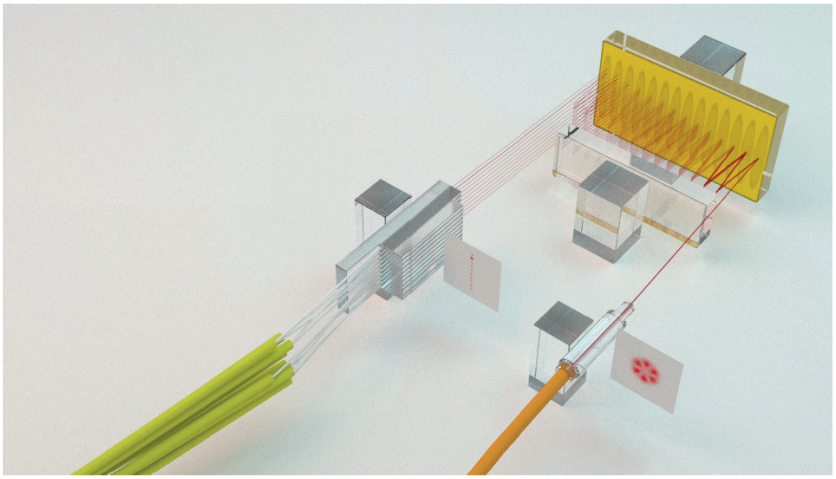

Figure 1.11: Multi-Plane Light Conversion (MPLC) ©Cailabs.

More specifically a MPLC allows to decompose the distorted field on Hermite-Gaussian (HG) modes. In his thesis [6], Rinaldi shows that HG modes are nearly the optimal basis to fit a distorted field with a minimum number of modes. In this thesis, the HG modes are sorted in a triangular pattern as $HG_{n,m}$:

n \ m	0	1	2	⋯
0	0	2	5	9
1	1	4	8	12
2	3	7	11	⋰
⋮	6	10	⋰	⋰

Figure 1.12: $HG_{n,m}$ mode numbering.

1.4.1.4 Optical phase array antenna

The modal decomposition can be performed directly inside the PIC [77]. 2D optical phase arrays antenna [78] based on grating couplers [79] are used to perform the FSO beam injection in the PIC [80, 81]. Only a few modes of decomposition have been demonstrated [82, 80, 83] up to 16 modes [2]. However, the distorted field modal decomposition efficiency and losses are still to be evaluated.

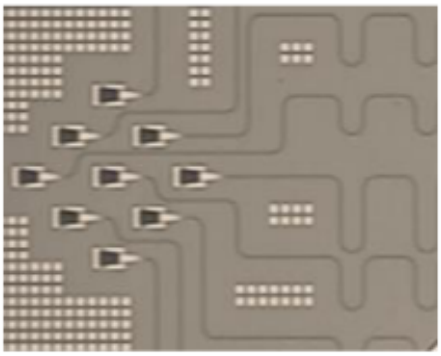

Figure 1.13: Optical phase array antenna from [84].

1.4.2 PICs coherent combination as integrated DMs

Modal decomposition of $P\Psi^{turb}$ in several guided waves using spatial demultiplexers is the first step of integrated-AO. The second step corresponds to the coherent combination of the complex amplitudes of the guided waves using a Photonic Integrated Circuit (PIC).

In this thesis, the spatial demultiplexer output complex amplitudes are associated with the PIC guided waves for simplification.

To perform the coherent combination, a PIC comprises several couplers allowing the complex amplitudes to interfere. As a DM is composed of actuators, a PIC comprises phase shifters to control the output interference states of the couplers.

1.4.2.1 Simple coupler model

Let $E_1 = |E_1|e^{i\varphi_1}$ and $E_2 = |E_2|e^{i\varphi_2}$ be two complex amplitudes at the input of a coupler. A coupler is characterized by its coupling coefficient c. Let E_a and E_b be two complex amplitudes at a coupler outputs corresponding to the interference between E_1 and E_2, we have the relation [85]:

$$\begin{pmatrix} E_a \\ E_b \end{pmatrix} = c \begin{pmatrix} i & 1 \\ 1 & i \end{pmatrix} \begin{pmatrix} E_1 \\ E_2 \end{pmatrix} . \tag{1.39}$$

For a balanced couplers we have $c = \sqrt{2}/2$ giving:

$$\begin{cases} |E_a|^2 = \frac{1}{2}\left(|E_1|^2 + |E_2|^2\right) - |E_1||E_2|sin(\varphi_1 - \varphi_2) \ , \\ |E_b|^2 = \frac{1}{2}\left(|E_1|^2 + |E_2|^2\right) + |E_1||E_2|sin(\varphi_1 - \varphi_2) \end{cases} . \tag{1.40}$$

With a balanced coupler if $\varphi_1 = \varphi_2$ we have balanced intensities at the outputs of the coupler. In the following the notation 50:50 denotes a balanced coupler.

By adding a phase-shifter at the input of a coupler, it is possible to control the relative phase between the two input complex amplitudes. Figure 1.14 depicts a simple coupler with a phase shifter.

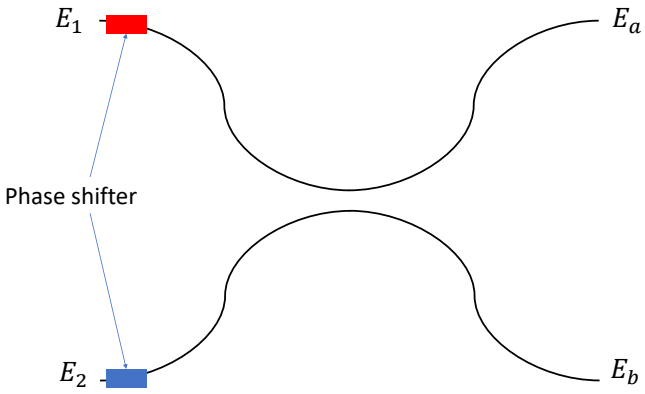

Figure 1.14: Simple coupler with one phase-shifter. It can be placed on the input top arm, red rectangle, or in the input bottom arm, blue rectangle, or in push-pull, both blue and red rectangles, with opposite phase shift.

The phase-shifter can be placed on the input top arm, red rectangle, or placed on the input bottom arm, blue rectangle, or placed in push-pull, both red and blue rectangle with opposite phase, meaning if a phase φ^{ps} is applied on the coupler top arm a phase $-\varphi^{ps}$ is applied on the coupler bottom arm.

For example, for a phase-shifter, introducing a phase φ^{ps}, placed on the input top arm of a 50:50 coupler, then, the matrix of the coupler becomes:

$$\frac{\sqrt{2}}{2} \begin{pmatrix} ie^{i\varphi^{ps}} & 1 \\ 1e^{i\varphi^{ps}} & i \end{pmatrix} . \tag{1.41}$$

With a 50:50 coupler, by setting the phase shifter to compensate for the phase difference between the input complex amplitudes, one output intensity can be maximized and the other minimized. Having 0 on one output and $|E_1|^2 + |E_2|^2$ on the other one is possible only if $|E_1| = |E_2|$.

1.4.2.2 PIC architectures as integrated-DM

To coherently recombine the complex amplitudes obtained from the modal decomposition of $P\Psi^{turb}$, two architectures of PIC have been proposed in the literature and are presented

below.

Geometric architecture as an integrated-DM: The first architecture was proposed by N.Schwartz [1]. It allows us to combine the PIC input complex amplitudes in a binary tree-like architecture, referred to here as geometric architecture, see Figure 1.15. It is the most compact architecture to combine N complex amplitudes in one output. For N inputs, it possesses $N-1$ output intensity measurements and one coherent output (or telecom output) in which the N input complex amplitudes may be coherently combined. The telecom output corresponds to the OGS SMF. In the following, we denote the PIC coherent output by s_0. For the coherent combination, $N-1$ couplers are spread in $k = ln(N)/ln(2)$ stages, which makes it a compact architecture. $N-1$ phase-shifters are used to control the phase differences between the inputs of the couplers allowing for a phase-only correction. They can be placed at the PIC inputs, as a DM in classic AO, hence the denomination integrated-DM.

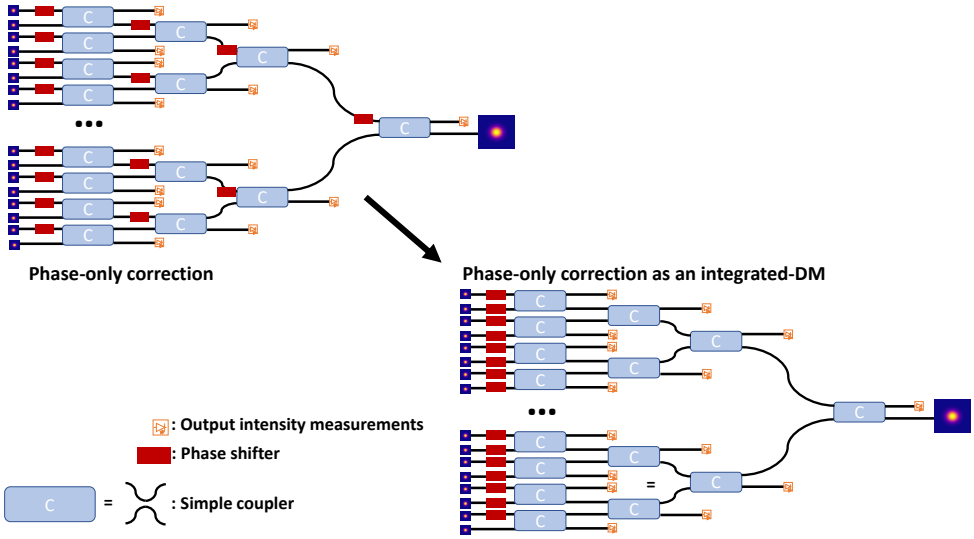

Figure 1.15: Geometric architecture for phase-only correction.

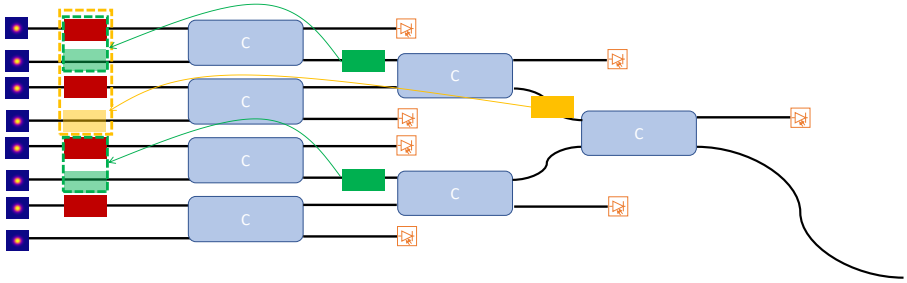

Figure 1.16: Schema demonstrating the equivalence with the phase shifters moved to the PIC input.

Figure 1.16 demonstrates the equivalence of the phase shifters moved to the PIC input. The dark green phase shifters can be moved to the position of the transparent green one. Then, setting the dark green phase shifters is equivalent to setting both transparent green and dark red phase shifters framed by dotted green lines (thus, the phase piston is not seen by the first coupler but by the second one at the location of the dark green rectangle).

With such an architecture, to perform measurement intensities, most of the outputs need to cross waveguides, perform 180° bend, or need integrated photodiodes.

Arithmetic architecture as an integrated-DM: The second architecture was proposed by K.Saab [85]. With this architecture, the input complex amplitudes are combined one by one in an arithmetic sequence with a common difference of 1. We named this architecture: arithmetic architecture, see Figure 1.17. For N inputs, it possesses $N-1$ output intensity measurements and one coherent output (or telecom output) s_0. It also possesses, $N-1$ couplers spread in $k = \frac{N}{2}$ stages. Unlike geometric architecture, arithmetic architecture is not compact and becomes relatively long when N increases. As for the geometrical architecture, it possesses $N-1$ phase-shifters for phase-only correction that can be placed at the PIC inputs.
The main advantage of this architecture is that all output intensity measurements are placed at the output of the circuits, meaning one waveguide does not have to cross another one or to go back 180° to be coupled an measured out of the PIC.

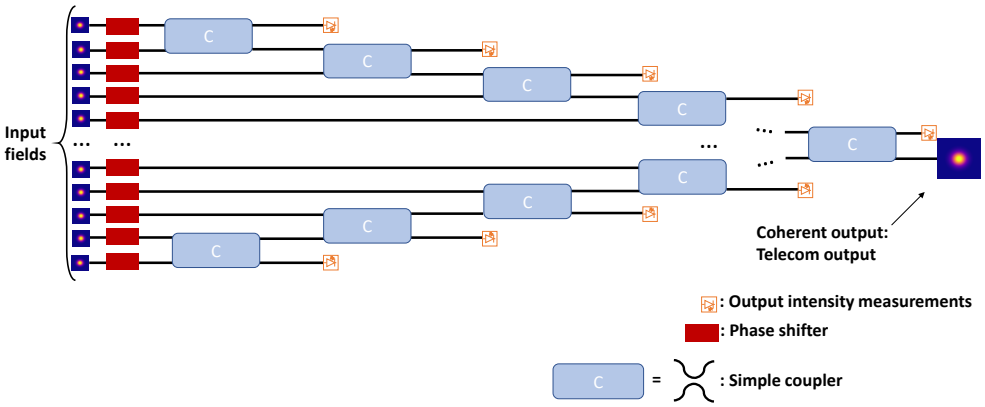

Figure 1.17: PIC arithmetic architecture for phase-only correction.

However, the deeper in the PIC stages, the more a coupler sees unbalanced input complex amplitudes. We denote by U_n the sequence corresponding to half of the energy in s_0 (half of the PIC). Thus, the total energy in s_0 is $2U_n$. Considering uniform modulus of input complex amplitudes, all equals to U_0, the energy after one coupler is $U_1 = 2U_0$ and the energy after k couplers is:

$$U_n = \left[\frac{\sqrt{2}}{2}\left(\sqrt{U_{n-1}} + \sqrt{U_0}\right)\right]^2 . \tag{1.42}$$

Denoting $V_n = \sqrt{U_n}$, it comes:

$$V_n = \frac{\sqrt{2}}{2}V_{n-1} + \frac{\sqrt{2}}{2}V_0 , \tag{1.43}$$

corresponding to an arithmetico-geometric sequence. Because $\sqrt{2}/2 < 1$, V_n converges to:

$$\begin{aligned} l &= \frac{V_0\sqrt{2}}{2-\sqrt{2}} \\ &= 2.41 \times V_0 \end{aligned}$$

Thus, the total energy in s_0 converges to $2 \times (2.41V_0)^2 = 11.65 \times U_0$ for an infinite number of PIC inputs.
Figure 1.18 plots sequence 1.42, which converges quickly after $n = 10$. Thus, arithmetic architecture with phase-only correction only allows the coherent combination of a few inputs.

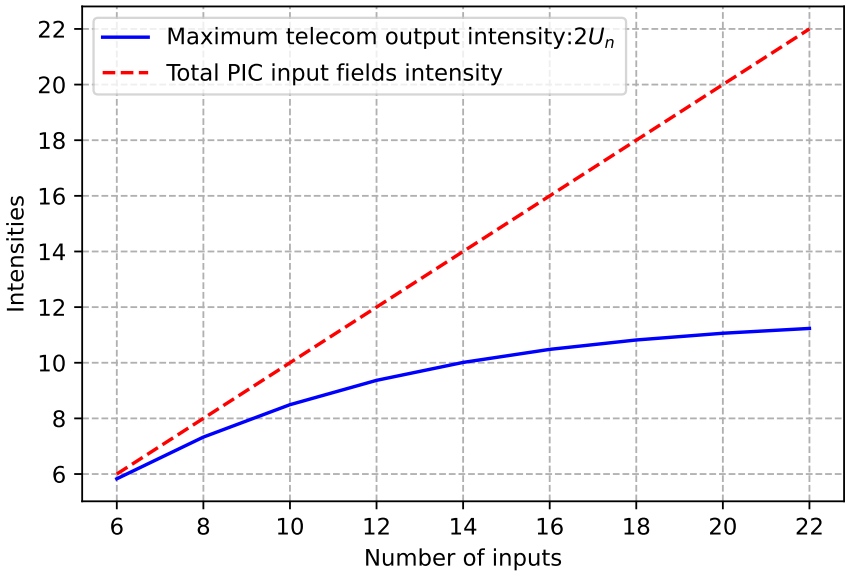

Figure 1.18: Blue curve corresponds to the maximum of s_0 with arithmetic architecture considering uniform input intensities $U_0 = 1$. Red dotted curve corresponds to the total PIC input energy, both curves are function of the number of PIC inputs.

1.4.3 PIC architecture for phase and amplitude correction

As developed above, PICs with simple couplers such as integrated-DM allow for phase-only correction. Thus, the maximum energy in s_0 equals the PIC input energy only if the modulus of its input complex amplitudes are all equals. Otherwise, the maximum energy in s_0 is lower than the total PIC input energy. The theoretical correction efficiency of such PIC is the same as with classic AO.
As developed in [1], integrated optics allows the integration of Mach-Zehnder Interferometer (MZI)s, thus allowing MZI-based PIC to perform phase and amplitude correction.

1.4.3.1 Mach-Zehnder Interferometer (MZI)

As depicted in Figure 1.19, a Mach-Zehnder Interferometer (MZI) is composed of two following couplers with one external phase-shifter placed before the first coupler and one internal phase-shifter placed between the two couplers. Both phase shifters are placed

in position blue or red or both in push-pull (meaning if a phase φ^{ps} is applied on the coupler top arm, a phase $-\varphi^{ps}$ is applied on the coupler bottom arm). As demonstrated in Appendix A a MZI allows for phase and amplitude correction.

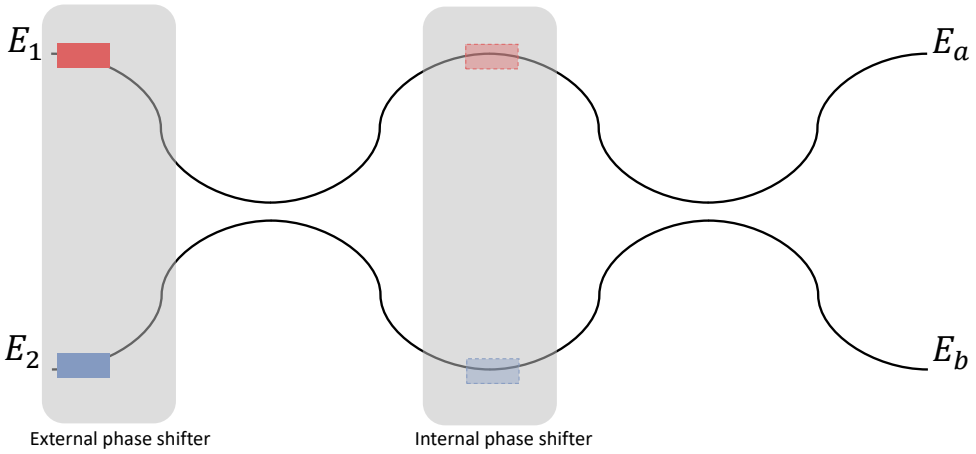

Figure 1.19: Mach-Zehnder Interferometer (MZI) composed of two couplers with two independent phase shifters: one external phase-shifter placed in position blue or red or both in push-pull, and one internal phase-shifter in position blue or red or both in push-pull.

For example, if both external phase-shifter φ^{ps^e} and internal phase-shifter φ^{ps^i} are placed in the top arm position (red rectangle), the MZI matrix for 50:50 couplers is:

$$\frac{1}{2}\begin{pmatrix} ie^{i\varphi^{ps^i}} & 1 \\ e^{i\varphi^{ps^i}} & i \end{pmatrix}\begin{pmatrix} ie^{i\varphi^{ps^e}} & 1 \\ e^{i\varphi^{ps^e}} & i \end{pmatrix} = \frac{1}{2}\begin{pmatrix} e^{i\varphi^{ps^e}}\left(1-e^{i\varphi^{ps^i}}\right) & i\left(1+e^{i\varphi^{ps^i}}\right) \\ ie^{i\varphi^{ps^e}}\left(1+e^{i\varphi^{ps^i}}\right) & e^{i\varphi^{ps^e}}-1 \end{pmatrix} \tag{1.44}$$

1.4.3.2 Architecture for phase and amplitude correction

The geometric and arithmetic architectures described in section 1.4.2.2 can be modified to replace simple couplers by MZIs for phase and amplitude correction, see Figures 1.20 and 1.21.

Compared to phase-only correction PIC, the number of couplers and phase-shifters is multiplied by two for phase and amplitude correction, thus implying more complex architectures.

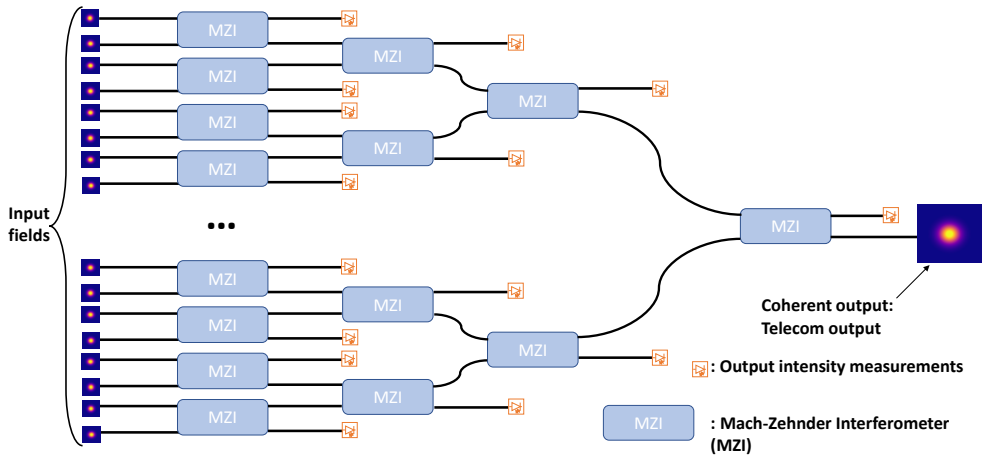

Figure 1.20: PIC geometric architecture with MZI for phase and amplitude correction.

With MZIs, the problem of arithmetic architecture with phase-only correction implying s_0 being a sequence converging quickly after ten inputs is solved.

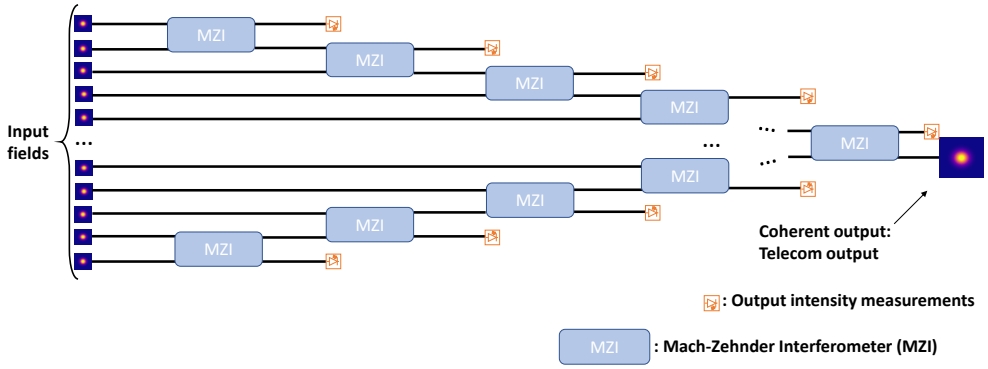

Figure 1.21: PIC arithmetic architecture with MZI for phase and amplitude correction.

The external phase shifters of MZI can all be placed at the PIC inputs as with a PIC as an integrated-DM. However, the internal phase shifter of a MZI cannot be removed from between the two couplers.

1.5 Phase shifters control methods review

The PIC phase-shifters must be controlled in real-time to perform its input guided waves coherent combination in s_0. In the following, the problem of phase shifter real-time control is split into two cases.
We will first address the case of PIC as integrated-DM (phase-only correction). Indeed, the problem of phase shifters real-time control to maximize s_0 in the case of PIC as integrated-DM is similar to the control of a DM in sensorless AO or the problem of

coherent combination of N laser beams through the turbulent atmosphere. Thus, in the following Section 1.5.1, I propose a review of the different control methods for sensorless AO or laser beams coherent combination through the turbulent atmosphere.
Then, I address the problem of phase shifters real-time control for phase and amplitude correction with MZI-based PIC.

1.5.1 Sensorless control methods

These methods can be apply to a wide range of problems and not just PIC with phase-only correction, their review is given by defining a general class of problem to which they are applicable: a Single Mode Injection Device (SMID).

1.5.1.1 Single Mode Injection Device (SMID) definition

Let us define a Single Mode Injection Device (SMID) as a programmable optical device, applying some linear transformation on N input complex amplitudes to inject them in one single output mode of the SMID.
Let H_a be the SMID input space composed of N complex amplitudes, and H_e the SMID output space composed of N_e complex amplitudes.
A SMID is also defined to possess N_{ps} programmable phase elements placed at the input of the injection device. Programmable phase elements can be actuators or phase-shifters, for example. With such a definition a SMID is a linear programmable system, mapping from input space H_a to output space H_e. Figure 1.22 depicts such an optical device.

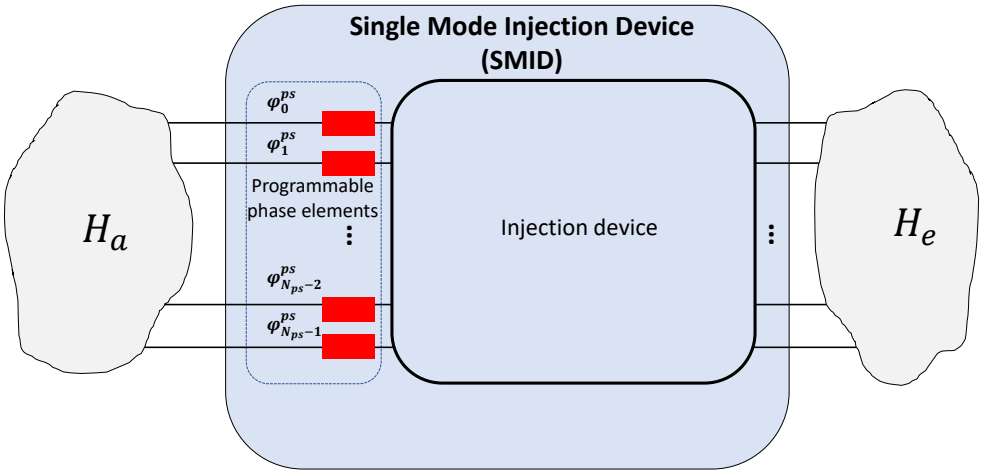

Figure 1.22: Single mode injection device schema. With N complex amplitudes at its input: $dim(H_a) = N$, N_e complex amplitudes at its output: $dim(H_e) = N_e$ and N_{ps} programmable phase elements.

Thus, a SMID can be defined by a matrix $\boldsymbol{C^{ps}}$ of N_e lines and N rows, composed of complex elements $C_{k,l}^{ps}$ depending on the SMID fixed architecture and programmable phase elements state, $\boldsymbol{\varphi^{ps}} = (\varphi_k^{ps})$, with $k \in (0, N_{ps} - 1)$.
Let, $\boldsymbol{a} = (a_l)$, be a SMID input vector composed of complex amplitudes a_l, with $l \in (0, N - 1)$, of input space H_a. Let, $\boldsymbol{e} = (e_j)$, be a SMID output vector composed of complex amplitudes e_j, with $j \in (0, N_e - 1)$, of output space H_e. The output vector $\boldsymbol{e}$ is a linear combination of input vector $\boldsymbol{a}$ by the SMID matrix $\boldsymbol{C^{ps}}$ such as:

$$\boldsymbol{e} = \boldsymbol{C^{ps}}\boldsymbol{a}\,. \tag{1.45}$$

From Expression 1.45, the SMID j^{th} output complex amplitude is:

$$e_j = \sum_{l=0}^{N-1} C_{j,l}^{ps} a_l\,. \tag{1.46}$$

With $a_l = |a_l| \times e^{i\varphi_{a_l}}$, from Expression 1.46, the SMID j^{th} output complex amplitude intensity is:

$$\begin{aligned} s_j &= e_j \times e_j^* \\ &= \sum_k \sum_l c_{j,k}^{ps} c_{j,k}^{ps^*} |a_k||a_l| e^{i(\varphi_{a_k} - \varphi_{a_l})}\,, \end{aligned} \tag{1.47}$$

with $*$ denoting the complex conjugate.
The purpose of a SMID is to set the programmable phase elements in such a state that all input complex amplitudes a_l are coherently combined in one single output of H_e. I arbitrarily designate such an output by index 0. Thus, the programmable phase elements must be set to maximize s_0.
With all programmable phase elements place at the SMID input, the matrix $\boldsymbol{C^{ps}}$ can be rewritten:

$$\boldsymbol{C^{ps}} = \boldsymbol{C^f}\,\boldsymbol{D^{ps}}\,, \tag{1.48}$$

with $\boldsymbol{C^f} = (c_{k,l}^f)$ a fixed matrix of complex elements only depending on the SMID architecture, with $c_{k,l}^f = |c_{k,l}^f| e^{i\varphi_{k,l}^f}$. And $\boldsymbol{D^{ps}}$ the diagonal matrix of programmable phase elements phasors $\left(e^{i\varphi_j^{ps}}\right)$. With this decomposition of $\boldsymbol{C^{ps}}$ **our SMID is defined for phase-only correction!**
From this, the j^{th} output intensity becomes:

$$\begin{aligned} s_j &= \sum_{k=0}^{N-1}\sum_{l=0}^{N-1} |c_{j,k}^f||c_{j,k}^f||a_k||a_l| e^{i(\varphi_{a_k} - \varphi_{a_l} + \varphi_k^{ps} - \varphi_l^{ps} + \varphi_{j,k}^f - \varphi_{j,l}^f)} \\ &= \sum_k |c_{j,k}^f|^2 |a_k|^2 + 2\sum_k \sum_{l>k} |c_{j,k}^f||c_{j,l}^f||a_k||a_l| cos\left(\varphi_{a_k} - \varphi_{a_l} + \varphi_k^{ps} - \varphi_l^{ps} + \varphi_{j,k}^f - \varphi_{j,l}^f\right) \end{aligned}\,. \tag{1.49}$$

$N_{ps} = N - 1$ programmable phase elements are required to maximize s_0 by phase-only correction. The number of programmable elements can be equal to the number of inputs $N_{ps} = N$ [86] with one programmable phase elements controlling for the global phase piston. For s_0 to be maximized, the $N_{ps} = N$ programmable phase elements must be adjusted so that we have the relation:

$$\varphi_{a_k} - \varphi_{a_l} + \varphi_k^{ps} - \varphi_l^{ps} + \varphi_{0,k}^f - \varphi_{0,l}^f = 2n\pi,\ \forall (k,l) \in (0, N-1),\ \text{and},\ n \in \mathbb{N}\,. \tag{1.50}$$

When s_0 is maximized, by energy conservation, s_j are minimized for $j \in (1, N_e - 1)$, and we have the relation:

$$\varphi_{0,l}^f - \varphi_{0,k}^f + \varphi_{j,k}^f - \varphi_{j,l}^f = (2n+1)\pi,\ \forall (k,l) \in (0, N-1),\ \text{and},\ n \in \mathbb{N}\,. \tag{1.51}$$

For example, specific cases of SMID can be deformable mirrors or spatial light modulators shaping input fields to obtain diffraction limited spots or performing SMF injection. An array of lasers with phase piston control to perform coherent combinations. PIC to perform SMF injection, etc.
Now that we have defined a SMID, the following section gives a review of the real-time control methods available.

1.5.1.2 SMID control methods review

Control methods developed in sensorless AO or coherent beam combining, used to perform single field mode injection can use one output intensity measurement or several output intensity measurements as criterion metrics to minimize or maximize. With our SMID definition, to mitigate atmospheric turbulence effects, the programmable phase elements must be controlled in real-time to maximize s_0.
In the following, Multiple-Inputs Single-Output (MISO) refer to control methods using one output measurement as a metric to maximize or minimize, and Multiple-Inputs Multiple-Outputs (MIMO) refer to control methods using several output measurements to maximize or minimize a specific metric.

1.5.1.2.1 MISO control methods

MISO control methods are usually applied directly on s_0 as the metric to maximize. It is also possible to apply them in N_e independent control loops using other output measurements to be minimized or maximized as s_j for $j \in (1, N_e - 1)$, for example.
The general idea is to apply modulations on the programmable phase elements and measure the response on the measurement metric to determine a correction to be applied to the programmable phase elements as hill-climbing algorithms. For this, one needs to separate the influence of each programmable phase element on the measurement metric.
This can be achieved with model-free algorithms using frequency coding [61, 86, 87, 88, 89, 90], sequential coding [91, 92, 63], stochastic coding [63, 93, 94, 60, 95] using gradient descent algorithms. Other model-free algorithm can be use such as Nelder-Mead algorithm [96, 3]. Model based control methods have also been developed [62, 59, 58].

MISO Frequency coding: To separate the influence of each programmable phase elements on the measurement metric, multidither principle was implemented in adaptive optics by O'Meara [61].
In multidither, each programmable phase element is modulated with a small amplitude dither, tagged with a unique frequency. Then, using synchronous detection on the measurement metric to be maximized, s_0, one obtains an error signal that can be used as a correction to perform an hill-climbing control loop.
The same control method was used by Shay [86] to perform LOCSET for multiple lasers coherent combination. Using our SMID definition, the theory of multidither is described below:

Let $\delta\varphi_k$, be a small amplitude modulation (the dither) applied on the k^{th} programmable phase element using a sinusoidal carrier at frequency f_k so that the modulation is applied as, $\delta\varphi_k sin(w_k t)$, with $w_k = 2\pi f_k$. Using Expression 1.49, the modulated metric measure-

ment, s_0, is:

$$\begin{aligned} s_0 = & \overbrace{\sum_k |c_{0,k}^f|^2 |a_k|^2}^{C_0} \\ & + 2 \sum_k \sum_{l>k} |c_{0k}^f||c_{0l}^f||a_k||a_l| \\ & cos\left(\underbrace{\varphi_{a_k} - \varphi_{a_l} + \varphi_k^{ps} - \varphi_l^{ps} + \varphi_{0,k}^f - \varphi_{0,l}^f}_{\Phi_{k,l}} + \delta\varphi_k sin(w_k t) - \delta\varphi_l sin(w_l t) \right) \end{aligned} , \quad (1.52)$$

with $C_0 = \sum_k |c_{0,k}^f|^2 |a_k|^2$ the unmodulated intensity term and $\Phi_{k,l} = \varphi_{a_k} - \varphi_{a_l} + \varphi_k^{ps} - \varphi_l^{ps} + \varphi_{0,k}^f - \varphi_{0,l}^f$ the unmodulated phase term. Using trigonometric identities it comes:

$$\begin{aligned} s_0 = C_0 + & 2 \sum_k \sum_{l>k} |c_{0k}^f||c_{0l}^f||a_k||a_l| \\ & \Big[cos\left(\Phi_{k,l}\right) \Big(cos[\delta\varphi_k sin(w_k t)] cos[\delta\varphi_l sin(w_l t)] + sin[\delta\varphi_k sin(w_k t)] sin[\delta\varphi_l sin(w_l t)] \Big) \\ & - sin\left(\Phi_{k,l}\right) \Big(sin[\delta\varphi_k sin(w_k t)] cos[\delta\varphi_l sin(w_l t)] - sin[\delta\varphi_l sin(w_l t)] cos[\delta\varphi_k sin(w_k t)] \Big) \Big] \end{aligned} . \quad (1.53)$$

Using the Jacobi-Anger expansions:

$$\begin{aligned} sin[\delta\varphi_k sin(w_k t)] &= 2 \sum_{n=1}^{\infty} J_{2n-1}(\delta\varphi_k) sin[(2n-1) w_k t], \\ cos[\delta\varphi_k sin(w_k t)] &= J_0(\delta\varphi_k) + 2 \sum_{n=1}^{\infty} J_{2n}(\delta\varphi_k) sin[(2n w_k t] \end{aligned} , \quad (1.54)$$

with J_x the Bessel fonction of order x:

$$J_x(\delta\varphi_k) = \sum_{p=0}^{\infty} \frac{(-1)^p}{p!(x+p)!} \left(\frac{\delta\varphi_k}{2} \right)^{2p+x} , \quad (1.55)$$

the modulated Expression 1.53 becomes:

$$\begin{aligned} s_0 = C_0 + & 2 \sum_k \sum_{l>k} |c_{0k}^f||c_{0l}^f||a_k||a_l| \\ & \Big[cos(\Phi_{k,l}) \Big(\big[J_0(\delta\varphi_k) + 2 \sum_{n=1}^{\infty} J_{2n}(\delta\varphi_k) sin(2n w_k t) \big] \big[J_0(\delta\varphi_l) + 2 \sum_{n=1}^{\infty} J_{2n}(\delta\varphi_l) sin(2n w_l t) \big] \\ & + 4 \sum_{n=1}^{\infty} \sum_{m=1}^{\infty} J_{2n-1}(\delta\varphi_k) J_{2m-1}(\delta\varphi_l) sin[(2n-1) w_k t] sin[(2m-1) w_l t] \Big) \\ & - sin(\Phi_{k,l}) \Big(\big[2 \sum_{n=1}^{\infty} J_{2n-1}(\delta\varphi_k) sin[(2n-1) w_k t] \big] \big[J_0(\delta\varphi_l) + 2 \sum_{n=1}^{\infty} J_{2n}(\delta\varphi_l) sin(2n w_l t) \big] \\ & - \big[2 \sum_{n=1}^{\infty} J_{2n-1}(\delta\varphi_l) sin[(2n-1) w_l t] \big] \big[J_0(\delta\varphi_k) + 2 \sum_{n=1}^{\infty} J_{2k}(\delta\varphi_k) sin(2n w_k t) \big] \Big) \Big] \end{aligned} . \quad (1.56)$$

To obtain the error signal of the p^{th} programmable phase element, the modulated signal s_0 is demodulated at frequency f_p. This is done by integrating the modulated signal multiplied by a sinusoidal term oscillating at the same frequency f_p on several 2π periods. Let s_0^p be the demodulated signal at frequency f_p, we have:

$$s_0^p = \frac{1}{\tau}\int_0^\tau s_0 \times sin(w_p t)dt\,, \tag{1.57}$$

with $\tau >> \frac{2\pi}{w_p}$ and $\tau >> \frac{2\pi}{w_p - w_k}$, $\forall k \neq p$. In Expression 1.56, only the integral term proportional to $sin(w_p t)^2$ will be different from zero thus giving:

$$s_0^p = 2J_1(\delta\varphi_p)|a_p||c_{0,p}^f| \sum_k |a_k||c_{0,k}^f| J_0(\delta\varphi_k) sin(\varphi_{a_k} - \varphi_{a_p} + \varphi_k^{ps} - \varphi_p^{ps} + \varphi_{0,k}^f - \varphi_{0,p}^f)\,. \tag{1.58}$$

Amplitude modulations $\delta\varphi_k$ are small compared to one radian thus, we can approximate the Bessel functions as $J_1(\delta\varphi_p) = \frac{\delta\varphi_p}{2}$ and $J_0(\delta\varphi_k) = 1$ giving:

$$s_0^p = \delta\varphi_p|a_p||c_{0,p}^f| \sum_k |a_k||c_{0,k}^f| sin(\varphi_{a_k} - \varphi_{a_p} + \varphi_k^{ps} - \varphi_p^{ps} + \varphi_{0,k}^f - \varphi_{0,p}^f)\,. \tag{1.59}$$

As shown in Expression 1.50, maximizing s_0 implies setting the programmable phase elements so that $\varphi_{a_k} - \varphi_{a_p} + \varphi_k^{ps} - \varphi_p^{ps} + \varphi_{0,k}^f - \varphi_{0,p}^f = 0$. It is equivalent to driving s_0^p to zero. Thus, the demodulated signal s_0^p can be used as an error signal to subtract to the p^{th} programmable phase elements in a hill-climbing control loop to maximize s_0.

Furthermore, near the maximum of s_0, using Expression 1.50, and defining residual phases φ_k with $k \in (0, N-1)$ in the programmable phase elements space, s_0^p is minimum (denoted $s_0^p|_{min}$) and equal to:

$$s_0^p|_{min} = \delta\varphi_p|a_p||c_{0,p}^f| \sum_k |a_k||c_{0,k}^f|(\varphi_k - \varphi_p)\,, \tag{1.60}$$

O'Meara demonstrates the stability of such a control loop in the case of uniform amplitude fields [97]. We can perform the same kind of development in the case of our SMID:

$$\begin{aligned} s_0^p|_{min} &= \delta\varphi_p|a_p||c_{0,p}^f| \left(-\varphi_p \sum_k |a_k||c_{0,k}^f| + \sum_k |a_k||c_{0,k}^f|\varphi_k \right) \\ &= -\delta\varphi_p|a_p||c_{0,p}^f| \left(\sum_k |a_k||c_{0,k}^f| \left(\varphi_p - \frac{\sum_k |a_k||c_{0,k}^f|\varphi_k}{\sum_k |a_k||c_{0,k}^f|} \right) \right) \end{aligned}\,. \tag{1.61}$$

With such a control loop, driving the s_0^p signal to zero, is equivalent to make the p^{th} residual phase converge to the weighted arithmetic mean of the other residual phases.
An other way to demonstrate the stability is to consider that maximizing s_0 is equivalent to maximize the Strehl ratio, $e^{-\sigma_\varphi^2}$, which is equivalent to minimize the residual phase variance. The residual phase variance is express as:

$$\sigma_\varphi^2 = \frac{\sum_k |a_k||c_{0,k}^f|\varphi_k^2}{\sum_k |a_k||c_{0,k}^f|} - \left(\frac{\sum_k |a_k||c_{0,k}^f|\varphi_k}{\sum_k |a_k||c_{0,k}^f|} \right)^2\,. \tag{1.62}$$

Minimizing the residual phase variance with respect to the p^{th} residual phase is equivalent to solve:

$$\frac{\partial\sigma_\varphi^2}{\partial\varphi_p} = 0\,, \tag{1.63}$$

which leads to solve:

$$\varphi_p - \frac{\sum_k |a_k||c^f_{0,k}|\varphi_k}{\sum_k |a_k||c^f_{0,k}|} = 0\,. \tag{1.64}$$

Expressions 1.61 and 1.64 show that using s_0^p as correction signals, for all $p \in (0, N-1)$, to drive them to zero, leads to maximizing s_0.

With multidither, each programmable phase element is tagged with a unique frequency. When increasing the number of complex amplitudes to be combined coherently, the number of tagging frequencies increases significantly. Thus, the number of possible complex amplitudes to be combined is limited and depends on the mitigation technology. To overcome this issue, the use of sine-cosine single-frequency dither was proposed [92], allowing to divide by two the number of tagging frequencies. This last method was upgraded in [98] to tag several complex amplitudes with the same frequency using orthogonal temporal coding. It was also upgraded in [87] introducing temporal orthogonal coding using Walsh modes. The methods presented above always use the coherent combination area s_0 as a quality metric measurement to be maximized. Using mid-range intensity measurements to tag several modes with the same dither frequency is also possible [90, 89].
In [88] multidither is introduced from the point of view of a gradient descent algorithm. But still, all these multidither methods face the problem of modulation bandwidth depending on the number of complex amplitudes to be combined, and in the end, are limited in the number of complex amplitudes they allow to coherently combine.
In the same way, a temporal coding of the modulation was proposed using a unique tagging frequency applied sequentially [91]. It is thus technologically more simple to implement.

MISO Sequential coding: In sequential coding, a small amplitude modulation, compared to one radian, $\delta\varphi$ (the dither), is applied sequentially on each programmable phase element. It can be applied as a step dither or with a sinusoidal carrier applied at frequency f, as $\delta\varphi sin(wt)$, with $w = 2\pi f$. Sequential coding was used by Ma [91] in the context of lasers coherent combining as a proposition to overcome the issue faced by multidither (frequential coding) with the limited tagging frequency accessible when the number of inputs N increase. The development of sequential coding applied with a sinusoidal dither with demodulation of s_0 at frequency f to obtain the error signal is similar to the development of multidither described above. The development as a step dither is developed below:

First the modulation, $\delta\varphi$ is added on the p^{th} programmable phase element and the metric $s_0^p(+\delta\varphi)$ (denoted s_0^+ for simplicity) is measured:

$$\begin{aligned} s_0^+ = C_0 &+ 2\sum_{k\neq p}\sum_{l>k} |c^f_{0k}||c^f_{0l}||a_k||a_l|cos(\Phi_{k,l}) \\ &+ 2\sum_{l>p} |c^f_{0p}||c^f_{0l}||a_p||a_l|cos(\Phi_{p,l} + \delta\varphi) \\ &+ 2\sum_{k<p} |c^f_{0p}||c^f_{0k}||a_p||a_k|cos(\Phi_{k,p} - \delta\varphi) \end{aligned}\,, \tag{1.65}$$

with $C_0 = \sum_k |c^f_{0,k}|^2|a_k|^2$ the unmodulated intensity term and $\Phi_{k,l} = \varphi_{a_k} - \varphi_{a_l} + \varphi^{ps}_k - \varphi^{ps}_l + \varphi^f_{0,k} - \varphi^f_{0,l}$ the unmodulated phase term. Then, the modulation $-\delta\varphi$ is applyied on

the p^{th} programmable phase element and the metric $s_0^p(-\delta\varphi) = s_0^-$ is measured:

$$\begin{aligned} s_0^- = C_0 &+ 2\sum_{k\neq p}\sum_{l>k}|c_{0k}^f||c_{0l}^f||a_k||a_l|cos(\Phi_{k,l}) \\ &+ 2\sum_{l>p}|c_{0p}^f||c_{0l}^f||a_p||a_l|cos(\Phi_{p,l}-\delta\varphi) \\ &+ 2\sum_{k<p}|c_{0p}^f||c_{0k}^f||a_p||a_k|cos(\Phi_{k,p}+\delta\varphi) \end{aligned} . \tag{1.66}$$

Let Δs_0^p be the difference between measured signals s_0^+ and s_0^-, it comes using some trigonometric identities and noting that $\Phi_{k,l} = -\Phi_{l,k}$:

$$\begin{aligned} \Delta s_0^p &= -4\sum_{l>p}|c_{0p}^f||c_{0l}^f||a_p||a_l|sin(\Phi_{p,l})sin(\delta\varphi) - 4\sum_{k<p}|c_{0k}^f||c_{0p}^f||a_k||a_p|sin(\Phi_{k,p})sin(-\delta\varphi) \\ &= -4\sum_{l>p}|c_{0p}^f||c_{0l}^f||a_p||a_l|sin(\Phi_{p,l})sin(\delta\varphi) - 4\sum_{k<p}|c_{0k}^f||c_{0p}^f||a_k||a_p|sin(\Phi_{p,k})sin(\delta\varphi) \\ &= -4\sum_{k\neq p}|c_{0k}^f||c_{0p}^f||a_k||a_p|sin(\Phi_{p,k})sin(\delta\varphi) \end{aligned} . \tag{1.67}$$

The modulation amplitude being small compared to one radian it comes:

$$\Delta s_0^p = 4\delta\varphi|a_p||c_{0p}^f|\sum_{k\neq p}|c_{0k}^f||a_k|sin(\varphi_{a_k} - \varphi_{a_p} + \varphi_k^{ps} - \varphi_p^{ps} + \varphi_{0,k}^f - \varphi_{0,p}^f) . \tag{1.68}$$

The error signal Δs_0^p obtained with a sequential coding is the same expression (to a factor 4 due to the step dither instead of a sinusoidal dither) as the demodulated signal s_0^p obtained with multidither. Thus, for the same reason as in multidither, sequential coding allows the use of the error signal Δs_0^p to be subtracted to the p^{th} programmable phase element in a hill-climbing control loop to maximize s_0.

In sequential coding the metric Δs_0^p can also be used to approximate the true gradient component $\frac{\partial s_0}{\partial \delta\varphi_p^{ps}}$ by $\frac{\Delta s_0^p}{\delta\varphi}$ [99]. From this, gradient descent can be performed sequentially on each programmable phase element such as:

$$\varphi_p^{ps^{(n)}} = \varphi_p^{ps^{(n-1)}} - g\frac{\Delta s_0^p}{\delta\varphi} , \tag{1.69}$$

with $\varphi_p^{ps^{(n)}}$ the p^{th} programmable phase element at iteration n, and g a gain.

With sequential coding, the problem of limited frequencies in multidither is shifted to a problem of a slower control loop. Because we look for real-time atmospheric effects mitigation, a higher dither frequency is then required with sequential coding implying the same problem as multidither in the end.
To overcome this issue, the use of stochastic coding as the Stochastic Parallel Gradient Descent (SPGD) [63] algorithm allows the modulation of all programmable phase elements at the same time at the same frequency.

MISO Stochastic coding: Vorontsov used SPGD to perform phase correction [63, 93] enabling to get rid of the frequency modulation issue with frequency or sequential coding. SPGD principle is summarized below:

Let, $\boldsymbol{\delta u} = (\delta u_k)$ with $k \in (0, N-1)$ be a vector of small amplitude perturbations applied simultaneously on all the programmable phase elements. Let, δs_0, be the variation of s_0 when perturbation vector $\boldsymbol{\delta u}$ is applied on the programmable phase elements such as $\delta s_0 = s_0(\boldsymbol{\varphi^{ps}} + \boldsymbol{\delta u}) - s_0(\boldsymbol{\varphi^{ps}})$.
In the basic SPGD method [63], the perturbations (δu_k) have uniform amplitude, $|\delta u_k| = \delta u$, and random signs with equal probability so that $\delta u_k = \pm \delta u$. It is equivalent to exploring random directions of corrections, thus allowing a gain in robustness and convergence. The gradient of the k^{th} programmable phase element is approximated by $\frac{\delta s_0}{\delta u_k}$. From this the gradient descent algorithm on the p^{th} programmable phase element is:

$$\varphi_p^{ps^{(n)}} = \varphi_p^{ps^{(n-1)}} - g\frac{\delta s_0}{\delta u_p}\,, \tag{1.70}$$

with g a gain.
Then Vorontsov showed [93], that the perturbations (δu_k) should be chosen as statistically independent variables with zero mean and equal variances and should follow statistical properties of the distorted phase in the programmable phase elements space to be mitigated. Then, the true gradient of the p^{th} component is approximated by $\delta s_0 \delta u_p$, and the gradient descent algorithm becomes:

$$\varphi_p^{ps^{(n)}} = \varphi_p^{ps^{(n-1)}} - g\delta s_0 \delta u_p\,. \tag{1.71}$$

This was used to mitigate perturbation following Kolmogorov statistic [100]. The modulation vectors $\boldsymbol{\delta u}$ can also be chosen so that they are orthonormal to each other for each algorithm iteration [101].
With the SPGD, all programmable phase elements can be controlled simultaneously thus resolving issues faced by sequential and frequency coding to mitigate atmospheric turbulence effects. With the SPGD the average maximum convergence time is a factor $\sqrt{N}$ faster than with sequential modulation or classic gradient descent [93]. The setting of the gain g is not trivial, and several works propose various methods to perform gain adaptation, such as [94, 95, 60].

MISO Modal control methods: All methods described above use one measurement metric to be maximized (or minimized) to control the programmable phase elements either with hill-climbing or gradient descent control algorithms. Such methods are referred to as zonal methods because the mitigation of atmospheric turbulence effects is performed directly by optimization of each programmable phase elements. Other ways to compute the corrections came as modal methods which use a decomposition of the distorted phase on a modal basis such as Walsh or Zernike basis for example [62, 59, 58].
A modal method estimates a finite number of phase coefficients in a chosen modal basis. If one estimates enough phase mode coefficients to fit properly the distorted phase, then, it can be mitigated with the programmable phase elements.
In Wang algorithm [62], the modal basis for phase decomposition is Walsh modes. Each Walsh mode coefficient of the distorted phase is estimated by sequential modulation, see [62]. This work is generalized to sinusoidal carrier modulation and frequency coding for different modal basis decomposition in [58].
To mitigate atmospheric turbulence effects in real-time with modal methods, each coefficient needs to be estimated sequentially or in frequency, and we face the same problem as frequency or sequential coding methods described above.

1.5.1.3 MIMO control methods

All the control methods described above use one output intensity measurement as a metric to control the programmable phase elements (MISO). Their required modulation bandwidth depends on the number of inputs of the device. Thus, MISO control methods are limited in the number of complex amplitudes they allow to combine.

To overcome these issues, Vorontsov proposed to merge model-free hill-climbing and gradient descent control methods with wavefront sensor information in a solution that came as Decoupled-SPGD (DSPGD) [102].
With such a system, the wavefront sensor allows the use of not just one intensity measurement like in MISO device, as a metric to minimize or maximize, but several intensity measurements. Thus, additional informations are accessible to control the programmable phase elements, and control methods become Multiple-Inputs Multiple-Outputs (MIMO) methods. Still, the gradient descent nature of DSPGD makes it less robust near the optimum than a specific optimized model.

To overcome issues faced by temporal or sequential modulation coding and issues faced by gradient descent algorithm, Rinaldi proposed a specific control algorithm using multiple outputs of a spatial demultiplexer to control a DM in one step near an optimum by the use of a spatial modulation [7]. The original control method implemented in this thesis to control the PIC is based on Rinaldi's control method.

1.5.1.4 Deep Learning (DL) control methods

In sensorless AO or AO using non-linear wavefront sensor [73], the programmable phase elements are controlled using intensity measurements as a metric being non-linear functions of programmable phase elements. With such a device, Deep Learning (DL) methods can be implemented to learn the non-linearity to infer the distorted wavefront.
In [103], a multi-agent model-free reinforcement learning control method of an AO system using Shack-Hartmann measurements is studied to control a DM. The first issue with DL is the required time to infer the wavefront. It needs to be quicker than atmospheric decorrelation time for DL to be used in real-time control. DL wavefront inference is much more time-consuming than classic linear wavefront estimation. Thus, DL real-time wavefront inference may not be reachable with standard software and hardware [104]. Wavefront inference in [105] takes 9.2 ms for the DL method based on convolutional neural network to directly estimate Zernike coefficients of the distorted wavefront from image-based WFS. In [106], it takes around 2 ms for DL control methods proposed for sensorless AO. For the DL multi-agent model-free reinforcement learning control method [103], it takes around 1.5 ms to infer the distorted wavefront from a Shack-Hartmann WFS AO. With these methods, inference times are far too slow compared to the characteristic time of evolution of atmospheric turbulence effects. However, in [107], the DL method proposed to combine 100 laser beams coherently shows computation times of 50 µs thanks to a quasi-reinforcement learning process. Thus, specific architectures of DL methods are a promising solution for real-time control.
Another issue with DL control methods is the evolving atmospheric turbulent conditions. Training is usually performed on frozen perturbation while in realistic conditions, a DL control method needs to be robust to evolving atmospheric turbulent conditions in terms of seeing and wind speed [103, 108].
Noise is another issue for DL, raising the question of DL training robustness to different levels and variety of noise, which can make wavefront inference to fail. In [103], a specific DL (different from the one used for wavefront inference) is trained to denoise measurements used by the DL control method to infer the wavefront.

In a nutshell, DL control methods are promising solutions, but considering time inference, noise robustness, and required training for a variety of evolving atmospheric turbulent conditions, especially for LEO FSO, DL control methods still require improvements.

1.5.2 MZI-based PIC control

With MZI-based PIC, the external phase-shifters of the MZIs can be placed at the PIC inputs. Thus, the problem of the real-time control of the external phase shifters can be treated as the control of a PIC as an integrated-DM.

The internal phase shifter must remain between the two couplers of an MZI. However, control methods based on modulation presented for SMID control can be applied to control internal phase shifters of MZIs as shown in [89].

1.6 High-level specifications for PIC coherent combination

1.6.1 Sizing of PIC for integrated AO

To mitigate atmospheric turbulence effects with integrated-AO, the number of guided waves issued from the modal decomposition must be high enough to fit properly the distorted field collected by the telescope. In his thesis, L.Rinaldi studied the average fitting ratio between the spatial demultiplexer output total intensity and the input distorted field intensity for different modal decomposition and different seeing conditions [6]. Below in this section, a 'mode' refers to one output guided wave of a spatial demultiplexer. A spatial demultiplexer with N outputs (N guided waves) means a modal decomposition of the distorted field over N modes. Fitting efficiency will refer to the ratio between the average total intensity at the output of the spatial demultiplexer by the average total intensity of the distorted field such as:

$$\langle \eta_{demux} \rangle = \frac{\sum_j \langle |a_j|^2 \rangle}{\langle |P\Psi^{turb}|^2 \rangle} \,. \tag{1.72}$$

Coefficients (a_j) are defined as: $a_j = \langle P\Psi^{turb} | M_j \rangle$ from Expression 1.38, with M_j the j^{th} mode of the modal decomposition of the distorted field.

The coupling efficiency in the PIC telecom output s_0 is defined as:

$$\langle \eta \rangle = \frac{\langle s_0 \rangle}{\langle |P\Psi^{turb}|^2 \rangle} \,. \tag{1.73}$$

1.6.1.1 Distorted field fitting function of the modal decomposition

L.Rinaldi compared the fitting efficiency of microlens arrays and HG modes. He showed that considering the same number of modes, the fitting efficiencies are similar [6]. However, the maximum fitting efficiency with microlens arrays is always 0.82 due to the mismatch between a microlens diffraction pattern and a SMF mode, whereas with HG modes, considering a large number of modes N, the maximum fitting efficiency converges to 1.
Then, Rinaldi compares HG modes decomposition to Laguerre-Gaussian (LG) modes. While HG modes are defined on Cartesian orthogonal directions, LG modes are defined on their radial and azimuth degrees. Rinaldi showed that LG modes are nearly twice less efficient than HG modes to fit distorted fields considering the same number of modes [6]. Furthermore, he showed that for HG modes decomposition, the correlations between modes in the covariance matrix are weak compared to the diagonal elements. The fitting efficiency is nearly the same, up to a few %, between a modal decomposition on HG modes

and eigenvector modes. Thus, the HG modal basis decomposition is nearly optimal for fitting the distorted field with a minimum of modes [6].

1.6.1.2 Impact of beam wandering

In his thesis, Rinaldi showed that tip-tilt modes, in the meaning of beam wandering stabilization, cannot be described with just a few modes. Thus, adding a tip-tilt mirror to stabilize beam wandering before the spatial demultiplexer allows for a significant increase in the fitting efficiency. With one mode, the gain brought by tip-tilt correction is 5. Then, it decreases as the number of modes increases and is equal to 1.5 for hundreds of modes [6].

1.6.1.3 Order of magnitude for PIC sizing

Considering perfect instantaneous coherent combination with geometrical architecture and without losses, Rinaldi studied the number of modes, N (i.e. PIC input guided waves to be combined), required to reach an average coupling efficiency of $\langle\eta\rangle = 3\ dB$ (50%) with HG modes decomposition. His study is based on both analytical expressions and End-two-End (E2E) simulations for different conditions of D/r_0, with and without tip-tilt correction and for phase-only correction or phase and amplitude correction. With the hypothesis of perfect instantaneous correction without losses we have $\langle\eta\rangle = \langle\eta_{demux}\rangle$ for phase and amplitude correction and $\langle\eta\rangle < \langle\eta_{demux}\rangle$ for phase-only correction.

The results he obtained are summarized in Table 1.1, using theoretical analytical expression, and in Table 1.2 using E2E simulations.

D/r_0	5		10	
tip-tilt (no/yes)	no	yes	no	yes
number of modes N	20	10	70	40

Table 1.1: Order of magnitude of the number of modes N required for the modal decomposition to obtain $\langle\eta_{demux}\rangle \approx 50\%$. Theoretical values obtained analytically by Rinaldi [6].

D/r_0	5				10			
tip-tilt (no/yes)	no		yes		no		yes	
MZI or simple couplers (C)	MZI	C	MZI	C	MZI	C	MZI	C
number of modes N	16	25	X	16	49	121	36	64

Table 1.2: Order of magnitude of the number of modes N required for the modal decomposition to obtain $\langle\eta_{demux}\rangle \approx 50\%$ for both phase-only correction (simple coupler denoted 'C') and phase and amplitude correction (MZI-based PIC). Values obtained by Rinaldi using E2E simulations [6].

It is clear that a tip-tilt correction before modal decomposition with the spatial demultiplexer allows to reduce the number of required modes to reach a fitting efficiency of 50%.
More inputs are required for phase-only correction PIC to reach the same average intensity than MZI-based PIC. However, this study was performed independently of the PIC complexity and characteristics such as internal losses. Thus, the choice for MZI-based PIC for phase and amplitude correction may not be straightforward and requires a more detailed analysis.

1.6.2 Impacts of unbalance couplers

Due to manufacturing imperfections, couplers coupling coefficients may move apart from $\sqrt{2}/2$. Such couplers are unbalanced and possess a reduced extinction power (meaning their capacity to coherently combine two guided waves with the same amplitude). To overcome this issue, Miller proposed an architecture and a setting algorithm to realize 'perfect optics with imperfect components' [109]. By replacing a simple unbalanced coupler with two couplers, presenting split ratios up to 85:15 to 15:85, and by adding a phase-shifter between the two unbalanced couplers, this last one can be set to obtain an equivalent 50:50 balanced coupler [109].
Considering the already complex architectures of PIC for coherent combination: tens to hundreds of inputs N, with $N-1$ couplers (phase-only correction) and $2N-2$ couplers (phase and amplitude correction), multiplying by two the number of couplers and phase-shifters to compensate for unbalance couplers is not worth considering.
In his thesis, K.Saab studied the impact of unbalanced couplers on the coupling coefficient $\langle\eta\rangle$ for both phase-only and phase and amplitude correction supposing perfect instantaneous corrections for different distributions of variances of the modulus of the complex amplitudes at the PIC input [85]. His analysis was performed for different couplers split ratios and different numbers of PIC inputs. He found that for MZI-based PIC, the impact of unbalanced couplers up to 70:30 was negligible with attenuation below 1% of the total PIC input intensity even for strong fluctuations between PIC input complex amplitudes. For phase-only correction PIC, the average attenuation due to unbalanced couplers is of a few % for split ratios up to 60:40 even for strong fluctuations between PIC inputs.
Thus, couplers for PIC coherent combination can be unbalanced up to 60:40 split ratio without significant impact on $\langle\eta\rangle$.

1.6.3 PIC technological platforms overview

Accounting from the above development, I develop below the characteristics required by PICs for integrated-AO:

- Telecom wavelength compatible: 1.5 µm,
- Tens to a hundred of inputs,
- Low propagation and insertion losses, to reach a spatial demultiplexer plus PIC total loss of 4 dB (maximum loss of 60 %),
- Phase shifters rising and falling time must allow real-time mitigation of atmospheric turbulence effects i.e 0.1 ms,
- Couplers should aim for 50:50 split ratio and not be higher than 60:40,
- Small bending radii to allow for geometrical architecture (a few μm),
- Integrated photodetectors or alternative solutions to access internal couplers or MZIs output intensities.
- Must avoid thermal and light cross talk,
- If there are polarization dependencies, it needs to be taken into account for the spatial demultiplexer outputs PIC injection.

The mainstream PIC technological platform is the silicon one with Silicon On Insulator (SOI) and more recently Silicon Nitride (SiN), it allows 1.5 µm applications, a review is

given in [110]. Figure 1.23 gives an overview of the silicon photonics foundries and services (taken from [110]). Another technological platform we are interested in is the Lithium Niobate (LiNbO3) one. It is already mainly used in fibre telecom applications for its electro-optic properties.

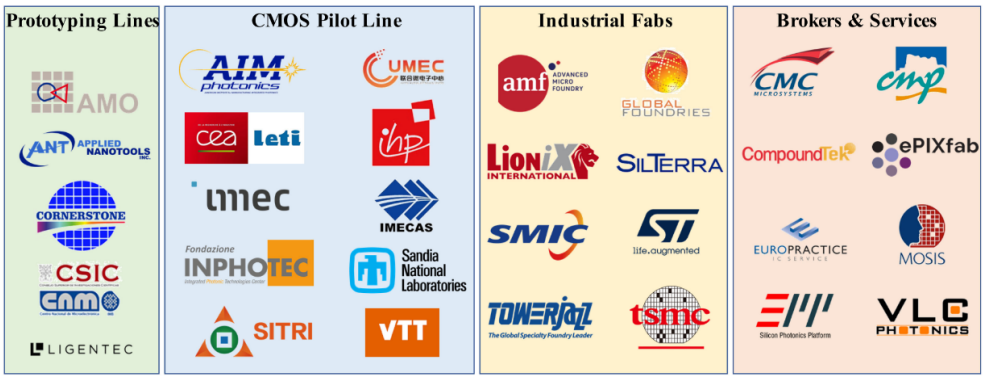

Figure 1.23: Silicon photonics foundries and services from review [110].

1.6.3.1 Silicon On Insulator

Most foundries provide SOI platforms with a few hundreds of nm silicon waveguide layers allowing between 1 and 2 dB.cm^{-1} losses with insertion losses between 0.7 and 2 dB [110]. Such propagation losses are unsuitable with our application of atmospheric effects mitigation using PIC coherent combination. However, VTT propose a 3 µm silicon waveguide layer platform enabling strong modes confinement, allowing propagation losses of 0.1 dB.cm^{-1} [111]. Furthermore, VTT also integrate an adaptation size mode between SMF and waveguide allowing for approximately 1.5 dB coupling losses [111].
Rib waveguides allow single-mode propagation by radiating higher order modes in evanescent waves, but they require large bending radii [112, 113]. VTT SOI platform uses strip waveguides allowing small bending radii due to strong mode confinement [111]. However, strong mode confinement implies very high numerical apertures and small mode sizes ill-suited to coupling with fibres. Furthermore, strip waveguides propagate high-order modes, and VTT uses a combination of rib and strip waveguides to ensure monomode guiding with small bending radii as 1.3 µm [111].
Directional couplers cannot be used due to strip waveguides strong mode confinement, and Multimode Interference Splitters (MMI) are used instead [111].
The phase shifters are based on thermal resistance, allowing for tens of µs of response time with p_π of a few tens of mW [111]. VTT reports 30 µs phase shifters response time.
SOI MZIs typical losses reported in [110] are between 0.4 and 1 dB (between 0.2 and 0.5 dB per MMI). The VTT MZI losses are below 0.5 dB [111].
For phase shifters perspective performance, SOI allows plasma dispersion effects-based phase shifters instead of the classic thermal phase shifters. Plasma dispersion effect allows SOI phase shifters based on PN junction to reach tens of GHz bandwidth contrary to classic thermal resistance phase shifters [110]. However, such PN junction-based phase shifters are much more complex to implement for dense integration and present high losses between 0.9 and 2 dB.mm^{-1} [110, 114], for a few mm length [110].
Unbalanced couplers and cross-talk remain negligible, see technological comparison [110].
Most silicon platforms propose integrated photodetector germanium (Ge) based with responsivity, dark current, and bandwidth summarize in [110].

1.6.3.2 Silicon Nitride

Silicon Nitride (SiN) platforms are expanding with 1.5 µm solution proposed by LioniX, LigenTec and AMF [110]. Compared to SOI, SiN allows really small propagation losses between 0.08 and 0.4 dB.cm^{-1}.
However, bending radii are larger with SiN than with SOI with tens of µm [110].
As with SOI, SiN phase shifters are based on thermal resistance, allowing for tens of µs of response time. However, SiN thermal phase shifters are less efficient than SOI ones. SiN thermal phase shifters require ten times more applied power than for SOI for the same resulting phase shift due to a low thermo-optic coefficient [115]. Thus, SiN thermal phase shifter can lead to heat dissipation and thermal cross-talk issues [115, 4]. Thermal compensation is possible using Peltier cooler [4], or using thermal eigenmodes decomposition method [116].
Unbalanced couplers and cross-talk remain negligible, see technological comparison [110].
For the phase shifters perspective performances, piezo-optomechanics-based phase shifters were integrated on SiN 4x4 (inputs/outputs) PIC with 6 MZIs allowing for hundreds of MHz of bandwidth but with 3.5 dB losses per MZI [117]. Still, it is a promising technology [118].

1.6.3.3 Lithium Niobate

Lithium Niobate (LiNbO3) platform is used in fibre telecommunication networks [119] for its electro-optic effects, allowing for bandwidth of hundreds of GHz [120].
In the standard X-cut LiNbO3 configuration, the phase shifters are polarization dependent due to electro-optics effects [121].
Bulk LiNbO3 allows low propagation losses of 0.1 dB/cm [119]. However, due to a low refractive index, LiNbO3 accept only large bending radii of a few mm [122] increasing the total circuit length and limiting the number of integrated components.
With the recent development of high-quality thin-film Lithium Niobate On Insulator (LNOI) with high mode confinement in waveguide allowing for small bending radii of tens of µm [123, 124, 125] compared to bulk LiNbO3 [126, 122] the use of LiNbO3 remains a promising prospective solution.
Low losses waveguides are reported around 0.01 dB.mm^{-1} in review [120] for LNOI.
However, SOI based PIC maturity (compared to LNOI) offers lower cost and higher integration than LNOI [127]. Concerning the integrated detectors on LNOI, some proof of concept has been made, but it is still in development [122].

1.6.3.4 Technological platforms comparison

The PIC technological platforms comparison with regard to the above requirements for integrated-AO are summarized in tables 1.3 and 1.4. For SOI and SiN, other solutions than thermal phase shifters are not retained due to a lack of technological maturity and the need for a high number of integrated components.

	Integrated components	losses (dB)	Modulation bandwidth	Bending radii
SOI	high	≈ a few to ten	tens of kHz	≈ µm
SiN	high	lower than SOI	tens of kHz	≈ tens of µm
LNOI	low	≈ a few to ten	GHz	≈ tens of µm
LN	low	≈ ten	GHz	≈ mm

Table 1.3: PIC platform comparison.

	Integrated photodetectors	Thermal issues	Polarization dependent
SOI	yes	low	no
SiN	yes	yes	no
LNOI	no	no	yes
LN	no	no	yes

Table 1.4: PIC platform comparison next part.

As shown in tables 1.3 and 1.4, considering requirements for integrated-AO, one of the most suitable PIC platform technologies appears as the SOI one with thermal phase-shifters and VTT 3 µm silicon waveguide layer. Although the relatively low bandwidth of thermal phase shifters may be incompatible with modulation-based control methods, the SOI platform allows for complex architectures with many integrated components.
However, even if LNOI technological platform is not suitable for our use with the current level of maturity, it remains a promising solution considering its high bandwidth of phase shifters and its potential future developments and gains in maturity.

1.6.4 Losses comparison between phase and amplitude correction PIC (MZI-based PIC) and phase-only correction PIC (based on simple couplers)

In the following, we consider that, in a PIC, the main losses (except for the coupling losses) are induced by couplers. Let P_c be the losses of a coupler in dB. The PIC total losses in dB, induced by couplers for N inputs, are for a geometrical architecture:

$$P_{geo} = \begin{cases} P_c \frac{ln(N)}{ln(2)} & \text{for simple couplers} \\ 2 \times P_c \frac{ln(N)}{ln(2)} & \text{for MZI} \end{cases} . \tag{1.74}$$

For an arithmetical architecture with MZIs, the total losses considering uniform input intensities are:

$$P_{arithm} = 10log\left(\frac{4 \times 10^{\left(\frac{(N-1)P_c}{10}\right)}}{N}\left[1 + \frac{1}{2}\sum_{j=1}^{\frac{N-4}{2}} 10^{\left(\frac{-j2P_c}{10}\right)}\right]\right) , \tag{1.75}$$

Expressions 1.74 and 1.75 are plotted in Figure 1.24 for 8, 16, 32 and 64 PIC inputs and considering $P_c = 1\ dB$. When the number of inputs increases, arithmetic architecture is not exploitable because its couplers induced losses increasing linearly with the number of inputs N. Geometric architecture is the most promising, with its couplers-induced losses increasing logarithmically with N, especially with simple couplers-based PIC, which presents twice fewer losses than geometrical MZI-based PIC.
Arithmetical architecture is advantageous when the number of inputs is small, and the platform technology does not allow strong waveguide bending.

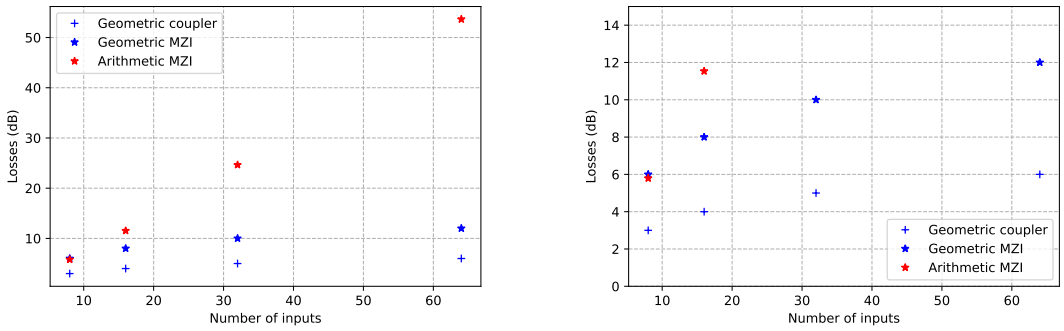

Figure 1.24: PIC couplers induced losses comparison between geometric, in blue, and arithmetic, in red, architectures. Symbol '+' denotes simple couplers based architecture, and symbol '∗' denotes MZI-based architecture. Left figure plots expressions 1.74 and 1.75 for 8, 16, 32 and 64 inputs, N, with $P_c = 1\ dB$. Right figure is a focus of the left figure up to 15 dB losses.

Considering a PIC with geometrical architecture, as shown in expression 1.74, a PIC with phase-only correction presents twice fewer losses in dB than a phase and amplitude correction PIC (MZI-based PIC). This loss comparison must be considered when discussing phase-only or phase and amplitude corrections choice.

1.6.5 Overview of PIC-based coherent combination demonstrations

This Section list the few communications available on the mitigation of atmospheric turbulence effects by coherent combination of spatial demultiplexer outputs using PICs.

Billaut [3, 128] reports a 15 inputs SOI based PIC with geometrical architecture composed of MZI to perform the coherent combination of 15 HG modes coming from a 15 modes MPLC. The PIC possess 16 dB losses. The MZIs are controlled using a Nelder-Mead algorithm. The PIC is used on a bench emulating atmospheric turbulence for a GEO-to-ground FSO link at 30° elevation with a telescope diameter of 50 cm.

Billaud [4] reports a 8 inputs SOI based PIC composed of MZI. It possesses 10 dB losses, the thermal phase-shifters rising time is of 10 µs, and fall time is of 7.5 µs. A coherent combination of 8 HG modes coming from an MPLC on horizontal links of 200 m and 10 km are reported.

Melloni [2] reports a 16 inputs PIC realized on silicon platform with a geometrical architecture with MZI used to mitigate atmospheric turbulence effects on short horizontal links emulated with an optical bench. A dielectric mirror and a biconcave lens are used to couple the distorted field on a 2D optical phased array composed of 16 grating couplers integrated on the PIC. Germanium photodetectors are integrated on the PIC after each MZI outputs. It allows to get rid of waveguide-to-SMF coupling losses.

Cailabs is developing an OGS with a 80 cm telescope to perform LEO downlinks with a 45 inputs PIC coherently combining the output of a 45 modes MPLC [129, 5].

A SOI PIC with a 2 by 2 array is tested as a proof of concept and compared to DMs in [130]. It possesses 3.5 dB losses, and the thermal phase shifters allow to drive the PIC up to 70 kHZ. A SPGD control method is implemented to control the phase shifters in

weak turbulence conditions.

In a nutshell, proofs of atmospheric turbulence effects mitigation by PIC coherent combination have been demonstrated. However, the ultimate performances of integrated-AO in realistic turbulence conditions have not been studied, and no specific control method adapted to PIC coherent combination was reported.

Problem positioning and thesis approach

The classic AO is being implemented in OGSs to mitigate atmospheric turbulence effects for increasing SMF coupling in the case of FSO links.
However, a classic AO is a bulky solution complex to implement. Furthermore, in strong perturbation conditions such as LEO satellite at low elevation, AO WFS performance degrades. Sensorless AO have been proposed, but DMs bandwidth may be limited for modulation-based control methods in the case of LEO satellite scrolling.
With OGS network developments, there is a need for compact, robust and easy deployment solutions. Solutions of fully integrated and low-cost instruments to be mounted on existing telescopes to provide easy deployment and cost-effective OGSs have been proposed. However, such systems do not provide atmospheric turbulence effects mitigation, limiting the FSO link bandwidth.
In this way, integrated-AO promises a compact, robust and easy deployment atmospheric turbulence effects mitigation solution to increase the SMF coupling.

Some principle demonstrations of PIC coherent combination have been reported. Different PIC technological platforms have been considered to perform the coherent combination of a few modes with architecture for phase and amplitude corrections. These principle demonstrations reported high losses incompatible with proper atmospheric turbulence effects mitigation, and the classic control methods used with thermal phase shifters limit the number of modes it is possible to combine coherently in realistic atmospheric turbulence conditions. Thus, the ultimate performances of integrated-AO have not been studied.

Indeed, the high losses of PICs question the usefulness of phase and amplitude correction PICs for integrated-AO with optimal performances. Although the coherent combination efficiency of phase-only correction PICs is lower than that of phase and amplitude correction, the gain in losses brought by their simplified architecture could allow phase-only correction integrated-AO to outperform those with phase and amplitude correction. However, a joint study of the coherent combination efficiency of phase-only correction PICs with respect to the statistics of the complex amplitudes at the output of spatial demultiplexers has yet to be performed to evaluate the gain or loss induced by phase-only correction compared to phase and amplitude correction.

The temporal evolution of distorted fields is well known; however, the impact of the spatial demultiplexer on the temporal statistics of the guided waves to combine has not been studied yet. It needs to be studied to characterize the phase shifters required bandwidth for an integrated-AO to mitigate atmospheric turbulence effects in real-time.

To realize PIC with tens to hundred of inputs, the most mature technological platform is the SOI one with thermal phase shifters. Considering their limited bandwidth of tens of kHz, the classic sensorless control methods, whose required modulation bandwidth depends on the number of phase shifters to control, may not allow the real-time mitigation of atmospheric turbulence effects with PIC with tens to hundred of inputs. For this, the sensorless control method based on a spatial coding of the modulation developed by

Rinaldi offers a promising solution. However, its adaptation and implementation for the real-time control of integrated-AO as yet to be done and the spatial coding choice and noise propagation of this method have not been studied.
The implementation of this method on experimental PIC needs to be studied as well as its performances in realistic turbulent atmospheric conditions.

This thesis focuses on the analysis of the ultimate performances of an integrated-AO in the presence of atmospheric turbulence, based on the development of an original control method for photonic integrated circuit architecture dedicated to coherent combination.

To develop an integrated-AO with optimal performances considering the important internal losses of PICs, the benefits of architectures allowing phase and amplitude correction compared to architectures allowing phase-only correction can be questioned. Indeed, phase-only correction PIC allows twice as few losses in dB as phase and amplitude correction. However, compared to phase and amplitude correction, the coherent combination efficiency of phase-only correction PIC depends on the statistics of its input complex amplitudes guided wave. These complex amplitude statistics depend on the turbulence strength and on the spatial demultiplexer choice. In Chapter 2, I start by studying the statistics of the complex amplitudes at the PIC input function of the turbulent strength and spatial demultiplexer choice. Then, I jointly study the coherent combination efficiency of phase-only correction PIC with respect to the statistical properties of the complex amplitudes of the guided waves at the PIC input.
The phase shifters required bandwidth depends on the temporal evolution of the complex amplitudes to be coherently combined in real-time. Although the temporal evolution of fields distorted by atmospheric effects is well known, the impact of the spatial demultiplexer is unknown. For this, I study the temporal evolution of the guided waves complex amplitudes at the PIC inputs by deriving an analytical expression of their temporal decorrelations in Chapter 2.

To overcome the modulation bandwidth constraints of classic sensorless control methods, in Chapter 3, I adapt the sensorless method of L.Rinaldi to control phase-only correction PIC with a spatial coding of the modulation. This method is referred to here as the spatial modulation control method. In this chapter, considering perfect PIC, I study the linear regime of such a method and analyze its noise propagation. From this, I discuss the choice of the amplitude of the spatial coding. Finally, I study the choice of the spatial coding of the modulation with regard to noise propagation.

In Chapter 4, I give a general method for the sizing of integrated-AO and apply it to a specific satellite-to-ground downlink scenario with the sizing of a perfect phase-only correction PIC as an integrated-DM. Then, I use this scenario to validate the performances of the spatial modulation control method with a numerical experiment. For this, I perform an end-to-end simulation and implement the spatial modulation control method in a control loop, I evaluate its capacity to close the loop and analyze its closed-loop performances as well as its robustness to noises. I compare the performances of the spatial modulation control method to the classic sequential modulation control method. Finally, I study the usefulness of a slightly modified architecture to simplify the control law.

After evaluating the performances of the spatial modulation control method on perfect theoretical PIC, I study in Chapter 5 its implementation difficulties on an experimental PIC in Lithium Niobate that I characterize beforehand. Finally, I discuss the design and sizing of an experimental realistic PIC to reach optimal performances from the characterization of a Silicon On Insulator experimental PIC.

CHAPTER 2

Statistical performances and required bandwidth of integrated-AO

Contents

2.1 Introduction

The integrated-AO atmospheric turbulent effects mitigation method described in this manuscript is based on two functions. The first function performs a modal decomposition of the distorted field into a finite set of guided waves by a device called a spatial demultiplexer. The second function performs the coherent combination of guided waves using a Photonic Integrated Circuit (PIC). In Luca Rinladi's thesis, these two functions were analyzed separately [6]. He statistically characterized the coupling efficiency of a

distorted field for different mode families. In other words, he characterized how well a spatial demultiplexer fits a distorted field given a specific modal decomposition on a finite set of modes-guided waves. Then, he studied numerically the guided waves coherent combination by the PIC assuming instantaneous and perfect correction.

This chapter addresses two questions: the guided waves coherent combination efficiency with a phase-only correction PIC? The PIC phase shifters required bandwidth for real-time guided waves coherent combination?

To address the first question, the phase-only coherent combination efficiency must be characterized together with the statistics of the complex amplitude of the guided waves at the outcome of spatial demultiplexers. For this, Section 2.2 develops the statistics of the complex amplitudes of the guided waves after distorted field modal decomposition performed with the different possibilities of spatial demultiplexers. Then, Section 2.3 analyses the coherent combination efficiency of a phase-only correction PIC depending on the statistics of its input guided waves complex amplitude.

To address the second question, Section 2.4 develops the analytical expression of the time covariance of the complex amplitude of a guided wave function of the turbulence strength and distorted field mode decomposition. Then, a numerical application is performed with a reference link scenario presented in Appendix B. Finally, the phase shifters bandwidth requirements for real-time coherent combination are discussed in the case of the reference link scenario.

2.2 Statistical properties of spatial demultiplexers output complex amplitudes

In this section, we study, depending on the spatial demultiplexer choice, the statistics of the complex amplitudes at the PIC inputs and the distribution of average intensities.
The complex amplitude on the j^{th} demultiplexer output is given by:

$$a_j = \int P(\boldsymbol{r})\Psi^{turb}(\boldsymbol{r})M_j^*(\boldsymbol{r})d\boldsymbol{r}\,, \tag{2.1}$$

With $P(\boldsymbol{r})$ the transmittance function of the telescope pupil, $\Psi^{turb}(\boldsymbol{r})$ the distorted field received by the telescope and $M_j(\boldsymbol{r})$ the j^{th} projection mode of a spatial demultiplexer.

2.2.1 Microlens array

With a microlens array as a spatial demultiplexer, the guided waves at the PIC inputs correspond to the complex amplitudes at the microlenses focal planes. The statistics of these complex amplitudes depend on whether the microlens array is located in the pupil or focal plane.

2.2.1.1 Microlens array in pupil plane

If the microlens array is placed in the pupil plane, each microlens sampled a part of the incident distorted field. We consider atmospheric turbulent perturbations characterized by the Fried parameter, r_0, and microlenses of diameter d. Two different configurations are highlighted. The first one is for a microlens array well sized for the turbulence strength, we have $d \leq r_0$. The other one is for $d >> r_0$ (several coherence area per microlens).

- In the case of $d \leq r_0$, we can consider that the statistics of a_j follow the distorted field statistics. Thus, the modulus of the complex amplitudes, $|a_j|$, at the PIC inputs follow the statistic of the distorted field modulus. The statistic of the distorted field depends on the turbulence strength. As seen in Section 1.2.2.7, two models are used: Log-normal statistic in weak turbulence regime and Rayleigh statistic in strong turbulence regime. In this case, by invariance of a_j by permutation we can consider that the complex amplitude at the PIC inputs all follow the same statistic with the same moments. Thus, the average intensity distributions are identical at the PIC inputs.

- In the case of $d >> r_0$, we have many coherence areas per microlens and with Expression 2.1 we can consider that a_j is a sum of independent phasors. Thus, by random phasor sums, we can consider that the modulus of the complex amplitudes, $|a_j|$, follow Rayleigh distributions [21]. Furthermore, because two different microlenses see different coherent areas, we can consider that the $|a_j|$ are independent random variables with the same first and second-order moments, which is a model used in Rinaldi's thesis [6]. Thus, the average intensity distribution at the PIC inputs are also identical in this case.

2.2.1.2 Microlens array in focal plane

If the microlens array is placed in the focal plane, each microlens samples a part of the focal plane speckle. Thus, the statistics of the modulus of the complex amplitudes, $|a_j|$, at the PIC inputs are the same as the speckle amplitude statistics: a Rayleigh distribution [33].
In this case, we cannot assume that the complex amplitudes follow statistics with the same moments. Indeed, the average intensity decreases in the focal plane with the distance from the optical axis. Thus, the average intensity distribution at the PIC inputs are not identical.

2.2.2 MPLC

Rinladi shows in his thesis that the Hermite-Gaussian (HG) modes basis is nearly optimal to decompose a distorted field after turbulent atmospheric propagation [6]. Indeed, the modes that maximize the coupling efficiency are the eigenmodes of the covariance matrix of coefficients $\left\langle a_j a_j^* \right\rangle$. And Rinaldi shows that the covariance matrix is nearly diagonal with Hermite-Gaussian (HG) modes decomposition. Moreover, MPLCs are available on the market and provide HG modes decomposition [131]. Thus, we look for the statistical properties of the complex amplitudes resulting from the distorted field decomposition on HG modes. We can consider two configurations: $D < r_0$ and $D > r_0$, with D the telescope diameter.

- With $D < r_0$, the telescope sees weak turbulence and $|a_j|$ follows the same statistics as the distorted field, a log-normal distribution [21]. In this case, the intensity distribution at the PIC inputs is not uniform and decreases rapidly with the order of the modes.

- With $D > r_0$, and many coherence areas in the telescope pupil, the HG mode projection in Expression 2.1 can be seen as a sum of independent phasors. Thus, by random phasor sums, we can consider that the modulus of complex amplitudes,

$|a_j|$, follow Rayleigh distributions [21]. Moreover, Rinaldi shows in his thesis that, in such a case, the covariance matrix $< a_k a_l^* >$ is nearly diagonal and the first $(D/r_0)^2$ terms are slowly decreasing. Thus, we can consider that the $|a_j|$ are independent random variables and that the first $(D/r_0)^2$ modes follow Rayleigh distributions with the same first and second-order moment. In other words, the intensity distribution functions of the PIC inputs are identical for the first $(D/r_0)^2$ modes.

2.2.3 Photonic Lantern

The Photonic Lanterns (PL) is generally placed in the focal plane [73]. As for a microlens array placed in the focal plane, the PL sampled the speckle. Thus, the statistics of the modulus of the complex amplitudes, $|a_j|$, at the PIC inputs are the same as the speckle amplitude statistic, which follows a Rayleigh distribution [33].

2.3 Phase-only correction

2.3.1 Why phase-only correction?

A phase-only correction PIC comprises twice fewer couplers and phase shifters than a phase and amplitude correction PIC. Thus, for a PIC with tens of inputs, the architecture of a phase-only correction PIC, as an integrated DM, for example, is much simpler than a MZI-based PIC. Furthermore, a phase-only correction PIC presents twice fewer losses in dB than a MZI-based PIC. And, as developed in Section 1.6, with the actual level of losses encountered by PICs (1 dB per coupler), simplified PIC architectures may be more advantageous.
Moreover, considering a PIC as an integrated DM, all the phase shifters are placed at the PIC inputs. The PIC matrix can be decomposed in a fixed one multiplied by a diagonal matrix corresponding to the phase shifters states. Thus, real-time control of the phase shifters is simplified with phase-only correction.
However, phase-only correction raises the question of the average coherent combination efficiency in the telecom output, s_0, compared to phase and amplitude correction. This average combination efficiency depends on the statistics of the complex amplitudes.

2.3.2 Impact of the statistics for coherent combination with phase-only correction

In the case of phase and amplitude corrections, considering perfect instantaneous correction there is energy conservation in the telecom output, s_0, independently of the statistics of the complex amplitudes. This section discusses the impacts of phase-only correction on the combined energy in s_0 function of the PIC input complex amplitudes statistics. As developed in Section 1.4.2.2, the arithmetical architecture is unsuited to combine more than ten inputs with phase-only correction. Thus, in the following, we consider the geometrical architecture. For simplicity, the PIC input complex amplitudes are supposed equals to the demultiplexer output complex amplitudes.

Considering perfect phase-shifters correction, the telecom output intensity of a MZI-based PIC with N inputs is equal to:

$$s_0^{MZI} = \sum_{j=0}^{N-1} |a_j|^2 , \tag{2.2}$$

corresponding to the total PIC input energy.

For phase-only correction PICs, the telecom output is equal to:

$$s_0^c = \sum_{k=0}^{N-1} \sum_{l=0}^{N-1} |C_{0,k}^f||C_{0,l}^f||a_k||a_l| \,, \tag{2.3}$$

with $|C_{0,k}^f|$ the coefficients of the PIC matrix. For m stages of couplers, we have $|C_{0,k}^f| = c^m \ \forall k$, with $c = \frac{\sqrt{2}}{2}$ the coupling coefficient of a balance coupler. And for N inputs we have $m = \frac{ln(N)}{ln(2)}$ which gives:

$$\begin{aligned} |C_{0,k}^f||C_{0,l}^f| &= c^{\frac{ln(N)}{ln(2)}} c^{\frac{ln(N)}{ln(2)}}, \ \forall k,l \\ &= \left(\frac{1}{2}\right)^{\frac{ln(N)}{ln(2)}} \\ &= 2^{\frac{ln(N^{-1})}{ln(2)}} \\ &= \frac{1}{N} \end{aligned} \,. \tag{2.4}$$

It comes:

$$s_0^c = \frac{1}{N} \sum_{k=0}^{N-1} \sum_{l=0}^{N-1} |a_k||a_l| \,. \tag{2.5}$$

Four cases can be distinguished. Statistics with the same moments corresponding to homogeneous intensity distribution at the PIC inputs or statistics with different moments corresponding to heterogeneous intensity distribution, both with Rayleigh or Log-normal distribution. The average combined power in s_0 will differ with the different cases.

2.3.3 Homogeneous intensity distribution at the PIC inputs

2.3.3.1 With Rayleigh statistics

We consider that the modulus of the complex amplitudes (at the PIC inputs) all follow Rayleigh distributions with the same moments and that they are independent random variables so that: $\langle |a_j||a_k| \rangle = \langle |a_j| \rangle \langle |a_k| \rangle$. Rinaldi shows that for phase-only correction [6], the average coupling ratio, $\langle \eta_0 \rangle = \frac{\langle s_0^c \rangle}{\sum_{j=0}^{N-1} \langle |a_j|^2 \rangle}$, in the telecom output is:

$$\langle \eta_0 \rangle \approx \frac{\pi/4 \sum_{j=0}^{N-1} \sum_{k \neq j}^{N-1} \sqrt{\langle |a_j|^2 \rangle \langle |a_k|^2 \rangle}}{N \sum_{j=0}^{N-1} \langle |a_j|^2 \rangle} \,. \tag{2.6}$$

Considering distribution with the same first and second-order moments (Homogeneous intensity distribution), it comes:

$$\langle \eta_0 \rangle \approx \frac{\pi}{4} \,. \tag{2.7}$$

Thus, the average intensity combined in the telecom output is:

$$\langle s_0^c \rangle \approx \frac{\pi}{4} \sum_j \left\langle |a_j|^2 \right\rangle \,, \tag{2.8}$$

corresponding to an average loss of 1 dB compared to phase and amplitude correction. The model of Rayleigh distributions with homogeneous intensity distribution at the PIC inputs is valid for HG modes up to $(D/r_0)^2$, microlens array placed in the pupil plane with $d >> r_0$ and microlens array placed in the pupil plane with $d \leq r_0$ and strong turbulent regime.

2.3.3.2 With Log-normal statistics

Considering Log-normal statistics with the same moments and a standard deviation parameter σ, for the modulus of the complex amplitudes we have:

$$\begin{aligned}\langle \eta_0 \rangle &= \frac{\sum_{i=0}^{N-1} \left\langle |a_i|^2 \right\rangle + \sum_{k=0}^{N-1} \sum_{l \neq k}^{N-1} \langle |a_k| \rangle \langle |a_l| \rangle}{N \sum_{j=0}^{N-1} \langle |a_j|^2 \rangle} \\ &= \frac{\sum_{i=0}^{N-1} \left\langle |a_i|^2 \right\rangle + e^{-\sigma^2} \sum_{k=0}^{N-1} \sum_{l \neq k}^{N-1} \sqrt{\langle |a_k|^2 \rangle \langle |a_l|^2 \rangle}}{N \sum_{j=0}^{N-1} \langle |a_j|^2 \rangle}\end{aligned} \tag{2.9}$$

Considering their is a number of cross terms far larger than diagonal terms it comes:

$$\langle \eta_0 \rangle \approx e^{-\sigma^2} . \tag{2.10}$$

For $\sigma < 0.5$ we have:

$$\langle s_0^c \rangle > \frac{\pi}{4} \sum_j \left\langle |a_j|^2 \right\rangle . \tag{2.11}$$

This model is valid for a well-sized microlens array ($d < r_0$) placed in the pupil plane in weak turbulence regime. In this case, the average loss compared to phase and amplitude correction becomes less than 1 dB.

2.3.4 Heterogeneous intensity distribution at the PIC inputs

2.3.4.1 With Rayleigh statistics

Considering that the modulus of the complex amplitudes at the PIC inputs follow Rayleigh distributions with different moments and are independent random variables, the average coupling ratio is (with much more cross terms than diagonal terms):

$$\langle \eta_0 \rangle \approx \frac{\pi/4 \sum_{j=0}^{N-1} \sum_{k \neq j}^{N-1} \sqrt{\mu_{2,j} \mu_{2,k}}}{N \sum_{j=0}^{N-1} \mu_{2,j}} , \tag{2.12}$$

with $\mu_{2,j}$ the different second order moments. In this case, the average intensity combined in s_0 decreases compared to the homogeneous case:

$$\langle s_0^c \rangle < \frac{\pi}{4} \sum_j \left\langle |a_j|^2 \right\rangle . \tag{2.13}$$

This model is valid for photonic lanterns and microlens arrays placed in the focal plane.

2.3.4.2 With Log-normal statistics

Considering that the modulus of the complex amplitudes at the PIC inputs follow Log-normal distributions with different moments and are not independent random variables anymore, all we can say is that the average coupling ratio in s_0 is:

$$\langle \eta_0 \rangle \approx \frac{\sum_{j=0}^{N-1} \sum_{k \neq j}^{N-1} \langle |a_j||a_k| \rangle}{N \sum_{j=0}^{N-1} \langle |a_j|^2 \rangle} . \tag{2.14}$$

And that the average energy combined in s_0 is:

$$\langle s_0^c \rangle < \frac{\pi}{4} \sum_j \langle |a_j|^2 \rangle . \tag{2.15}$$

This model is valid for a MPLC in weak turbulence conditions such as $D < r_0$.

2.3.5 Summary

As developed in Section 1.6, the simplified architecture of phase-only correction significantly reduces the losses compared to phase and amplitude correction (MZI-based PIC). Considering microlens arrays placed in the pupil plane, the loss compared to phase and amplitude correction is equal or lower than 1 dB. For HG modes lower than $(D/r_0)^2$ the loss is 1 dB compared to phase and amplitude correction. Thus, in most realistic cases with the actual losses of PIC discussed in Section 1.6.4, it is advantageous to consider PIC with phase-only correction compared to phase and amplitude correction. For example, considering a 32-input PIC with 1 dB loss per coupler, a phase and amplitude correction PIC total internal losses is 10 dB against 5 dB with phase-only correction, which gives around 6 dB taking into account the phase-only average error. Furthermore, the gap in internal losses between phase-only correction and phase and amplitude correction increases with the number of PIC inputs.

2.3.6 Numerical application with HG modes projection

We consider the reference scenario, presented in Appendix B, of a LEO satellite at 30° elevation with $D/r_0 = 5$. The probability densities of the modulus of the complex amplitudes obtained by End-to-End simulation after a decomposition on thirty-two HG modes are presented for a few modes in Figure 2.1.

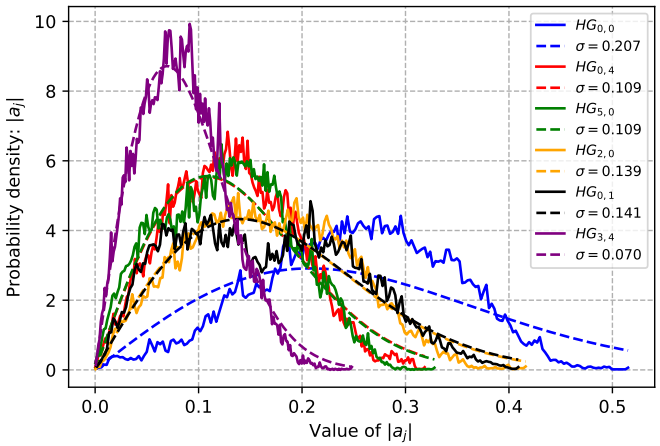

Figure 2.1: Continuous lines: density probability of the modulus of the complex amplitudes obtained by End-to-End simulation with HG modes projection. Dotted lines: Rayleigh's law fit.

The probability densities of the modulus of the complex amplitudes are plotted in continuous lines for $HG_{0,0}$, $HG_{0,4}$, $HG_{5,0}$, $HG_{2,0}$, $HG_{0,1}$ and $HG_{1,4}$ giving an overview of different modes spatial frequencies in the first 32 HG modes.

The dotted lines are the fits for Rayleigh statistics. We can observe that the probability densities follow Rayleigh statistics with some differences. It could be explained by the $D/r_0 = 5$ not being high enough to be fully in Rayleigh statistics. Furthermore, the moments of the statistics are not the same and the average intensity distributions at the PIC inputs are not uniform but decreasing as shown in Figure 2.2.

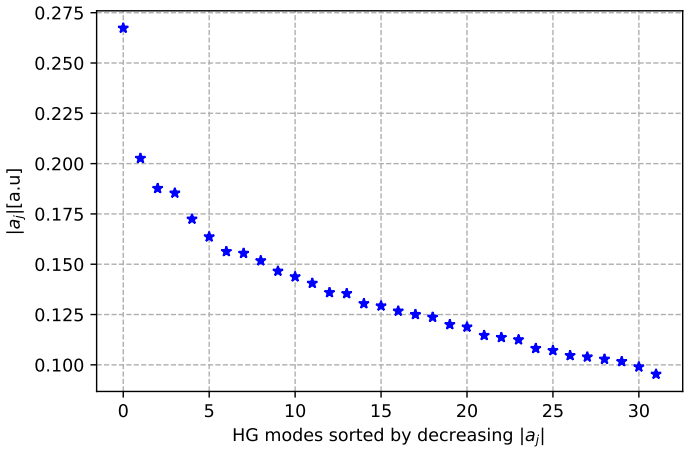

Figure 2.2: Average intensity of the first thirty-two HG modes (sorted by decreasing $|a_j|$) in the case of a LEO satellite with 30° elevation with the paramters developed in Appendix B.

Thus, the considered link scenario diverges from the model of homogeneous intensity distribution at the PIC inputs with Rayleigh statistics. The average coupling is s_0 should be lower than $\pi/4 \sum_j \langle |a_j|^2 \rangle$. A complete analysis of this scenario with a numerical estimation of s_0^c is performed in Chapter 4.

2.4 Time evolution of the complex amplitude at the demultiplexer outputs

Above we studied the statistics of the complex amplitude at the outputs of spatial demultiplexers. This Section focuses on the temporal statistic properties of the complex amplitudes at the outputs of spatial demultiplexers: the temporal covariance.

2.4.1 Analytical expression of the time covariance of the complex amplitude of a given mode

In Section 1.2.2.3, we saw that the spatio-temporal covariance of the distorted field, Ψ^{turb}, after turbulent atmospheric propagation through one turbulent layer at altitude h is [29]:

$$B_{\Psi,h}(\boldsymbol{\rho},\tau) = e^{-3.44\left|\frac{\boldsymbol{\rho}-\tau\boldsymbol{v_h}}{r_{0,h}}\right|^{5/3}}, \tag{2.16}$$

with $\boldsymbol{v_h}$ the velocity, transverse to the direction of propagation, undergoes by the layer at altitude h. $\boldsymbol{v_h}$ is composed of the natural wind speed and the velocity induced by the satellite scrolling. $r_{0,h}$ is the equivalent Fried parameter of a layer at altitude h.
For propagation through the entire atmosphere, the spatio-temporal covariance is given by [29]:

$$B_{\Psi}(\boldsymbol{\rho},\tau) = e^{-3.44\frac{\int C_n^2(h)|\boldsymbol{\rho}-\boldsymbol{\tau v_h}|^{5/3}dh}{r_0^{5/3}\int C_n^2(h)dh}} \tag{2.17}$$

Considering a discrete atmosphere composed of N layers, the total spatio-temporal covariance is the product of the spatio-temporal covariance per layers [29]:

$$B_{\Psi}(\boldsymbol{\rho},\tau) = \prod_{k}^{N} e^{-3.44\left|\frac{\boldsymbol{\rho}-\tau\boldsymbol{v_k}}{r_{0,k}}\right|^{5/3}}. \tag{2.18}$$

The distorted field, $P\Psi^{turb}$, in the pupil plane of the telescope is decomposed by the spatial demultiplexer on a modal basis (M_j), such as $a_j = \int P(\boldsymbol{r})\Psi^{turb}(\boldsymbol{r})M_j^*(\boldsymbol{r})d\boldsymbol{r}$. The temporal covariance of the j^{th} PIC input complex amplitude, a_j, is:

$$\begin{aligned} B_{a_j}(\tau) &= \left\langle a_j(t)a_j^*(t-\tau)\right\rangle \\ &= \left\langle \int_{\boldsymbol{r}} \Psi^{turb}(\boldsymbol{r},t)P(\boldsymbol{r})M_j^*(\boldsymbol{r})d\boldsymbol{r} \int_{\boldsymbol{r'}} \Psi^{turb^*}(\boldsymbol{r'},t-\tau)P(\boldsymbol{r'})M_j(\boldsymbol{r'})d\boldsymbol{r'} \right\rangle, \end{aligned} \tag{2.19}$$

with $\langle\rangle$ the ensemble average. By substitution of $\boldsymbol{r'}$ with $\boldsymbol{r}+\boldsymbol{\rho}$ it comes:

$$B_{a_j}(\tau) = \int_{\boldsymbol{r}}\int_{\boldsymbol{\rho}} \left\langle \Psi^{turb}(\boldsymbol{r},t)P(\boldsymbol{r})M_j^*(\boldsymbol{r})\Psi^{turb^*}(\boldsymbol{r}+\boldsymbol{\rho},t-\tau)P(\boldsymbol{r}+\boldsymbol{\rho})M_j(\boldsymbol{r}+\boldsymbol{\rho})\right\rangle d\boldsymbol{r}d\boldsymbol{\rho}\,. \tag{2.20}$$

Given Taylor's hypothesis, a turbulent layer is considered frozen but shifted by the wind [29]. Thus, we can consider that the distorted field at time $t-\tau$ is the distorted field at

time t shifted by $-\tau \times \boldsymbol{v_h}$. The temporal covariance becomes:

$$\begin{aligned} B_{a_j}(\tau) &= \int_{\boldsymbol{r}} \int_{\boldsymbol{\rho}} \prod_k \underbrace{\int_{h_k}^{h_k+\delta h_k} \left\langle \Psi^{turb}(\boldsymbol{r},t)\Psi^{turb^*}(\boldsymbol{r}+\boldsymbol{\rho}-\tau\times\boldsymbol{v_k}(h),t)\right\rangle dh}_{B_{\boldsymbol{\Psi^{turb}},h_k}(\boldsymbol{\rho}-\tau\times\boldsymbol{v_k}(h))} \\ &\quad \times P(\boldsymbol{r})M_j^*(\boldsymbol{r})P(\boldsymbol{r}+\boldsymbol{\rho})M_j(\boldsymbol{r}+\boldsymbol{\rho})d\boldsymbol{r}d\boldsymbol{\rho} \\ &= \int_{\boldsymbol{r}} \int_{\boldsymbol{\rho}} \underbrace{\prod_k B_{\boldsymbol{\Psi^{turb}},h_k}(\boldsymbol{\rho}-\tau\times\boldsymbol{v_k}(h))}_{B_{\Psi turb}(\boldsymbol{\rho},\boldsymbol{\tau})} P(\boldsymbol{r})M_j^*(\boldsymbol{r})P(\boldsymbol{r}+\boldsymbol{\rho})M_j(\boldsymbol{r}+\boldsymbol{\rho})d\boldsymbol{r}d\boldsymbol{\rho}\,. \quad (2.21) \\ &= \int_{\boldsymbol{\rho}} B_{\boldsymbol{\Psi^{turb}}}(\boldsymbol{\rho},\boldsymbol{\tau}) \underbrace{\int_{\boldsymbol{r}} P(\boldsymbol{r})M_j^*(\boldsymbol{r})P(\boldsymbol{r}+\boldsymbol{\rho})\boldsymbol{M_j}(\boldsymbol{r}+\boldsymbol{\rho})d\boldsymbol{r}}_{F_{P,M_j}(\boldsymbol{\rho})} d\boldsymbol{\rho} \end{aligned}$$

$B_{\boldsymbol{\Psi^{turb}},h_k}(\boldsymbol{\rho}-\tau\times\boldsymbol{v_k}(h))$ is the distorted field spatio-temporal covariance for a given layer, and its product gives the total spatio-temporal covariance $B_{\Psi^{turb}}(\boldsymbol{\rho},\boldsymbol{\tau})$. Moreover, $F_{P,M_j}(\boldsymbol{\rho})$ corresponds to the spatial autocorrelation of the projection mode, weighted by the telescope pupil. This integral can be interpreted as the optical transfer function of the projection mode in the telescope pupil plane. For a discrete atmosphere composed of N layers, it comes:

$$B_{a_j}(\tau) = \int_{\boldsymbol{\rho}} \underbrace{\prod_k^N e^{-3.44\left|\frac{\boldsymbol{\rho}-\tau\boldsymbol{v_k}}{r_{0,k}}\right|^{5/3}}}_{B_{\Psi^{turb}(\boldsymbol{\rho},\tau)}} \underbrace{\int_{\boldsymbol{r}} P(\boldsymbol{r})M_j^*(\boldsymbol{r})P(\boldsymbol{r}+\boldsymbol{\rho})\boldsymbol{M_j}(\boldsymbol{r}+\boldsymbol{\rho})d\boldsymbol{r}}_{F_{P,M_j}(\boldsymbol{\rho})} d\boldsymbol{\rho}\,. \quad (2.22)$$

Finally, $B_{a_j}(\tau)$ is expressed as the integral of the spatio-temporal covariance of the distorted field, $B_{\Psi^{turb}}(\boldsymbol{\rho},\tau)$, multiplied by the optical transfer function of the j^{th} mode projection.

To fully understand the impact of spatial demultiplexers on the temporal properties of the complex amplitude at the PIC inputs, the following subsection analyses the different terms of Expression 2.22.

2.4.2 Numerical application

This section aims to give a physical understanding of the temporal evolution of the complex amplitudes at the PIC inputs. For this, we analyse the effects of each term in Expression 2.22 in the reference scenario of a LEO-to-ground downlink at 30° elevation presented in Appendix B.

2.4.2.1 Application case: 30° satellite elevation LEO-to-ground downlink

We consider a LEO satellite orbiting at 550 km. The scenario is defined in Appendix B. The C_n^2 profile is depicted in Figure 2.3 function of distance to the telescope along the propagation path. The r_0 is 0.1 m, and the log-amplitude variance is $\sigma_\chi^2 = 0.085$.

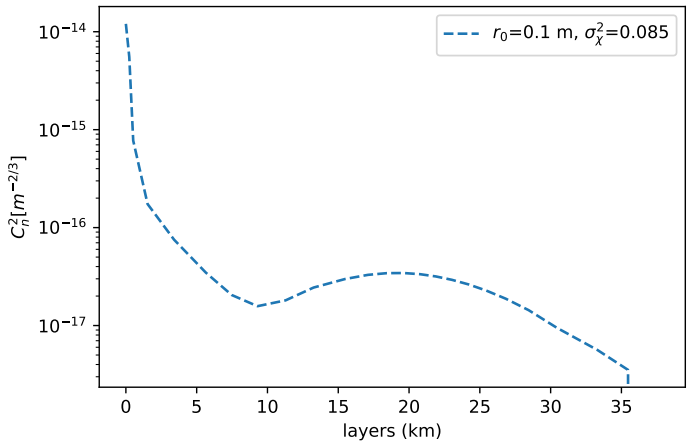

Figure 2.3: C_n^2 profile ($r_0 = 0.1$ m, $\sigma_\chi^2 = 0.085$).

For the Fried parameter and wind velocity to be well sampled, the atmosphere is decomposed into 25 layers along the propagation path, subfigures 2.4a and 2.4b show the velocity $|\boldsymbol{v_h}|$ and $r_{0,h}$ of each layer.

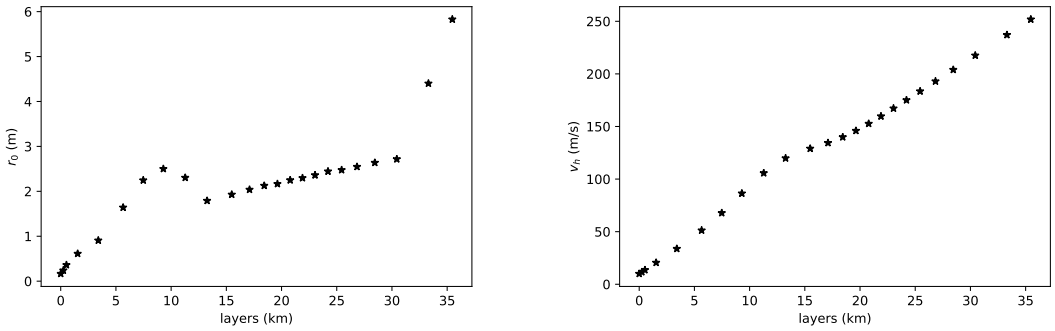

(a) $r_{0,h}$ per layer

(b) Total velocity, $|\boldsymbol{v_h}|$, undergoes by each layer.

Figure 2.4: $r_{0,h}$ and velocity per layer.

A general behaviour we can observe with increasing altitude is the decrease in atmospheric turbulence strength and the increase in total velocity due to satellite scrolling. Each layer velocity can be decomposed in an orthonormal coordinate system (x,y). In the following, we consider that the velocities of each layer are applied in the x direction.

2.4.2.2 Impacts of $B_\Psi(\boldsymbol{\rho}, \tau)$ and $F_{P,M_j}(\boldsymbol{\rho})$

Physical behaviour of $B_\Psi(\boldsymbol{\rho}, \tau)$: The spatio-temporal covariance of the distorted field, $B_\Psi(\boldsymbol{\rho}, \tau)$, after propagation through all atmospheric layers is the product of the $B_{\Psi,h}(\boldsymbol{\rho}, \tau)$ of each layer, see Expression 2.18. To depict the physical behaviour of $B_\Psi(\boldsymbol{\rho}, \tau)$, we need to understand the impact of the $B_{\Psi,h}(\boldsymbol{\rho}, \tau)$.

For a given layer, h we have $B_{\Psi,h}(\boldsymbol{\rho}, \tau) = e^{-3.44\left|\frac{\boldsymbol{\rho}-\tau\boldsymbol{v_h}}{r_{0,h}}\right|^{5/3}}$. $B_{\Psi,h}(\boldsymbol{\rho}, \tau)$ is of width $r_{0,h}$ and is not centred on 0 but on $\tau\boldsymbol{v_h}$ (because of Taylor's hypothesis considering frozen perturbation shifted by wind velocity). As shown in Figure 2.4, the higher the distance h, the

higher the velocity and the Fried parameter. Increasing h gives wider $B_{\Psi,h}(\boldsymbol{\rho},\tau)$ (because of larger $r_{0,h}$) and being more shifted relatively to 0 (more decentered). This behaviour is depicted in Figure 2.5, which plots cross-sections of $B_{\Psi,h}(\boldsymbol{\rho},\tau)$ at different distances h for fixed $\tau = 2$ ms.

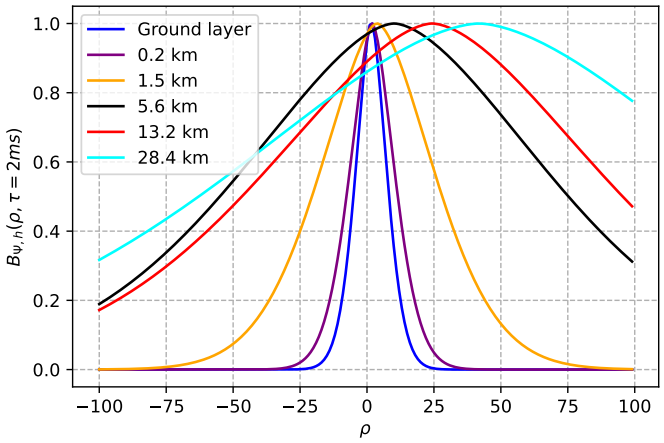

Figure 2.5: $B_{\Psi,h}(\boldsymbol{\rho},\tau = 2\text{ms})$ cross-section for $\tau = 2$ ms and for different distances h.

For low distances h, the Fried parameters are small and the velocity of the layers as well; thus, the $B_{\Psi,h}(\boldsymbol{\rho},\tau)$ are narrow and centred around 0 (blue, purple and orange curves). For higher distances h, the Fried parameters become larger as well as the velocity of the layers and the $B_{\Psi,h}(\boldsymbol{\rho},\tau)$ becomes wider and decentered (black, red and cyan curves). Figure 2.6 illustrates the same behaviour in 2D.

Expression 2.18 gives the $B_{\Psi}(\boldsymbol{\rho},\tau)$ as the product over h of all the $B_{\Psi,h}(\boldsymbol{\rho},\tau)$. Thus, the width of the $B_{\Psi}(\boldsymbol{\rho},\tau)$ is given by layers near the ground (narrow $B_{\Psi,h}(\boldsymbol{\rho},\tau)$) and the maximum value of the $B_{\Psi}(\boldsymbol{\rho},\tau)$, as well as its shift, is given by high altitude layers (shifted $B_{\Psi,h}(\boldsymbol{\rho},\tau)$)). This behaviour of $B_{\Psi}(\boldsymbol{\rho},\tau)$ is depicted in Figure 2.7 for different value of time τ. The width of the $B_{\Psi}(\boldsymbol{\rho},\tau)$ is given by the ground layers, which are almost independent of τ which implies the width of the $B_{\Psi}(\boldsymbol{\rho},\tau)$ being constant with τ. The maximum value is given by $B_{\Psi}(\boldsymbol{\rho} = \mathbf{0},\tau = 0)$, see blue curve. As τ increases higher altitude $B_{\Psi,h}(\boldsymbol{\rho},\tau)$ are more shifted, implying their product to make the maximum value of $B_{\Psi}(\boldsymbol{\rho},\tau)$ to decrease as shown with curves red, green and orange. At some point, $B_{\Psi}(\boldsymbol{\rho},\tau)$ reaches 0, meaning the distorted field is completely decorrelated.

Thus, we explained the physical behaviour leading to the decorrelation of the distorted field received by the telescope. Now, we focus on the impacts of the demultiplexer on the decorrelation.

Impacts of $F_{P,M_j}(\boldsymbol{\rho})$: As developed in Section 2.4.1, $B_{a_j}(\tau)$ is the integral over $\boldsymbol{\rho}$ of the product of $B_{\Psi}(\boldsymbol{\rho},\tau)$ by $F_{P,M_j}(\boldsymbol{\rho})$, see Expression 2.22. In the above section, we studied the physical behaviour of $B_{\Psi}(\boldsymbol{\rho},\tau)$, which gives the decorrelation of the distorted field received by the telescope. Thus, $B_{a_j}(\tau)$ corresponds to the integral over $\boldsymbol{\rho}$ of the distorted field decorrelation weighted by $F_{P,M_j}(\boldsymbol{\rho})$, the mode optical transfer function.

Each Subfigure of Figure 2.8 plot $B_{\Psi}(\boldsymbol{\rho},\tau)$ for different τ (0, 0.5, 1, 2 ms) as in Figure 2.7 (blue, red, green, orange curves) and are compared with $F_{P,M_j}(\boldsymbol{\rho})$ for HG mode projections (black curves). The considered HG modes are: $HG_{0,0}$ the fundamental mode, $HG_{0,5}$, $HG_{0,6}$ and $HG_{0,12}$ corresponding to modes with the high frequencies in the

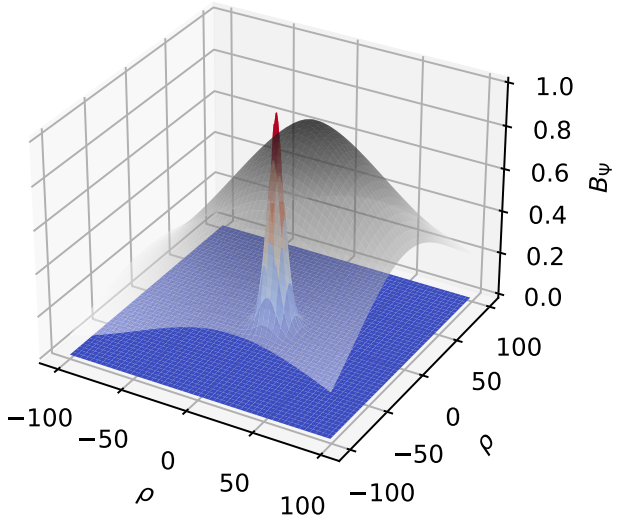

Figure 2.6: In color,$B_{\Psi,h=0}(\boldsymbol{\rho},\tau = 2ms)$, the spatio-temporal covariance of the distorted field for the ground layer at a fixed time, τ of 2 ms. In grey, $B_{\Psi,h=15}(\boldsymbol{\rho},\tau = 2ms)$, the spatio-temporal covariance of the distorted field for a layer at 15 km at a fixed time, τ of 2 ms.

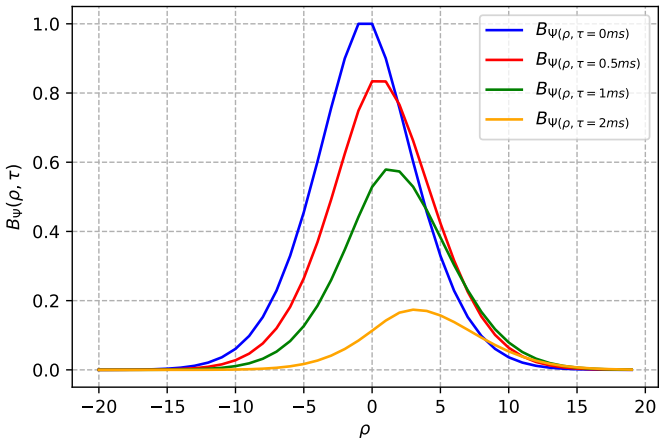

Figure 2.7: $B_\Psi(\boldsymbol{\rho},\tau)$ cross-section for different time τ.

direction of the layers displacement, see Figure 2.9. Subfigure 2.8a compares the impact of $B_\Psi(\boldsymbol{\rho},\tau)$ and $F_{P,HG_{0,0}}(\boldsymbol{\rho})$. For all τ, $F_{P,HG_{0,0}}(\boldsymbol{\rho})$ is wider than $B_\Psi(\boldsymbol{\rho},\tau)$, thus, the integral of the product of $B_\Psi(\boldsymbol{\rho},\tau)$ by $F_{P,HG_{0,0}}(\boldsymbol{\rho})$ is given by $B_\Psi(\boldsymbol{\rho},\tau)$. Thus, the projection on $HG_{0,0}$ has no influence and $B_{a_0}(\tau)$ is given by $B_\Psi(\boldsymbol{\rho},\tau)$. However, in Subfigures 2.8b and 2.8c, $F_{P,M_j}(\boldsymbol{\rho})$ is narrower than $B_\Psi(\boldsymbol{\rho},\tau)$. For time τ around 0 ms (blue curve), $B_{a_j}(\tau)$ is given by $F_{P,M_j}(\boldsymbol{\rho})$. But when τ increases (red, green and orange cruves) the $B_\Psi(\boldsymbol{\rho},\tau)$ are lower and shifted and thus prevail in $B_{a_j}(\tau)$. In Subfigure 2.8d $F_{P,M_j}(\boldsymbol{\rho})$ is much narrower than $B_\Psi(\boldsymbol{\rho},\tau)$, thus compared to Subfigures 2.8b and 2.8c, $F_{P,M_j}(\boldsymbol{\rho})$ prevails for longer

time τ (around 1 ms, green curve) in $B_{a_j}(\tau)$. Still, for long times τ, the $B_\Psi(\boldsymbol{\rho}, \tau)$ value tends toward 0 and is shifted (around 2 ms, orange curve), and thus it prevails again in $B_{a_j}(\tau)$. In other words, for time τ long enough for the distorted field to be decorrelated, $B_\Psi(\boldsymbol{\rho}, \tau)$ prevails whatever the projection mode and a_j are decorrelated.

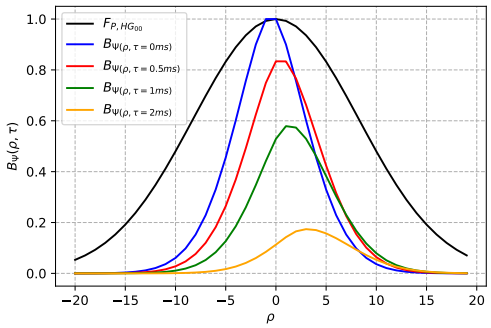

(a) Spatio-temporal covariance cross section of $B_\Psi(\boldsymbol{\rho}, \tau)$, for $\tau = 0$, $\tau = 0.5$, $\tau = 1$, $\tau = 2$ ms respectively in blue, red, green and orange. In black $F_{P,M_j}(\boldsymbol{\rho})$ of the first HG mode HG_{00}.

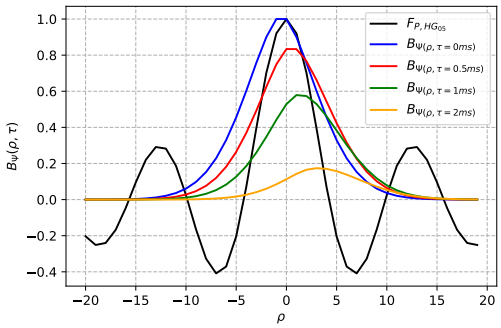

(b) Spatio-temporal covariance cross section of $B_\Psi(\boldsymbol{\rho}, \tau)$, for $\tau = 0$, $\tau = 0.5$, $\tau = 1$, $\tau = 2$ ms respectively in blue, red, green and orange. In black $F_{P,M_j}(\boldsymbol{\rho})$ of $HG_{0,5}$.

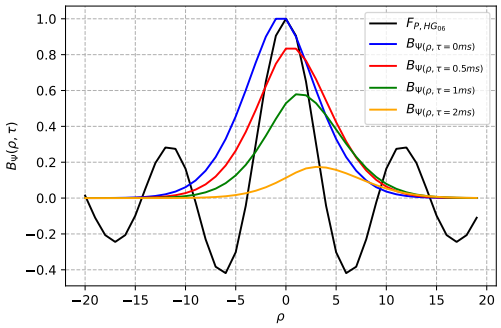

(c) Spatio-temporal covariance cross section of $B_\Psi(\boldsymbol{\rho}, \tau)$, for $\tau = 0$, $\tau = 0.5$, $\tau = 1$, $\tau = 2$ ms respectively in blue, red, green and orange. In black $F_{P,M_j}(\boldsymbol{\rho})$ of $HG_{0,6}$.

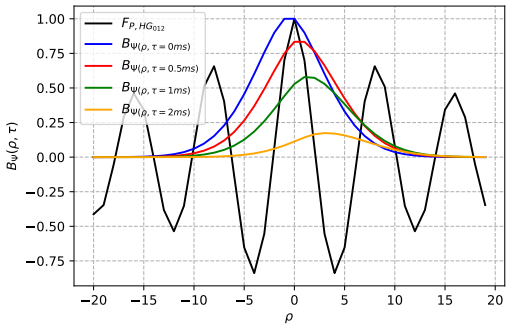

(d) Spatio-temporal covariance cross section of $B_\Psi(\boldsymbol{\rho}, \tau)$, for $\tau = 0$, $\tau = 0.5$, $\tau = 1$, $\tau = 2$ ms respectively in blue, red, green and orange. In black $F_{P,M_j}(\boldsymbol{\rho})$ of $HG_{0,12}$.

Figure 2.8: Comparison of the impacts of $B_\Psi(\boldsymbol{\rho}, \tau)$ and $F_{P,M_j}(\boldsymbol{\rho})$ for HG mode projection.

In a nutshell, the complete decorrelation of a_j is given by the distorted field decorrelation. The mode projection impacts $B_{a_j}(\tau)$ if the mode spatial frequency are high enough for $F_{P,M_j}(\boldsymbol{\rho})$ to be wider than $B_\Psi(\boldsymbol{\rho}, \tau)$. For a given mode, the more high spatial frequencies it possesses, the more it prevails in $B_{a_j}(\tau)$.

2.4.3 Complex amplitude temporal covariance

From analytical Expression 2.22, Figure 2.10 plots the temporal covariances of the complex amplitudes at the PIC input, B_a, for HG modes decomposition of the distorted field. Subfigure 2.10a, corresponds to HG modes whose spatial frequencies are transverse to the layers displacement. The high spatial frequencies of the modes are almost not seen, and the decorrelations of such modes are close to the decorrelation of the distorted field in the telescope pupil plane, around 1.2 ms at half height. However, for HG modes whose spatial frequencies are in the same direction as the layers displacement, Subfigure 2.10b, the spatial covariance of the mode projection prevails. The decorrelation times of complex

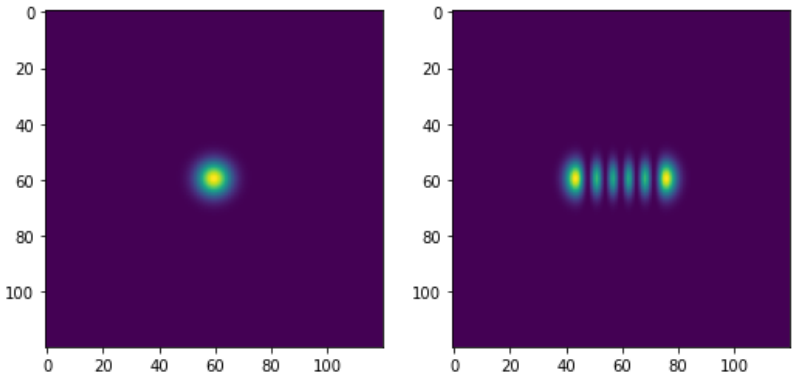

(a) $HG_{0,0}$ (b) $HG_{0,5}$

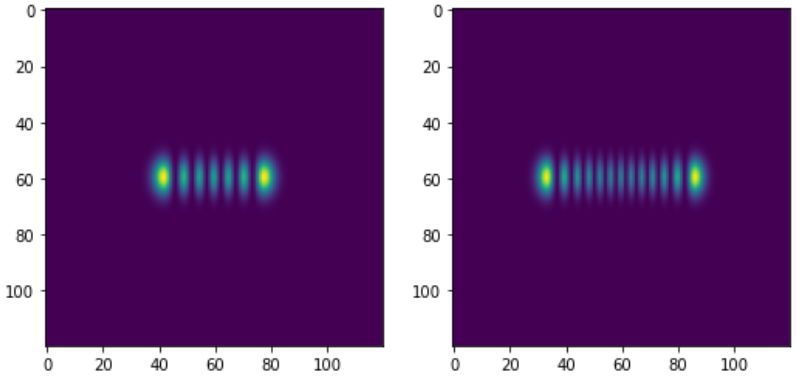

(c) $HG_{0,6}$ (d) $HG_{0,12}$

Figure 2.9: HG mode with high spatial frequency in the direction of the layers displacement.

amplitudes at the PIC input decrease with HG modes with higher spatial frequencies. For the first hundred HG modes, the decorrelation time is minimum for $HG_{0,12}$, around 0.8 ms at half height. Within the HG modes considered here, it corresponds to the one with the highest spatial frequency in the layers displacement direction, see Figure 2.9.

Thus, for a decomposition over the first hundred HG modes, the complex amplitudes decorrelation time ranges from 0.8 to 1.2 ms.
We can compare the complex amplitudes temporal covariances obtained with analytical Expression 2.22, with the one obtained by End-to-End simulation with the TURANDOT code, presented in Section 1.2.2.4. The simulation parameters are those of the reference scenario presented in Appendix B. The results are plotted in Figure 2.11 for the first thirty-two HG modes.

The temporal covariances obtained by End-to-End simulation decrease more slowly and are more spread out than the the one obtained analytically. The coherence times obtained at half height range from 1 to 2 ms compared to 0.8 to 1.2 ms with the analytical expression. The decorrelation times are of the same order of magnitude, and the differences can be explained by the fact that B_{a_j} are obtained with a Kolmogorov spectrum while the TURANDOT code takes into account an inner and external scale.
Now, considering a microlens array placed in the pupil plane as a spatial demultiplexer, the distorted field is projected on Fourier modes. Thus, the impact of the modal projection is the same for each microlens. The complex amplitude temporal covariance for microlens array projection is plotted in Figure 2.12. The decorrelation time at half height is around 1 ms.

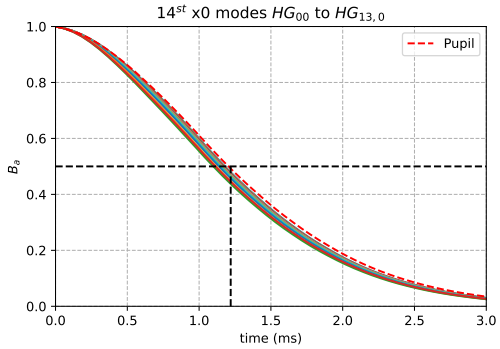

(a) Temporal covariance, B_a, of the complex amplitudes at the PIC input for the first fourteen HG modes transverse to the layers displacement.

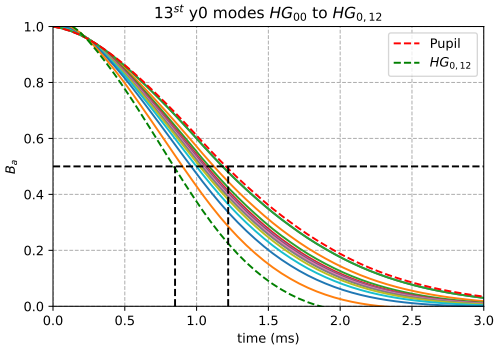

(b) Temporal covariance, B_a, of the complex amplitudes at the PIC input for the first thirteen HG modes in the direction of the layers displacement.

Figure 2.10: Comparison between temporal covariances, B_a, of the complex amplitudes at the PIC input. The red dotted line is the temporal covariance of the distorted field in the telescope pupil plane.

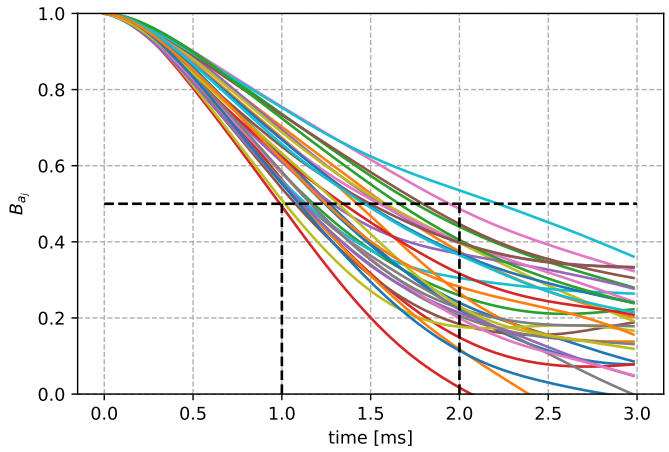

Figure 2.11: Complex amplitudes temporal covariances obtained by End-to-End simulation with the first thirty-two HG modes.

In a nutshell, the main impact on the temporal covariance in the distorted field modal projection comes from the high spatial frequencies of the modes. For a LEO-to-ground downlink at 30° satellite elevation, the decorrelation time at half height after modal projection is of the order of the millisecond.
From this result, the following section discusses the bandwidth the phase shifters require to perform the PIC input complex amplitudes coherent combination.

2.4.4 PIC phase shifters bandwidth requirements discussions

In the case of phase-only correction and external phase shifters of MZI, the phase shifters only correct for the complex amplitudes phase differences, independently of their modulus. The required bandwidth of such phase shifters only depends on the temporal decorrelations of the phases of the complex amplitudes. However, with Expression 2.22, we only have access to the temporal decorrelation of the complex amplitudes. Yet, by decomposing the

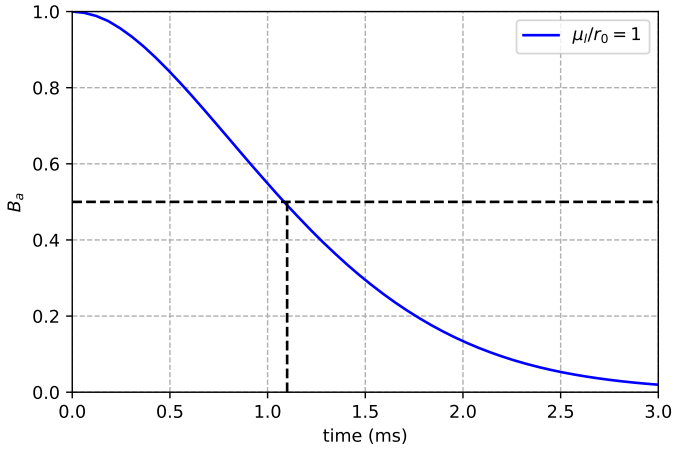

Figure 2.12: PIC input complex amplitude temporal covariance, B_a, for microlens array projection.

complex amplitudes in phase and modulus, we have:

$$\begin{aligned} B_{a_j}(\tau) &= \left\langle |a_j(t)| e^{i\varphi_{a_j}(t)} \times |a_j(t-\tau)| e^{i\varphi_{a_j}(t-\tau)} \right\rangle \\ &= \left\langle |a_j(t)||a_j(t-\tau)| e^{i\left[\varphi_{a_j}(t)-\varphi_{a_j}(t-\tau)\right]} \right\rangle \end{aligned} . \tag{2.23}$$

With our 30° satellite elevation scenario, the correlation of $|a_j|$ and $e^{i\varphi_{a_j}}$ are plotted in Figure 2.13 for the thirty-two first HG modes.

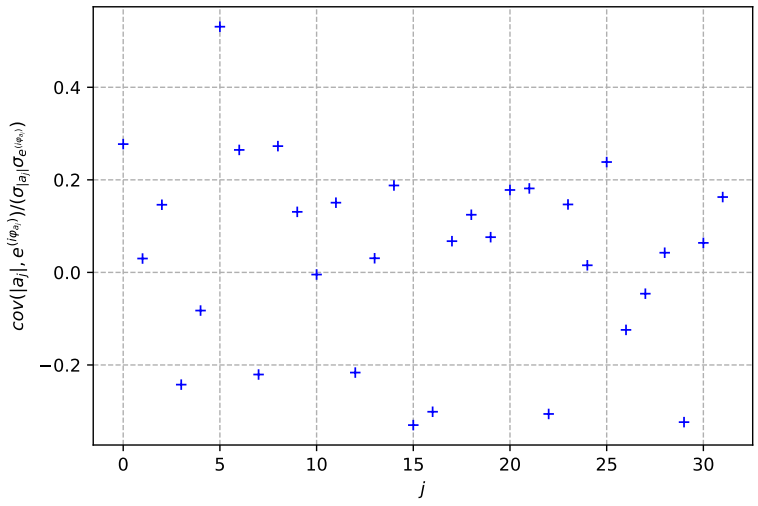

Figure 2.13: Correlation of $|a_j|$ and $e^{i\varphi_{a_j}}$ for the first thirty-two complex amplitudes in the case of the 30° satellite elevation scenario.

As shown in Figure 2.13 the correlation between $|a_j|$ and $e^{i\varphi_{a_j}}$ is weak. Thus, we can consider that they are independent variables, and Expression 2.23 becomes:

$$\begin{aligned} B_{a_j}(\tau) &= \langle |a_j(t)||a_j(t-\tau)| \rangle \times \left\langle e^{i\left[\varphi_{a_j}(t)-\varphi_{a_j}(t-\tau)\right]} \right\rangle \\ &= B_{|a_j|}(\tau) \times B_{e^{i\varphi_{a_j}}}(\tau) \end{aligned} . \tag{2.24}$$

When $B_{|a_j|}(\tau)$ or $B_{e^{i\varphi_{a_j}}}(\tau)$ are decorrelated, $B_{a_j}(\tau)$ reaches zero. If $B_{a_j}(\tau)$ reaches zero while the modulus is still correlated, it means that the phase is completely decorrelated. Thus, $B_{a_j}(\tau)$ is a lower bound for $B_{e^{i\varphi_{a_j}}}(\tau)$ such as: $B_{a_j}(\tau) \leq B_{e^{i\varphi_{a_j}}}(\tau)$.
In other words, the complex amplitude decorrelation time gives a minimum for the phase decorrelation time such as: $\tau_{a_j} \leq \tau_{e^{i\varphi_{a_j}}}$ and we can discuss the bandwidth the phase shifter requires with the complex amplitude decorrelation time.

In classic AO, the temporal error is defined as:

$$\langle \eta_{tempo} \rangle = e^{-\sigma^2_{tempo}}$$

$\sigma^2_{tempo} = 6.88 \left(\frac{v_h \tau_c}{r_0}\right)^{\frac{5}{3}} rad^2$ is the mean quadratic difference from a turbulence at time t and a turbulence at time $t + \tau_c$. $\langle \eta_{tempo} \rangle$ equal 1 without temporal error and converge to 0 as the temporal error increases.

In our case, the temporal error induced on the intensity combine in the telecom output s_0 by corrections applied with a rate delay τ_c is given by our analytical expression 2.22 of the temporal decorrelation of the complex amplitudes at the PIC input.

With the scenario of a LEO 30° satellite elevation used above, the PIC inputs complex amplitudes decorrelation time at half height are of the order of 1 ms. Thus, a correction frequency of around 1 kHz should induce a temporal error of 50%. For the temporal error to be negligible, $B_{a_j}(\tau_c)$ must be close to 1. As we can see in Figure 2.10b, it can be obtained for correction frequency of around 10 kHz.

2.5 Conclusion

The statistics of the complex amplitudes at the PIC inputs were studied in the case of a microlens array, a MPLC and a photonic lantern as spatial demultiplexers. Then, the impact of the complex amplitudes statistics on phase-only correction PICs was discussed. Considering a spatial demultiplexer as a microlens array in the pupil plane, the average loss induced by phase-only correction compared to phase and amplitude correction is equal to or lower than 1 dB. Considering a MPLC with HG modes up to $(D/r_0)^2$, the loss induced by phase-only correction efficiency is 1 dB. As seen in Section 1.6.4, phase and amplitude correction PICs have twice as many dB losses as phase-only correction PICs. Considering PIC with tens to a hundred inputs, the gain brought by internal loss reduction by phase-only correction PIC outperform the 1 dB loss induced by coherent combination efficiency. Thus, to reach integrated-AO optimal performances, we will consider phase-only correction PIC in the rest of the manuscript.
The temporal properties of the complex amplitude were studied by developing a numerical expression of their temporal decorrelations. This expression was validated by End-to-End simulation with a reference scenario. From this, the bandwidth required by the phase shifters to perform the real-time control of the PIC was discussed. A numerical application with a 30° LEO satellite elevation was performed, and frequency correction of 10 kHz was determined for the temporal error to be negligible.

In Section 1.6.3, we saw that to realize PIC with tens to a hundred of inputs, the most mature technological platform is the SOI one with thermal phase shifters allowing tens of kHz of bandwidth. Thus, the modulation bandwidth constraints of classic sensorless control methods may not allow the real-time mitigation of atmospheric turbulence with integrated-AO. Thus, the following Chapter adapts the sensorless method of L.Rinaldi to control phase-only correction PIC with a spatial coding of the modulation, allowing to overcome issues faced by classic sensorless control methods.

CHAPTER 3

An original control method based on a spatial coding of the modulation

Contents

3.1 Introduction

This Chapter addresses the question of the real-time control of the PIC. As presented in Section 1.5.1, the classic modulation-based control methods, such as sequential or frequency coding, require modulation bandwidth depending on the number of phase shifters to control. To mitigate atmospheric turbulence effects, we saw in Section 2.4 that the typical phase shifters required frequency is of ten kHz, and we saw in Section 1.6 that a PIC requires tens to a hundred inputs (tens to hundreds of phase shifters to control). The most mature technological platform allowing the development of such PIC is the SOI one with thermal phase shifters. The maximum bandwidth of thermal phase shifters is

of the order of 100 kHz, which can be limiting for the control of tens to hundreds of phase shifters with classic modulation-based control methods (whose required bandwidth depends on the number of phase shifters to control).

To overcome the constraints on phase shifters bandwidth faced by classic modulation-based control methods, I develop in this Chapter an original control method based on a spatial coding of the modulation, referred to here as the spatial modulation control method. This method is adapted from Rinaldi's sensorless method [7]. As developed in Section 2.3, with the actual level of PIC losses, it is advantageous to use phase-only correction PIC instead of phase and amplitude correction. Thus, in the following, we focus on phase-only correction PIC.
Before developing the principle of the spatial modulation control method, Section 3.2 discusses the application of sequential and frequency modulation control methods (presented in Section 1.5.1) applied to phase-only correction PIC. Then, Section 3.3 develops the notations and the principle of the spatial modulation control method for phase-only correction PIC. The linearity range of this method is studied in Section 3.4 in the case of a 32-inputs PIC, the choice of the amplitude of the modulation is also discussed. Then, Section 3.5 addresses the choice of the spatial coding of the spatial modulation with regards to additive Gaussian noise, decorrelated and uniform. Finally, Section 3.6 discusses the extension of the spatial modulation control method to phase and amplitude correction with MZI-based PIC.

3.2 Classic sequential and frequency modulation-based control methods applied on the PIC

Sequential or frequency modulation presented in Section 1.5.1.2.1 in the general case of a SMID can be applied to control the phase shifters of the PIC to perform the coherent combination of its inputs. In Section 1.5.1.2.1 we saw that sequential or frequency modulation are Multiple-Inputs Single-Output (MISO) control methods but can be applied in several independent control loops if one has access to several independent intensity measurements. This is the case with our PIC architecture decomposed in K stages. In Figure 3.1, the colored rectangles represent the different stages. In a given stage, each phase shifter only influences one intensity measurement of this stage. In other words, within one given stage, the phase shifters and intensity measurements are independent. Thus, it is possible to control simultaneously the phase shifters within one stage with sequential or frequency modulation. Sequential modulation requires only one tagging frequency to be applied sequentially, stage by stage. Frequency modulation requires K tagging frequencies (one per stage) to be applied simultaneously on all phase shifters.

As developed in Section 2.4.4, an order of magnitude for correction frequency of the phase shifters is around 10 kHz (in the case of the scenario developed in Appendix B). However, with frequency and sequential modulation control methods, because the PIC is controlled stage by stage, their required control and modulation frequencies depend on the number of stages of the PIC and, therefore, on the number of complex amplitudes to coherently combine. Thus, depending on the number of stages of the PIC, frequency and sequential modulation control methods may require correction or modulation frequencies higher than the phase shifters maximum allowed bandwidth. The coherent combination of the PIC inputs complex amplitudes will fail in such a case.

To overcome this issue, L. Rinaldi developed a control method based on a spatial coding of the modulation and applies it on a DM associated with a spatial demultiplexer, allowing the correction of residual phases in one modulation period. [7]. The following section

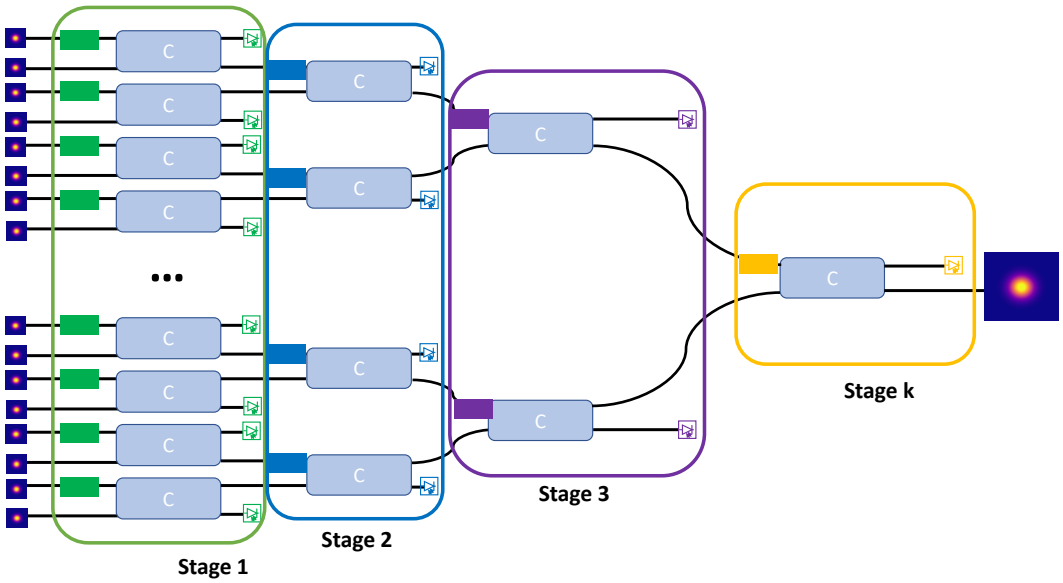

Figure 3.1: Control stage by stage of a phase-only correction PIC.

adapts Rinaldi's method to simultaneously control all the phase shifters as a Multiple-Inputs Multiple-Outputs (MIMO) control method.

3.3 Spatial modulation: a Multiple-Inputs Multiple-Outputs (MIMO) control method

3.3.1 Notation and PIC architecture for phase-only correction

In the following, we are considering a phase-only correction PIC with a geometrical architecture as an integrated-DM. Let N be the number of inputs of the PIC, as seen in Section 1.4.2.2, with the geometric architecture we have $N-1$ couplers spread in $K = ln(N)/ln(2)$ stages.

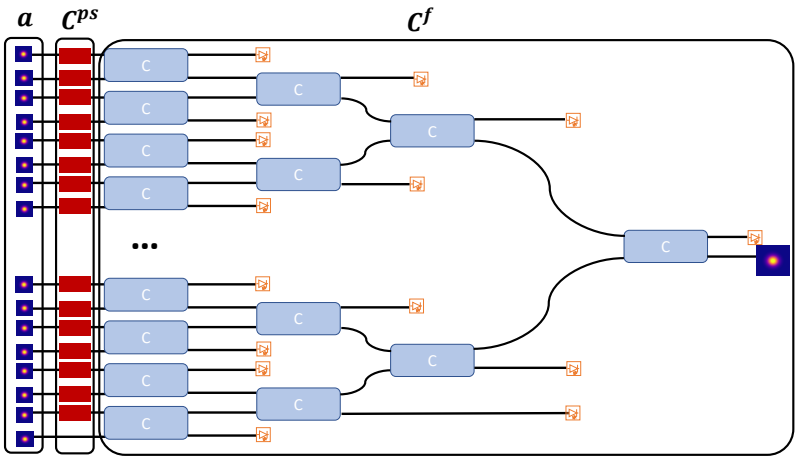

Figure 3.2: Schema of a PIC as an integrated-DM with geometrical architecture.

Let $\boldsymbol{a} = (a_i)$, with $i \in (0, N-1)$, be the vector of complex amplitudes of the guided waves at the inputs of the PIC. We define the modulus of a_i by $|a_i|$ and its phase by φ_{a_i} so that $(a_i) = \left(|a_i|e^{i\varphi_{a_i}}\right)$. Let $\boldsymbol{\varphi^{ps}} = (\varphi_k^{ps})$, with $k \in (0, N-2)$, be the vector of phases applied on the phase shifters. Let $\boldsymbol{e} = (e_j)$, with $j \in (0, N-1)$, be the vector of complex amplitudes at the PIC outputs. We define the modulus of e_j by $|e_j|$ and its phase by φ_{e_j} so that $(e_j) = \left(|e_j|e^{i\varphi_{e_j}}\right)$. We define e_0 as the complex amplitude of the telecom output. The PIC is a programmable linear device between (a_i) and (e_j), as seen in Section 1.5.1.1, we have the relation:

$$\boldsymbol{e} = \boldsymbol{C_{pic}}\boldsymbol{a}\,, \tag{3.1}$$

with $\boldsymbol{C_{pic}}$ being the matrix of the PIC.
In Expression 3.1, $\boldsymbol{C_{pic}}$ is a function of the architecture of the PIC and of $\boldsymbol{\varphi^{ps}}$. Thus, $\boldsymbol{C_{pic}}$ is modified when changing the phase applied by the phase-shifters. In the case of our integrated-DM PIC depicted in Figure 3.2, it is possible to write $\boldsymbol{C_{pic}}$ as the product of two matrices:

$$\boldsymbol{C_{pic}} = \boldsymbol{C^f}\boldsymbol{C^{ps}}\,. \tag{3.2}$$

$\boldsymbol{C^f} = (c_{j,i}^f)$ accounts for the fixed architecture of the PIC. We define the modulus of $c_{j,i}^f$ by $|c_{j,i}^f|$ and its phase by $\varphi_{j,i}^f$ so that $(c_{j,i}^f) = \left(|c_{j,i}^f|e^{i\varphi_{j,i}^f}\right)$. $\boldsymbol{C^{ps}}$ describes the phase shifters of $\boldsymbol{C_{pic}}$. Thus, $\boldsymbol{C^{ps}}$ is a diagonal matrix of elements (φ_k^{ps}).
We define the PIC output intensities as:

$$\begin{aligned} \boldsymbol{s} &= (s_j) \\ &= e_j \times e_j^* \end{aligned} \tag{3.3}$$

with $j \in (0, N-1)$. s_0 corresponds to the telecom output intensity in which the elements of $\boldsymbol{a}$ must be combined coherently. Thus, to control the $N-1$ phase shifters we have access to $N-1$ intensity measurements: (s_j) for $j \in (1, N-1)$.

3.3.2 Spatial modulation control method: Principle and hypotheses

Let $\boldsymbol{\delta\varphi^m}$ be a vector of phase elements $(\delta\varphi_k^m)$, with $k \in (0, N-2)$, of small amplitudes. The elements $(\delta\varphi_k^m)$ can take positive or negative values and are chosen once and for all so that $\boldsymbol{\delta\varphi^m}$ is a fixed vector that remains unchanged. In the following, we call $\boldsymbol{\delta\varphi^m}$ the spatial modulation vector. When we say that we apply $+\boldsymbol{\delta\varphi^m}$ on the phase shifters, it means that the phase elements $(\delta\varphi_k^m)$ are added to the phase shifters values (φ_k^{ps}) simultaneously so that for all phase shifters we have: $\varphi_k^{ps} + \delta\varphi_k^m$. In the same way when we say we apply $-\boldsymbol{\delta\varphi^m}$ on the phase shifters, we have simultaneously for all phase shifters: $\varphi_k^{ps} - \delta\varphi_k^m$. Modulating the phase shifters with the spatial modulation vector comes to apply simultaneously a phase pattern on the phase shifters (the spatial coding).

The principle of the spatial modulation control method is as follows:
The $N-1$ phase shifters are modulated simultaneously with $\boldsymbol{\delta\varphi^m}$. The $N-1$ intensity measurements fluctuations resulting from the phase shifters modulation are measured simultaneously. As for classic modulation-based methods presented in Section 1.5.1, $\boldsymbol{\delta\varphi^m}$ can be applied as a step dither or as a sinusoidal dither. In the following, to ease the calculus, we consider that the spatial modulation is applied as a step dither. We denote by $\boldsymbol{\Delta s}$ the vector of elements (Δs_j) with $j \in (1, N-1)$ defined as:

$$\boldsymbol{\Delta s} = \boldsymbol{s}(\boldsymbol{a}, \boldsymbol{\varphi^{ps}} + \boldsymbol{\delta\varphi^{m}}) - \boldsymbol{s}(\boldsymbol{a}, \boldsymbol{\varphi^{ps}} - \boldsymbol{\delta\varphi^{m}})\,. \tag{3.4}$$

$\boldsymbol{\Delta s}$ corresponds to the differential measurement between intensity measurements when the spatial modulation is applied in positive and when it is applied in negative.
The spatial modulation control method uses the following hypothesis:

1. $\boldsymbol{a}$ is unchanged during one modulation period. It means that the atmospheric turbulent effects are supposed to be the same (frozen) when applying $+\boldsymbol{\delta\varphi^{m}}$ and $-\boldsymbol{\delta\varphi^{m}}$.
2. For a given $\boldsymbol{a}$, s_0 is supposed to be around its maximum, and the intensity measurements (s_j) are supposed to be around their minimums.

It must be noted that hypothesis 1 is also used by classic modulation-based control methods such as sequential and frequency modulation.
Let $\boldsymbol{\varphi}$ be the residual phase vector, in the phase shifters space, of elements (φ_k) with $k \in (0, N-2)$ of small amplitudes. (φ_k) correspond to residual phases of small amplitudes drifting the phase shifters from their optimal setting maximizing s_0. Thus, with such hypotheses, the spatial modulation control method yields a linear relationship between $\boldsymbol{\Delta s}$ and $\boldsymbol{\varphi}$ such as:

$$\boldsymbol{\Delta s} = \boldsymbol{M_{int}}(\boldsymbol{\delta\varphi^{m}}, |\boldsymbol{a}|).\boldsymbol{\varphi} \quad \text{, see Section 3.3.2.1}$$

$\boldsymbol{M_{int}}(\boldsymbol{\delta\varphi^{m}}, |\boldsymbol{a}|)$ is an interaction matrix function of the chosen spatial modulation vector, $\boldsymbol{\delta\varphi^{m}}$, and of the modulus of the complex amplitude at the PIC inputs, $(|a_i|)$.

However, for the real-time control of the PIC, $\boldsymbol{a}$ is constantly evolving implying that the determination of $\boldsymbol{M_{int}}(\boldsymbol{\delta\varphi^{m}}, |\boldsymbol{a}|)$ implies the constant knowledge of $(|a_i|)$ which is not possible. To overcome this issue, a third hypothesis is made:

3. The modulus of the complex amplitude at the PIC inputs are supposed to be constant and uniform.

Thus, we obtain the following linear relation:

$$\boldsymbol{\Delta s} = \boldsymbol{M_{int}}(\boldsymbol{\delta\varphi^{m}}).\boldsymbol{\varphi} \tag{3.5}$$

With this third hypothesis, $\boldsymbol{M_{int}}(\boldsymbol{\delta\varphi^{m}})$ is an interaction matrix function of $\boldsymbol{\delta\varphi^{m}}$ only which is a fixed chosen vector. This assumption is strong, and its impact will be studied in the following Chapter 4.

3.3.2.1 Determination of the interaction matrix

As demonstrate in Appendix D, the interaction matrix can be written as:

$$\boldsymbol{M_{int}} = (\boldsymbol{\delta\varphi^{m}})^{t}\,.\boldsymbol{T}\,, \tag{3.6}$$

$(\boldsymbol{\delta\varphi^{m}})^{t}$ is the transpose of $\boldsymbol{\delta\varphi^{m}}$ and $\boldsymbol{T}$ is the PIC curvature tensor defined as:

$$T_{k,l,j} = \begin{cases} -4|c^{f}_{j,k}||c^{f}_{j,l}||a_k||a_l| & \text{if } k \neq l \\ \sum_{n\neq k} 4|c^{f}_{j,k}||c^{f}_{j,n}||a_k||a_n| & \text{if } k = l \end{cases}\,, \tag{3.7}$$

and we have the relation:

$$\begin{aligned} \left.\frac{\partial^2 s_j}{\partial\varphi_p^{ps}\partial\varphi_q^{ps}}\right|_{min} &= -2|c_{j,p}^f||c_{j,q}^f||a_p||a_q| \text{ if } p \neq q \text{ and,} \\ \left.\frac{\partial^2 s_j}{\partial\varphi_p^{ps^2}}\right|_{min} &= \sum_{q\neq p} 2|c_{j,p}^f||c_{j,q}^f||a_p||a_q| \end{aligned} \tag{3.8}$$

Thus, the j^{th} matrix of the curvature tensor is equal two times the Hessian matrix of the j^{th} output measurements near its minimum, which corresponds to the curvature of the j^{th} intensity measurements with respect to the phase shifters.

The PIC curvature tensor depends on the modulus of the complex amplitudes of the PIC input guided waves. Using hypothesis 3, i.e. supposing that (a_k) are constant for all k we obtain the linear relation:

$$\begin{aligned} \boldsymbol{\Delta s} &= (\boldsymbol{\delta\varphi^m})^t.\boldsymbol{T}.\boldsymbol{\varphi} \\ &= \boldsymbol{M_{int}}.\boldsymbol{\varphi} \end{aligned}, \tag{3.9}$$

with the interaction matrix $\boldsymbol{M_{int}} = (\boldsymbol{\delta\varphi^m})^t.\boldsymbol{T}$, so that the j^{th} line in $\boldsymbol{M_{int}}$ corresponds to the product between $(\boldsymbol{\delta\varphi^m})^t$ (the transpose of $\boldsymbol{\delta\varphi^m}$) and the j^{th} matrix of the curvature tensor $\boldsymbol{T}$.

3.3.2.2 Residual phase estimation: the command matrix

The previous Section 3.3.2.1 established the direct model between the differential measurements and the residual phases. The inversion of this model gives an estimation of the residual phases. However, several errors and noises impact the differential measurements influencing the inversion of $\boldsymbol{M_{int}}$. We list below the different errors and noises:

- The photodetector read-out noise is additive with Gaussian distribution, decorrelated and uniform (the same on each photodetector).
- The photon noise is additive with a Poisson distribution, decorrelated and not uniform (it depends on the number of photons received by each photodetector).
- Hypothesis 1 depends on the modulation frequency. Deviations from this hypothesis imply an additive noise on the spatial modulation vector equivalent to a multiplicative noise on $\boldsymbol{M_{int}}$.
- Hypothesis 3 is wrong in our integrated-AO application, implying a multiplicative noise on $\boldsymbol{M_{int}}$.

The two multiplicative noises are induced by hypotheses 1 and 3 used to establish the direct model. Thus, they are not taken into account in the inversion of $\boldsymbol{M_{int}}$. In the presence of photon noise, the inversion of $\boldsymbol{M_{int}}$ can be given by a maximum likelihood estimation, then the residual phase estimation, $\hat{\varphi}$, is given by:

$$\hat{\boldsymbol{\varphi}} = \left((\boldsymbol{M_{int}})^t.\boldsymbol{C_b^{-1}}.\boldsymbol{M_{int}}\right)^{-1}.(\boldsymbol{M_{int}})^t.\boldsymbol{C_b^{-1}}.\boldsymbol{\Delta s} \tag{3.10}$$

$\boldsymbol{C_b}$ is the diagonal (decorrelated noise) noise covariance matrix.
In the following, we suppose the noise is uniform, $C_b = \sigma_b^2\mathbb{I}$. In such a case the inversion of $\boldsymbol{M_{int}}$ is given by a least square estimation and Expression 3.10 becomes:

$$\begin{aligned}\hat{\boldsymbol{\varphi}} &= \left((\boldsymbol{M_{int}})^t.\boldsymbol{M_{int}}\right)^{-1}.(\boldsymbol{M_{int}})^t.\boldsymbol{\Delta s} \\ &= \boldsymbol{M_{int}^{\dagger}}.\boldsymbol{\Delta s} \\ &= \boldsymbol{M_{com}}.\boldsymbol{\Delta s}\end{aligned} \tag{3.11}$$

$\boldsymbol{M_{com}} = \boldsymbol{M_{int}^{\dagger}}$ is the command matrix being the general inverse of $\boldsymbol{M_{int}}$.

Finally, the spatial modulation control method allows the estimation of residual phases in one step independently of the number of guided waves to be combined coherently by the PIC, contrary to sequential and frequency modulation control methods. Thus, with the spatial modulation control method, the number of guided waves the PIC allows to combine coherently is no longer dependent on the phase shifters bandwidth. In other words, the spatial modulation control method uses the PIC as a wavefront sensor to estimate residual phases.

3.4 Linearity range of the direct model in a perfect case: Application to a 32-inputs PIC as an integrated DM

This Section aims to evaluate the linearity range of the direct model given by Expression 3.9 function of the amplitudes of the residual phase and of the spatial modulation by numerical simulation in a perfect case. The modulus of the complex amplitudes at the inputs of the PIC all equals 1, so that hypothesis 3 is verified. The frequency modulation is infinite, so hypothesis 1 is verified. The measurements are performed without noise.

We implement the spatial modulation control method on a 32-inputs PIC as an integrated-DM. The PIC is perfectly symmetric with 50:50 balanced couplers and without losses. This section is a first step to assess the spatial modulation control method in a prefect ideal case.

3.4.1 Linearity range: Impacts of the amplitude of the spatial modulation

In this Subsection, we compare the estimated phase of a fixed residual phase of zero means ranging from -0.1 to $+0.1$ radian function of the amplitude of the modulation.
The spatial modulation is chosen as a simple phase ramp of zero mean. The choice of the spatial coding of the spatial modulation vector is discussed in Section 3.5. In the following, the spatial modulation vector and residual phase are plotted in the PIC inputs space for simplicity.

Figure 3.3 compares the differences between estimated phases of a small amplitude residual phase for different amplitudes of the spatial modulation vector.

Figures 3.3a and 3.3b are obtained respectively with a spatial modulation vector with a standard deviation of 0.00176 *rad* and a norm of 0.01 *rad* and with a spatial modulation vector with a standard deviation of 0.176 *rad* and a norm of 1 *rad*. We can observe that with such spatial modulation amplitudes, the residual phase is well estimated. This means that such amplitudes of spatial modulation vectors allow the spatial modulation method to remain in the linear range of the direct model. However, when the amplitude of the spatial modulation increases, the residual phase estimation degrades, as shown in Figures 3.3c and 3.3d. Thus, for spatial modulations of zero means with standard deviations higher

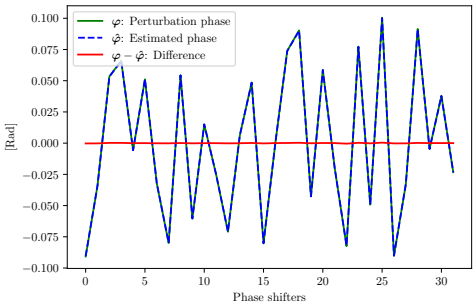

(a) In green, the residual perturbation phase ranges from -0.1 to $+0.1$ radian; in blue, the estimated phase and in red, their differences with a variance of 3×10^{-8} rad^2. Result obtained with a spatial modulation vector as a phase ramp of zero means ranging from -0.003 to $+0.003$ radian corresponding to a variance of 3.1×10^{-6} rad^2 and a norm of 0.01 rad.

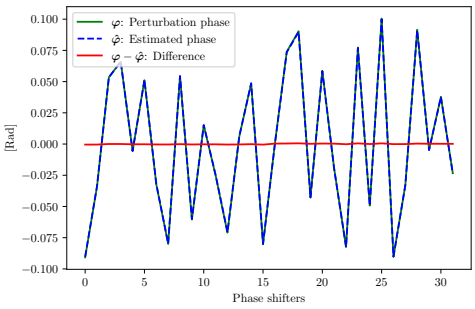

(b) In green, the residual perturbation phase ranges from -0.1 to $+0.1$ radian; in blue, the estimated phase and in red, their differences with a variance of 9×10^{-8} rad^2. Result obtained with a spatial modulation vector as a phase ramp of zero means ranging from -0.3 to $+0.3$ radian corresponding to a variance of 0.031 rad^2 and a norm of 1 rad.

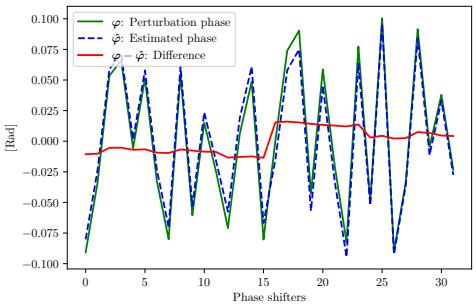

(c) In green, the residual perturbation phase ranges from -0.1 to $+0.1$ radian; in blue, the estimated phase and in red, their differences with a variance of 1×10^{-4} rad^2. Result obtained with a spatial modulation vector as a phase ramp of zero means ranging from -3 to $+3$ radian corresponding to a variance of 3.1 rad^2 and a norm of 10 rad.

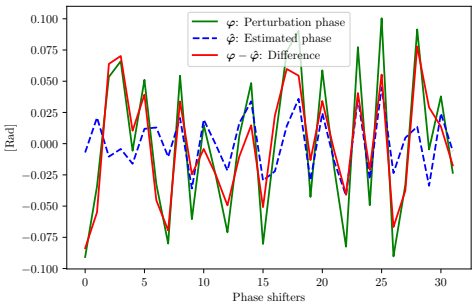

(d) In green, the residual perturbation phase ranges from -0.1 to $+0.1$ radian; in blue, the estimated phase and in red, their differences with a variance of 1×10^{-3} rad^2. Result obtained with a spatial modulation vector as a phase ramp of zero means ranging from -30 to $+30$ radian corresponding to a variance of 311 rad^2 and a norm of 100 rad.

Figure 3.3: Impact of the amplitude of the spatial modulation vector on the estimation of a residual phase ranging from -0.1 to +0.1 rad.

than a radian or spatial modulations with a norm higher than 10, the spatial modulation vector goes beyond the linear range of the direct model.
In the following, for the spatial modulation method to remain in the linear range of the direct model, we restrain the spatial modulation vector of zero mean to a standard deviation of one-tenth of a radian or a spatial modulation vector with a norm of 1 rad.

3.4.2 Linearity range: Impacts of the amplitude of the residual phases

This Subsection aims to evaluate the linearity range of the direct model function of the amplitude of the residual phases for a fixed spatial modulation vector. With regards to the above developments, the chosen spatial modulation vector for this Subsection is the

one with a norm of 1 *rad* depicted in Figure 3.3b.

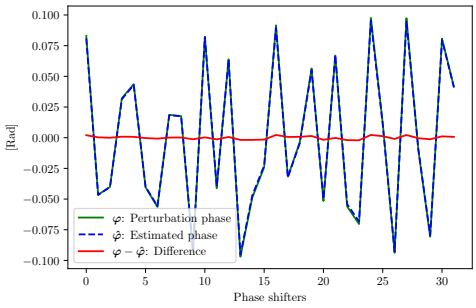

(a) Perturbation phases ranging from −0.1 to +0.1 radian.

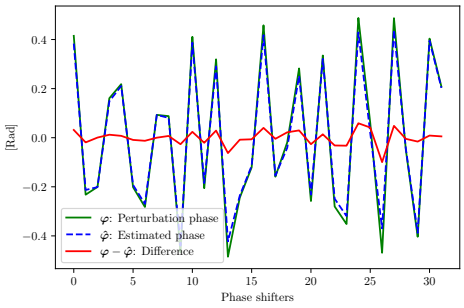

(b) Perturbation phases ranging from −0.5 to +0.5 radian.

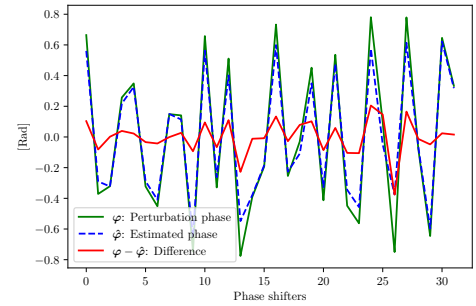

(c) Perturbation phases ranging from −0.8 to +0.8 radian.

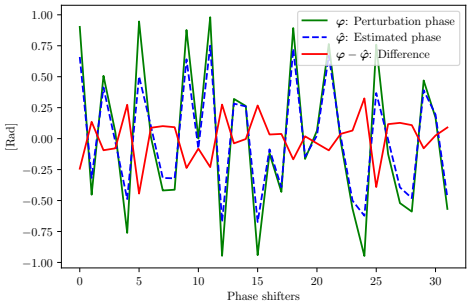

(d) Perturbation phases ranging from −1 to +1 radian.

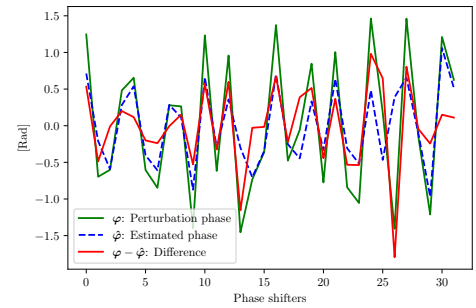

(e) Perturbation phases ranging from −1.5 to +1.5 radian.

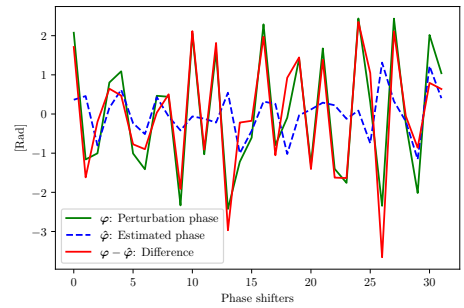

(f) Perturbation phases ranging from −2.5 to +3.5 radian.

Figure 3.4: Estimation of residual perturbation phases for different amplitudes. Green plots correspond to residual perturbation phases, blue dotted plots correspond to the estimates, and red plots correspond to their differences.

In Figure 3.4, the green plots correspond to the residual perturbation phases, the blue dotted plots correspond to the estimated phases, and the red plots correspond to the difference between the residual phases and their estimates.

In Figure 3.4, the phase coefficients are plotted in the PIC input space.
Estimated phases are nearly perfect for perturbations ranging from −0.1 and +0.1 radian, see Figure 3.4a and for perturbations ranging from −0.5 and +0.5 radian, see Figure 3.4b. However, in the control of the PIC, only the phase difference between the inputs matters. As seen in Figures 3.4a and 3.4b, residual phases with phase differences up to 1 *rad*

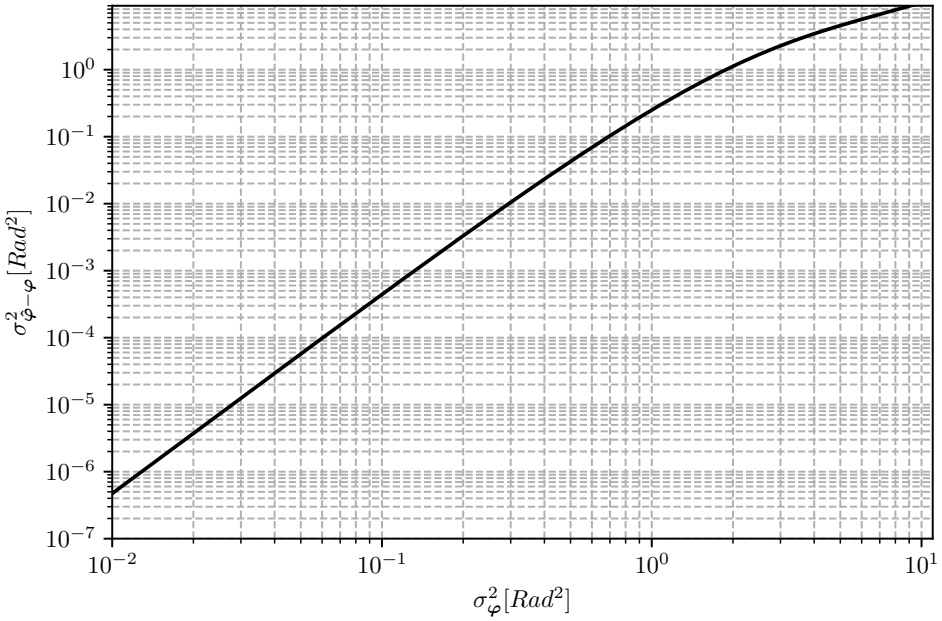

Figure 3.5: Linear regime of the spatial modulation control method. Variance of the difference between the perturbation phases and their estimates function of the perturbation phase variances.

between PIC inputs can be estimated in one step. In Figures 3.4d and 3.4e for phase difference up to 2 to 3 rad, the residual phase shape is still estimated but with underestimated coefficients. For phase differences up to 3 to 5 rad, see Figure 3.4f, the direct model fails to estimate the perturbation phase.
Thus, the control method based on spatial modulation can estimate small residual phases, below 1 radian of phase difference, in one step. As the amplitude of the phase perturbations increases, the quadratic model becomes less valid, and the phase estimations are degraded, as shown in Figure 3.4c and 3.4d. The shape of the phase perturbation is preserved, but the phase amplitudes of the coefficients with high values are underestimated. Considering high residual phases so that hypothesis 2 is wrong when we are not in the linear range anymore, the spatial modulation method can still estimate the shape of the residual phases but with an underestimation of the phase coefficients. Thus, the perturbation phases should decrease in a control loop as with a hill-climbing algorithm until the quadratic model becomes valid. Thus, the spatial modulation control method should allow for the closing of the loop.

Figure 3.5 plots the variance of the difference between residual phases and their estimate, function of the variance of residual phases of zero mean.

For a residual phase variance of 1 rad^2, the variance of the difference between the residual phase and its estimate is 0.2 rad^2. As expected, the dynamic of this method, restricted by the poor quadratic model, is low compared to other wavefront sensors. However, it is enough for closed-loop operation in case of low residual phases. This method seems well-suited for optical communication which requires high level of atmospheric effect mitigation.

3.5 Choice of the spatial coding of the spatial modulation vector: case of additive Gaussian noise, decorrelated and uniform

The above developments considered perfect intensity measurements and without noise to study the linear range of the direct model in a perfect case. However, in the presence of additive noise the estimated phase writes:

$$\hat{\boldsymbol{\varphi}} = \boldsymbol{M}_{\boldsymbol{int}}^{\dagger}.\boldsymbol{\Delta s}^{\boldsymbol{wn}} + \boldsymbol{M}_{\boldsymbol{int}}^{\dagger}.\boldsymbol{b} \tag{3.12}$$

With $\boldsymbol{b}$ an additive noise and $\boldsymbol{\Delta s}^{\boldsymbol{wn}}$ the differential measurements without additive noise. The covariance of the estimated phase error induced by additive noise $\boldsymbol{b}$ writes:

$$< \boldsymbol{\varphi_b}{\boldsymbol{\varphi_b}}^t >=< \boldsymbol{M}_{\boldsymbol{int}}^{\dagger}\boldsymbol{C_b}{\boldsymbol{M}_{\boldsymbol{int}}^{\dagger}}^t > \tag{3.13}$$

With $\boldsymbol{C_b}$ the covariance matrix of $\boldsymbol{b}$.

Impact of the spatial modulation amplitude: In Section 3.4.1 we obtain an upper bound for the amplitude of the spatial modulation vector. Furthermore, with a perfect model of PIC and measurements performed without noise there is no lower bound for the amplitude of the modulation. However, considering additive noise on the measurements, increasing the amplitude of the spatial modulation vector reduces $< \boldsymbol{\varphi_b}{\boldsymbol{\varphi_b}}^t >$ and thus the noise propagation on $\hat{\boldsymbol{\varphi}}$ (as a reminder $\boldsymbol{M_{int}}$ is function of $\boldsymbol{\delta\varphi_m}$). The higher the spatial modulation amplitude, the lower the noise propagation.
Thus, in a realistic case with additive noise, the spatial modulation vector amplitude must be set at the upper bound to remain in the linear range of the direct model while minimizing the noise propagation.

Impact of the spatial modulation coding: In expression 3.11 we inverse the direct model with a least square estimation considering additive Gaussian noise, decorrelated and uniform. In such a case, the covariance matrix $\boldsymbol{C_b}$ becomes $\boldsymbol{C_b} = \sigma_{\boldsymbol{b}}^2\mathbb{I}$, with $\sigma_{\boldsymbol{b}}^2$ the noise variance and $\mathbb{I}$ the identity matrix. Thus, the covariance of the estimated phase error in Expression 3.13 becomes:

$$< \boldsymbol{\varphi_b}{\boldsymbol{\varphi_b}}^t >= \sigma_{\boldsymbol{b}}^2 < \boldsymbol{M}_{\boldsymbol{int}}^{\dagger}{\boldsymbol{M}_{\boldsymbol{int}}^{\dagger}}^t > \tag{3.14}$$

The mean quadratic error on the estimated phase induced by noise is given by:

$$\begin{aligned} < |\boldsymbol{\varphi_b}|^2 > &= tr\left(< \boldsymbol{\varphi_b}{\boldsymbol{\varphi_b}}^t >\right) \\ &= \sigma_{\boldsymbol{b}}^2 tr\left(< \boldsymbol{M}_{\boldsymbol{int}}^{\dagger}{\boldsymbol{M}_{\boldsymbol{int}}^{\dagger}}^t >\right), \end{aligned} \tag{3.15}$$

with '$tr()$' denoting the trace. By performing the Singular Value Decomposition (SVD) of $\boldsymbol{M_{int}}(\boldsymbol{\delta\varphi^m})$ ($\boldsymbol{M_{int}}$ is function of the spatial modulation vector) it comes:

$$\begin{aligned} < |\boldsymbol{\varphi_b}|^2 > &= \sigma_{\boldsymbol{b}}^2 tr < \boldsymbol{V}(\boldsymbol{\delta\varphi^m})\left(\boldsymbol{\Sigma}(\boldsymbol{\delta\varphi^m})^{\dagger}\right)^2 \boldsymbol{V}(\boldsymbol{\delta\varphi^m})^t > \\ &\propto \sigma_{\boldsymbol{b}}^2 \sum_s \frac{1}{\left(V_s(\boldsymbol{\delta\varphi^m})\right)^2} \end{aligned}, \tag{3.16}$$

with $V_s(\boldsymbol{\delta\varphi^m})$ the s^{th} singular value of the interaction matrix $\boldsymbol{M_{int}(\delta\varphi^m)}$. The interaction matrix is built for a fixed chosen $\boldsymbol{\delta\varphi^m}$. We have seen above that increasing the amplitude of the spatial modulation vector reduces the noise propagation. And that spatial modulation vectors with a fixed norm of 1 *rad* are the upper bound for the linear range of our direct model.

However, at fixed norm, changing the spatial coding of $\boldsymbol{\delta\varphi^m}$ modify $\boldsymbol{M_{int}(\delta\varphi^m)}$. Thus, changing the spatial coding of $\boldsymbol{\delta\varphi^m}$ (at fixed norm) gives another SVD implying a different noise propagation. Finally, at fixed norm, the noise propagation depends on the choice of spatial coding for the spatial modulation vector.
The minimum noise propagation is reached for a spatial modulation vector minimizing the term $\sum \frac{1}{(V_s(\boldsymbol{\delta\varphi^m}))^2}$ (at fixed norm).

This Section aims to identify the spatial coding for the spatial modulation vector at a fixed norm that minimises noise propagation.

3.5.1 Analytical method to determine the spatial coding minimizing the noise propagation

To determine an analytical expression of the spatial modulation vector minimizing the noise propagation, we need to express Expression 3.16 explicitly as a function of the coefficients of $\boldsymbol{\delta\varphi^m}$. From this, the derivative of Expression 3.16 can be computed analytically with respect to the coefficients of $\boldsymbol{\delta\varphi^m}$. Then, a linear system of equations whose solution is the minimum of Expression 3.16 can be written. Solving this linear system of equations gives the spatial coding minimizing the noise propagation.

To express Expression 3.16 explicitly as a function of the coefficients of $\boldsymbol{\delta\varphi^m}$ we need to express $\boldsymbol{\delta\varphi^m}$ and $\boldsymbol{\varphi}$ in another basis.
With our direct model, see Equation 3.9, the j^{th} output measurement is given by:

$$\Delta s_j = (\boldsymbol{\delta\varphi_m})^t . \boldsymbol{T_j} . \boldsymbol{\varphi} \tag{3.17}$$

With $\boldsymbol{T_j}$ the j^{th} matrix of the tensor $\boldsymbol{T}$ defined with Expression 3.7. The PIC is supposed to be perfectly symmetric with 50:50 couplers. Thus, the matrices $(\boldsymbol{T_j})$ are symmetric by construction.

Let $(\boldsymbol{t_k})$ for $k \in (0, N-2)$ be $N-1$ vectors of $N-1$ unknown each. Supposing that the linear system defined as:

$$\begin{cases} \boldsymbol{T_j}.\boldsymbol{t_k} = \boldsymbol{0} & \forall k \neq j,\ k \in (0, N-2) \\ \boldsymbol{T_j}.\boldsymbol{t_k} \neq \boldsymbol{0} & \text{if } k = j \end{cases} , \tag{3.18}$$

has a solution, it gives an orthogonal family of vectors $(\boldsymbol{t_k})$. Its dimension is equal to $N-1$, thus $(\boldsymbol{t_k})$ is a basis for $\boldsymbol{\delta\varphi^m}$ and for $\boldsymbol{\varphi}$. We can decompose the spatial modulation vector $\boldsymbol{\delta\varphi^m}$ and the residual phase vector $\boldsymbol{\varphi}$ in the basis formed by vectors $\boldsymbol{t_k}$:

$$\begin{aligned} \boldsymbol{\delta\varphi^m} &= \sum_i \delta\alpha_i^m \boldsymbol{t_i} \\ \boldsymbol{\varphi} &= \sum_l \alpha_l \boldsymbol{t_l} \end{aligned} . \tag{3.19}$$

$(\delta\alpha_i^m)$ are $N-1$ unknown coefficients of the spatial modulation vector in the $(\boldsymbol{t_k})$ basis. (α_l) are $N-1$ unknown coefficients of the residual phase vector in the $(\boldsymbol{t_k})$ basis.

Thus, the j^{th} differential measurement in Expression 3.17 can be rewritten it the $(\boldsymbol{t_k})$ basis:

$$\begin{aligned}\Delta s_j &= (\sum_i \delta\alpha_i^m \boldsymbol{t_i})^t \boldsymbol{T}_j \sum_l \alpha_l \boldsymbol{t_l} \\ &= \sum_l \sum_i \delta\alpha_i^m \alpha_l \boldsymbol{t_i}^t.\boldsymbol{T_j}.\boldsymbol{t_l} \\ &= \sum_l \sum_i \delta\alpha_i^m \alpha_l \boldsymbol{t_i}^t.\boldsymbol{T_j}.\boldsymbol{t_l}\delta_{ji}\delta_{jl} \\ &= \delta\alpha_j^m \boldsymbol{t_j^t T_j t_j} \alpha_j\end{aligned} , \tag{3.20}$$

with δ_{jl} the Kronecker delta.
Finally, the differential measurement vector is Expression 3.9 can be written as:

$$\boldsymbol{\Delta s} = \boldsymbol{D\alpha}\,, \tag{3.21}$$

With $\boldsymbol{D}$ the diagonal matrix of elements $(\delta\alpha_{mj}\boldsymbol{t_j^t T_j t_j})$.
Now that we have rewritten the direct model in the $(\boldsymbol{t_k})$ basis, the mean quadratic error induced by noise in expression 3.16 can be written as a direct function of $(\delta\alpha_i^m)$ such as:

$$< |\varphi_{\boldsymbol{b}}|^2 >= \sigma_b^2 \sum_j \frac{1}{(\delta\alpha_j^m \epsilon_j)^2}\,. \tag{3.22}$$

With $\epsilon_j = \boldsymbol{t_j^t T_j t_j}$.

Finally, the noise propagation is expressed as a direct function of the spatial modulation vector coefficients $(\delta\alpha_j^m)$. We can derive Expression 3.22 with respect to the $N-1$ coefficients $(\delta\alpha_j^m)$. Thus, determining the spatial coding of the spatial modulation vector at constant norm in the $(\boldsymbol{t_k})$ basis, minimizing Expression 3.22 is equivalent to solving the system of equations of unknown $(\delta\alpha_j^m)$:

$$\frac{\partial(\sigma_b^2 \sum_j \frac{1}{(\delta\alpha_j^m \epsilon_j)^2} + \sum_j \delta{\alpha_j^m}^2)}{\partial\delta\alpha_j^m} = 0,\ \forall j \in (0, N-2)\,. \tag{3.23}$$

The analytical solution of Equation 3.23 is:

$$\delta\alpha_j^{opt} = \sqrt{\frac{\sigma_b}{\epsilon_j}},\ \forall j \in (0, N-2)\,. \tag{3.24}$$

Thus, we express the coefficients of the spatial modulation vector minimizing Expression 3.22 in the $(\boldsymbol{t_k})$ basis as a function of the vectors $(\boldsymbol{t_k})$.
Going back to the canonical basis, we have:

$$\boldsymbol{\delta\varphi^{opt}} = \boldsymbol{P\delta\alpha^{opt}}\,. \tag{3.25}$$

$\boldsymbol{P}$ is the matrix formed by vectors $(\boldsymbol{t_k})$.

Finally, supposing the linear system 3.18 admit a solution, its resolution gives the analytical expression of the spatial coding of the spatial modulation vector minimizing the noise propagation in Expression 3.16 at constant norm: $\boldsymbol{\delta\varphi^{opt}}$. It only depends on the PIC curvature tensor, $\boldsymbol{T}$, which depends on the PIC architecture.

3.5.2 Numerical method to compute the spatial coding minimizing the noise propagation

The method developed above is based on the analytical determination of a basis $(\boldsymbol{t_k})$, by solving Expression 3.18, allowing to analytically compute the partial derivatives of the noise propagation of Expression 3.16 with respect to the spatial modulation vector coefficients. Then, solving the system of equations 3.23 gives $\boldsymbol{\delta\varphi^{opt}}$. However, the determination of a basis $(\boldsymbol{t_k})$ by solving Expression 3.18 is not trivial, and a solution may not exist. Nevertheless, computing the partial derivatives of the noise propagation of Expression 3.16 with respect to the spatial modulation vector coefficients is possible without the determination of a basis $(\boldsymbol{t_k})$. Indeed, Expression 3.16 depends on the SVD which depends on the coefficients of $\boldsymbol{M_{int}(\delta\varphi^m)}$ themselves depending on the spatial coding of $\boldsymbol{\delta\varphi^m}$. From reference [132], it is possible to derive the singular values of a matrix compared to the matrix coefficients. Thus, it is possible to compute directly the partial derivatives of Expression 3.16 with respect to the spatial modulation vector coefficients at constant norm such as:

$$\begin{aligned}\left(\frac{\partial < |\boldsymbol{\varphi_b}|^2 > + \sum_j (\delta\varphi_j^m)^2}{\partial \delta\varphi_j^m}\right) = & \frac{\partial < |\boldsymbol{\varphi_b}|^2 > + \sum_j (\delta\varphi_j^m)^2}{\partial V_s(\boldsymbol{\delta\varphi^m})} \\ & \times \frac{\partial V_s(\boldsymbol{\delta\varphi^m})}{\partial \boldsymbol{M_{int}(\delta\varphi^m)}} \times \frac{\partial \boldsymbol{M_{int}(\delta\varphi^m)}}{\delta\varphi_j^m}\end{aligned} \tag{3.26}$$

Thus, from Expression 3.26 a gradient descent loop can be applied to minimize $\left(\frac{\partial < |\boldsymbol{\varphi_b}|^2 > + \sum_j (\delta\varphi_j^m)^2}{\partial \delta\varphi_j^m}\right)$ with respect to the spatial coding of $\boldsymbol{\delta\varphi^m}$. Algorithm 1 implements such a gradient descent loop using an ADAM method [133].

Algorithm 1 : Gradient descent loop to minimize Expression 3.16

Initiate:
$\boldsymbol{\delta\varphi^m} \leftarrow \frac{\boldsymbol{\delta\varphi^m}}{|\boldsymbol{\delta\varphi^m}|}$, Initiate the spatial coding with a normalized vector.
$loss \leftarrow loss$, Initiate the loss function.
$\epsilon \leftarrow \epsilon$, Initiate the precision to reach on the loss function.
while $loss > \epsilon$ **do**
  $V_s(\boldsymbol{\delta\varphi^m}) \leftarrow SVD(\boldsymbol{M_{int}(\delta\varphi^m)})$, Compute the SVD of $\boldsymbol{M_{int}(\delta\varphi^m)}$).
  $loss \leftarrow \sum \frac{1}{(V_s(\boldsymbol{\delta\varphi^m}))^2} + \sum_j (\delta\varphi_j^m)^2$, Update the loss function.
  $\boldsymbol{\nabla} \leftarrow \frac{\partial \text{loss}}{\partial \boldsymbol{\delta\varphi^m}}$, Compute Expression 3.26.
  $\boldsymbol{\delta\varphi^m} \leftarrow ADAM(\boldsymbol{\delta\varphi^m}, \boldsymbol{\nabla})$, Update $\boldsymbol{\delta\varphi^m}$ in a gradient descent loop with an ADAM method.
end while

In the following, algorithm 1, is implemented using PyTorch to compute expression 3.26 and implement the ADAM gradient descent loop.

3.5.3 Spatial coding minimizing additive Gaussian noise, decorrelated and uniform: Application to a 32-inputs PIC as an integrated DM

This Subsection implements Algorithm 1 to determine the spatial coding of the spatial modulation vector minimizing the error induced on $\hat{\boldsymbol{\varphi}}$ by additive Gaussian noise, decorrelated and uniform. We take the case of the 32-inputs PIC as an integrated-DM perfectly symmetric with 50:50 couplers and without losses depicted in Figure 3.2. The modulus of

the complex amplitudes at the PIC inputs are all set to 1.
Algorithm 1 is initiated with a spatial modulation vector chosen as a phase ramp and is run for thousands of iterations. Figure 3.6 plots the loss function of algorithm 1 with respect to the number of iterations of the algorithm.

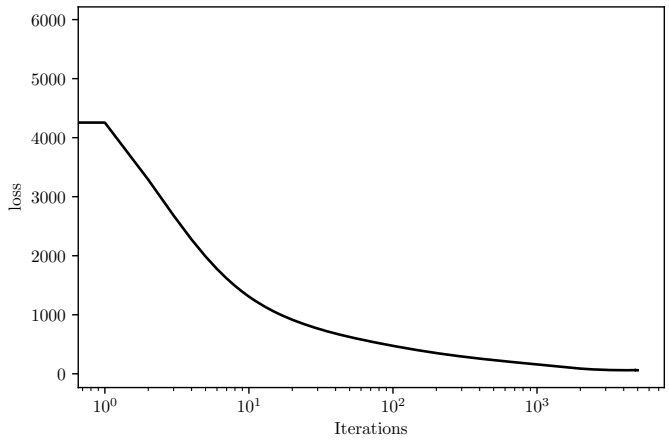

Figure 3.6: Loss function when applying Algorithm 1.

Algorithm 1 converges, after a thousand iterations, to the spatial modulation vector denoted, $\boldsymbol{\delta\varphi^{opt}}$, and plotted in Figure 3.7.

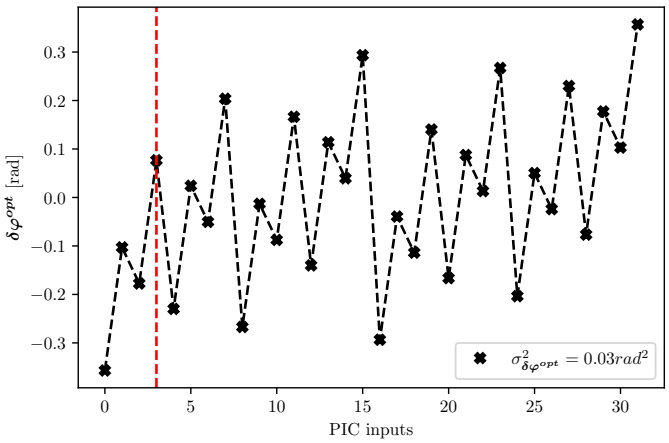

Figure 3.7: Spatial modulation vector, $\boldsymbol{\delta\varphi^{opt}}$, obtained after a thousand iteration of Algorithm 1.

This spatial modulation vector $\boldsymbol{\delta\varphi^{opt}}$ is plotted in the PIC input phase space. It follows the PIC symmetry with an elementary pattern formed by the fourth first phase shifters numbered 0 to 3 (red dotted line). Thus, $\boldsymbol{\delta\varphi^{opt}}$ can be determined by mathematical induction for other sizing of PIC. The norm of $\boldsymbol{\delta\varphi^{opt}}$ is 1 *rad* and its standard deviation is 0.17 *rad*. It corresponds to the upper bond discussed in Section 3.4 to remain in the linear range of the direct model.

With the phase shifters set to maximize s_0, Figure 3.8 compares the output intensity measurements of the PIC with a spatial coding chosen as $\boldsymbol{\delta\varphi^{opt}}$ and as a phase ramp.

With both spatial coding, modulating the PIC takes 3% of the total PIC input intensity to perform the measurements. However, $\boldsymbol{\delta\varphi^{opt}}$ allows to uniformly stimulates the output measurements whereas the spatial coding as a phase ramp stimulates the output measurements only uniformly stage by stage of the PIC.

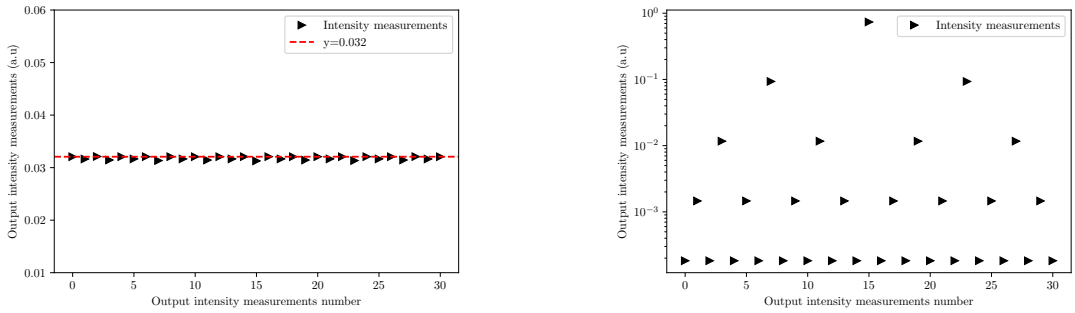

(a) (b)

Figure 3.8: (a): Intensity measurements at the outputs of the PIC with the phase shifters set to maximize s_0 and with $\boldsymbol{\delta\varphi^{opt}}$, depicted in Figure 3.7, applied as a positive step dither. (b): Intensity measurements at the outputs of the PIC with the phase shifters set to maximize s_0 and with a spatial coding as a phase ramp, applied as a positive step dither.

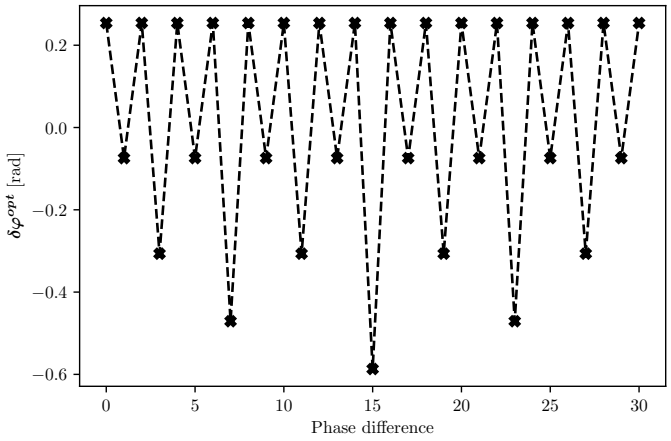

Figure 3.9: Phase differences of $\boldsymbol{\delta\varphi^{opt}}$ depicted in Figure 3.7.

Figure 3.9, presents the difference phases of $\boldsymbol{\delta\varphi^{opt}}$. We can observe that the phase differences are the same stage by stage but with amplitudes increasing with the stages. This allows for the compensation of spatial coding as a phase ramp, which stimulates the output measurements only uniformly stage by stage.

Figure 3.10 presents the singular value decomposition of the interaction matrix obtained with $\boldsymbol{\delta\varphi^{opt}}$, Figure 3.10a, and obtained with a spatial coding as a phase ramp depicted in Figure 3.3b. Thus, $\boldsymbol{\delta\varphi^{opt}}$ allows us to build an interaction matrix with a condition number of 1, i.e. all singular values equals the same value: 0.718, and we have $\sum \frac{1}{\left(V_{s_{\boldsymbol{\delta\varphi^{opt}}}}\right)^2} = 60$. Whereas, with a spatial coding as a phase ramp, the singular val-

ues are only equal stage by stage of the PIC and we have $\sum \frac{1}{\left(V_{s_{\boldsymbol{\delta\varphi^m}}}\right)^2} = 5836$ with an interaction matrix condition number of 64.

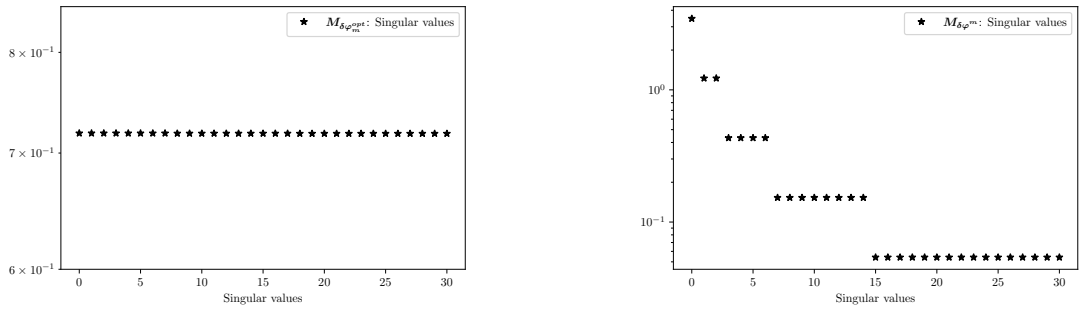

(a) (b)

Figure 3.10: (a): Singular values of the interaction matrix built with $\boldsymbol{\delta\varphi^{opt}}$. (b): Singular values of the interaction matrix built with a spatial coding as a phase ramp.

It must be highlighted that the interaction matrix built with a spatial coding as a phase ramp is still well conditioned, and the inversion of the direct model should not be too much degraded compared with $\boldsymbol{\delta\varphi^{opt}}$.

All developments on noise propagation and its minimization were based on the hypothesis of additive Gaussian noise, uniform and decorrelated. As discussed in Section 3.3.2.2, such a model is valid for photodetector read-out noise but not for photon noise. However, as developed above, modulating the phase shifters with $\boldsymbol{\delta\varphi^{opt}}$ allows to stimulate uniformly the intensity measurements of the PIC. Thus, the hypothesis of additive Gaussian noise, uniform and decorrelated, is also valid for photon noise with $\boldsymbol{\delta\varphi^{opt}}$.

To evaluate the photon noise propagation of the equivalent WFS formed by the PIC with the direct model, we compute the mean quadratic error induced by photon noise, $< |\boldsymbol{\varphi_b}|^2 >$, from Expression 3.15. The photon noise variance equals two times the signal measured during one modulation. Let N_{ph} be the number of photons per input of the PIC and per modulation cycle so that a differential measurement, Δs_j, corresponds to $2N_{ph}$ photons.

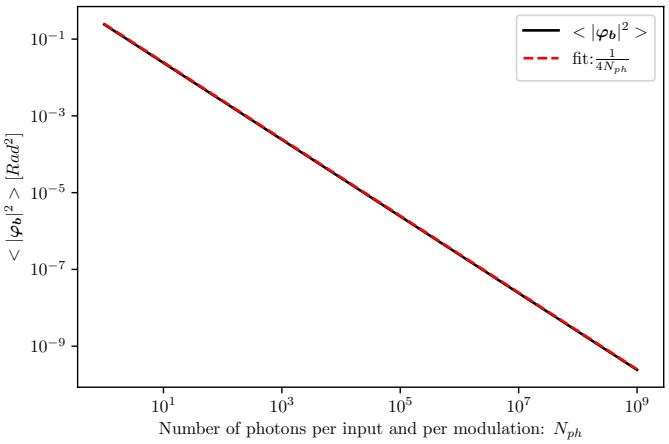

Figure 3.11: Black curve: Mean quadratic error, $< |\boldsymbol{\varphi_b}|^2 >$, induced by photon noise with $\boldsymbol{\delta\varphi^{opt}}$. Red dotted curve: fit in $1/(4N_{ph})$

Figure 3.11 plots the noise propagation obtained with $\boldsymbol{\delta\varphi^{opt}}$. It follows the law in $< |\boldsymbol{\varphi_b}|^2 >= \frac{0.25}{N_{ph}}$ (black curve) which perfectly fits the law in $\frac{1}{4N_{ph}}$ (red curve) corresponding to the theoretical minimum photon noise propagation as developed in references [134, 135]. Thus, $\boldsymbol{\delta\varphi^{opt}}$ enables the direct model to reach the fundamental limit of photon noise propagation.

As a comparison, Figure 3.12 plots the photon noise propagation obtained with a spatial coding as a phase ramp (see Figure 3.3b) using $tr\left(< \boldsymbol{M^{\dagger}_{\delta\varphi^m} C_b M^{\dagger}_{\delta\varphi^m}}^{t} >\right)$. The mean quadratic error induced by photon noise with a spatial coding as a phase ramp is a hundred times higher than with $\boldsymbol{\delta\varphi^{opt}}$.

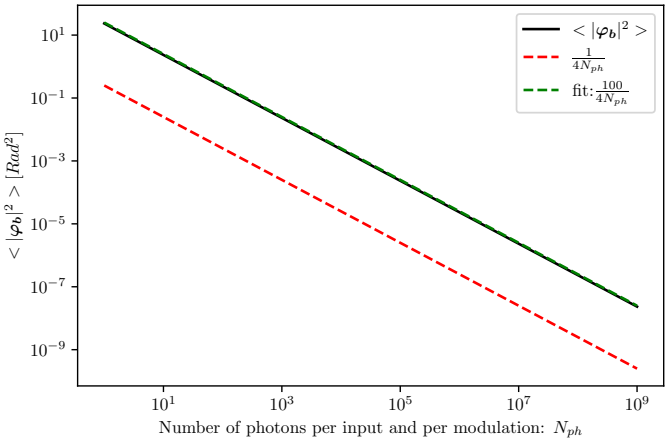

Figure 3.12: Black curve: Mean quadratic error, $< |\boldsymbol{\varphi_b}|^2 >$, induced by photon noise with a phase ramp. Red dotted curve: fit in $1/(4N_{ph})$. Green dotted curve: fit in $100/(4N_{ph})$.

3.6 Generalization for amplitude correction

Considering a phase and amplitude correction with a PIC composed of MZIs, there are still $N-1$ intensity measurement outputs, but there are $2N-2$ phase shifters to be controlled. In such a case, one spatial coding of the modulation should be used to control for

the external phase shifters of the MZIs (same case as integrated-DM) and another one, with a different interaction matrix, should be used to control for the internal phase shifters.

With a PIC composed of MZIs, the internal phase shifters of the MZIs cannot be moved elsewhere in the PIC contrary to external phase shifters which can be moved at the inputs of the PIC as in the integrated-DM case. Thus, the matrix of the PIC, $\boldsymbol{C_{pic}}$, cannot be decomposed as the product of a fixed matrix, $\boldsymbol{C^f}$, and a diagonal matrix of phase shifters, $\boldsymbol{C^{ps}}$ as in Expression 3.2. Thus, establishing the interaction matrix for the internal phase shifters from the PIC output intensity measurements as in Section 3.3.2.1 is not trivial.
However, near the optimum, when s_0 is near the maximum, and the intensity measurements are near minimums, the j^{th} intensity measurement is a function of the residual phases. Thus, it can be decomposed with a Taylor expansion, especially for the residual phase in the internal phase shifter space as:

$$s_j(\boldsymbol{\varphi}) = s_j(\boldsymbol{\varphi})|_{\boldsymbol{min}} + \sum_k \left.\frac{\partial s_j(\boldsymbol{\varphi})}{\partial \varphi_k^{ps}}\right|_{\boldsymbol{min}} \varphi_k + \frac{1}{2}\sum_k\sum_l \left.\frac{\partial^2 s_j(\boldsymbol{\varphi})}{\partial \varphi_k^{ps}\partial \varphi_l^{ps}}\right|_{\boldsymbol{min}} \varphi_k\varphi_l \,. \tag{3.27}$$

The physical behaviour of the PIC is included in the partial derivative terms. Near the optimum, considering a quadratic model, the first order derivatives can be neglected and by applying the spatial modulation, $\boldsymbol{\delta\varphi^m}$, the j^{th} differential measurement becomes:

$$\begin{aligned}\Delta s_j &= \frac{1}{2}\sum_k\sum_l \left.\frac{\partial^2 s_j(\boldsymbol{\varphi})}{\partial \varphi_k^{ps}\partial \varphi_l^{ps}}\right|_{\boldsymbol{min}} [(\varphi_k+\delta\varphi_k)(\varphi_l+\delta\varphi_l) - (\varphi_k-\delta\varphi_k)(\varphi_l-\delta\varphi_l)] \\ &= \sum_k\sum_l 2\left.\frac{\partial^2 s_j(\boldsymbol{\varphi})}{\partial \varphi_k^{ps}\partial \varphi_l^{ps}}\right|_{\boldsymbol{min}} \delta\varphi_l\varphi_k\end{aligned} \,. \tag{3.28}$$

With the curvature tensor $\boldsymbol{T}$ defined in Expression 3.7 and with relation 3.8 we obtain the same linear relation between the differential measurements and the residual phases as in Expression 3.9:

$$\begin{aligned}\boldsymbol{\Delta s} &= (\boldsymbol{\delta\varphi^m})^t \boldsymbol{T}\boldsymbol{\varphi} \\ &= \boldsymbol{M_{int}}\boldsymbol{\varphi}\end{aligned} \tag{3.29}$$

3.7 conclusion

Unlike sequential and frequency modulation control methods, the spatial modulation control method allows the estimate of the residual phase in one step. Thus, the bandwidth required by the phase shifters is independent of the number of complex amplitudes to combine coherently. We established the direct model, based on three hypotheses, of the spatial modulation control method in the case of phase-only correction PICs and discussed its extension to phase and amplitude correction with MZI-based PICs. The inversion of the direct model allowing the use of the PIC as a WFS was discussed regarding the noise and errors impacting the measurements. The spatial modulation control method was applied with a 32-inputs perfect PIC without noises and losses. An upper bound of a norm of 1 *rad* for the spatial modulation vector was determined to stay in the linear range of the direct model. Then, the linearity range of the direct model was studied as a function of the amplitude of the perturbations. Even beyond the linear range of the direct

model, the shape of the residual phase is well estimated but with an underestimation of its amplitude. Thus, it should allow for the spatial modulation control method to close the loop as a hill-climbing algorithm. Finally, the choice of the spatial coding of the spatial modulation vector at a fixed norm was discussed. An analytical method was developed to determine the general expression of the spatial coding minimizing the propagation of additive Gaussian noise decorrelated and uniform function of the PIC architecture. Then, a numerical method based on a gradient descent optimization algorithm was developed to determine the spatial coding, minimizing the propagation of additive Gaussian noise, decorrelated and uniform without the need to perform complex analytical calculus. From this numerical method, the choice of the spatial coding was discussed in the case of the 32-inputs perfect PIC. We showed that the optimized spatial coding allows to reach the fundamental limits of photon noise propagation for WFS.

In the following chapter, I develop a general method for the sizing of an integrated-AO. This chapter aims to study the performance of the spatial modulation control method in realistic conditions. We will address the aspect of finite frequency modulation so that hypothesis 1 will be wrong. Fluctuating non-uniform modulus of the complex amplitudes so that hypothesis 3 will be wrong. The questions of closing the loop with the spatial modulation control method and closed-loop performances in the presence of noises will be addressed.

CHAPTER 4

Perfect integrated-AO performances: End-to-End simulation

Contents

4.1 Introduction

In the previous chapter, we developed and explained the principle of the spatial modulation control method, allowing the use of the PIC as a wavefront sensor in closed-loop. Strong hypotheses such as uniform and constant modulus of the complex amplitudes and infinite modulation frequency are used to establish the interaction matrix of the direct model.

This chapter addresses the spatial modulation control method behaviour in realistic atmospheric turbulence conditions. How does the spatial modulation control method behave in a closed-loop with fluctuating modulus of the complex amplitudes? With finite modulation frequency? With noise? And with open loop phase perturbations, can we close the loop with spatial modulation?

More generally, this chapter aims to present a general method for the desing of an integrated-AO with respect to the different error terms impacting the power coupled in the telecom output.

For this, Section 4.2 develops the different error terms impacting the power coupled in the telecom output. Then, a method for integrated-AO design is presented in Section 4.3 and applied in the specific case of the downlink scenario presented in Appendix B. The theoretical impact of each error term is evaluated with the integrated-AO design. Section 4.4 develops an end-to-end simulation to test the spatial modulation control method in the realistic downlink scenario used for the integrated-AO design. The impacts of the different measurement error terms are analyzed in a closed-loop. Then, the use of photometric measurements to increase the closed-loop performances is studied in Section 4.5. Finally, closed-loop performances using the spatial modulation control method are compared to closed-loop performances using sequential modulation in Section 4.6.

4.2 Integrated-AO performances: the different error terms

As the Strehl ratio is commonly used as a criterion in adaptive optics, here to evaluate the performances of an integrated-AO we rely on the average power coupled into the telecom output, s_0, compared to the total average power of the distorted field Ψ^{turb} collected by the telescope:

$$\langle \eta \rangle = \frac{< s_0 >}{< |P\Psi^{turb}|^2 >} . \tag{4.1}$$

P is the transmittance function of the telescope pupil.
Different error terms impact $\langle \eta \rangle$ such as:

- The fitting error of $P\Psi^{turb}$ by the spatial demultiplexer.
- The phase-only correction error.
- The temporal error.
- The measurement errors.

These error terms are developed below.

4.2.1 The fitting error

As presented in Section 1.6, the average power attenuation induced by the projection of the distorted field on a finite number of guided waves depends on the choice of the spatial demultiplexer and the number of modes onto which the distorted field is decomposed. We define:

$$\langle \eta_{demux} \rangle = \frac{\sum_{j=0}^{N-1} \langle |a_j|^2 \rangle}{\langle |P\Psi^{turb}|^2 \rangle}, \tag{4.2}$$

the average power at the demultiplexer output normalized by the average power collected by the telescope. Considering a projection on a mode M_j, we have:

$$a_j = \frac{\int \Psi^{turb}(\boldsymbol{r}) M_j^*(\boldsymbol{r}) P(\boldsymbol{r}) d\boldsymbol{r}}{\sqrt{\int M_j^*(\boldsymbol{r}) P(\boldsymbol{r}) M_j(\boldsymbol{r}) P(\boldsymbol{r}) d\boldsymbol{r}}}, \tag{4.3}$$

Luca Rinaldi analytically calculated this attenuation for different families of modes [6]. With a $D/r_0 = 5$, he showed that a decomposition around thirty HG-modes gives an average power: $\langle \eta_{demux} \rangle = 0.65$.

4.2.2 The phase-only correction error

As developed in Section 2.3, a phase-only correction PIC is advantageous compared to phase and amplitude correction when the complex amplitudes at the PIC input follow the same statistic with the same moments. The average power coupled in the telecom output for a phase-only correction normalized by the total PIC input average power is:

$$\langle \eta_0 \rangle = \frac{\left\langle \frac{1}{N} \sum_{k=0}^{N-1} \sum_{l=0}^{N-1} |a_k||a_l| \right\rangle}{\sum_{j=0}^{N-1} \langle |a_j|^2 \rangle} \tag{4.4}$$

In the case of a microlens array placed in the pupil plane or a MPLC with HG modes up to $(D/r_0)^2$ for $D >> r_0$ we saw in Section 2.3.3 that: $\langle \eta_0 \rangle \geq \pi/4$.

4.2.3 The temporal error

For the spatial modulation control method we consider the control loop timing diagram illustrated in Figure 4.1. The correction is renewed at time intervals of duration τ_c (correction frequency f_c). During a time interval defined by two new corrections, the applied correction is constant, $\boldsymbol{\varphi}_{\tau_c}^{\boldsymbol{corr}}$, and measurements are carried out by spatial modulation. We denote τ_m (modulation frequency f_m) as the modulation period. During a time interval between two corrections, $p = \frac{\tau_c}{\tau_m}$ differential measurements are carried out.

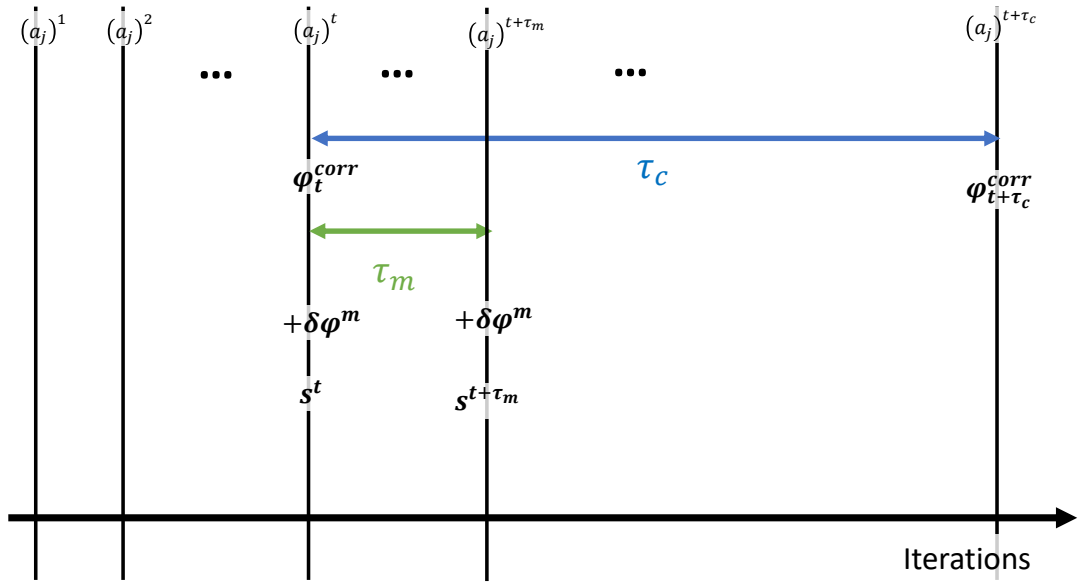

Figure 4.1: Control loop timing diagram of the spatial modulation control method.

The temporal error is induced by the evolution of the complex amplitudes at the PIC input during the time τ_c while the correction is constant. It can be roughly evaluated using the approach developed for adaptive optics. Therefore, assuming that all the turbulence effects can be mitigated by the loop we have:

$$\langle \eta_{tempo} \rangle = e^{-\sigma^2_{tempo}}.$$

It corresponds to the average intensity coupled in s_0 normalized by the average total intensity at the input of the PIC, considering only the temporal error.

Considering one turbulent layer ($r_{0,h}$) in uniform translation at the velocity v_h and that the log-amplitude fluctuations are weak compared to phase fluctuations, the turbulence at time $t + \tau_c$ differs in root mean square from turbulence at time t by [43]:

$$\sigma^2_{tempo} = 6.88 \left(\frac{v_{moy}\tau_c}{r_{0,h}} \right)^{\frac{5}{3}} rad^2, \tag{4.5}$$

It can be extended to multilayer cases, giving an approximate [43]:

$$\sigma^2_{tempo} = 6.88 \left(\frac{v_{moy}\tau_c}{r_0} \right)^{\frac{5}{3}} rad^2, \tag{4.6}$$

v_{moy} is the average transverse wind velocity and r_0 is the Fried parameter along the propagation path.

In section 2.4.4 we have seen that our analytical expression of the temporal decorrelation of the complex amplitudes at the PIC input can be used to estimate the temporal error. In section 4.3.4 we will compare the temporal error given by the approach in classic AO and the one given by our analytical expression 2.22.

The temporal error is the same for all control algorithms, and it fixes the correction frequency.

4.2.4 The measurement errors

The different measurement errors are:

- The Read Out Noise (RON), which is additive decorrelated and uniform on each output measurement.
- The photon noise which is additive and decorrelated.
- The modulation error induced by hypothesis 1 assuming the perturbation is frozen during one spatial modulation period, which is false in practice, see Section 3.3.2.
- The error induced by the fluctuation of the modulus of the complex amplitudes at the PIC input implying hypothesis 3 to be false, see Section 3.3.2.

In Section 3.5, we have developed a method to determine the spatial modulation vector minimizing additive gaussian decorrelated and uniform noise propagation. We saw that such a spatial modulation vector allows to reach the theoretical minimum noise propagation of RON and photon noise.

The RON, σ^2_{RON}, induces an efficiency $\langle \eta_{RON} \rangle = e^{-\left\langle |\hat{\varphi}_{RON}|^2 \right\rangle}$ with $\left\langle |\hat{\varphi}_{RON}|^2 \right\rangle$ the mean quadratic error on the estimated phase induced by the RON. $\langle \eta_{RON} \rangle$ corresponds to the average intensity coupled in s_0 normalized by the average total intensity at the input of the PIC, considering only the RON error.

In the same way the photon noise σ^2_{phn} induces an efficiency $\langle \eta_{phn} \rangle = e^{-\left\langle |\hat{\varphi}_{nph}|^2 \right\rangle}$ with $\left\langle |\hat{\varphi}_{nph}|^2 \right\rangle$ the mean quadratic error on the estimated phase induced by the photon noise. $\langle \eta_{nph} \rangle$ corresponds to the average intensity coupled in s_0 normalized by the average total intensity at the input of the PIC, considering only the error induced by photon noise.

4.2.4.1 The modulation error

As depicted on Figure 4.1, during one modulation period, τ_m, there are two intensity measurements: $\boldsymbol{s^t}$ measured at iteration t when the spatial modulation is applied with a positive sign, and $\boldsymbol{s^{t+\tau_m/2}}$ measured at iteration $t + \tau_m/2$ when the spatial modulation is applied with a negative sign. For simplicity, the phases are supposed to be applied instantaneously in one iteration on the phase shifters by updating the diagonal matrix $\boldsymbol{C^{ps}}$ (of diagonal elements $(e^{i\varphi^{ps}_k})$ see Section 3.3.1).

As seen in Section 3.3.2 to build the interaction matrix the phase perturbations are supposed to be constant during a modulation period τ_m, which is not verified in practice. However, all modulation-based control algorithms make this assumption and are all impacted by it, not just our spatial modulation control method.
Let us examine the consequence of this modulation error. We assume the signal is sampled at frequency $2 \times f_m$. We denote by p the p^{th} sample, and $\boldsymbol{\varphi^{turb}}$, the phase disturbance to be measured. The average of $\boldsymbol{\varphi^{turb}}$ during modulation is:

$$\boldsymbol{\varphi^{turb}_{moy}}(p) = \frac{\boldsymbol{\varphi^{turb}}(p) + \boldsymbol{\varphi^{turb}}(p+1)}{2}.$$

The differential measurement resulting from the modulation can be interpreted as a measurement obtained with a $\boldsymbol{\varphi^{turb}_{moy}}(p)$ disturbance and a modulation equal to $\boldsymbol{\delta\varphi^m} + \boldsymbol{\delta\varphi^{turb}}$, where:

$$\boldsymbol{\delta\varphi^{turb}}(p) = \frac{\boldsymbol{\varphi^{turb}}(p) - \boldsymbol{\varphi^{turb}}(p+1)}{2},$$

corresponding to a modulation error term. Therefore, this error results in an error on the command matrix $\boldsymbol{M}_{\boldsymbol{int}}^{\dagger}$ equivalent to a multiplicative noise. Since the correction induced by the phase shifters is constant during modulation, $\boldsymbol{\varphi}^{\boldsymbol{turb}}$ only depends on the complex amplitude of the guided waves at the PIC input. However, the modulation error depends on the modulation frequency and amplitude. Indeed, $\boldsymbol{\delta\varphi}^{\boldsymbol{turb}}$ may be reduced by increasing f_m or the amplitude of the modulation. At constant $|\boldsymbol{\delta\varphi}^{\boldsymbol{turb}}|$, the higher the spatial modulation amplitude, the lower the relative modulation error. Therefore, this error will determine the choice of frequency and modulation amplitude.

4.2.4.2 The error induced by the fluctuations of the modulus of the complex amplitudes

The interaction matrix is established by assuming that the modulus of the input-guided waves complex amplitudes are all equal, see Section 3.3.2. While the interaction matrix coefficients are a function of the modulus of the complex amplitudes at the PIC input. Thus, any fluctuation of the PIC input complex amplitude modulus generates an error on the interaction matrix $\boldsymbol{M}_{\boldsymbol{int}}$ and therefore on the command matrix $\boldsymbol{M}_{\boldsymbol{int}}^{\dagger}$ and hence on the estimated perturbation phase $\hat{\boldsymbol{\varphi}}$. This error is equivalent to a multiplicative noise.

4.2.5 Total error terms

Considering that all the error terms can be interpreted as additive decorrelated centred noise, the total average power $\langle\eta\rangle$ writes:

$$\langle\eta\rangle = \langle\eta_{demux}\rangle \times \langle\eta_0\rangle \times \langle\eta_{tempo}\rangle \times \langle\eta_{RON}\rangle \times \langle\eta_{nph}\rangle \times \langle\eta_{mod}\rangle \times \langle\eta_{fluct_p}\rangle \times \langle\eta_{fluct_m}\rangle \quad (4.7)$$

$1 - \langle\eta_{mod}\rangle$ corresponds to the attenuation induced by the intensity used for the measurements with the spatial modulation vector, $1 - \langle\eta_{fluct_p}\rangle$ corresponds to the attenuation induced by the modulation error and $1 - \langle\eta_{fluct_m}\rangle$ corresponds to the attenuation induced by the error induced by the fluctuation of the modulus of the complex amplitudes, all normalized by the total PIC input intensity.

The design of an integrated-AO is performed by evaluating all these error terms.

4.3 Integrated-AO design

We have developed above the different error terms impacting the performances of an integrated-AO. This section presents a general method for integrated-AO design applied to the specific case of a LEO satellite downlink scenario.

4.3.1 LEO satellite downlink scenario

The link parameters are those of the reference scenario presented in Appendix B. The main parameters are recalled here:

The elevation of the receiving satellite-telescope axis is $\theta_{sat} = 30°$. The C_n^2 profile is a Hufnagel-Valley profile representative of an average daytime site, which leads to propagation conditions with a Fried parameter $r_0 = 0.1\ m$, and a Rytov variance $\sigma_\chi^2 = 0.085$. The wind profile is a Bufton profile. Considering the satellite apparent trajectory, the natural wind is negligible compared to the apparent wind except for the first few hundred meters before the ground station: the mean wind velocity is $v_{moy} = 125\ m.s^{-1}$.

This scenario makes it possible to reveal field disturbances that are sufficiently complex to test the performance of a control loop while having the advantage of moderate complexity in terms of numerical modelling.

Optical propagation through the turbulent atmosphere is modelled with the TURANDOT code [18]. A time sequence of 1 s of the optical power collected by a 0.5 m telescope, $|P\boldsymbol{\Psi}^{\boldsymbol{turb}}|^2$, is shown in Figure 4.2 with a time step of 0.2 ms. It can be observed that the retained diameter is sufficient to avoid deep fading. The complete assessment of the link, including the transmitted power data, is not given here. The characterization of the performance of the telecom link is not the subject of the study.

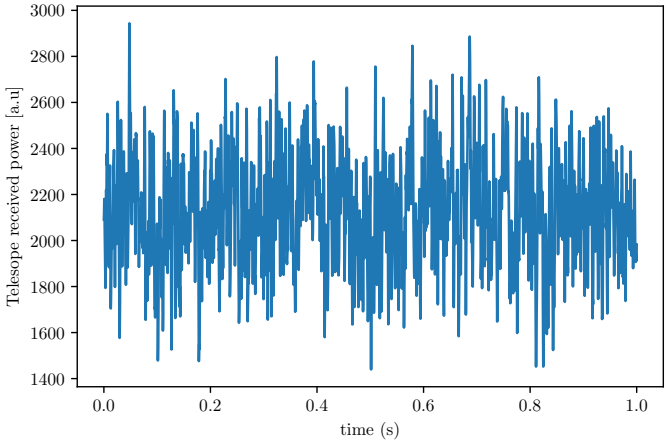

Figure 4.2: Collected power by the 0.5 m telescope during 1 s of turbulent atmospheric propagation, modelled with the TURANDOT code.

4.3.2 Spatial design

The presence of fading is also a criterion for a system dedicated to communications. Therefore, we seek a system with high coupled power and limited power fluctuation. The temporal sequence of fields created with the TURANDOT code is projected on a set of 32 HG modes corresponding to a realistic design of PIC as we will see in Section 5.3.2. The average coupled power is:

$$\langle \eta_{demux} \rangle = 0.64\,.$$

Which is very close to that obtained analytically by L.Rinaldi as seen in Section 4.2.1. The temporal power sequence at the PIC input is presented in Figure 4.3.

We can see on Figure 4.3 that a decomposition over 32 HG modes allows to avoid deep fading and we have: $\langle \eta_{demux} \rangle / \sigma_{\eta_{demux}} = 13$.

4.3.3 Phase-only correction

With the scenario described above, we have seen in Section 2.3.6 that the modulus of the complex amplitudes at the PIC input follow Rayleigh statistics with different moments. Thus, the expected average power coupled in s_0 with phase-only correction should be $\langle \eta_0 \rangle < \pi/4$. However, as shown in figure 4.4a we have:

$$\langle \eta_0 \rangle = 0.76$$

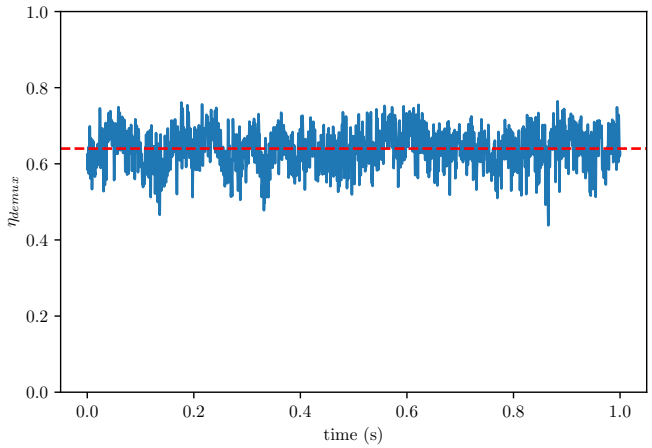

Figure 4.3: Temporal variations of the total PIC input intensity with distorted fields decomposed over 32 HG modes. In red $\langle \eta_{demux} \rangle = 0.64$.

which is close to $\pi/4 (\approx 0.785)$. Furthermore, as shown in figure 4.4b there is no deep fading with phase-only correction: $\langle \eta_0 \times \eta_{demux} \rangle / \sigma_{\eta_0 \times \eta_{demux}} = 11$ and:

$$\langle \eta_0 \times \eta_{demux} \rangle = \langle \eta_0 \rangle \times \langle \eta_{demux} \rangle = 0.486$$

It allows an average coupling power in s_0 of approximately 50% of the power collected by the telescope against 65% with phase and amplitude correction. Thus, in the link scenario described above, it is still advantageous to perform phase-only correction, considering there will be twice as few losses (in dB) induced by PIC imperfections compared to phase and amplitude correction.

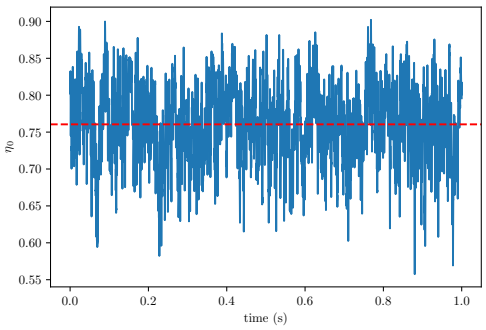

(a) Temporal variations of the coupled power in the telecom output with phase-only correction normalized by the total PIC input power. In red: $\langle \eta_0 \rangle = 0.76$.

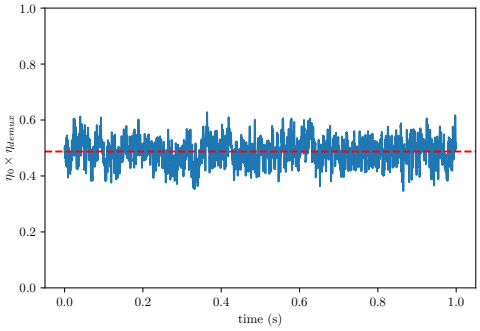

(b) Temporal variations of the coupled energy in the telecom output with phase-only correction normalized by the total power received by the telescope. In red: $\langle \eta_0 \times \eta_{demux} \rangle = 0.486$.

Figure 4.4: Phase-only correction error.

4.3.4 Temporal error design

Expression 4.6 is used to obtain an approximation of $\langle \eta_{tempo} \rangle$. For correction frequencies $f_c = 1/\tau_c = 12\ kHz$, $6\ kHz$, $3\ kHz$ we obtain respectively $\langle \eta_{tempo} \rangle = 0.85$, 0.6, 0.2. Thus, with this approximation of $\langle \eta_{tempo} \rangle$, a correction frequency of around $10\ kHz$ is required. In Section 2.4.4, the analytical expression we developed for the time covariance of the

complex amplitude gives us an order of magnitude of the temporal error. Temporal errors given by our time covariance analytical expression differs from temporal errors obtained with Expression 4.6. Indeed, with our time covariance analytical expression, a correction frequency of 5 kHz gives a temporal error of around 0.90, and with a correction frequency of 12 kHz, the temporal error starts to be negligible. The temporal errors obtained with our analytical expression of the time covariance seem more realistic, and in the following, we consider $\langle \eta_{tempo} \rangle = 0.90$.

4.3.5 Amplitude of the spatial modulation

To minimize the noise propagation and the modulation error the amplitude of the spatial modulation vector must be as high as possible while remaining in the linearity domain (see Section 3.4). Thus we use the spatial modulation vector obtained in Section 3.5.3 with the optimization algorithm and depicted in Figure 4.5.

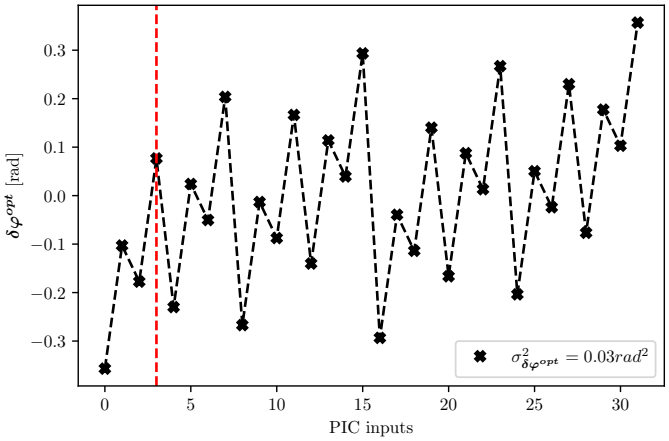

Figure 4.5: Spatial modulation vector, $\boldsymbol{\delta\varphi^{opt}}$.

Its norm is 1 rad with a standard deviation of 0.17 rad, allowing to minimize the noise propagation while remaining in the linear regime as seen in Section 3.4. Modulating the PIC with $\boldsymbol{\delta\varphi^{opt}}$ takes around 3% of the PIC input power to perform the measurements. Thus we have:

$$\langle \eta_{mod} \rangle = 0.97$$

4.3.6 Photon noise error

We consider the link budget developed in L. Rinaldi's thesis [6], the power collected by the OGS telescope is -45 dBm, which gives $\langle |P\Psi^{turb}|^2 \rangle = 3.8 \times 10^{11}$ ph/s at 1550 nm. As seen in Section 4.3.2, with a modal decomposition over 32 HG modes, the PIC receives in average 64% of $\langle |P\Psi^{turb}|^2 \rangle$. Thus, the PIC received a total power $P_{pic} = 2.3 \times 10^{11}$ ph/s. With phase-only correction, we can consider that 24% of P_{pic} is split between the 31 measurement outputs ($\eta_0 = 0.76$). Considering a modulation frequency $f_m = 25$ kHz, the signal-to-noise ratio associated with the photon noise per output is $SNR_{photon} = \sqrt{0.24 \times 2.3 \times 10^{11}/31 \times 20 \times 10^{-6}} = 188$ (with $\tau_m/2 = 20 \times 10^{-6}$ s).

As seen in Section 3.5.3, with the optimized spatial modulation vector the mean quadratic error on the estimated phase induced by photon noise is: $\langle |\hat{\varphi}_{nph}|^2 \rangle = 1/(4N_{ph})$

with N_{ph} the number of photons per input of the PIC and per modulation cycle. Considering a modulation frequency $f_m = 25\ kHz$, with the link budget we have $N_{ph} = 2.3 \times 10^{11}/32 \times 20 \times 10^{-6}$ (with $t_m/2 = 20 \times 10^{-6}\ s$).

Thus, we obtain:

$$\begin{aligned}\langle \eta_{phn} \rangle &= e^{-\langle |\hat{\varphi}_{nph}|^2 \rangle} \\ &= 0.99\end{aligned}$$

4.3.7 RON error

To derive typical read-out-noise in our link scenario, we use Thorlabs FGA01FC photodiodes characteristics with a $NEP = 4.5 \times 10^{-15}\ W/\sqrt{Hz}$. With a modulation frequency $f_m = 25\ kHz$, the read-out-noise is $\sigma_{RON} = 4.5 \times 10^{-15} \times \sqrt{25 \times 10^3} = 7 \times 10^{-13}\ W$. Converted in ph/s with hc/λ, it comes $\sigma_{RON} = 5.5 \times 10^6\ ph/s$. Finally the typical signal-to-noise ratio given by the read-out-noise is $SNR_{fm} = (0.24 \times 2.3 \times 10^{11}/31)/(5.5 \times 10^6) = 323$.

As seen in Section 3.5.3, with the optimized spatial modulation vector the mean quadratic error on the estimated phase induced by additive, uniform, decorrelated and Gaussian noise is $\langle |\hat{\varphi}_{RON}|^2 \rangle = \sigma^2_{RON} \times tr\left(< \boldsymbol{M}^{\dagger}_{\boldsymbol{int}} \boldsymbol{M}^{\dagger\ t}_{\boldsymbol{int}} > \right)$. The command matrix $\boldsymbol{M_{com}} = \boldsymbol{M}^{\dagger}_{\boldsymbol{int}}$ is built has developed in Section 3.3.2.2 considering that the modulus of the complex amplitudes of the input guided waves all equal the same average value (Hypothesis 3 see Section 3.3.2). This value corresponds to the average power received by one input of the PIC. Thus we obtain a negligible RON propagation with:

$$\begin{aligned}\langle \eta_{RON} \rangle &= e^{-\langle |\varphi_{RON}|^2 \rangle} \\ &= 1\end{aligned}$$

4.3.8 Integrated-AO total design

Taking into account the spatial design of 32 HG modes: $\langle \eta_{demux} \rangle = 0.64$, the phase-only correction: $\langle \eta_0 \rangle = 0.76$, the temporal error: $\langle \eta_{tempo} \rangle = 0.90$, the amplitude of the spatial modulation: $\langle \eta_{mod} \rangle = 0.97$, the photon noise: $\langle \eta_{nph} \rangle = 0.99$ and the RON: $\langle \eta_{RON} \rangle = 1$ we obtain with Expression 4.7:

$$\frac{\langle \eta \rangle}{\langle \eta_{fluct_p} \rangle \times \langle \eta_{fluct_m} \rangle} = 0.42 \tag{4.8}$$

The main attenuations are induced by the spatial design and the phase-only correction. As developed in Section 1.6.4 a phase and amplitude correction could lead to a worst average coupled power if taking into account the PIC losses in this integrated-AO design. To reduce the spatial design error, a solution could be to increase the number of modes, which will be discussed in Section 5.3.3. Another solution could be to add a tip-tilt correction before the spatial demultiplexer as proposed by Rinaldi [6] and presented in Section 1.6.

With our optimized spatial modulation, the errors induced by photon and read-out noise propagation are negligible.

We have addressed the different error terms impacting the average power coupled in the telecom output in Expression 4.7 except for the modulation error terms (Section 4.2.4.1) and the error induced by the fluctuations of the modulus of the complex amplitudes (Section 4.2.4.2). The impact of those two errors is difficult to evaluate theoretically and will be studied by end-to-end simulation in the following.

4.4 End-to-End simulation

This section implements an end-to-end simulation to study the performances of the real-time control of a PIC using the spatial modulation control method. We use the 30° satellite elevation downlink scenario (see Appendix B). Accounting for the integrated-AO design performed above, we consider a 32 inputs PIC as an integrated-DM (phase-only correction) with geometrical architecture as the one depicted in Section 3.3.1 with the link budget presented in Section 4.3.6.

4.4.1 Architecture of the simulation

The end-to-end simulation comprises four main parts as depicted in Figure 4.6. The first one is the TURANDOT code used to emulate the optical propagation through the turbulent atmosphere with our downlink scenario (Appendix B) and returning a time series of distorted fields received by the telescope of 50 cm. A second part decomposed the distorted field collected by the telescope on a set of 32 HG modes such as:

$$a_j = \frac{\int P(\boldsymbol{r})\Psi^{turb^*}(\boldsymbol{r})HG_j(\boldsymbol{r})d\boldsymbol{r}}{\sqrt{\int P(\boldsymbol{r})P(\boldsymbol{r})HG_j(\boldsymbol{r})HG_j^*(\boldsymbol{r})d\boldsymbol{r}}}\,.$$

The third part encodes for the fixed matrix, $\boldsymbol{C^f}$, corresponding to the architecture of a 32-input geometrical PIC for phase-only correction as an integrated-DM and the diagonal matrix, $\boldsymbol{D^{ps}}$, of phase shifters such as:

$$\boldsymbol{e} = \boldsymbol{C^f}\,\boldsymbol{D^{ps}}\boldsymbol{a}\,. \tag{4.9}$$

With $\boldsymbol{a} = (a_j)$, the vector of elements corresponding to the demultiplexer outputs associated with the vector of PIC input. And $\boldsymbol{e} = (e_j)$ the vector of complex amplitudes at the PIC output. Thus, the intensity measurements at the PIC outputs are:

$$s_j = e_j \times e_j^*\,, \tag{4.10}$$

for $j \in (1, 31)$. Index 0 corresponds to the telecom output s_0, which is not used as an intensity measurement. In the simulation, the PIC is supposed to be perfect and without losses.

Finally, the fourth part of the simulation implements the control loop. It receives the PIC output intensity measurements and determines phase errors using a control algorithm. The correction phases to be applied on the phase shifters are computed in a simple integrator control loop. To study the performances of the spatial modulation control method we rely on the intensity coupled in the telecom output, s_0, normalized by the theoretical maximum intensity coupled with phase-only correction:

$$\eta_{po} = \frac{s_0}{\frac{1}{N}\sum_{k=0}^{N-1}\sum_{l=0}^{N-1}|a_k||a_l|} \tag{4.11}$$

In the following we analyze in the end-to-end simulation the impact of the different error terms presented above in Section 4.2.

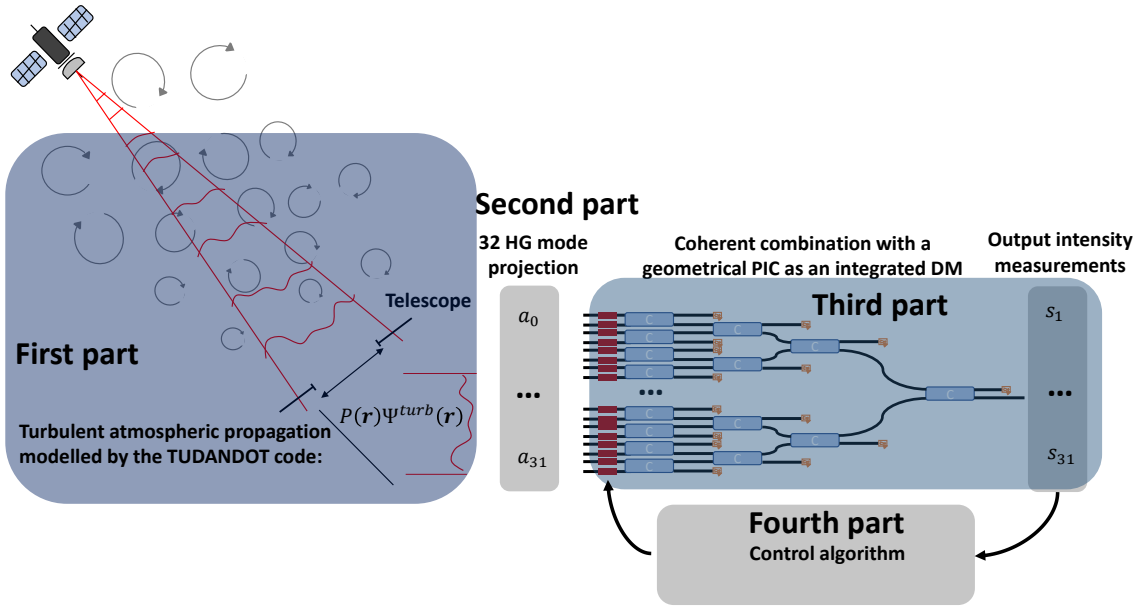

Figure 4.6: End-to-End simulation block diagram.

4.4.2 Temporal error with perfect measurements

First, we compare the impact of the temporal error on η_{po} with perfect measurements in the end-to-end simulation to the temporal error $\langle \eta_{tempo} \rangle$ estimated in Section 4.2.3. For this, we close the loop in the end-to-end simulation considering perfect measurements (meaning the perturbation phases are perfectly estimated without noise or errors induced by the control algorithm) applied with one frame rate delay corresponding to a time τ_c. Thus, the correction phases are the exact phases to be applied to maximize s_0, with one frame rate delay, and the control loop is:

$$\boldsymbol{\varphi}_{\boldsymbol{t}}^{\boldsymbol{ds}} = \boldsymbol{\varphi}_{\boldsymbol{t-\tau_c}}^{\boldsymbol{ds}} - 1 \times \boldsymbol{\varphi}_{\boldsymbol{t-\tau_c}}^{\boldsymbol{true}}, \tag{4.12}$$

with $\boldsymbol{\varphi}_{\boldsymbol{t}}^{\boldsymbol{ds}}$ the phase shifters phase at iteration t and $\boldsymbol{\varphi}_{\boldsymbol{t-\tau_c}}^{\boldsymbol{true}}$ the exact turbulent phase to be mitigated to maximized s_0 at iteration $t - \tau_c$.

Figure 4.7 shows η_{po} for different correction frequency. As τ_c increases, $\langle \eta_{po} \rangle$ decreases. For $f_c = 12.5\ kHz$ and $f_c = 6\ kHz$, $\langle \eta_{po} \rangle = 0.96$ and 0.93 respectively. Thus, the temporal error is negligible at such correction frequency. At $f_c = 3\ kHz$ and $f_c = 1.5\ kHz$, the coupled power degrades $\langle \eta_{po} \rangle = 0.85$ and 0.72 respectively and fading starts to appear as we can observe in Figures 4.7c and 4.7d, degrading the combined intensity in s_0.

The analytical expression 4.6 from classic AO used in Section 4.2.3 overestimates the temporal error. Indeed the results obtained are closer to the one given by our analytical expression of the temporal covariance (see Section 2.4) and correction frequency of a few kHz can be used to control our integrated-AO.

Given the limited number of guided waves to be combined (32) and thermal phase shifters with a typical rising time of 10 μs, it must be emphasized that if we were to consider the implementation of a control-loop in a real case, a simple sequential modulation could be used. Still, we use this scenario to evaluate the possibility of PIC real-time control by spatial modulation in realistic conditions.

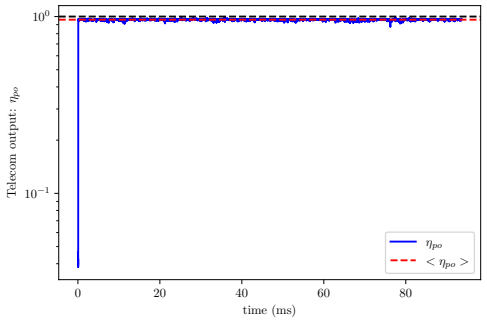

(a) In blue, η_{po} with a correction frequency $f_c = 12.5\ kHz$ and with perfect measurements. In red, $\langle \eta_{po} \rangle = 0.96$. Time step is 10 μs.

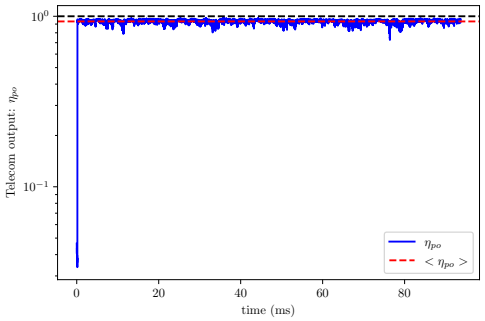

(b) In blue, η_{po} with a correction frequency $f_c = 6\ kHz$ and with perfect measurements. In red, $\langle \eta_{po} \rangle = 0.93$. Time step is 10 μs.

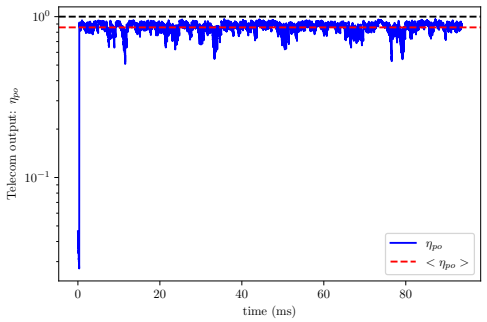

(c) In blue, η_{po} with a correction frequency $f_c = 3\ kHz$ and with perfect measurements. In red, $\langle \eta_{po} \rangle = 0.85$. Time step is 10 μs.

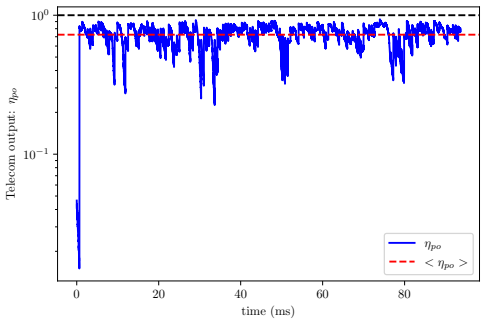

(d) In blue, η_{po} with a correction frequency $f_c = 1.5\ kHz$ and with perfect measurements. In red, $\langle \eta_{po} \rangle = 0.72$. Time step is 10 μs.

Figure 4.7: Closed-loop temporal error on the telecom output intensity normalized by the theoretical maximum phase-only intensity for different correction frequencies. Phase corrections applied at f_c correspond to the exact phases maximizing s_0 but applied with one frame rate delay (τ_c).

In the following, for the temporal error to be negligible, we set $f_c = 12.5\ kHz$.

4.4.3 Measurement errors

In what follows we study the impacts of the measurements errors on η_{po} (developed in Section 4.2.4) and impacting the spatial modulation control method.

4.4.3.1 With optimized spatial modulation vector

In this subsection, the interaction matrix is built with the spatial modulation vector determined in Section 3.5: $\boldsymbol{\delta\varphi^{opt}}$, which minimizes noise propagation. The values of the curvatures in the interaction matrix are taken as a uniform and identical gain equal to the time average modulus of the complex amplitudes at the PIC inputs. Thus, the interaction matrix condition number is one, and the estimated phases are:

$$\hat{\boldsymbol{\varphi}} = \boldsymbol{M_{int}^{\dagger}}(\boldsymbol{\delta\varphi^{opt}})\boldsymbol{\Delta s}\,. \tag{4.13}$$

4.4.3.1.1 Considering fluctuations in the modulus of complex amplitudes

As developed in Section 4.2.4.2, with fluctuating, non-identical and non-uniform modulus of the complex amplitudes at the PIC input, $\boldsymbol{M}_{\boldsymbol{int}}^{\dagger}(\boldsymbol{\delta\varphi^{opt}})$ is a biased estimator of the residual phases $\boldsymbol{\varphi}$. To analyze its impact on the closed-loop performances (in addition to temporal error), we suppose $f_m = \infty$ to eliminate the modulation error term. Thus, the integrator control loop is:

$$\boldsymbol{\varphi^{ds}}_{t} = \boldsymbol{\varphi^{ds}}_{t-\tau_c} - 0.5 \times \hat{\boldsymbol{\varphi}}_t \,, \tag{4.14}$$

with $\hat{\boldsymbol{\varphi}}_t = \boldsymbol{M}_{\boldsymbol{int}}^{\dagger}(\boldsymbol{\delta\varphi^{opt}}) \left\langle \left[\boldsymbol{s}\left(\boldsymbol{\varphi_k} + \boldsymbol{\delta\varphi^{opt}}\right) - \boldsymbol{s}\left(\boldsymbol{\varphi_k} - \boldsymbol{\delta\varphi^{opt}}\right) \right] \right\rangle_k$, and $\langle . \rangle_k$ denoting the average on iterations k other a time τ_c. The correction phase is $\boldsymbol{\varphi_t^{corr}} = 0.5 \times \hat{\boldsymbol{\varphi}}_t$.
Figure 4.8 plots η_{po} with $f_m = \infty$ and $f_c = 12.5\ kHz$, the time step is 10 μs and $\tau_c/\tau_m = 8$. Considering the impact of the fluctuations in the modulus of complex amplitudes on $\hat{\boldsymbol{\varphi}}$: $\langle \eta_{po} \rangle = 0.81$ compared to 0.96 with temporal error only. Furthermore, $\sigma^2_{\eta_{po}} = 0.024$ against 6.10^{-5} with temporal error only. Thus, fluctuations in the modulus of the complex amplitudes increase the variations of η_{po} and reduce the average intensity coupled in s_0 by 15% compared to temporal error only.

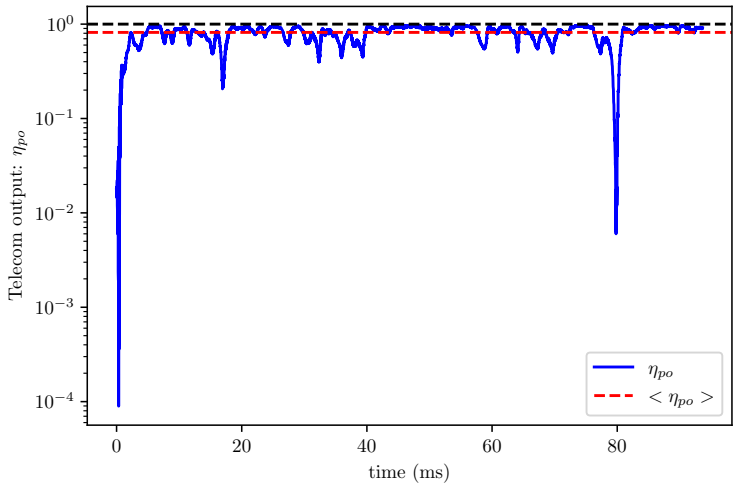

Figure 4.8: In blue closed-loop signal η_{po} with $f_m = \infty$ and $f_c = 12.5\ kHz$. In red, $\langle \eta_{po} \rangle = 0.81$

With the relation:

$$\langle \eta \rangle = \langle \eta_{demux} \rangle \times \langle \eta_0 \rangle \times \langle \eta_{po} \rangle \tag{4.15}$$

we obtain an average coupling power of the distorted field in s_0 of $\langle \eta \rangle = 0.64 \times 0.76 \times 0.81 = 0.39$

The spatial modulation control method is based on a quadratic model valid when s_0 is near its maximum. In Section 3.4.2, discussing the linear regime, we saw that the spatial modulation control methtod could be used as a hill-climbing algorithm beyond the quadratic model. This assumption is verified with the End-to-End simulation, as we can see in Figure 4.9, the spatial modulation control method can close the loop. Indeed, we can observe that s_0 increases step-by-step at each applied corrections, with fluctuations between corrections due to spatial modulation.

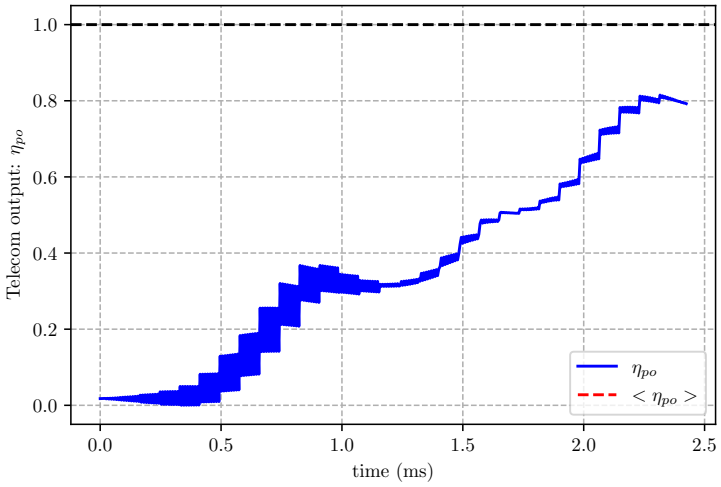

Figure 4.9: Zoom on the first 2.5 ms of Figure 4.8.

4.4.3.1.2 Considering fluctuations in the modulus of complex amplitudes and modulation noise

Now, in addition to the temporal error and fluctuating modulus of complex amplitudes, we add the impact of finite modulation frequency presented in Section 4.2.4.1. The control loop becomes:

$$\boldsymbol{\varphi^{ds}}_{t} = \boldsymbol{\varphi^{ds}}_{t-\tau_c} - 0.5 \times \hat{\boldsymbol{\varphi}}_t \,, \tag{4.16}$$

with $\hat{\boldsymbol{\varphi}}_t = \boldsymbol{M^{\dagger}_{int}}(\boldsymbol{\delta\varphi^{opt}}) \left\langle \left[\boldsymbol{s}\left(\boldsymbol{\varphi_k} + \boldsymbol{\delta\varphi^{opt}}\right) - \boldsymbol{s}\left(\boldsymbol{\varphi_{k+\tau_m/2}} - \boldsymbol{\delta\varphi^{opt}}\right) \right] \right\rangle_k$, and $\langle . \rangle_k$ denoting the average on iterations k other a time τ_c. Thus, a modulation noise is added to the spatial modulation.

Figure 4.10 plots η_{po} for $f_c = 12.5\ kHz$ and different modulation frequencies f_m. In each plot, intensities are only saved when modulation or correction are applied. Phase commands are applied instantaneously during one iteration. Thus, the time step differs for different f_m, and corrections are computed on different input complex amplitudes. For example, Subfigure 4.10a plots η_{po} with $f_m = 97\ kHz$ giving $\langle \eta_{po} \rangle = 0.81$, and Subfigure 4.10b plots η_{po} with $f_m = 48\ kHz$ giving $\langle \eta_{po} \rangle = 0.82$. $\langle \eta_{po} \rangle$ is higher with $f_m = 48\ kHz$ because some complex amplitudes implying a fading around 80 ms in Subfigure 4.10a are not used for computation in Subfigure 4.10b and the fading is not present. A more realistic loop implementation should consider a constant time step and modulation over several time steps with finite phase shifters response time.

Yet, for f_m ranging from 97 kHz to 12 kHz, $\langle \eta_{po} \rangle$ is constant and the fluctuations of η_{po} are similar. Thus, the impact of the modulation noise is negligible compared to the impacts of the fluctuations of the modulus of complex amplitudes, and the modulation frequency can be of the same order as the correction frequency.

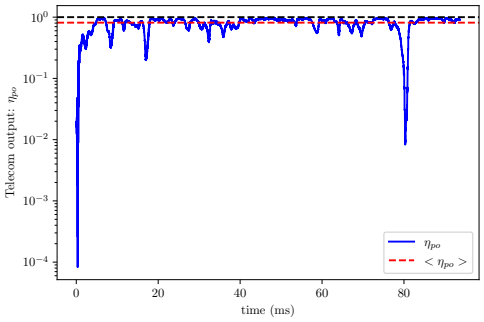

(a) In blue, η_{po} with $f_c = 12.5\ kHz$ and $f_m = 97\ kHz$. In red, $\langle \eta_{po} \rangle = 0.81$. Time step is $5\ \mu s$.

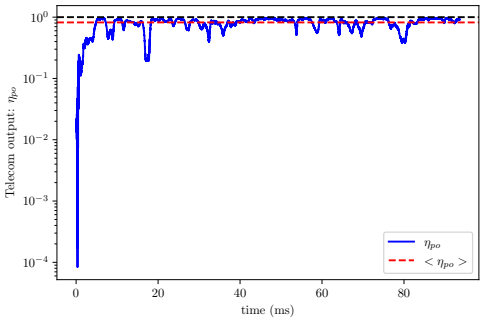

(b) In blue, η_{po} with $f_c = 12.5\ kHz$ and $f_m = 48\ kHz$. In red, $\langle \eta_{po} \rangle = 0.82$. Time step is $10\ \mu s$.

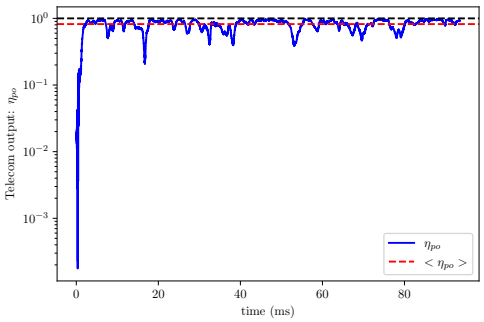

(c) In blue, η_{po} with $f_c = 12.5\ kHz$ and $f_m = 25\ kHz$. In red, $\langle \eta_{po} \rangle = 0.82$. Time step is $20\ \mu s$.

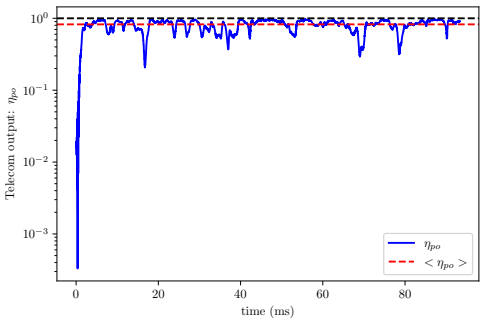

(d) In blue, η_{po} with $f_c = 12.5\ kHz$ and $f_m = 12\ kHz$. In red, $\langle \eta_{po} \rangle = 0.82$. Time step is $40\ \mu s$.

Figure 4.10: Closed-loop of the telecom output intensity normalized by the theoretical maximum phase-only intensity for different modulation frequencies. Phase corrections are applied at $f_c = 12.5\ kHz$.

4.4.3.1.3 Considering fluctuations in the modulus of complex amplitudes, modulation noise and photon noises

Now, in addition to temporal errors, fluctuations of the modulus of complex amplitudes and modulation noise, we add the impact of photon noise with the link budget presented in Section 4.3.6. Figure 4.11 compare closed-loop η_{po} with and without photon noise at $f_c = 12.5\ kHz$ and $f_m = 25\ kHz$. Subfigure 4.11a corresponds to η_{po} without photon noise giving $\langle \eta_{po} \rangle = 0.82$ with fluctuations $\sigma^2_{\eta_{po}} = 0.018$. Subfigure 4.11b corresponds to η_{po} with photon noise giving the same $\langle \eta_{po} \rangle = 0.82$ and fluctuations $\sigma^2_{\eta_{po}} = 0.018$. Thus, the closed-loop performances are similar to those without photon noise as discuss in Section 4.3.6.

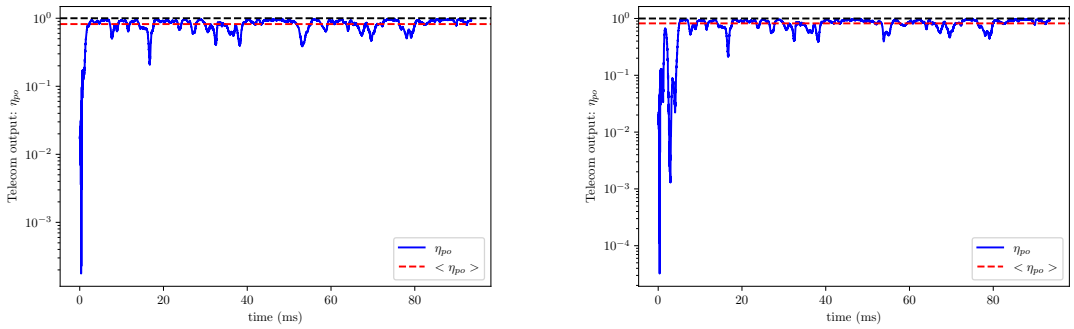

(a) In blue, η_{po} with $f_c = 12.5\ kHz$ and $f_m = 25\ kHz$ without photon noise.
In red, $\langle \eta_{po} \rangle = 0.82$. Time step is 20 μs.

(b) In blue, η_{po} with $f_c = 12.5\ kHz$ and $f_m = 25\ kHz$ with photon noise.
In red, $\langle \eta_{po} \rangle = 0.82$. Time step is 20 μs.

Figure 4.11: Comparison of closed-loop telecom output intensity (normalized by the theoretical maximum phase-only intensity) at $f_c = 10\ kHz$ and $f_m = 25\ kHz$ with and without photon noise.

4.4.3.1.4 Considering fluctuations in the modulus of complex amplitudes, modulation noise, photon noises and read-out noise

Now, in addition to temporal errors, fluctuations in the modulus of the complex amplitudes, modulation noise, and photon noise, we add the impact of photodetector RON as discussed in Section 4.3.7.
The total noise in the simulation on measurement output j is:

$$\begin{aligned} \sigma_{b_j} &= \sqrt{\sigma_{phn_j}^2 + \sigma_{RON}^2} \\ &= \sqrt{s_j + \left(\frac{s_j}{SNR_{RON}}\right)^2}, \end{aligned} \tag{4.17}$$

with σ_{phn_j} the photon noise on measurement output j and σ_{RON} the read-out noise, which is supposed to be equivalent on all measurements. SNR_{RON} corresponds to the chosen signal-to-noise ratio induced by RON.
In the simulation, the noise added to measurement output j follows a normal distribution of zero mean and standard deviation σ_{b_j}.

Figure 4.12 compares η_{po} for different value of SNR_{RON} at $f_c = 12.5\ kHz$ and $f_m = 25\ kHz$. Figure 4.12a corresponds to the typical RON encountered with our link scenario $SNR_{RON} = 323$ (see Section 4.3.7). The impact of the RON on the loop performances is negligible as expected: $\langle \eta_{po} \rangle = 0.81$ and $\sigma_{\eta_{po}}^2 = 0.018$. The main limitations still come from the fluctuations of the modulus of the complex amplitudes.

Figure 4.12b corresponds to a case of a degraded RON with $SNR_{RON} = 10$. The loop performances are similar to those with $SNR_{RON} = 323$ with $\langle \eta_{po} \rangle = 0.81$. But with more fluctuations in η_{po}: $\sigma_{\eta_{po}}^2 = 0.021$. However, the main limitations still come from the fluctuations of the modulus of the complex amplitudes. Figure 4.12c corresponds to a severely degraded RON with $SNR_{RON} = 2$. The average intensity in s_0 falls to $\langle \eta_{po} \rangle = 0.75$ and we observe a lot of fadings with $\sigma_{\eta_{po}}^2 = 0.036$. In such conditions, the loop performances are limited by the RON and not by fluctuations of the modulus of the complex amplitudes anymore. Figure 4.12d presents a last case with $SNR_{RON} = 1$. The

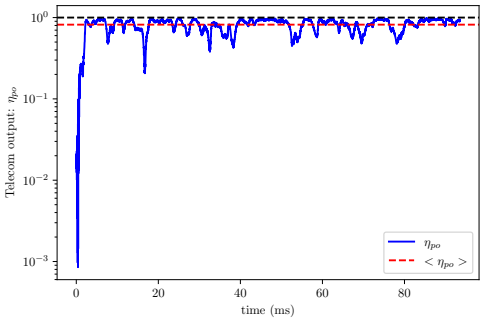

(a) In blue, η_{po} with $f_c = 12.5\ kHz$ and $f_m = 25\ kHz$. In red, $\langle \eta_{po} \rangle = 0.81$. $SNR_{RON} = 323$.

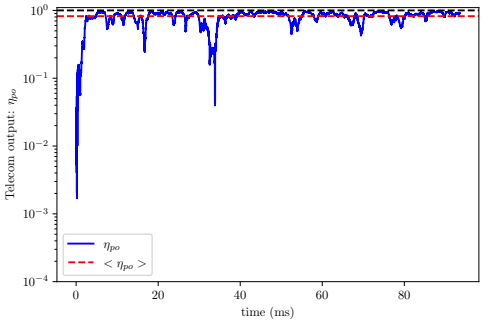

(b) In blue, η_{po} with $f_c = 12.5\ kHz$ and $f_m = 25\ kHz$. In red, $\langle \eta_{po} \rangle = 0.81$. $SNR_{RON} = 10$.

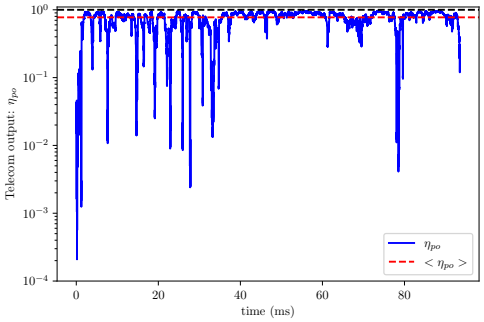

(c) In blue, η_{po} with $f_c = 12.5\ kHz$ and $f_m = 25\ kHz$. In red, $\langle \eta_{po} \rangle = 0.75$. $SNR_{RON} = 2$.

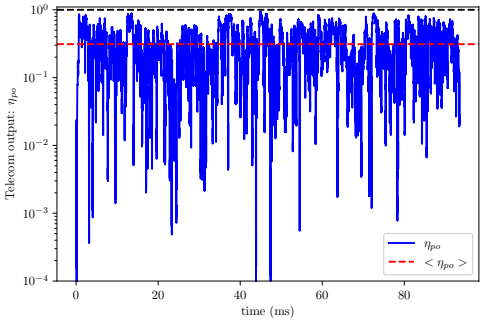

(d) In blue, η_{po} with $f_c = 12.5\ kHz$ and $f_m = 25\ kHz$. In red, $\langle \eta_{po} \rangle = 0.3$. $SNR_{RON} = 1$.

Figure 4.12: Comparison of closed-loop telecom output intensity η_{po} at $f_c = 12.5\ kHz$ and $f_m = 25\ kHz$ with photon noise and different levels of RON.

spatial modulation control method fails to perform the coherent combination in such a case.

The results presented above represent one random draw and should vary with different random draws. To analyze the exact behaviour of the spatial modulation with respect to noise, the loop performances should be studied over many random draws. However, with typical RON developed in Section 4.3.7 ($SNR_{RON} = 323$) the main degradation come from the impact of the fluctuations of the modulus of the complex amplitudes.

We have analyzed the impacts of the different measurement errors presented in Section 4.2.4 with the spatial modulation control method considering the spatial modulation minimizing uniform, additive, decorrelated and Gaussian noise: $\boldsymbol{\delta\varphi^{opt}}$. To validate the usefulness of the optimized spatial coding, the following section analyzed the impacts of the different measurement errors with non-optimized spatial coding.

4.4.3.2 With non-optimized spatial modulation vector

This subsection compares spatial modulation control method performances with two non-optimized spatial modulation vectors: one obtained with a random draw and the other being a phase ramp. Such non-optimized modulation vectors do not minimize uniform, additive, decorrelated, and Gaussian noise and do not give uniform PIC output modulated measurement intensities. In the following, the loop parameters are set to: $f_c = 12.5\ kHz$, $f_m = 25\ kHz$ and we consider fluctuations in the modulus of complex amplitudes, photon

noise and read-out noise with $SNR_{RON} = 323$.

4.4.3.2.1 Spatial modulation vector chosen randomly

Figure 4.13a depicts a spatial modulation vector with coefficients randomly drawn. The spatial modulation vector is of zero mean with a standard deviation of 0.017 to be comparable with $\boldsymbol{\delta\varphi^{opt}}$ in terms of modulation amplitude. The singular values associated with the interaction matrix are plotted in Figure 4.13b. The interaction matrix condition number is 74.

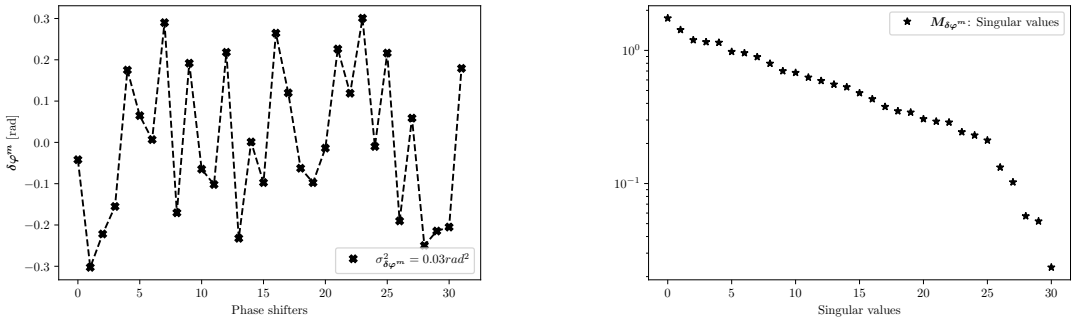

(a) Spatial modulation vector of zero mean and $\sigma^2_{\boldsymbol{\delta\varphi^m}} = 0.03\ rad^2$ with coefficients randomly drawn.

(b) Singular value decomposition of the interaction matrix $\boldsymbol{M}(\boldsymbol{\delta\varphi^m})$.

Figure 4.13: Spatial modulation vector with coefficients randomly drawn with uniform distribution (left). Singular value decomposition of the resulting interaction matrix (right).

Figure 4.14 plots η_{po} for $f_c = 12.5\ kHz$ and $f_m = 25\ kHz$ and a read-out noise $SNR_{RON} = 323$. The poor condition number of the interaction matrix implies a high noise propagation, and the spatial modulation control method failed to perform the coherent combination, $\langle \eta_{po} \rangle = 0.33$ with many fadings.

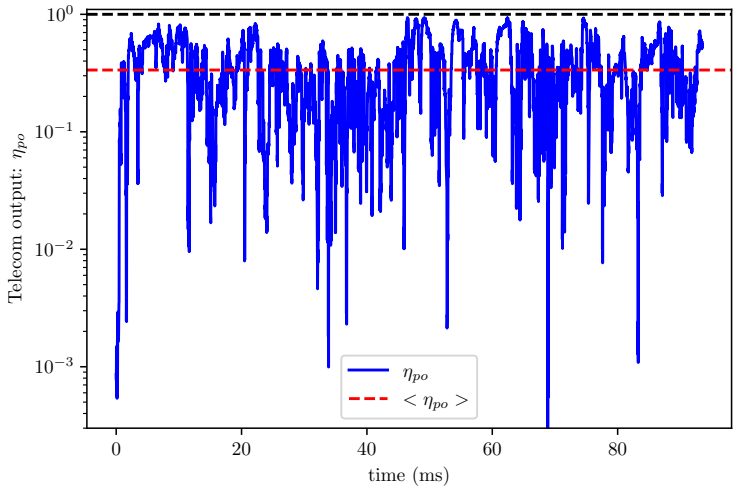

Figure 4.14: In blue closed-loop signal η_{po} with $\boldsymbol{\delta\varphi^m}$ randomly drawn, $f_c = 12.5\ kHz$ and $f_m = 25\ kHz$. In red, $\langle \eta_{po} \rangle = 0.33$. $SNR_{RON} = 323$.

4.4.3.2.2 Spatial modulation vector chosen as a phase ramp

A randomly drawn spatial modulation vector can lead to high noise propagation. A non-optimized spatial modulation vector chosen more intelligently than a random draw could be a phase ramp. Indeed, a phase ramp follows the PIC symmetry and allows the discrimination of phase pistons between the PIC stages. Thus, even if it is not the optimized spatial modulation, intuitively, it should perform better than a random draw.

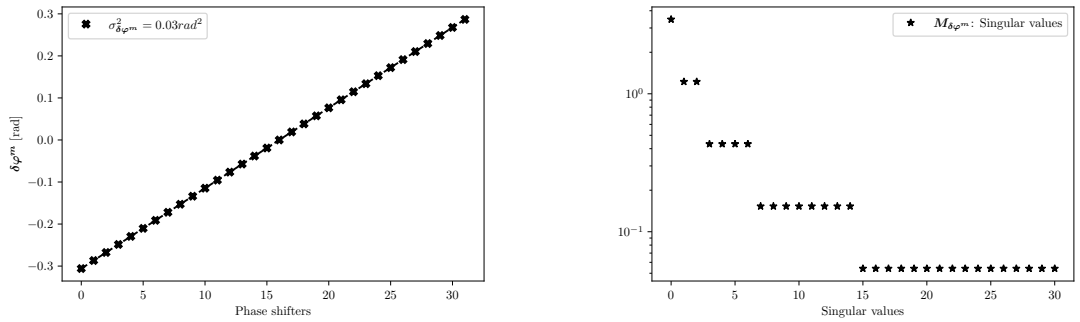

(a) Spatial modulation of zero mean and $\sigma^2_{\boldsymbol{\delta\varphi^m}} = 0.03\ rad^2$ with coefficient chosen as a phase ramp.

(b) Singular value decomposition of the interaction matrix $\boldsymbol{M}(\boldsymbol{\delta\varphi^m})$.

Figure 4.15: Spatial modulation chosen as a phase ramp (left). Singular value decomposition of the resulting interaction matrix.

Figure 4.15a depicts the spatial modulation vector as a phase ramp of zero mean with a standard deviation of 0.017 to be comparable with $\boldsymbol{\delta\varphi^{opt}}$ in term of modulation amplitude. The singular values associated with the interaction matrix are plotted in Figure 4.15b. The interaction matrix condition number is 64. We observe 5 groups of singular values corresponding to the 5 stages of phase pistons following the PIC architecture as depicted in Figure 4.16. The first group is comprised of 1 singular value, which is the higher one. It corresponds to the piston phase with symmetry centred on the last PIC stage, see the red dotted line in Figure 4.16. The second group is comprised of 2 singular values. It corresponds to the phase pistons with symmetry centred on the fourth PIC stage, see the blue dotted line in Figure 4.16. The third group is comprised of 4 singular values. It corresponds to the phase pistons with symmetry centred on the third PIC stage, see the green dotted line in Figure 4.16. The third group is comprised of 8 singular values. It corresponds to the phase pistons with symmetry centred on the second PIC stage, see the black dotted line in Figure 4.16. The last group is comprised of 16 singular values. It corresponds to the phase pistons with symmetry centred on the first PIC stage.

Figure 4.17 compares η_{po} obtained with the optimized spatial modulation vector $\boldsymbol{\delta\varphi^{opt}}$, see Subfigure 4.17a, and η_{po} obtained with the phase ramp spatial modulation vector, see Subfigure 4.17b, both with $f_c = 12.5\ kHz$, $f_m = 25\ kHz$ and a read-out noise $SNR_{RON} = 323$. The closed-loop obtained with a spatial modulation as a phase ramp underperform the one obtained with $\boldsymbol{\delta\varphi^{opt}}$. Indeed we obtained $\langle\eta_{po}\rangle = 0.79$ with spatial modulation as a phase ramp compared to $\langle\eta_{po}\rangle = 0.81$ with $\boldsymbol{\delta\varphi^{opt}}$. Furthermore, we can observe that there are more fluctuations in η_{po} with a phase ramp than with $\boldsymbol{\delta\varphi^{opt}}$. Thus, with a spatial modulation as a phase ramp, the noise propagation is not perfect as with $\boldsymbol{\delta\varphi^{opt}}$. The loop performances are not only limited by the fluctuations of the modulus of the complex amplitude but also by the noise propagation.

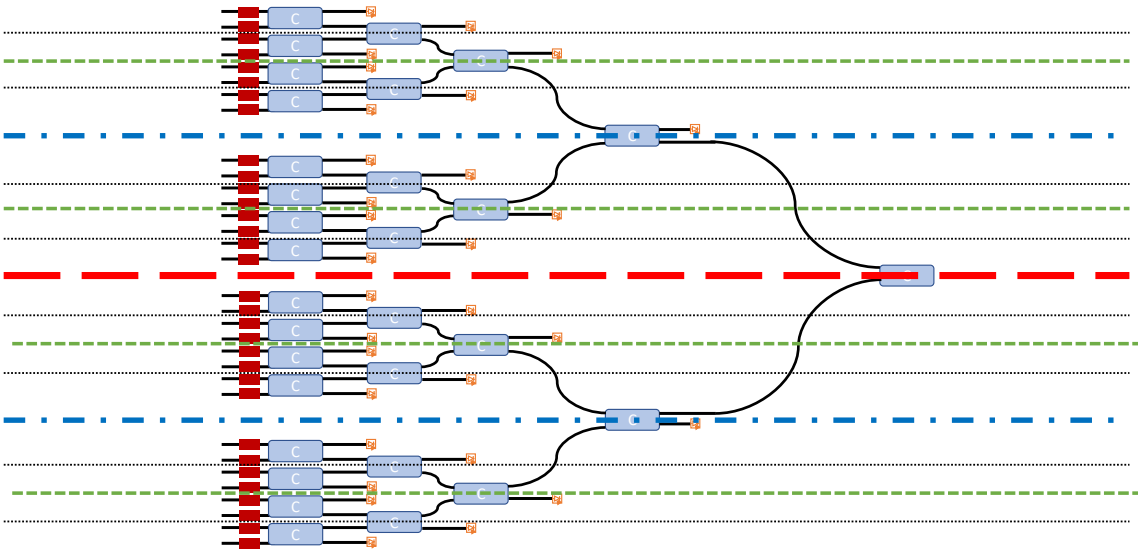

Figure 4.16: Symmetry of the phase pistons in the 32 inputs PIC with geometrical architecture.

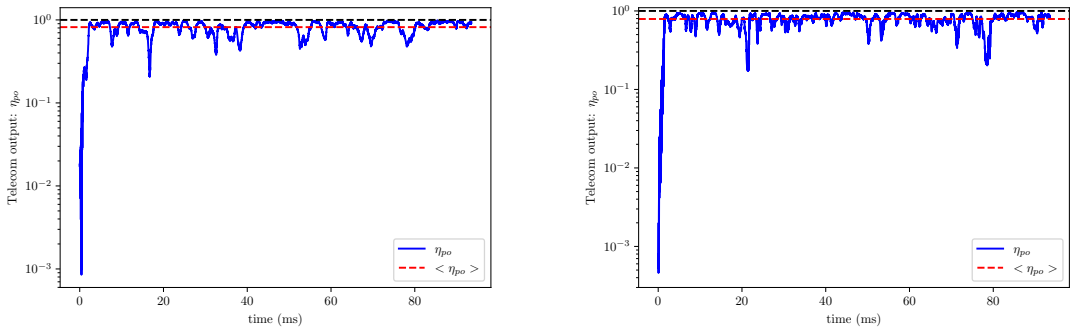

(a) In blue, η_{po} with $f_c = 12.5\ kHz$ and $f_m = 25\ kHz$ and with the interaction matrix built with $\boldsymbol{\delta\varphi^{opt}}$. In red, $\langle \eta_{po} \rangle = 0.81$.

(b) In blue, η_{po} with $f_c = 12.5\ kHz$ and $f_m = 25\ kHz$ and with the interaction matrix built with a phase ramp $\boldsymbol{\delta\varphi^{m}}$. In red, $\langle \eta_{po} \rangle = 0.79$.

Figure 4.17: Comparison of η_{po} with optimized spatial modulation vector and phase ramp spatial modulation vector. $SNR_{RON} = 323$.

In a nutshell, the optimized spatial modulation $\boldsymbol{\delta\varphi^{opt}}$ allows closed-loop performances to be limited only by the fluctuations of the modulus of the complex amplitudes. To overcome limitations induced by fluctuations of the modulus of the complex amplitudes, a solution would be to measure these fluctuations to take them into account in the interaction matrix.

4.5 Spatial modulation with photometric measurements

To mitigate the effects of the fluctuations of the modulus of the complex amplitudes of the PIC input guided waves, we propose to measure these amplitudes at the inputs of the PIC with detectors using a small percentage of the input intensities as depicted in Figure 4.18. With such measurements, called photometric measurements by astronomers,

it is possible to take into account in real-time the fluctuations of the modulus of the complex amplitudes to approximate signals measured in the absence of fluctuations. It is worth noting the Non-Invasive On-Chip Light Observation by Contactless Waveguide Conductivity Monitoring technology developed in [136] which could be used to perform the photometric measurements without impacting the total received power in s_0. With photometric measurements, the command matrix $\boldsymbol{M}_{\boldsymbol{int}}^{\dagger}(\boldsymbol{\delta\varphi^{opt}})$ is updated at a frequency f_{pm}. In the simulation, the modulus of the measured complex amplitudes $|\boldsymbol{a}| = (|a_j|)$ are computed such as:

$$|\boldsymbol{a^t}| = \frac{\sqrt{\boldsymbol{a^t a^{t^*}}} + \sqrt{\boldsymbol{a^{t+\tau_m/2} a^{t+\tau_m/2^*}}}}{2}, \tag{4.18}$$

with index t denoting for iteration t in the control loop. Thus, the interaction matrix is updated at frequency f_{pm} with (see Appendix D for the construction of the interaction matrix):

$$|a_k||a_l| = |a_k^{t_{pm}}||a_l^{t_{pm}}|, \tag{4.19}$$

instead of $|a_k||a_l| = 1$ with hypothesis 3. t_{pm} corresponds to the measurements performed before updating the interaction matrix.

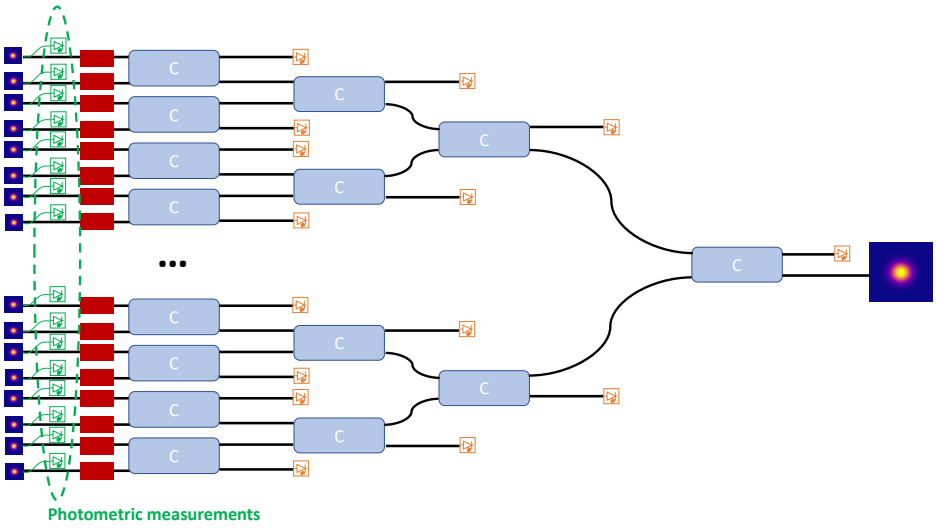

Figure 4.18: Schema of a geometrical PIC as an integrated-DM with photometric measurements at its inputs depicted by green photodiode symbols.

4.5.1 Optimized spatial modulation vector and photometric measurements

In the following, the closed-loop parameters are $f_c = 12.5\ kHz$, $f_m = 25\ kHz$ with photon noise and read-out noise with $SNR_{RON} = 323$. The interaction matrices are built with the optimized spatial modulation vector $\boldsymbol{\delta\varphi^{opt}}$.

4.5.1.1 Without singular value filtering

In this subsection, we consider that the command matrix $\boldsymbol{M}_{\boldsymbol{int}}^{\dagger}(\boldsymbol{\delta\varphi^{opt}})$ is computed at frequency f_{pm} by direct inversion of the interaction matrix $\boldsymbol{M_{int}}(\boldsymbol{\delta\varphi^{opt}})$.

As seen in Section 2.4, the decorrelation time at half height of (a_j) with the considered downlink scenario is of the order of 1 ms. Thus, the photometric measurements must be performed at a frequency higher than 1 kHz. This is illustrated in Figure 4.19 with η_{po} plotted for different f_{pm} with fixed $f_c = 12.5\ kHz$, $f_m = 25\ kHz$ and $SNR_{RON} = 323$. For $f_{pm} = 4\ kHz$, $\langle \eta_{po} \rangle = 0.90$ with photometric measurements compared to $\langle \eta_{po} \rangle = 0.81$ without. Thus, updating $\boldsymbol{M_{int}}(\boldsymbol{\delta\varphi^{opt}})$ at 4 kHz with photometric measurements allows a gain of 9 % of average combined intensity in s_0. However, as we can observe in Subfigure 4.19a, there are more and deeper fadings with photometric measurements than without. Furthermore, at $f_{pm} = 2\ kHz$, $f_{pm} = 1\ kHz$ and $f_{pm} = 0.5\ kHz$, we have respectively decreasing combined intensity $\langle \eta_{po} \rangle = 0.89$, $\langle \eta_{po} \rangle = 0.87$ and $\langle \eta_{po} \rangle = 0.81$ with an increasing number of fadings as we can observe in Subfigures 4.19b, 4.19c and 4.19d. With $f_{pm} = 0.5\ kHz$, the average combined intensity $\langle \eta_{po} \rangle$ is the same as without photometric measurements but η_{po} is severely degraded by photometric measurements regarding the number of deep fadings compared than without photometric measurements.

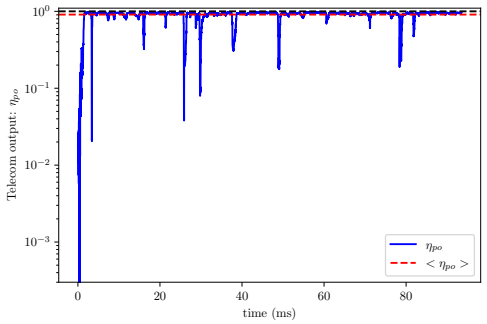

(a) In blue, η_{po} with $f_c = 12.5\ kHz$, $f_m = 25\ kHz$ and $f_{pm} = 4\ kHz$. In red, $\langle \eta_{po} \rangle = 0.90$. $SNR_{RON} = 323$.

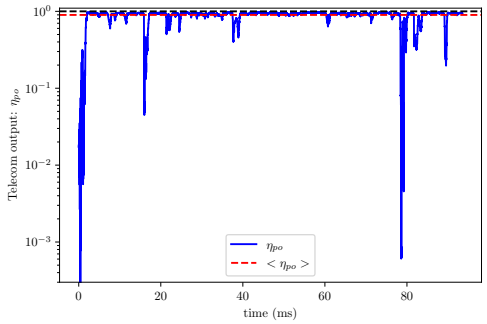

(b) In blue, η_{po} with $f_c = 12.5\ kHz$, $f_m = 25\ kHz$ and $f_{pm} = 2\ kHz$. In red, $\langle \eta_{po} \rangle = 0.89$. $SNR_{RON} = 323$.

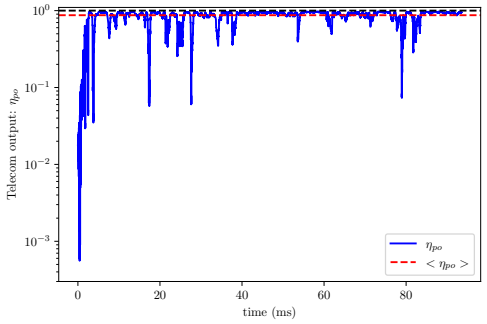

(c) In blue, η_{po} with $f_c = 12.5\ kHz$, $f_m = 25\ kHz$ and $f_{pm} = 1\ kHz$. In red, $\langle \eta_{po} \rangle = 0.87$. $SNR_{RON} = 323$.

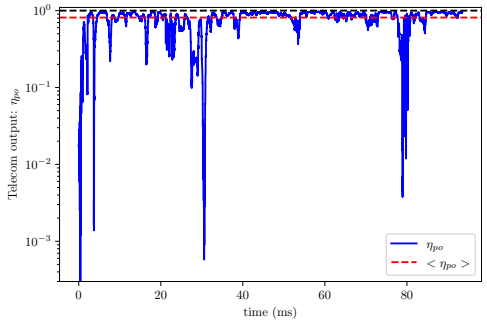

(d) In blue, η_{po} with $f_c = 12.5\ kHz$, $f_m = 25\ kHz$ and $f_{pm} = 0.5\ kHz$. In red, $\langle \eta_{po} \rangle = 0.81$. $SNR_{RON} = 323$.

Figure 4.19: Comparison of η_{po} at $f_c = 12.5\ kHz$ and $f_m = 25\ kHz$ with photon noise and read-out noise $SNR_{RON} = 323$, for: $f_{pm} = 4\ kHz$ (a), $f_{pm} = 2\ kHz$ (b), $f_{pm} = 1\ kHz$ (c) and $f_{pm} = 0.5\ kHz$ (d).

The emergence of many deep fadings with photometric measurement can be easily explained. Indeed, the interaction matrices computed at f_{pm} using the photometric measurements are built using $\boldsymbol{\delta\varphi^{opt}}$. However, $\boldsymbol{\delta\varphi^{opt}}$ was optimized for curvature tensor considering $|a_k||a_l| = 1$ (see Section 3.5.2). Thus, interaction matrices computed at f_{pm}

no longer have a condition number of one and are not minimizing the noise propagation. Thus, some interaction matrices are poorly conditioned with photometric measurements, propagating errors due to noise on the residual phases and inducing fadings.
To overcome such an issue, one could update the spatial modulation vector at frequency f_{pm} by optimizing it for each new interaction matrix with Algorithm 1. However, changing and optimizing the spatial modulation vector at f_{pm} is a complicated and costly computation solution. A more realistic solution is to keep $\boldsymbol{\delta\varphi^{opt}}$ as a spatial modulation vector but with singular value filtering.

4.5.1.2 With singular value filtering

In this subsection, we perform the same simulation as the previous subsection but with singular value filtering.

Figure 4.20 plots η_{po} for $f_{pm} = 4\ kHz$, $f_{pm} = 2\ kHz$. For these frequencies, the average combined powers are respectively $\langle\eta_{po}\rangle = 0.94$, $\langle\eta_{po}\rangle = 0.92$. As we can observe in Subfigures 4.20a and 4.20b, filtering the singular value with f_{pm} up to 2 kHz allows to get rid of the fading and to obtained average combined powers $\langle\eta_{po}\rangle$ close to the average combined power obtained considering temporal error only $\langle\eta_{po}\rangle = 0.96$ as shown in Subfigure 4.7a.

In a nutshell, in the presence of modulation noise, fluctuation of modulus of complex amplitudes, photon noise and read-out noise, photometric measurements at f_{pm} up to 2 kHz and singular value filtering with optimized spatial modulation vector allows to reach closed-loop performances equivalent to performances with temporal error only.

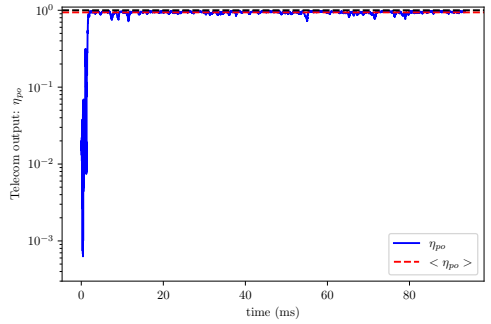

(a) In blue, η_{po} with $f_c = 12.5\ kHz$, $f_m = 25\ kHz$ and $f_{pm} = 4\ kHz$. In red, $\langle\eta_{po}\rangle = 0.94$. $SNR_{RON} = 323$.

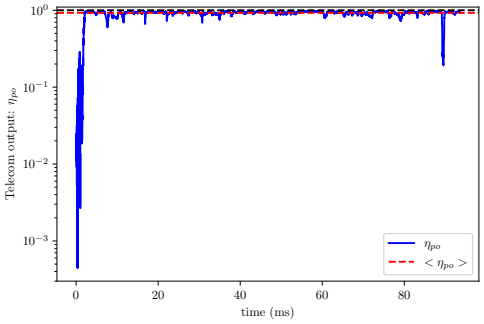

(b) In blue, η_{po} with $f_c = 12.5\ kHz$, $f_m = 25\ kHz$ and $f_{pm} = 2\ kHz$. In red, $\langle\eta_{po}\rangle = 0.92$. $SNR_{RON} = 323$.

Figure 4.20: Comparison of η_{po} at $f_c = 12.5\ kHz$ and $f_m = 25\ kHz$ with photon noise and read-out noise $SNR_{RON} = 323$, for: $f_{pm} = 4\ kHz$ (a), $f_{pm} = 2\ kHz$ (b) with singular values filtering.

4.5.2 Non-optimized spatial modulation vector and photometric measurements with singular values filtering

By updating the interaction matrix with photometric measurements, $\boldsymbol{\delta\varphi^{opt}}$ is no longer the optimized spatial modulation vector associated with the news interaction matrices. Thus, the benefit of using $\boldsymbol{\delta\varphi^{opt}}$ with photometric measurements may be questioned.

Figure 4.21 plots η_{po} with $f_c = 12.5\ kHz$, $f_m = 25\ kHz$, $f_{pm} = 4\ kHz$ with singular value filtering for a spatial modulation defined as a phase ramp, Subfigure 4.21a, and as

a random draw, Subfigure 4.21b. For a spatial modulation as a phase ramp, $\langle \eta_{po} \rangle = 0.80$ and there is no deep fading. It reaches the same loop performances as closed-loop using $\boldsymbol{\delta\varphi^{opt}}$ without photometric measurements. For a spatial modulation as a random draw, $\langle \eta_{po} \rangle = 0.77$ and deep fading are present. With a spatial modulation vector as a random draw, photometric measurement allows closed-loop combined power in s_0. In contrast, without photometric measurements, the coherent combination fails, as shown in Figure 4.14.

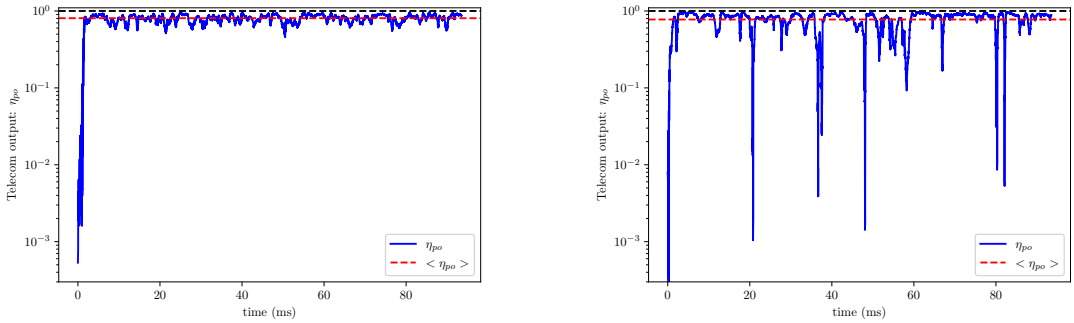

(a) In blue, η_{po} with $f_c = 12.5\ kHz$, $f_m = 25\ kHz$ and $f_{pm} = 4\ kHz$. In red, $\langle \eta_{po} \rangle = 0.80$. $SNR_{RON} = 323$. With partial modulation as a phase ramp.

(b) In blue, η_{po} with $f_c = 12.5\ kHz$, $f_m = 25\ kHz$ and $f_{pm} = 4\ kHz$. In red, $\langle \eta_{po} \rangle = 0.77$. $SNR_{RON} = 323$. With spatial modulation as a random draw.

Figure 4.21: Comparison between spatial modulation vector as a phase ramp and as a random draw for η_{po} at $f_c = 12.5\ kHz$, $f_m = 25\ kHz$ and $f_{pm} = 4\ kHz$ with photon noise and read-out noise $SNR_{RON} = 323$, and with singular values filtering.

In a nutshell, even with photometric measurements and proper singular value filtering, the use of $\boldsymbol{\delta\varphi^{opt}}$ is required to obtain optimal closed-loop performances.

4.5.3 Spatial modulation control method performances conclusion

With the integrated-AO design developed above for the downlink scenario presented in Appendix B, we have analyzed the spatial modulation control method performances by studying the intensity coupled in s_0 normalized by the theoretical maximum value reachable with phase-only correction: η_{po}. To evaluate the coherent combination performances compared to the PIC total input intensity, we analyze $\eta_{po} \times \eta_o$ corresponding to the intensity coupled in s_0 normalized by the total PIC input intensity.

The correction frequency is set to $f_c = 12.5\ kHz$, the modulation frequency is set to $f_m = 25\ kHz$, and we consider photon noise and read-out-noise $SNR_{RON} = 323$.

Figure 4.22a plots $\eta_{po} \times \eta_o$ without photometric measurements. The average coupled intensity $\langle \eta_{po} \times \eta_o \rangle$ is 68% of the total PIC input intensity. Figure 4.22b plots $\eta_{po} \times \eta_o$ with photometric measurements. The average coupled intensity $\langle \eta_{po} \times \eta_o \rangle$ is 77%, and the fluctuations are significantly reduced compared to without photometric measurements.

This is highlighted in Figure 4.23 with the comparison of the intensity coupled in s_0 (blue curves) with the total PIC input intensity (black curves) and maximum theoretical value reachable with phase-only correction (green curves). Figure 4.23a corresponds to the plots without photometric measurements which comprises significantly more fluctuations than Figure 4.23b corresponding to plots with photometric measurements.

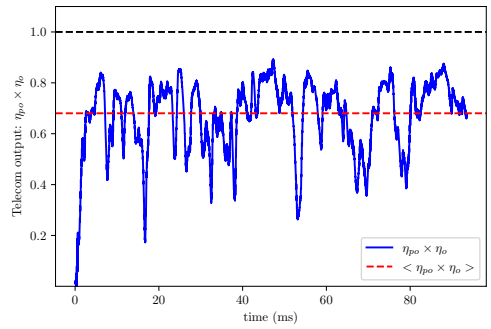

(a) In blue $\eta_{po} \times \eta_o$ corresponding to the intensity in s_0 normalized by the total PIC input intensity. In red $\langle \eta_{po} \times \eta_o \rangle = 0.68$.

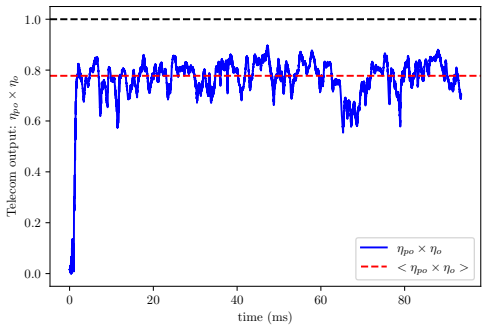

(b) In blue $\eta_{po} \times \eta_o$ corresponding to the intensity in s_0 normalized by the total PIC input intensity. In red $\langle \eta_{po} \times \eta_o \rangle = 0.77$. With photometric measurements at $f_{pm} = 4\ kHz$ with singular value filtering

Figure 4.22: Comparison of $\eta_{po} \times \eta_o$ with and without photometric measurements, $f_c = 12.5\ kHz$, $f_m = 25\ kHz$ with photon noise and read-out noise $SNR_{RON} = 323$.

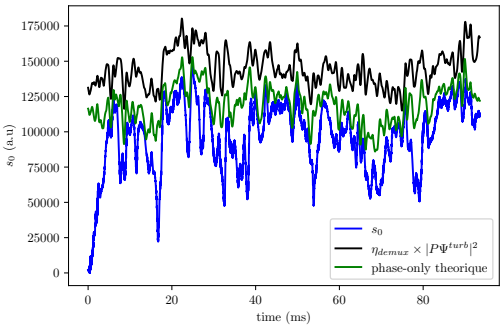

(a) Spatial modulation control method applied without photometric measurements.

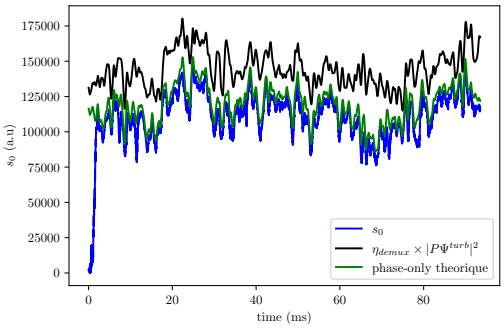

(b) Spatial modulation control method applied with photometric measurements at $f_{pm} = 4\ kHz$ with singular value filtering.

Figure 4.23: In blue intensity coupled in s_0, in black total PIC input intensity and in green maximum theoretical value with phase-only correction. $f_c = 12.5\ kHz$, $f_m = 25\ kHz$ with photon noise and read-out noise $SNR_{RON} = 323$.

Finally with photometric measurements the performance of the integrated-AO is:

$$\begin{aligned} \langle \eta \rangle &= \langle \eta_{demux} \rangle \times \langle \eta_{po} \times \eta_o \rangle \\ &= 0.64 \times 0.77 \\ &= 0.49 \end{aligned} \tag{4.20}$$

In Section 4.3.3 we obtained a theoretical value of $\langle \eta \rangle = 0.486$ with an average over 1 s against 100 ms here. Furthermore, as we can observe on Figure 4.23b the intensity coupled in the telecom output matchs almost perfectly the theoretical maximum coupled intensity with phase-only correction (green curve). Thus, the spatial modulation control method with photometric measurements reaches the theoretical maximum efficiency allowed by phase-only correction.

4.6 Closed-loop performances comparison between spatial modulation and sequential modulation control methods

As developed in Section 3.2 sequential modulation allows to correct the PIC stage by stage. Thus, with our 32-input PIC (composed of 5 stages), the sequential modulation maximum correction frequency at fixed modulation frequency is five times lower than with spatial modulation.

With a modulation frequency $f_m = 25\ kHz$, considering one modulation period τ_m for one correction period τ_c (p=1), with spatial modulation the maximum correction frequency is $f_c = 25\ kHz$ whereas with sequential modulation the maximum correction frequency is $f_c = 5\ kHz$ (5 stages to be modulated and corrected sequentially).

To illustrate the advantage of spatial modulation allowing for faster correction frequencies, we consider the following simulation parameters:

- $f_m = 25\ kHz$, for both spatial and sequential modulation.
- $f_c = 12.5\ kHz$, for the spatial modulation.
- $f_c^{seq} = 5\ kHz$, for the sequential modulation. It corresponds to the maximum applicable correction frequency with sequential modulation and $f_m = 25\ kHz$
- We consider fluctuations of the modulus of the complex amplitudes.
- We consider photon noise with the link budget developed in section 4.3.6
- We consider read-out noises with a $SNR_{RON} = 323$.
- The simulation is performed without photometric measurements.
- Spatial modulation is applied with $\boldsymbol{\delta\varphi^{opt}}$.
- Sequential modulation is applied with a modulation amplitude $\delta\varphi = 0.2\ rad$

Figure 4.24a plots the results of the simulation. The blue curve η_{po} corresponds to the closed-loop result obtained with spatial modulation in Section 4.4.3.1.4 with $\langle\eta_{po}\rangle = 0.81$. The green curve corresponds to the closed-loop result η_{po} for sequential modulation with $\langle\eta_{po}\rangle = 0.49$. It is clear that the spatial modulation control method outperforms sequential modulation thanks to its higher correction frequency. Figure 4.24b gives a zoom on closing the loop over the first 10 ms. It takes around 2 ms to close the loop with spatial modulation against around 10 ms for sequential modulation, which is five times more. This difference comes from the five stages of the PIC corrected sequentially with sequential modulation.

Those results are obtained with different correction frequencies for spatial and sequential modulation. At $f_m = 25\ kHz$, the maximum correction frequency allowed by sequential modulation being $f_c^{seq} = 5\ kHz$, below we compare the spatial and sequential modulation when both have a correction frequency of 5 kHz.

Figure 4.25 compares η_{po} for spatial and sequential modulation at $f_c = f_c^{seq} = 5\ kHz$. The closed-loop signal η_{po} is degraded for spatial modulation compared with η_{po} at $f_c = 12.5\ kHz$, see Figure 4.24. In Figure 4.25a we observe that η_{po} present similar fadings for

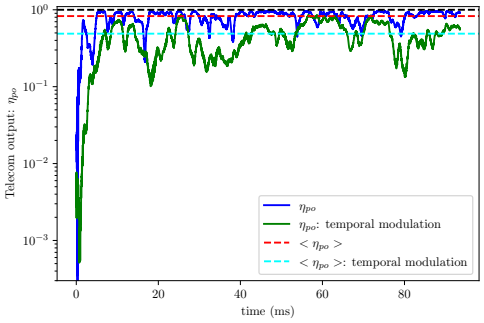

(a) In blue, η_{po} with spatial modulation: $f_c = 12.5\ kHz$, $f_m = 25\ kHz$ with, $\langle \eta_{po} \rangle = 0.81$ in red. In green, η_{po} with sequential modulation: $f_c^{seq} = 5\ kHz$, $f_m = 25\ kHz$ with, $\langle \eta_{po} \rangle = 0.49$ in cyan.

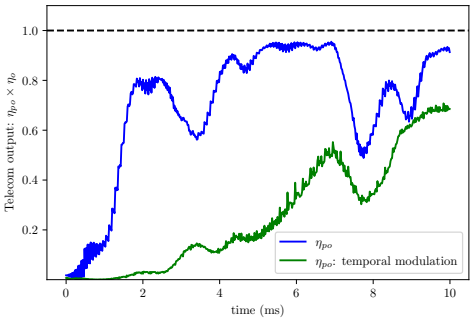

(b) Zoom on the first 10 ms

Figure 4.24: Comparison between spatial and sequential modulation. With $f_c = 12.5\ kHz$ for spatial modulation and $f_c^{seq} = 5\ kHz$ for sequential modulation being the maximum correction frequency allowed at $f_m = 25\ kHz$.

spatial and sequential modulation (respectively blue and green curves). Indeed, as developed in Appendix E, the noise propagation with sequential modulation near a maximum is the same as with spatial modulation control method with $\boldsymbol{\delta\varphi^{opt}}$. However, $\langle \eta_{po} \rangle = 0.68$ for spatial modulation against $\langle \eta_{po} \rangle = 0.49$ for sequential modulation. This difference can be explained by the fact that the correction is applied in one step with spatial modulation and stage by stage with sequential modulation. Furthermore, as shown in Figure 4.25b spatial modulation is still closing the loop faster than sequential modulation with approximately 4 ms for spatial modulation against 10 ms for sequential modulation which is 2.5 times slower.

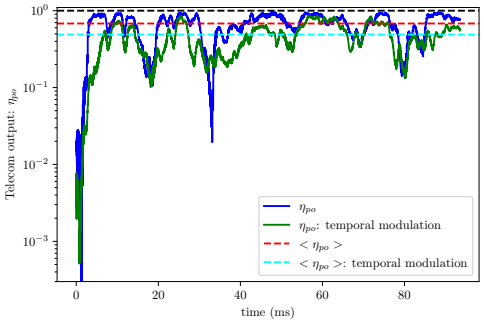

(a) In blue, η_{po} with spatial modulation: $f_c = 5\ kHz$, $f_m = 25\ kHz$ with, $\langle \eta_{po} \rangle = 0.68$ in red. In green, η_{po} with sequential modulation: $f_c^{seq} = 5\ kHz$, $f_m = 25\ kHz$ with, $\langle \eta_{po} \rangle = 0.49$ in cyan.

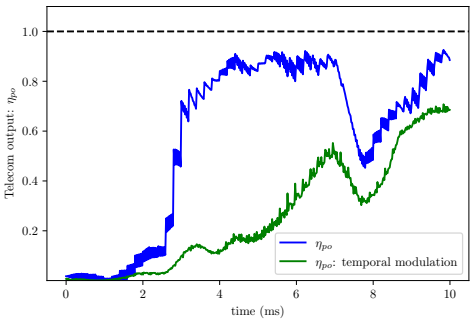

(b) Zoom on the first 10 ms.

Figure 4.25: Comparison between spatial and sequential modulation. With $f_c = f_c^{seq} = 5\ kHz$ for spatial and sequential modulation.

4.7 Conclusion

In this chapter, I developed all the error terms impacting integrated-AO performances. I proposed a general method for the design of an integrated-AO by evaluating the impact of the different error terms on the power coupled in the telecom output. Finally, I developed an end-to-end simulation to evaluate close-loop performances using the spatial modulation control method in realistic atmospheric turbulence conditions.

We have seen that our analytical expression of the time covariance of the complex amplitude of the PIC input (see Section 2.4) allows us to evaluate the temporal error and that the spatial modulation control method can close the loop by hill-climbing as it was discussed in the previous chapter. The main limitation in the close-loop performances with the spatial modulation control method is induced by fluctuations of the modulus of the complex amplitudes at the input of the PIC. To overcome this issue, I proposed a modification of the PIC architecture to add photometric measurements to measure such fluctuations of the modulus of the complex amplitudes at the PIC inputs. With photometric measurements, the spatial modulation control method allows for the same performances as the theoretical one with phase-only correction. Finally, spatial modulation control method closed-loop performances were compared with that of sequential modulation. As expected, the gain in correction frequency brought by spatial modulation allows it to outperform sequential modulation. However, even at equivalent correction frequency the spatial modulation control method shows higher performances due to its correction applied in one step and not sequentially.

The spatial modulation control method performances were tested in realistic atmospheric turbulence conditions but with a perfect theoretical PIC without losses. Therefore, the possibility of implementing the spatial modulation control method on a realistic PIC with all its imperfections is raised.

CHAPTER 5

Experimental implementation of the spatial modulation control method

Contents

5.1 Introduction

In the previous chapters, the spatial modulation control method was developed and implemented in an E2E simulation with a theoretical perfect PIC without losses, cross-talk, and with balanced couplers. However, due to the manufacturing process, a realistic PIC presents imperfections which can impair the control law. In this chapter two experimental PICs are characterized, and their properties are compared to those given in the specifications. One of the PICs is used to evaluate difficulties in implementing the spatial modulation control method on an experimental PIC with all its imperfections.

This chapter is structured as follows: Section 5.2 presents the background of the two PICs imposed and used in this thesis: a 8 inputs LiNbO3-PIC and a 32 inputs SOI-PIC. Section 5.3, develops the characterizations of the two PICs and discusses perspectives for future PIC realizations. Finally, Section 5.4, develops the implementation of the spatial modulation control method on the 8 inputs LiNbO3-PIC.

5.2 Foreword about the two PICs used in this thesis

In this thesis, I have two PICs at my disposal, a 8 inputs LiNbO3-PIC with arithmetical architecture as an integrated DM and a 32 inputs SOI-PIC with geometrical architecture composed of MZIs.
Their design and characteristics were defined before the start of my thesis. Thus, I did not participate in the discussions and choices of their architecture, sizing, phase-only or phase and amplitude correction, technological platform...

The 8 inputs LiNbO3-PIC was developed during L. Rinaldi's thesis [6]. It was fabricated by Nadèje Courjal at FEMTO-ST and designed by Guillermo Martin at IPAG for 1.5 µm applications with single mode waveguides confinement. The choice for a LiNbO3-PIC was retained in Rinaldi's thesis for the high modulation bandwidth, tens of GHz, allowed by LiNbO3 phase shifters. Moreover, electro-optics effect phase shifters avoid thermal cross-talk faced by thermal phase shifters. This PIC was realized as a proof of concept of coherent combination with LiNbO3. The PIC architecture and sizing were developed in Rinaldi's thesis [6], and I summarise them in section 5.3.1. Due to time constraints, L. Rinaldi was unable to characterize the PIC.

The 32 inputs SOI-PIC was developed by Scuola Superiore Sant'Anna Pisa, VTT and ONERA in an ActPhast project collaboration. The scope of the project was to define and produce a realistic PIC for atmospheric effects mitigation. Its high-level specifications were defined by ONERA (before the start of my thesis). L. Rinaldi's thesis work justified the choice of 32 inputs [6] while being compatible with available technological platforms. The choice for a phase and amplitude correction with MZI was retained to couple all the PIC input energy in the telecom output (s_0). Scuola Superiore Sant'Anna Pisa designed the PIC, and VTT was retained to manufacture it to take advantage of their 3-µm SOI platform.

The SOI-PIC was supposed to be delivered at the start of my thesis and then used to implement and test control algorithms to mitigate atmospheric turbulence effects emulated by an optical bench. However, due to delays undergone by VTT, it was delivered at the end of my thesis, and only its first characterizations could be performed. The SOI-PIC not being available, I decided to implement the spatial modulation control method on the 8 inputs LiNbO3-PIC. Due to a lack of time, developing a real-time control system for mitigating atmospheric turbulence effects was impossible. Thus, the PIC is not tested behind an optical bench emulating atmospheric turbulence effects but directly connected to a laser using a 1 to 8 fibre splitter in order to test the experimental implementation of the spatial modulation control method. Only slow phase variations induced by thermal drift perturbations between the PIC inputs impact the coherent combination in time.

5.3 LiNbO3 & SOI PICs characterizations

As developed in Section 1.6.3, the characteristics required by an integrated-AO for coherent combination to mitigate atmospheric turbulence effects are:

- Losses around 4 dB.
- Should avoid thermal cross-talk induced by thermal phase shifters not to impair the PIC control.

- Should avoid modulated light cross-talk so as not to impair modulation-based control methods.

- Phase shifters with tens of kHz bandwidth for real-time mitigation of atmospheric turbulence effects, as developed in the previous chapter.

- Phase shifters phase range of at least 2π, to apply corrections $[2\pi]$.

- Couplers split-ratio comprise between $60:40$ for the coherent combination in the telecom output not to be too much impacted as developed by [85] and resumed in Section 1.6.2

Thus, before implementing a control law on a PIC, we need to characterize its losses and analyze where they come from to discuss potential improvements, the phase shifters bandwidth, the phase shifters V_{pi} (the required voltage corresponding to a π phase shift) and light and thermal cross-talks.

5.3.1 LiNbO3-PIC

5.3.1.1 LiNbO3-PIC architecture and design

Due to LiNbO3 low bending radii allowed, the arithmetic architecture is retained, see Figure 5.1, also enabling all couplers measurement outputs to exit the PIC without crossing other waveguides.
The wafer size is limited to 84 mm in length, allowing for an 8 inputs/outputs PIC with simple couplers [6]. The coherent combination of 8 complex amplitudes is relatively low to consider optical communication. Still, this PIC was designed as a proof of concept to test and implement control methods.
The PIC is designed with 7 push-pull phase shifters placed at the PIC input.
Teem Photonics performed the encapsulation. The PIC inputs are connected to 8 polarization-maintaining SMF as well as the 8 outputs. See Figure 5.1 for the PIC schema and Figure 5.3 for a picture of the PIC.

The LiNbO3-PIC numbering and notations are given in Figure 5.1. The PIC inputs are numbered from 1 to 8, top to bottom, and the PIC outputs are numbered from 8 to 1, top to bottom, corresponding to the PIC input fibres numbering given by Teem Photonics. The phase shifters are in push-pull, depicted by green rectangle. A phase shifter comprises two electrodes spaced with a 7.5 µm gap, equivalent to a capacitance. The theoretical electro-optic efficiency is $V_\pi \times L_{elec} \approx 9$V.cm with electrode length $L_{elec} = 9.5\ mm$. To avoid capacity clamping, the maximum applicable voltage is 40 V. Figure 5.2 depicts the implementation of the electrodes of the phase shifters.

The voltages applied on the phase shifters are denoted V_i for $i \in (1,7)$. Each input waveguide-induced phase shift is denoted φ_j for $j \in (1,8)$. Differential voltages between input waveguides are defined as δV_i for $i \in (1,7)$ such as $\delta V_1 = V_2 - 2V_1$, $\delta V_7 = -2V_7 + V_6$ and $\delta V_i = V_{i+1} - 2V_i + V_{i-1}$ for $i \in (2,6)$. The phase difference between two input waveguides is denoted $\delta\varphi_j$ for $j \in (1,7)$ corresponding to the phase difference induced by the push-pull phase shifter so that $\delta\varphi_j \propto \delta V_j$, see Figure 5.1. When applying a voltage vector $\boldsymbol{V} = (V_j)$ we have the relation $\boldsymbol{\delta\varphi} \propto \boldsymbol{M_p V}$ with:

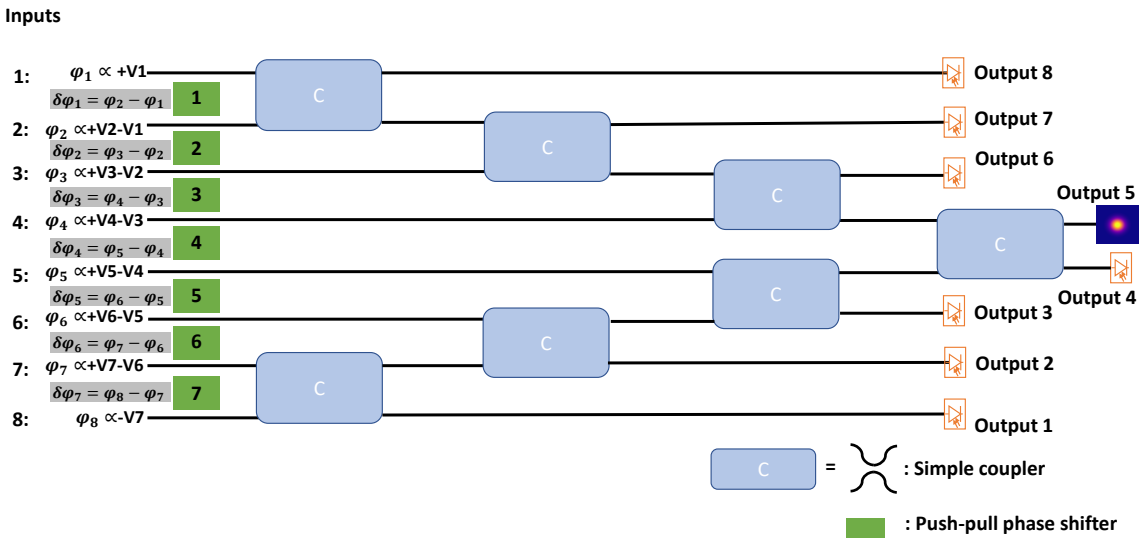

Figure 5.1: Schema of the experimental LiNbO3 PIC with its 8 inputs, 7 phase shifters in push-pull and 7 couplers.

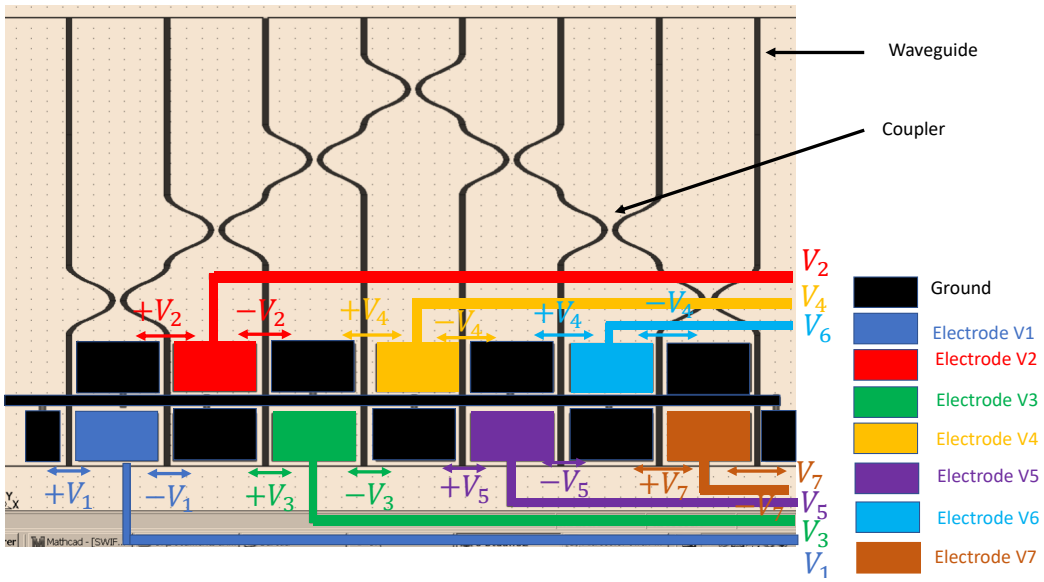

Figure 5.2: LiNbO3-PIC electrodes numbering defining the phase shifters.

$$\boldsymbol{M_p} = \begin{pmatrix} -2 & 1 & 0 & 0 & 0 & 0 & 0 \\ 1 & -2 & 1 & 0 & 0 & 0 & 0 \\ 0 & 1 & -2 & 1 & 0 & 0 & 0 \\ 0 & 0 & 1 & -2 & 1 & 0 & 0 \\ 0 & 0 & 0 & 1 & -2 & 1 & 0 \\ 0 & 0 & 0 & 0 & 1 & -2 & 1 \\ 0 & 0 & 0 & 0 & 0 & 1 & -2 \end{pmatrix}. \tag{5.1}$$

The LiNbO3-PIC is controlled in the phase difference space, $\boldsymbol{\delta\varphi}$, and the voltages to be applied are computed as:

$$\boldsymbol{V} \propto \boldsymbol{M_p^{-1}} \boldsymbol{\delta\varphi}\,, \tag{5.2}$$

The voltages are applied on the phase shifters using piezo-electric controllers realized by Polytec PI.

The PIC footprint is 5 mm×84 mm×500 µm, see Figure 5.3. The PIC waveguides are 7 µm width with a spacing of 127 µm between waveguides. The maximum bending radii is limited to 6.7 mm. For the couplers to be balanced, the coupling section is designed with a 6 µm gap of 100 µm length [6]. See Figure 5.4 for the design of a balanced coupler.

At the PIC input, the guided wave must be linearly polarized and injected horizontally in the waveguides to maximize the phase shifter electro-optics efficiency.
Before the encapsulation, performed by Teem Photonics, the outputs of the waveguides are imaged using a microscope objective, as shown in Figure 5.5a.

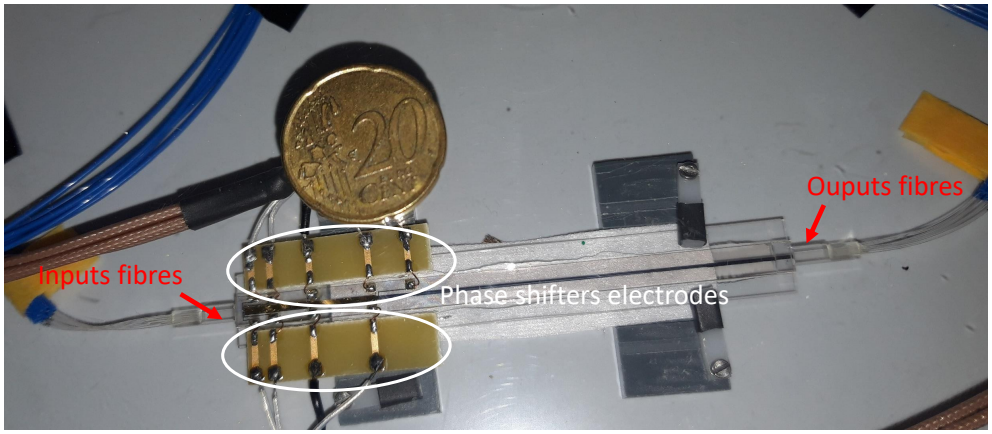

Figure 5.3: Picture of the LiNbO3-PIC.

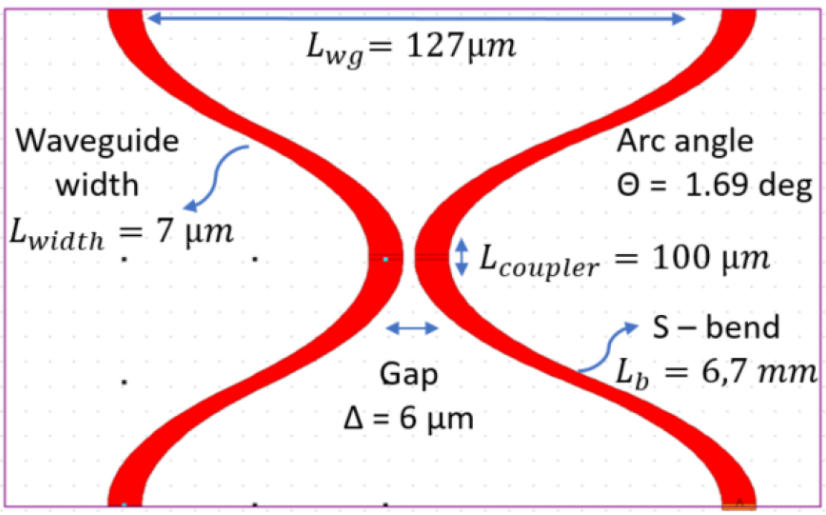

Figure 5.4: Sizing of a balanced coupler of the LiNbO3-PIC from Rinaldi's thesis [6].

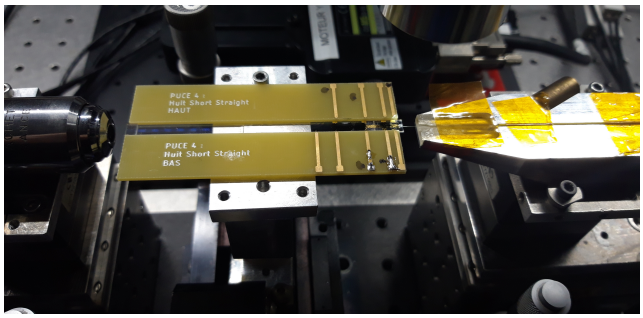

(a) Opto-mechanical mounting with microscope objective to image the PIC output waveguides at FEMTO-ST. A polarization-maintaining SMF end is placed at one PIC input waveguide to couple a 1.5 µm laser in the waveguide.

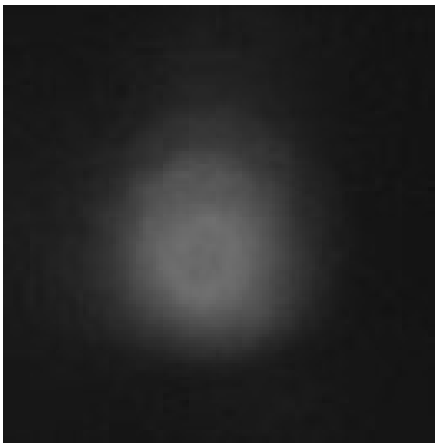

(b) Output waveguide number 6 intensity profile, imaged with the microscope objective. The laser is injected in PIC input number 3.

Figure 5.5: Opto-mechanical mounting at FEMTO-ST to imaged the laser mode at the PIC output waveguides.

Figure 5.5b shows the intensity profile of a guided mode. It corresponds to the fundamental monomode with a Gaussian intensity profile as shown in the image cross-section in Figure 5.6.

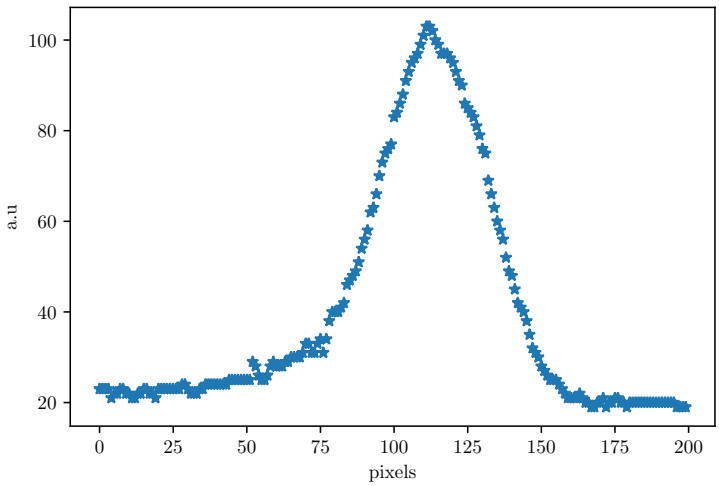

Figure 5.6: Figure 5.5 (b) cross-section.

5.3.1.2 LiNbO3-PIC characterizations

LiNbO3-PIC losses and light cross-talk: The PIC losses and light cross-talk can be measured simultaneously. The measurement procedure is as follows:
Intensity measurements are performed using a Femto photodiode DLPCA-200, whose output signal is read on an oscilloscope load at 1 $M\Omega$.
A 1.5 µm linearly polarized laser LP1550-PAD2 injects light in PIC input 1. The injected intensity is preliminary measured using the photodiode. Phase shifter 1 is modulated with a sinusoidal voltage. Then, all PIC outputs are measured one by one using the photodi-

ode. The maximum and minimum intensity fluctuation detected by the photodiode for each PIC output measurement is saved. If there is light cross-talk, the readout intensities should fluctuate, and the maximum and minimum intensity measurements will differ.
Then, the same process is repeated but with phase shifter 2 (only) being modulated with a sinusoidal voltage.
In a nutshell, we have light injected in input 1, modulation applied on phase shifter 2, and measurements of all output intensities performed one by one.
This process is repeated for all phase shifters modulated one by one with light injected in input 1.
The overall process is repeated for all inputs one by one.
Figure 5.7 shows the measurement results obtained for modulated phase shifter 3. Measurements accuracy is 5 mV due to readout noise. No signal variations were measured during modulation meaning there is no modulated-light cross-talk in the PIC for phase shifter 3. The results are similar for all phase shifters, meaning there is no modulated-light cross-talk in the PIC. Thus, modulation-based control methods will not be impaired by light cross-talk.

	Output 1 (mV):	Output 2 (mV):	Output 3 (mV):	Output 4 (mV):	Output 5 (mV):	Output 6 (mV):	Output 7 (mV):	Sum (mV):
Input 1	0	0	0	24	15	49,5	174	367,5
Input 2	0	0	0	17	30	124	496	711
Input 3	0	0	0	73	164	705	432	1374
Input 4	0	0	0	233	608	395	0	1236
Input 5	0	0	332	485	170	0	0	987
Input 6	0	409	677	170	67	0	0	1323
Input 7	465	800	210	59	29	0	0	1563
Input 8	1100	290	88,5	31,5	54	0	0	1564

Figure 5.7: Table of PIC output intensity measurements (in mV) function of the PIC input light injection for phase shifter 3 being modulated. Input intensity measured at 12 V.

For one input, the losses are defined as $10 \times log(Sum/12000)$ with Sum being the sum of the measured intensities over all outputs for one input. The PIC input/output total average losses are -10.6 dB. However, they are not uniform regarding inputs. Input 1 and 2 present respectively -15 and -12 dB losses. We suppose the strong losses in inputs 1 and 2 come from a misalignment of the input SMFs V-groove. Without inputs 1 and 2, the average losses fall to -9.5 dB. The mismatch between the LiNbO3 waveguide mode shape and size and the SMF mode generates around 3 dB losses, which makes a total of 6 dB losses for input/output mode mismatch. Such mode mismatch losses can be reduced by performing size mode adaptation [137, 138, 111], which is not the case for our LiNbO3 PIC.
Removing the 6 dB losses induced by modes mismatch, the average PIC losses fall to -3.5 dB due to couplers and linear losses.

5.3.1.2.1 LiNbO3-PIC phase shifters

The phase shifters characteristics we need to measure to determine their behaviour are as follows:

- Response time.
- Linearity coefficient: α so that $\delta\varphi = \alpha\delta V$.

In the following, the tensions are applied on one electrode, and the others are set to 0 V so that $\delta V_j = \pm V_j$.

Response time:
To characterize a phase shifter response time, the laser is injected in two PIC inputs, associated to a specific phase shifter, using a balanced fibre splitter. The output interference signal is measured with the photodiode DLPCA-200 with a gain set to 10^8 limiting its rising time to 2 µs.
Periodic square voltages of amplitude ranging from ±10 V are applied at 10 kHz on a phase shifter. An example is given in Figure 5.8 for phase shifter 7.

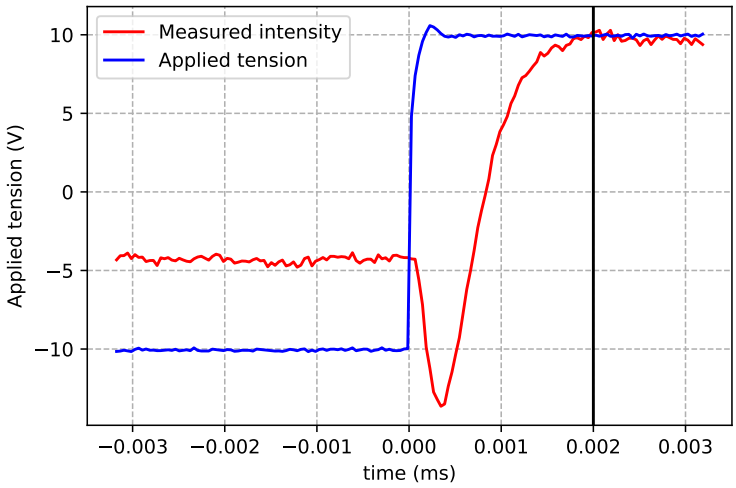

Figure 5.8: In blue: applied on phase shifter 7. In red: intensity response to square ramp of 20 V.

In Figure 5.8, the phase shifter applied voltage is plotted in blue, and the interference signal measured by the photodiode is plotted in red. The measured intensity response to 20 V applied on a phase shifter is sinusoidal. Thus, measuring a rising time between 10 % and 90 % is not simple. But when the interference signal reaches a static value it gives an upper bound for the response time, see the black vertical line on Figure 5.8. For phase shifter 7, the black vertical line (on Figure 5.8) gives an upper bound of 2 μs corresponding to the limited photodiode rising time as depicted above. Thus, being limited by the photodiode rising time, we cannot measure the response time of the phase shifters. However, even if the theoretical maximum frequency of LiNbO3-PIC electro-optic phase shifters (tens of GHz) cannot be measured, the phase shifters bandwidth is at least 500 kHz ($1/(2 \times 10^{-6})$) which is sufficient for the real-time control of the PIC as developed in Section 2.4.

Linearity coefficient:
With the electro-optics effect, a phase shifter response in phase is proportional to the applied voltage such as $\delta\varphi = \alpha\delta V$. To determine the coefficient α, periodic voltage ramps ranging from ±10 V of amplitude are applied on a phase shifter at 10 kHz. The laser is injected in two inputs of the PIC using a balanced fibre splitter, and one output of the

PIC is measured with the photodiode.
The resulting measured intensity is of the shape:

$$I_m = \frac{I_{max} + I_{min}}{2} + \frac{I_{max} - I_{min}}{2} \times cos(\delta\varphi + \delta\varphi_c)\,, \tag{5.3}$$

with I_{max} and I_{min} respectively the maximum and minimum intensity. $\delta\varphi_c$ is a constant phase difference. The intensity measured on output 3 when applying periodic voltage ramps on phase shifter 4 with the laser injected in PIC inputs 5 and 6 is plotted in Figure 5.10, see Figure 5.9 for the PIC connections. Only input 5 undergoes a phase shift $\varphi_5 \propto -V_4$ such as:

$$I_3^0 = I_5^i + I_6^i + 2\sqrt{I_5^i I_6^i} cos(\delta\varphi_5 + \delta\varphi_c)\,. \tag{5.4}$$

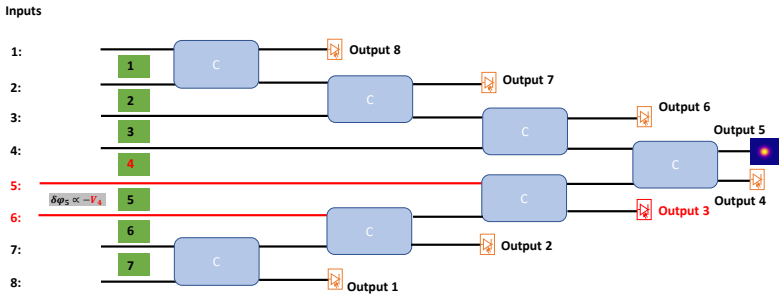

Figure 5.9: Intensity measurement on output 3, with the laser injected in inputs 5 and 6. Modulation applied on phase shifter 4.

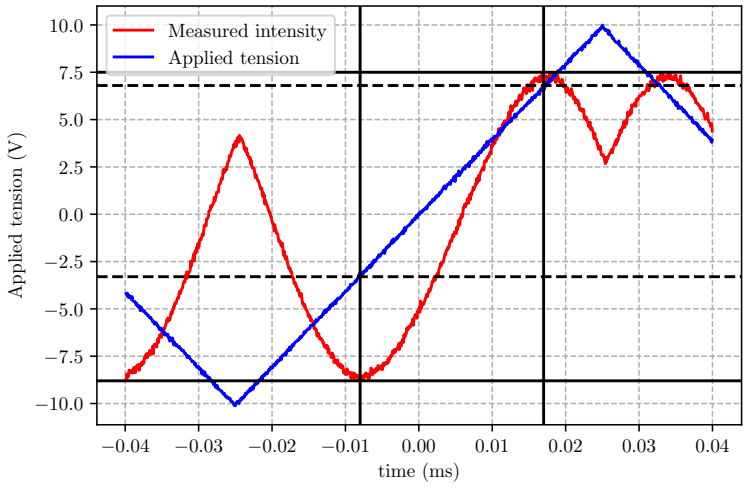

Figure 5.10: In red intensity response with phase shifter 4 modulated with a ramp of 20 V in blue.

Figure 5.10 plots the applied voltage on phase shifter 4 in blue and the PIC output 3 measured with the photodiode in red. The two vertical black lines delimit one half of

a period of the measured signal. We measure $I_{max} = 7.5\ V$ and $I_{min} = -8.5\ V$ with the horizontal continuous black lines. The horizontal dotted black lines give the voltage corresponding to V_π. Figure 5.11 gives the linear relation between the applied voltage and the induced phase shift, with $\langle I_m \rangle = (I_{max} + I_{min})/2 = -0.5$ and $A = (I_{max} - I_{min})/2 = 8$. It comes $\delta\varphi = 0.314\delta V$ and $V_\pi = 10\ V$.

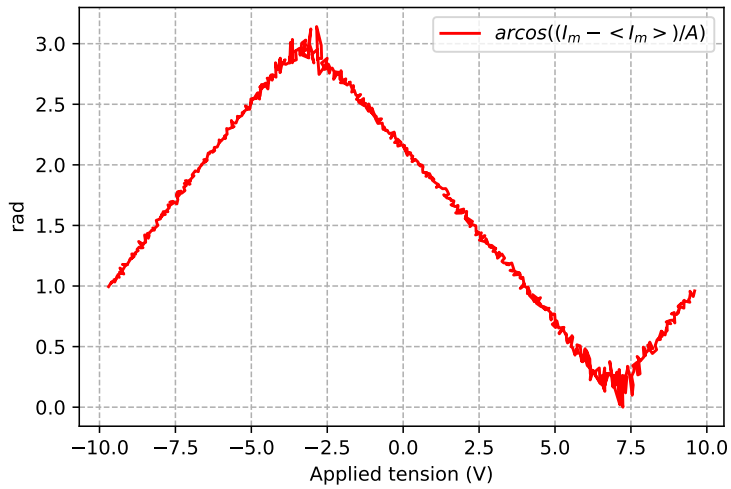

Figure 5.11: Induced phase shift function of the applied voltage, measured for phase shifter 4.

The V_π is not quite the same for all phase shifters. For example, Figure 5.12 plots the interference signal for phase shifter 5. We measure $V_\pi = 11\ V$.

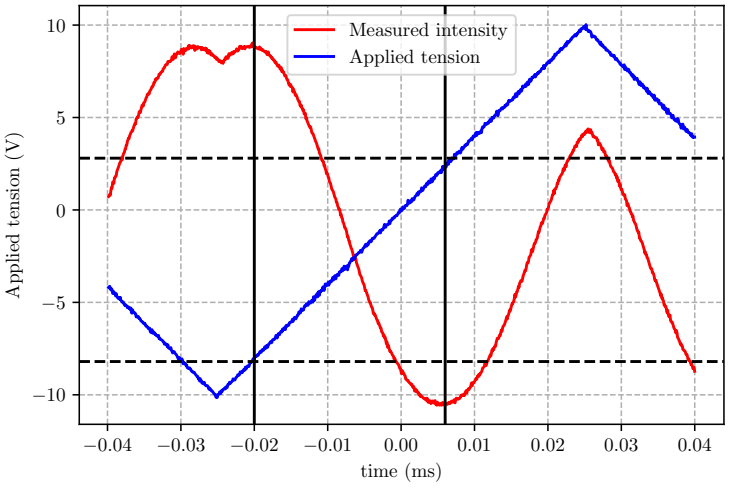

Figure 5.12: In red intensity response to phase shifter 5 modulated with a ramp of 20 V, in blue.

The maximum applicable voltage to avoid phase shifter clamping is 40 V. Thus, we can apply up to approximately 4π rad, allowing for $2 \times 2\pi$ phase range. Thus, correction can be applied $[2\pi]$.

5.3.2 SOI-PIC

The SOI-PIC was characterized during a one-week measurement campaign in collaboration with Scuola Superiore Sant'Anna Pisa. The losses, MZIs and thermal cross-talk were characterized. After the measurement campaign, additional measurements were performed by Scuola Superiore Sant'Anna Pisa to characterize the PIC integrated photodiodes. The characterization results are presented in an article written in collaboration between ONERA, Scuola Superiore Sant'Anna Pisa and VTT [139]. It is attached in Appendix C. The main results are summarized below to discuss prospects for future PIC realizations.

5.3.2.1 SOI-PIC architecture and design

Figure 5.13 depicts the PIC architecture and Figure 5.14 corresponds to the technical layout. The PIC comprises 32 inputs, 31 MZIs, 62 thermal phase shifters, 62 Multimode Interference Splitters (MMI)s (a MMI is equivalent to a simple coupler), 31 integrated photodiodes (one on each MZI output measurement) and 1 SMF output corresponding to the telecom output. The geometrical architecture allows for a compact PIC composed of 5 stages of MZIs with a footprint of 10×5 mm^2. The integrated photodiodes allow the elimination of waveguide-to-SMF coupling loss for the measurement outputs. On Figure 5.14, waveguide number 3 corresponds to the telecom output, s_0, the 32 inputs of the PIC are numbered from 4 to 35, the phase shifters numbering are P_i.j for external phase shifters of MZIs and I_i.j for internal phase shifters of MZIs, with i the numbering of the MZIs stage row from 1 to 5 and j the numbering of the MZI line from 1 to 2^{5-i}.

Photos of the PIC wire bonding realized by VTT are presented in Figure 5.15 with the phase shifters electric connections and the fibre array input-output connections.

To ensure the thermal stability of the PIC, it is integrated to a Thermoelectric Peltier Cooler (TEC). Finally, the PIC is placed in a protective box as shown in Figure 5.16. The input SMFs are polarization maintaining as well as the telecom SMF.

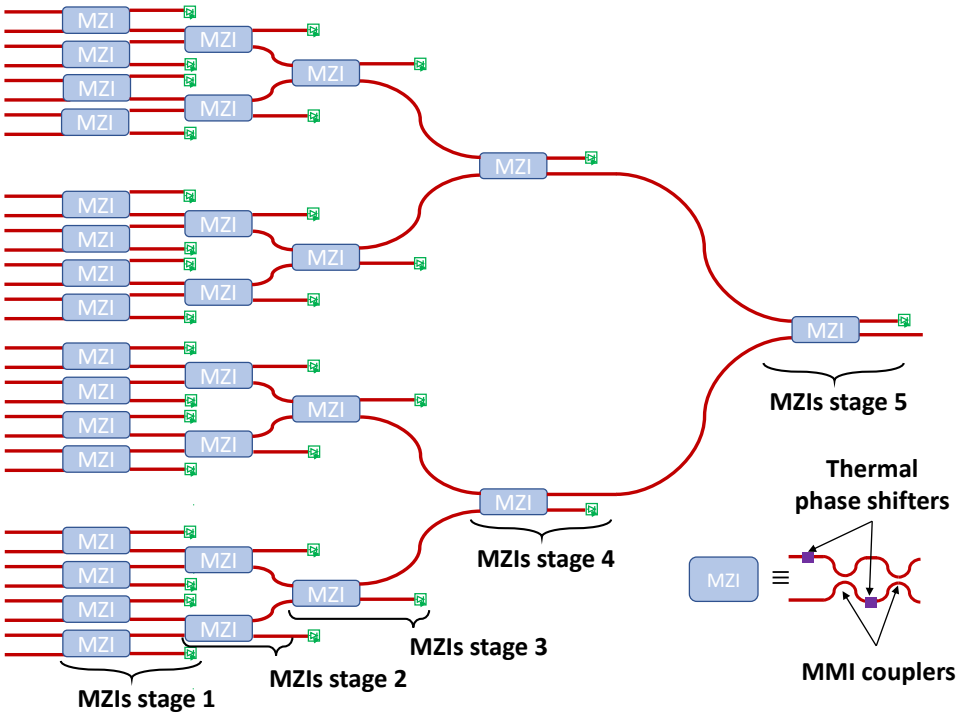

Figure 5.13: 32 inputs SOI-PIC schema with its 31 MZIs spread in 5 stages. Green rectangles represent the 31 integrated photodiodes and red wires represent the waveguides.

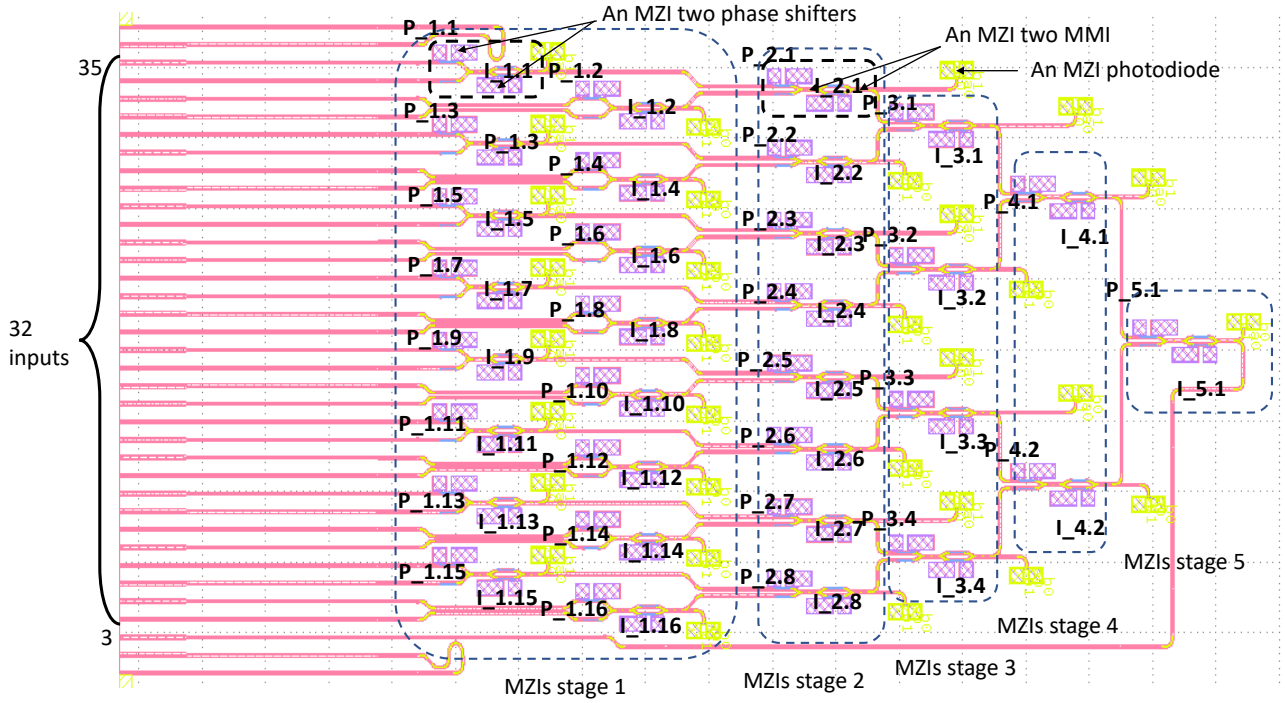

Figure 5.14: 32 inputs SOI-PIC layout with its 5 MZI stages marked by blue dotted lines. Green rectangles correspond to integrated photodiodes, purple rectangles correspond to thermal phase shifters, and red wires correspond to waveguides. Telecom output is numbered 3, and input waveguides are numbered 4 to 35. Layout adapted from VTT.

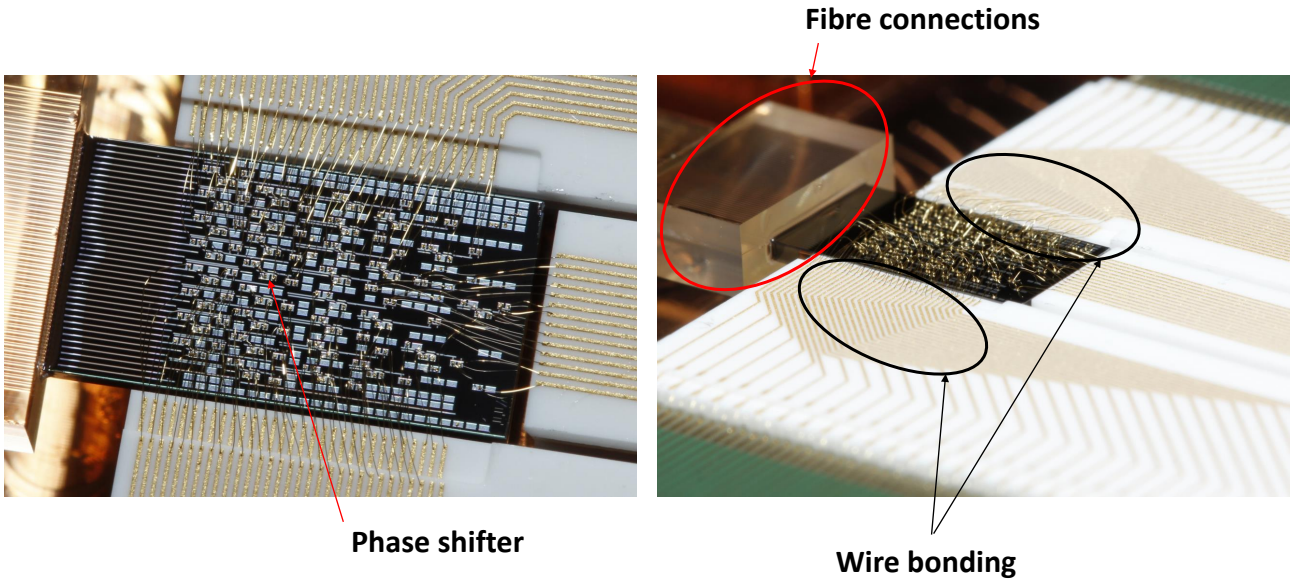

Figure 5.15: Photos of the SOI 32 inputs PIC after wire bonding and fibre array connections. Photo credit VTT.

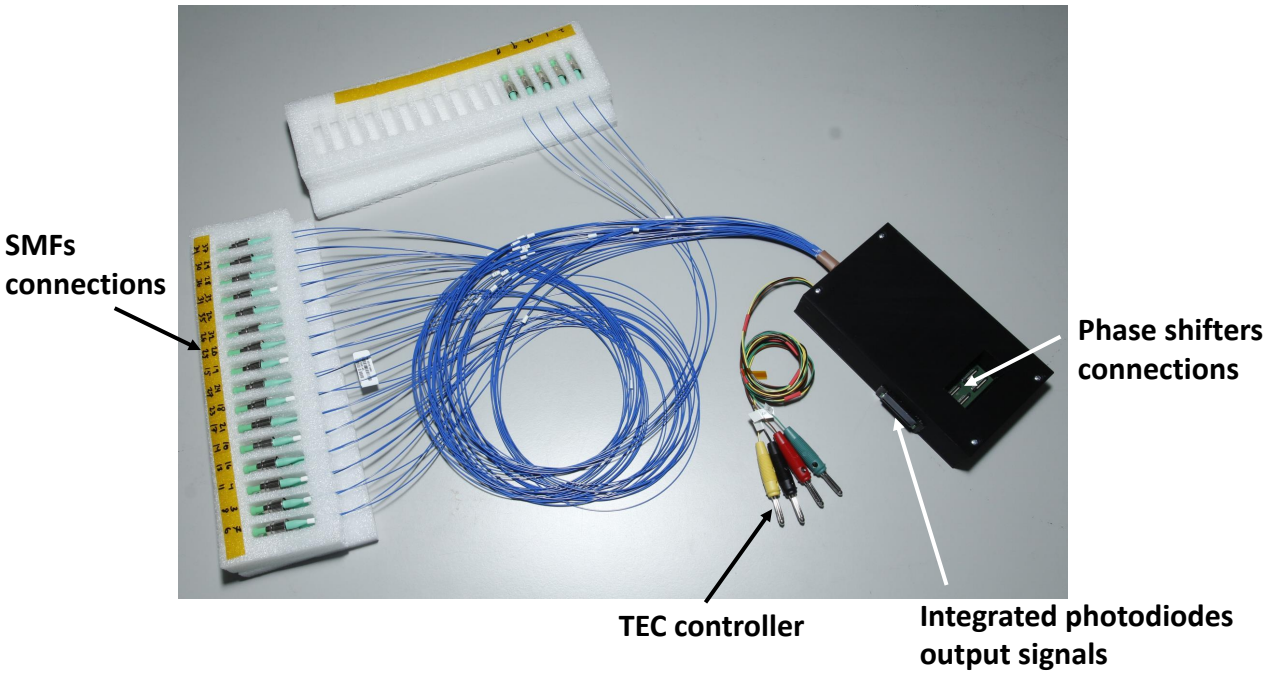

Figure 5.16: Photo of the SOI 32 inputs PIC in its protection box with SMFs, phase shifters, integrated photodiodes and TEC connections. Photo credit VTT.

5.3.2.2 SOI-PIC characterizations

5.3.2.2.1 SOI-PIC losses

The total PIC average losses are measured by injecting the laser in each input SMF one by one and by measuring the output power on the telecom SMF, which is maximized by tuning the phase shifters.
The mean PIC loss value is 15.7 dB, which is much more than the 4 dB target value to reach the same performance of a classic AO. Thus, it is straightforward that the fabricated 32 inputs SOI-PIC is unsuitable to be used as an integrated-AO to mitigate atmospheric turbulence effects. However, this does not mean that SOI-PICs cannot reach the target loss value, and a comprehension of the different loss sources is required to improve future runs.

First, VTT has developed a size mode converter interposer to reduce the insertion loss between SMF and waveguide mode to 1.5 dB. Unfortunately, for our PIC run, the optical interposer could not be positioned properly due to an error in the fabrication process. After discussion with VTT, the loss value they attribute to insertion between SMF and PIC waveguides is 5 dB. Thus, based on VTT estimation, the internal losses should be $15.7 - 2 \times 5 = 5.7$ dB. With the optical interposer, the insertion loss could be reduced by $2 \times (5 - 1.5) = 7$ dB to reach a PIC total loss of $5.7 + 3 = 8.7$ dB.
From discussion with VTT, we attribute 0.1 $\mathrm{dB\,cm^{-1}}$ of linear propagation losses due to waveguide imperfections. The remaining 5.6 dB loss comes from the 5 stages of the PIC composed of MZIs (a MZI is composed of two MMIs and two phase shifters). Considering that each stage introduces the same amount of losses, we have approximately 1.1 dB losses per stage.
After the measurement campaign, additional measurements performed by Scuola Superiore Sant'Anna Pisa, show that the total PIC losses were lower at 1.6 µm with an average total

loss of 13.8 dB. It can be explained by MMI being wider than expected. Thus, improving the MMI sizing could reduce the losses to 0.5 dB per stage.
Furthermore, improvement in the fabrication process could reduce linear loss to 0.027 $\mathrm{dB\,cm^{-1}}$ [140].

5.3.2.2.2 SOI-PIC MZIs

Each MZI comprises two MMIs and two thermal phase shifters. To characterize a MZI, we need to measure its phase shifters rise and fall time, the power P_π to be applied to obtain a π phase shift, the MZI extinction ratio and the thermal cross-talk induced by the thermal phase shifters.

Response time: To measure the response time of a phase shifter, periodic square voltages of V_π are applied to measure the rise and fall time, as shown in Figure 5.17 for phase shifter $I_{1.1}$.

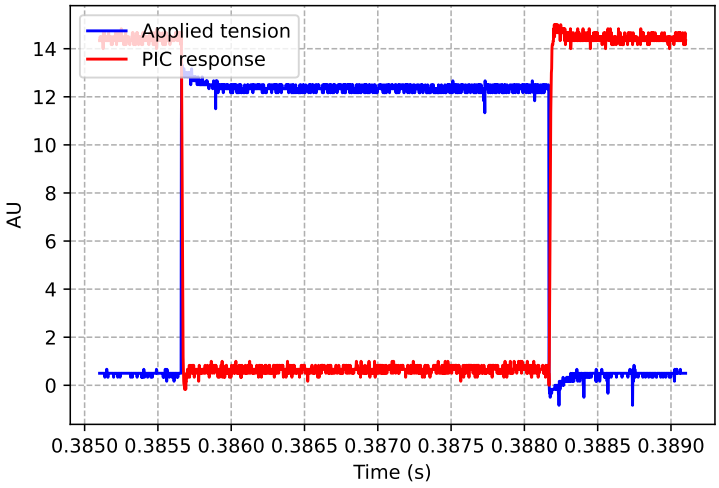

Figure 5.17: Phase shifter I_1.1 response (in red) to periodic square signals of voltage V_π (in blue).

The telecom output SMF interference signal is measured using a Thorlabs DET01CFC photodiode with a 1.2 GHz bandwidth. As shown in Figure 5.17, when applying periodic square voltage signals, in blue, the interference signal falls when voltage is applied and rises when the voltage is off.
We call rising time, t_r, the time measured at 10% and 90% it takes the interference signal to fall. It corresponds to the time it takes the phase shifter to heat up. We call falling, t_f, the time measured at 10% and 90% it takes the interference signal to rise. It corresponds to the time it takes the phase shifter to cool down.
Figure 5.18, shows the measured rising time of phase shifter number I_1.1 at 10% and 90% (vertical black dotted lines), which is $t_r = 10$ µs.

Figure 5.19, shows the measured falling time of phase shifter number I_1.1 at 10% and 90% (vertical black dotted lines), which is $t_f = 13$ µs.

We present the characterisation of one phase shifter here but rise and fall times were measured for a few phase shifters and are equivalent. Small differences between phase shifters are due to the equivalent resistance values diverging from different phase shifters.

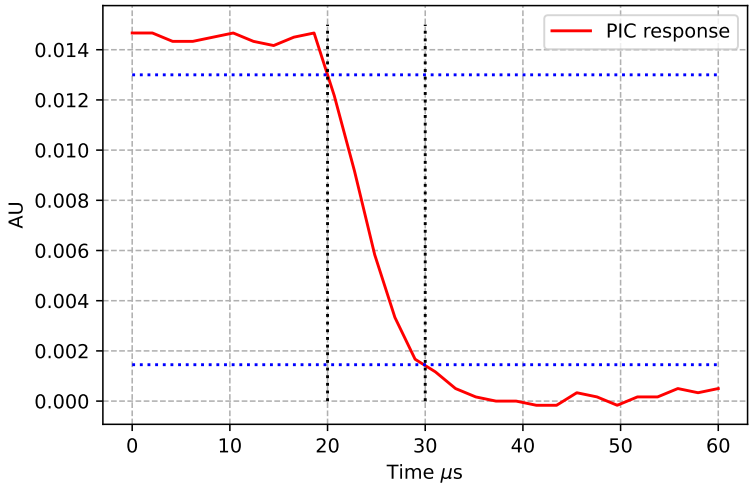

Figure 5.18: Phase shifter I_1.1 rise time at 10% and 90% (vertical black dotted lines).

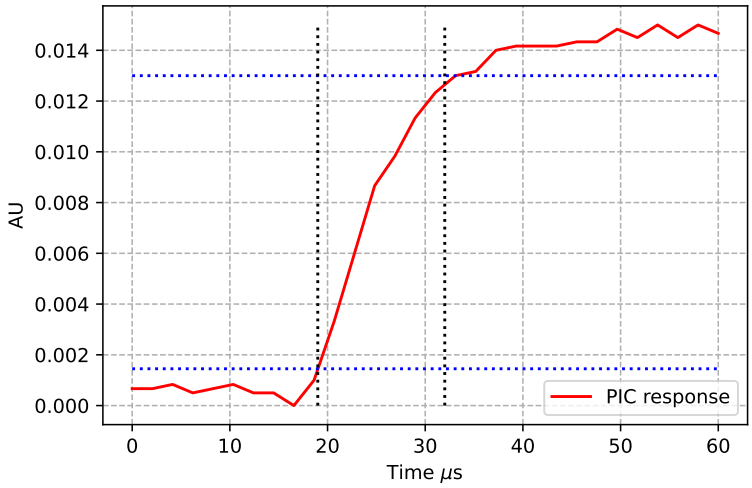

Figure 5.19: Phase shifter I_1.1 fall time at 10% and 90% (vertical black dotted lines).

Finally, the mean measured rise time is 9.4 µs and the mean measured fall time is 12.4 µs.

We observe that the phase shifters take more time to cool down than to heat up. This comes from the limited heat dissipation in the PIC.
To test the thermal stability of the SOI PIC, the rise and fall time were measured for PIC temperature ranging from 10 C° to 40 C° as plotted in Figure 5.20.

The rise and fall time remains uniform with temperature. Thus, the PIC is thermally stable thanks to the isolation trenches and the TEC.

Balanced couplers and MZI extinction ratio: An MZI extinction ratio corresponds to the minimum power on an MZI output when its two phase shifters are adjusted to have destructive interference on one output and constructive interference on the other.
Figure 5.21 shows the extinction ratio of MZI 1.1 as an example. It reaches -30 dBm minimum power when its maximum power reaches -5 dBm. Thus, the extinction ratio is

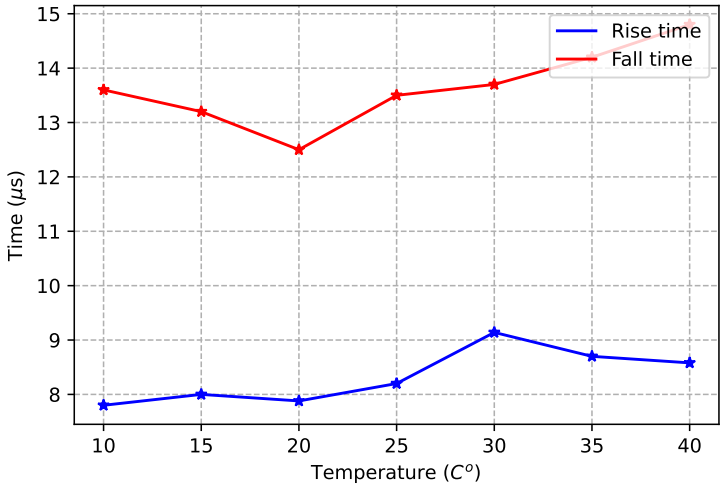

Figure 5.20: Phase shifter time response function of the SOI PIC temperature.

$-25\ dB$. From the point of view of coherent combination, the MMIs are well balanced, as discussed in the Section 1.6.2 on unbalanced couplers impact. This means the PIC can coherently combine all input intensity in the telecom SMF.

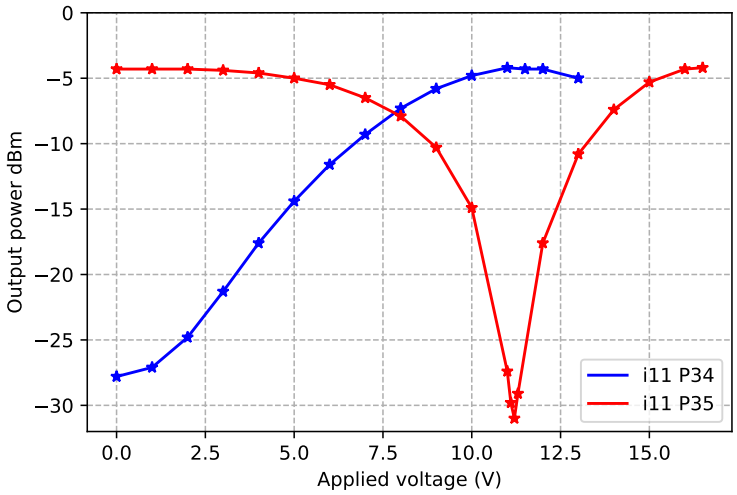

Figure 5.21: Extinction ratio of MZI number 1.1.

To measure the P_π of a phase shifter, we measure the required power to be applied on a phase shifter for the resulting interference signal to go from its maximum value to its minimum value.
A mean value of P_π was deduced from the measurements of all MZIs internal phase shifter, giving $P_\pi = 34.1$ mW. The applicable phase range is 6π, which allows 3 complete interference signal periods before performing a 2π phase shift.

Thermal cross-talk: To measure the thermal cross-talk, the phase shifters of an MZI are set to minimize the PIC output SMF power. Then, a surrounding phase shifter is modulated, and we measure the SMF optical power variations.

The thermal cross-talk is characterized using a power meter.
The maximum change in measured power was from -31 dBm to -28.9 dBm on phase shifter P_1.1 while applying square voltages of 20 V. It corresponds to 0.074 rad. The amplitude of the modulation will be one order of magnitude higher; thus, thermal cross-talk should not be a problem.

5.3.3 PICs characterizations conclusion and discussions

With its 8 inputs and -10.6 dB losses, the LiNbO3-PIC is unsuitable for realistic use. However, it was not designed for such purpose, but as a proof of concept for atmospheric turbulence effects mitigation by coherent combination using LiNbO3 technology. The LiNbO3 electro-optics phase shifters bandwidth is higher than 500 kHz, which is more than enough compared to atmospheric turbulence effects temporal evolution. The PIC phase shifters have a V_π of approximately 10 V allowing to apply $2 \times 2\pi$ phase range. No modulated light cross-talk was measured with the electro-optics phase shifters, thus easing the control algorithm implementation.
To keep the advantages of LiNbO3 electro-optics phase shifters while increasing the number of PIC inputs and reducing the total PIC losses, a promising emerging solution to investigate is LNOI as discussed in Section 1.6.3.

Concerning the 32-inputs SOI-PIC, the thermal phase shifters are thermally stable thanks to the isolation trenches and the TEC. The phase shifters bandwidth is approximately 80 kHz, which is sufficient for LEO downlink atmospheric effects mitigation with spatial coding of the modulation control method.
The MMIs are well balanced from the point of view of the coherent combination, allowing complete constructive interference in the SMF telecom output.
The phase shifters mean P_π is 34 mW enabling $3 \times 2\pi$ applicable phase range before reaching a phase shifter end-stop.
Thermal cross-talks are of really low amplitude and can be neglected.
the measured total loss is 15.7 dB, which makes it unusable for atmospheric turbulence effects mitigation as well.
However, by improving the coupling and MMIs losses, the fabrication of a 32-inputs SOI PIC with 5.5 dB total loss is possible (3 dB for input-output coupling loss and 0.5 dB per stage and with negligible linear propagation losses).
Furthermore, as developed in Section 2.3.3, considering a microlens array or a MPLC as demultiplexer, a phase-only correction PIC can reach in average $\frac{\pi}{4} \approx 78\%$ of the total coherent combination of an amplitude and phase corrections MZI-based PIC. And more than $\frac{\pi}{4}$ with a microlens array and log-normal statistics. This represents a maximum loss of 1 dB compared to phase and amplitude corrections.
A phase-only correction PIC will be composed of simple MMI stages instead of MZI stages, representing twice less MMIs in the PIC. Moreover, the reduction in complexity will considerably ease the PIC fabrication process.
Considering 1.1 dB per MZI, meaning 0.55 dB per MMI, a 32-inputs phase-only correction PIC reaches 5.75 dB of total losses. Adding a maximum of 1 dB for phase-only correction, we obtain 6.75 dB of maximum total losses for phase-only correction compared to 8.5 dB of total losses for its equivalent MZI-based PIC.
Now, considering 0.5 dB per MZI meaning 0.25 dB per MMI, a 32-inputs phase-only correction PIC reaches 4.25 dB, and with a maximum of 1 dB for phase-only correction we obtain 5.25 dB of total losses, compared to 5.5 dB total losses for an MZI-based PIC.
The same reasoning can be performed for 64 inputs PIC by adding losses of one MMI or MZI stage thanks to geometrical architecture.

All these discussions are summarized in table 5.1.

PIC composed of	Simple MMI		MZI
		With PO 1 dB	
Actual 32-inputs PIC	X	X	15.7 dB
32 Inputs & 0.55 dB per MMI	$3 + 0.55 \times 5 = 5.75$	$5.75 + 1 = 6.75$	$3 + 2 \times 0.55 \times 5 = 8.5$
64 Inputs & 0.55 dB per MMI	$3 + 0.55 \times 6 = 6.3$	$6.3 + 1 = 7.3$	$3 + 2 \times 0.55 \times 6 = 9.6$
32 Inputs & 0.25 dB per MMI	$3 + 0.25 \times 5 = 4.25$	$4.25 + 1 = 5.25$	$3 + 2 \times 0.25 \times 5 = 5.5$
64 Inputs & 0.25 dB per MMI	$3 + 0.25 \times 6 = 4.5$	$4.5 + 1 = 5.5$	$3 + 2 \times 0.25 \times 6 = 6$

Table 5.1: SOI-PIC total losses comparison with different configurations. PO means phase-only, 1 dB (worst case) is added for average phase-only correction losses compared to phase and amplitude correction.

It appears that a phase-only correction PIC allows significant gains of 1.75 and 2.3 dB respectively for 32 and 64 inputs considering 0.55 dB loss per MMI. However, with losses per MMI reaching 0.25 dB, gains are reduced to 0.25 and 0.5 dB, respectively for 32 and 64 inputs. Thus, with low losses per MMI, the interest in phase-only correction is questionable.

In a nutshell, a 32 inputs SOI-PIC with the VTT 3-µm SOI platform with phase-only correction could be tested in future runs as a conceivable mitigation solution for atmospheric turbulence effects compared to a classic AO.

5.4 LiNbO3-PIC closed-loop implementation

This section develops the experimental implementation of a closed-loop with the spatial modulation control method. This experiment aims to evaluate the difficulties of the experimental implementation of the spatial modulation control method, and its robustness against PIC imperfections.

The experimental setup is presented in the following subsection.
Due to a lack of time, the LiNbO3-PIC could not be tested behind an optical bench emulating atmospheric turbulence effects. A RTC could not be developed and the loop runs at 12.5 Hz with the existing computer environment. Still, the experimental setup can be used to test implementation of spatial modulation control method.
The problem of measuring the curvature tensor of the LiNbO3-PIC is discussed. After its determination, the optimization algorithm 1 is applied to determine the spatial modulation vector to build the interaction matrix minimizing noise propagation. Finally, closed-loop measurements are presented and analyzed.

5.4.1 Experimental setup

The experimental setup is depicted in Figure 5.22. The 8 inputs of the LiNbO3-PIC are connected to the output of a 1 to 8 balanced fibre splitter (Thorlabs TPE1315HA) supply with the 1.5 µm linearly polarized laser, LP1550-PAD.

The only perturbations undergone by the PIC are the thermal drifts between the input fibres. The PIC output fibre intensities are measured using Thorlabs FGA01FC photodiodes returning values in volt. The photodiode outputs are digitized using a National Instrument ADC. A Labview program implements the control loop and receives the ADC outputs (PC in Figure 5.22). The command voltages, computed in the control loop, are

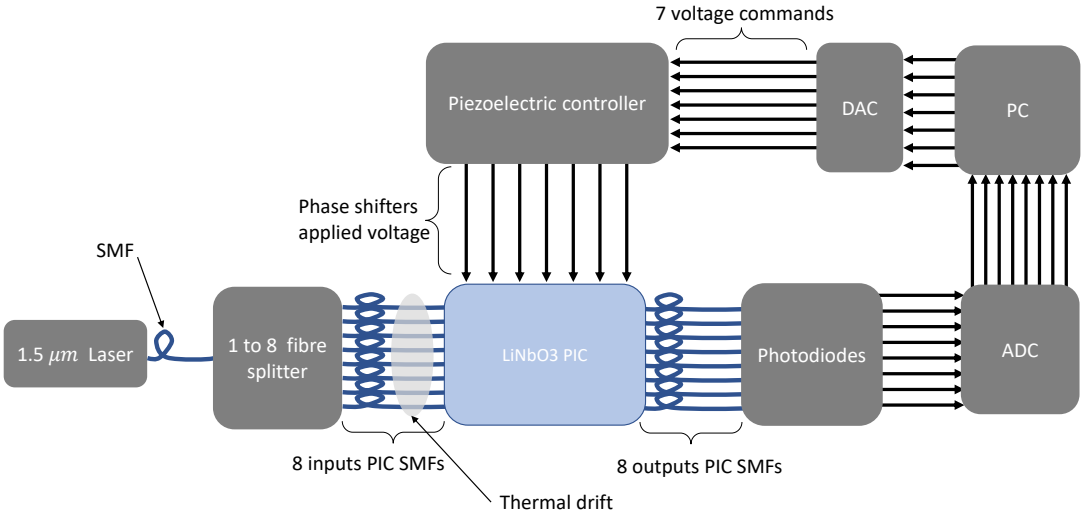

Figure 5.22: Schematic diagram of the experimental setup.

sent to the DAC. Finally, the piezoelectric controller applies the voltages on the PIC phase shifters.
To minimize the read-out noise, each measurement in the control loop is averaged over 2000 photodiode measurements sent by the ADC to the PC. Considering one loop period as the time for the PC to acquire the measurements, perform calculus, and send voltage commands and the piezoelectric controller to apply the voltage commands, the loop period is 80 ms. Thus, the loop runs at 12.5 Hz.
Figure 5.23 gives a picture of the experimental setup.

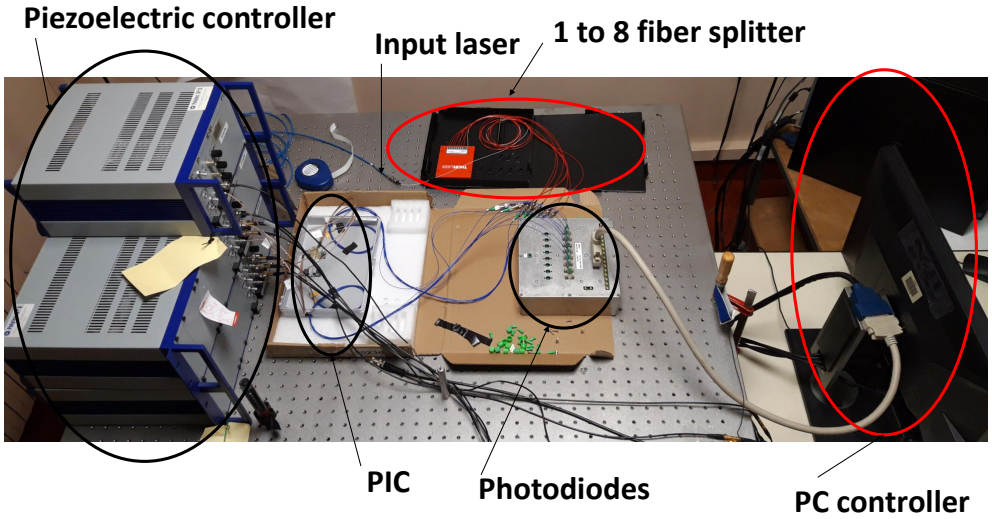

Figure 5.23: Experimental setup to test the spatial modulation control method on the LiNbO3-PIC.

With the spatial modulation control method, the residual phase to mitigate at iteration t is denoted $\boldsymbol{\varphi}^t$. As developed in Section 3.3.2 we have the linear relation $\boldsymbol{\Delta s}^t =$

$\boldsymbol{M_{int}(\delta\varphi^m)\varphi^t}$, with $\boldsymbol{\Delta s^t}$ the differential measurements vector at iteration t, and the interaction matrix $\boldsymbol{M_{int}(\delta\varphi^m) = (\delta\varphi^m)^t T}$ which depends on the transpose of the spatial modulation vector: $\boldsymbol{(\delta\varphi^m)^t}$, and the PIC curvature tensor: $\boldsymbol{T}$ in the phase differences space. The estimation of $\boldsymbol{\varphi^t}$ from the differential measurements at iteration t is obtained using the command matrix $\boldsymbol{M^{\dagger}_{int}(\delta\varphi^m)}$ such as: $\boldsymbol{\hat{\varphi}^t = M^{\dagger}_{int}(\delta\varphi^m)\Delta s^t}$. The optimization of the spatial modulation vector with algorithm 1 will be developed in Section 5.4.4. Estimated phases $\boldsymbol{\hat{\varphi}^t}$ are injected in an integrator controller with a gain of 0.5 so that the phase shifters are updated as:

$$\varphi^{ds^t} = \varphi^{ds^{t-1}} - 0.5 \times \hat{\varphi}^t \,, \tag{5.5}$$

with $\boldsymbol{\varphi^{ds^t}}$ the phase value taken by the phase shifters at iteration t and $\boldsymbol{0.5 \times \hat{\varphi}^t}$ the correction phase.

With our experimental setup presented in Figure 5.22, the control loop is implemented in a Labview program corresponding to the 'PC' block. The program is divided into two parts. The role of the first part is to sequence the loop, and the second part is to perform the calculations. The first part of the program was developed by ONERA and updated for this experimental setup. I developed the second part of the program, which corresponds to implementing control algorithms.
The first part of the program reads the photodiode measurements through the 'ADC' and sends them to the second part of the program, which performs calculations. The calculation part updates a vector, which is read by the first part of the program. Updating this vector consists of changing the sign of the spatial modulation vector and adding the computed phase corrections with the integrator control loop. Then, the first part of the program reads the updated vector of the second part of the program and updates the phase shifters commands through the 'DAC'. Figure 5.24 depicts the control loop digital diagram.

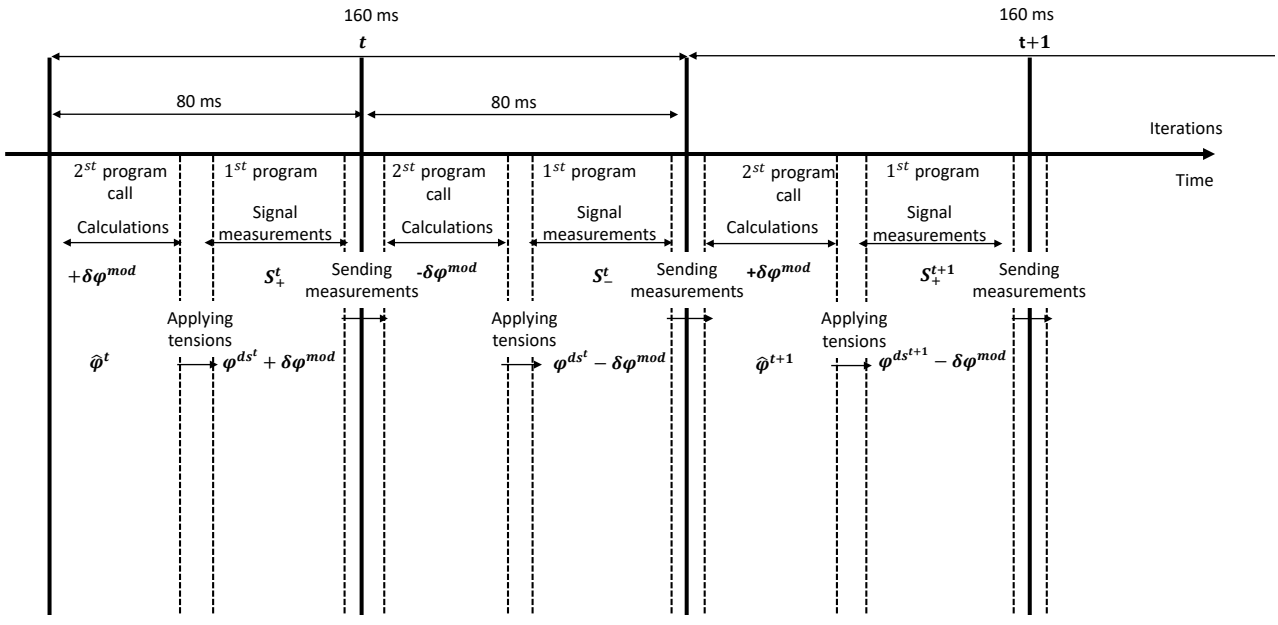

Figure 5.24: Control loop digital timing diagram.

In the Labview control loop program, we do not have access to the precise digital timing of the loop. The exact times it takes the program to communicate with the 'ADC' to acquire the intensity measurements, perform the calculations with the second part of the program, and send the updated phase shifters values to the 'DAC' are unknown. However, it takes 80 ms between two calls of the second program part. Thus, phase corrections are applied every 160 ms in the control loop. Therefore, the control loop runs at 6.25 Hz.

5.4.2 Preliminary characterizations

Before implementing the spatial modulation control method, the laser noise and the thermal drifts at the PIC input are characterized. In the following, the laser power is adjusted so that after the 1 to 8 fibre splitter, the power at one PIC input is 0.6 µW (measured with a Gentec power-meter).

5.4.2.1 Fluctuations of the measured laser signal

At 0.6 µW, the photodiodes with their amplifier are saturated. Thus, to measure the fluctuation of the laser signal, we connect only one output of the fibre splitter to PIC input 5. Then, PIC output 5 is connected to a photodiode. There are two couplers between PIC input 5 and PIC output 5. Thus, the measured laser signal is at least four times weaker at output 5 than it is at input 5 (without considering PIC losses).
A thousand points are measured with a sampling frequency of 10 Hz, corresponding to a time series of 100 s. The measurements are plotted in Figure 5.25. The average measured intensity is $\mu_l = 0.077\ V$ with a standard deviation of $\sigma_l = 0.00138\ V$.

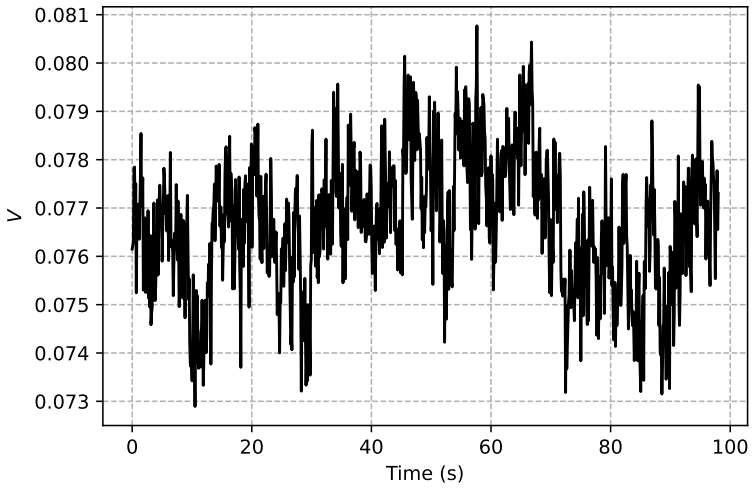

Figure 5.25: Laser signal detected by a photodiode at PIC output 5 with only PIC input 5 connected to one output of the fibre splitter. 1000 points sampled at 10 Hz corresponding to 100 s.

The signal-to-noise ratio, defined as the ratio between μ_l and σ_l is:

$$\begin{aligned} SNR &= \frac{\mu_l}{\sigma_l} \\ &= \frac{0.077}{0.00138} \\ &= 55 \end{aligned} \tag{5.6}$$

The measured signal should correspond to a mix between photodiode read-out and laser noise. The SNR should increase in a closed-loop with the 8 PIC inputs connected to the 8 outputs of the fibre splitter.

The Power Spectral Density (PSD) of the measured signal is plotted in Figure 5.26. It decreases in f^{-1} [V^2] with f in Hz. A PSD in f^{-1} can be associated with photodiode and laser noise. Thus, it is complicated to associate the measured noise with the laser or the photodiode.

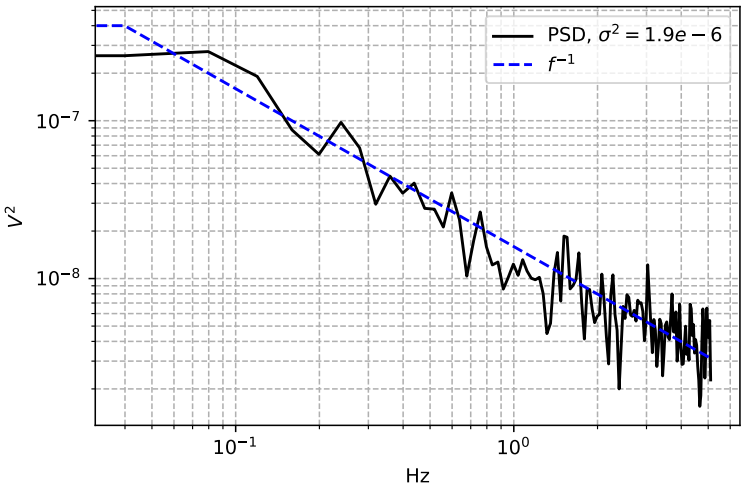

Figure 5.26: PSD of the signal detected by a photodiode in Figure 5.25.

5.4.2.2 SMFs and splitter thermal drift effects

Thermal fluctuations between the PIC input fibres induce phase variations between them resulting in intensity fluctuations at the PIC outputs. To characterize thermal induced fluctuations, the PIC inputs are connected to the 1 to 8 fibre splitter as in the experimental configuration described in Figure 5.22.

Intensity fluctuations at PIC output 5, are measured on 1000 points sampled at 12.5 Hz and plotted on Figure 5.27.

The measured thermal drift, shown in Figure 5.27, is composed of a linearly decreasing low-frequency component to which higher-frequency fluctuations are added. The linearly decreasing low-frequency component is part of a sinusoidal-shaped intensity fluctuation induced by thermal drifts.

We want to analyse the high-frequency components to verify that they correspond to measurement noises and not to thermal drifts. For this, we remove the linearly decreasing low-frequency component by removing the high frequency in the Fourier space corresponding to the observation window truncation. The resulting signal is plotted in Figure 5.28 (a). The variance of this high-frequency signal component is 2.39×10^{-6} V^2. Its PSD is plotted in Figure 5.28 (b). The PSD of the high-frequency signal component and its variance are identical to the measured noise in Figure 5.25. Thus, in the measured intensity fluctuations presented in Figure 5.27, the linearly decreasing low-frequency component is induced by thermal drift, and the high-frequency components correspond to measurement noises.

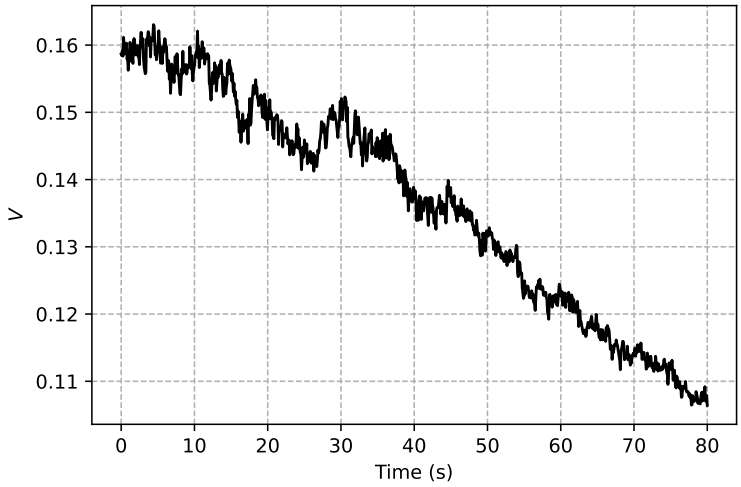

Figure 5.27: Intensity fluctuations at PIC output 5, induced by thermal drift. 1000 points sampled at 12.5 Hz.

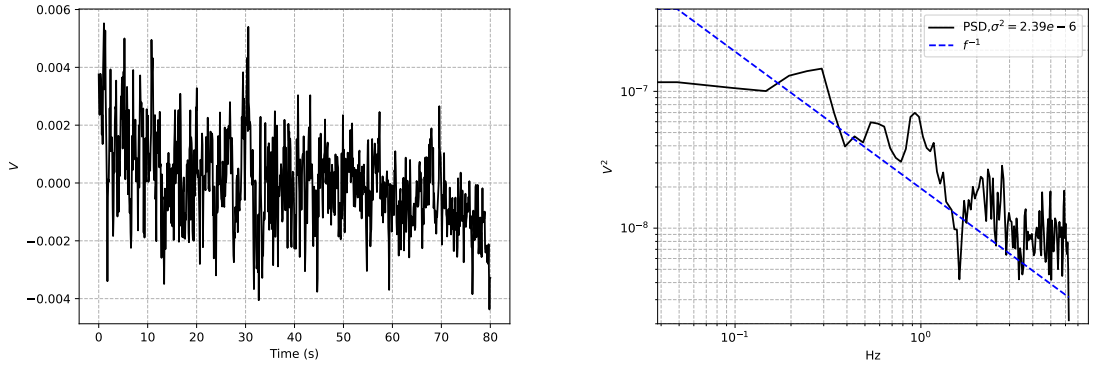

(a) (b)

Figure 5.28: Intensity fluctuations presented in Figure 5.27 without decreasing linear low-frequency component (a). PSD (b).

To implement the spatial modulation control method we need to build an interaction matrix and thus determine the PIC curvature tensor. However, the PIC curvature tensor measurement may be impaired by the thermal drift and its estimation is developed in the following section.

5.4.3 LiNbO3-PIC curvature tensor estimation

To build the interaction matrix we need to measure the PIC curvature tensor. It corresponds to the second-order derivative of each output intensity measurement measured near the minimum with respect to the phase shifters when the PIC inputs are evenly supplied with the laser. This is the case in our experimental setup because the PIC inputs are connected to the 1 to 8 balanced fibre splitter. Our experimental setup can be seen as a calibration bench to measure the PIC curvature tensor.
With the notation used for the LiNbO3-PIC (Figure 5.1), the telecom output (s_0) to be maximized is output 5. The PIC is controlled with the phase shifters to adjust the phase

differences, $(\delta\varphi_j)$, between the PIC inputs, see Figure 5.1. Thus, in the following, we place ourselves in the space of phase differences.
The PIC curvature tensor, $\boldsymbol{T} = (T_{j,k,l})$, is a $7 \times 7 \times 7$ matrix with l corresponding to outputs $\{1, 2, 3, 4, 6, 7, 8\}$, j and k corresponding to the phase differences $(\delta\varphi_j)$, see Figure 5.1, numbered 1 to 7. The telecom output is not used as a measurement and, thus, is not considered in the curvature tensor. With Expression 3.7 and 3.8 to establish the curvature tensor we need to measure the second-order derivatives of the measurement outputs with respect to the phase shifters.
Before measuring the second-order derivatives, the phase shifters must be set to maximize the telecom output s_0 for hypothesis 2 to be true (see Section 3.3.2). For this, an SPGD or classic sequential modulation algorithm can be used.
When s_0 is maximized, a first solution to measure the PIC curvature tensor is to apply phase ramps sequentially on all pairs of phase shifters $\{\delta\varphi_j, \delta\varphi_k\}$, $\forall k, j \in (1, 7)$ to measure the amplitude of the interferometric signals. It is a slow method compared to the high number of measurements to perform. Another solution is to measure directly the second-order derivatives using finite differences such as:

$$\frac{\partial^2 f(x,y)}{\partial x \partial y} \approx \frac{f(x+h, y+h) - f(x-h, y+h) - f(x+h, y-h) + f(x-h, y-h)}{(2h)^2}, \quad (5.7)$$

For both solutions, the main issue comes from the thermal drift between the eight input fibres, making s_0 move from its maximum.

Indeed, during experimental measurements of the PIC curvature tensor, the fluctuations induced by thermal drifts impair the measurements. For several tensor measurements, we obtained different curvature tensors each time. Thus, the experimental measurement of the curvature tensor remains a problem. Potential solutions could be the thermal isolation of the PIC or a faster loop frequency for the thermal drift to be negligible during measurements of the curvature tensor. Establishing the experimental interaction matrix is also problematic in classic AO [141]. One of the solutions proposed in the literature for classic AO is to establish the interaction matrix from a numerical model of the mitigation device [142].

Thus, I decided to estimate the curvature tensor numerically. For this, I use my numerical simulation of the PIC with uniform input and complex amplitudes set to 1 (arbitrary value). It assumes a PIC with perfect symmetry, balanced couplers and without losses. The curvature tensor calculated numerically does not integrate the PIC imperfections. Even so, it represents the LiNbO3-PIC architecture and can be used to build an interaction matrix.
The LiNbO3-PIC curvature tensor calculated with the numerical simulation is depicted in Figure 5.30.

As a reminder, the numbering of inputs, outputs and phase differences are described in figure 5.29.

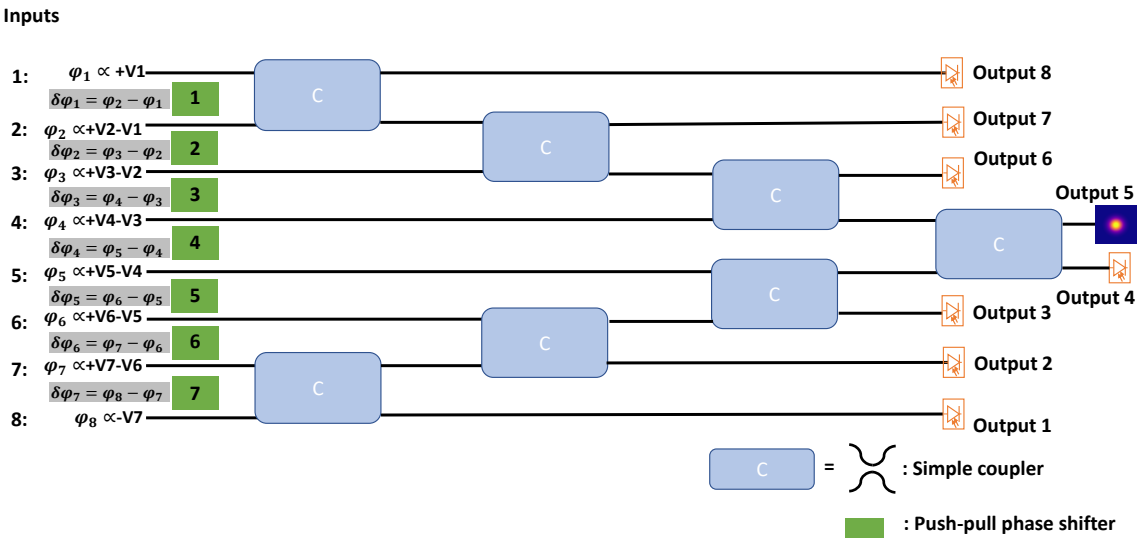

Figure 5.29: Schema of the experimental LiNbO3 PIC with its 8 inputs, 7 phase shifters in push-pull and 7 couplers.

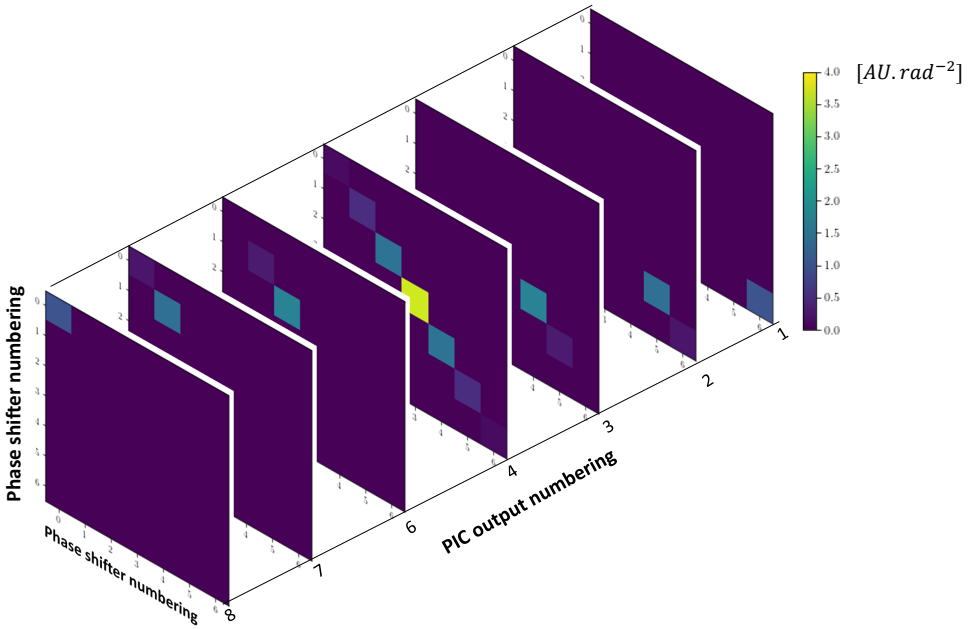

Figure 5.30: Arithmetical PIC curvature tensor measured with the numerical simulation of the PIC architecture in the phase differences space.

Each matrix is associated with a PIC output measurement (numbered 1,2,3,4,6,7,8). Output 5 corresponds to the telecom output, which is not used as a measurement and, thus, is not considered in the curvature tensor. Each matrix corresponds to the second-order derivative of the measurement intensity (to which the matrix refers) with respect to the phase shifters.
The curvature tensor follows the symmetry of the PIC and is mainly hollow. Each matrix is diagonal, so there is no cross-influence between phase shifters. With this perfect PIC model, differential measurements of output 8 are only influenced by $\delta\varphi_1$. Then, differ-

ential measurements of output 7 are influenced by $\delta\varphi_1$ and mainly by $\delta\varphi_2$. Differential measurements of output 6 are influenced by $\delta\varphi_1$, $\delta\varphi_2$ and mainly by $\delta\varphi_3$. Differential measurements of output 4 are influenced by all $\delta\varphi_j$ and mainly by $\delta\varphi_4$, and so on.

Although this curvature tensor does not represent imperfections of the real LiNbO3 PIC, it can be used as an approximation to build interaction matrices with spatial modulation vectors. The following section applies the optimization algorithm 1 to obtain the spatial modulation vector minimizing the noise propagation and build the interaction matrix we will use in closed-loop.

5.4.4 Spatial modulation vector choice

The spatial modulation vector used to build the interaction matrix is the one obtained using algorithm 1, described in Section 3.5.2, allowing minimum noise propagation with the spatial modulation control method. Algorithm 1 is applied with interaction matrices built with the PIC curvature tensor calculated numerically. The initial spatial modulation vector is chosen arbitrarily with a random uniform distribution.

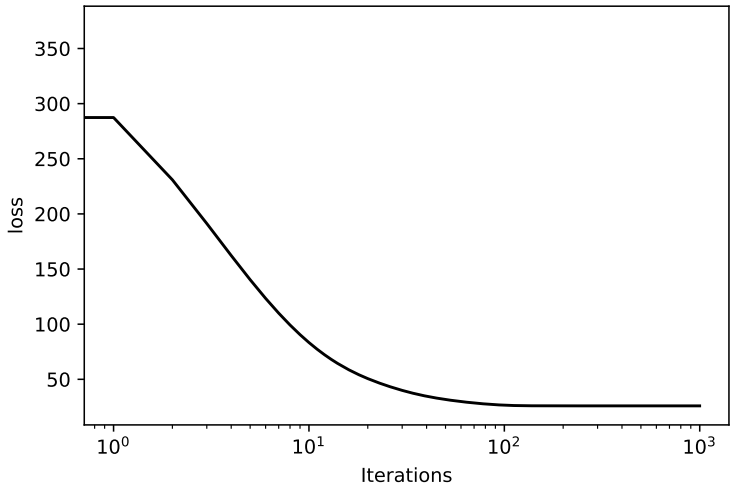

Figure 5.31: Loss function of algorithm 1, with respect to the number of iterations.

Figure 5.31, shows the decreasing loss function of algorithm 1 as a function of the algorithm iterations. The algorithm loop iterates a thousand times. After hundreds of iterations, it converges to the optimized spatial modulation vector depicted in Figure 5.32. The optimization algorithm was run several times with different initial random spatial modulation vectors and always converged to the same solution. Figure 5.32 corresponds to the spatial modulation used to modulate the phase differences and to build the interaction matrix in the experiment. The phase coefficients of the order of a few tenths of a radian allow the modulated signals on the photodiodes to be higher than the noise level while being small enough not to impair the spatial modulation control method hypothesis based on small amplitude modulations.

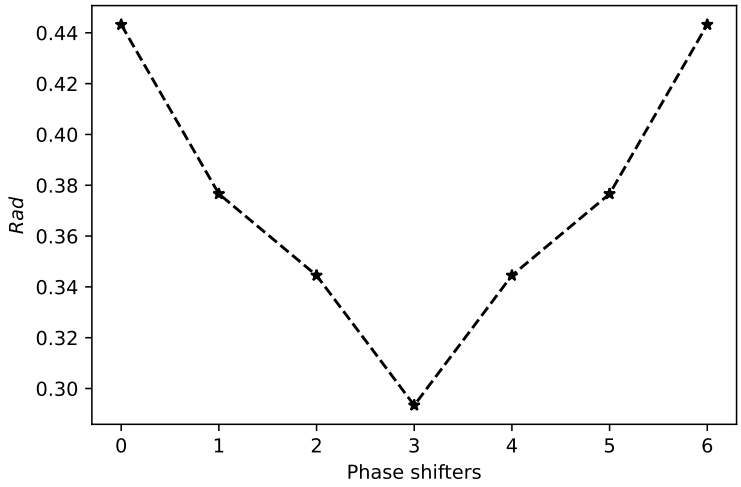

Figure 5.32: Spatial coding modulation vector obtained after thousand iterations of algorithm 1.

The optimized spatial modulation vector follows the PIC symmetry. We can observe that the optimization converges to a solution with higher lateral phase coefficients than the centred one. This should allow us to compensate for centred measurement outputs (seeing more phase shifters than the lateral one) to be less exited.
The interaction matrix is built from the optimized spatial modulation vector and the LiNbO3 PIC curvature tensor. The PIC curvature tensor was calculated with uniform input amplitudes set to 1. To account for the average flux received by the PIC in our experimental setup, the interaction matrix is multiplied by a coefficient of 0.7 $V.rad^{-1}$. This coefficient corresponds to the flux received by photodiode 8 when the signal is maximum. It gives an approximation of the coefficients $a_i a_j$ in the interaction matrix. Figure 5.33, plots the interaction matrix obtained.

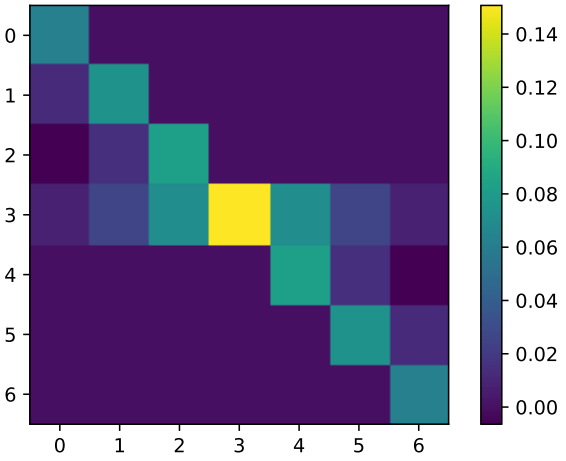

Figure 5.33: Interaction matrix built from the optimized spatial modulation vector and the PIC curvature tensor. Value in V.rad^{-1}.

The interaction matrix gives the linear response of differential output measurements of

the PIC to phase excitation in the phase differences space. The linear regime over which the interaction matrix is valid was studied in Section 3.4.2.

Figure 5.34 plots the measurement outputs (with the simulated PIC) with the phase shifters adjusted so that s_0 is maximum and modulated with the optimized spatial modulation vector. Contrary to the geometrical architecture, with arithmetical architecture, modulating the phase shifters with the optimized spatial modulation vector does not give uniform stimulation of the PIC output intensity measurements.

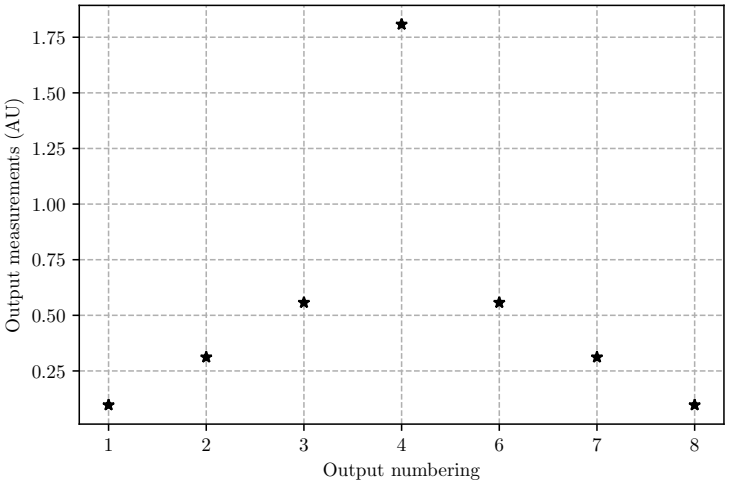

Figure 5.34: PIC measurement outputs from s_0 at its maximum while applying the optimized spatial modulation vector (numerical simulation).

Figure 5.35 plots the singular values of the interaction matrix. Contrary to the geometrical architecture, allowing an interaction matrix with a condition number of 1 as described in Section 3.5.3, the arithmetical architecture gives an interaction matrix with a condition number of 3.3 with the optimized spatial modulation vector. Still, the interaction matrix is well conditioned and the noise propagation will remain low.

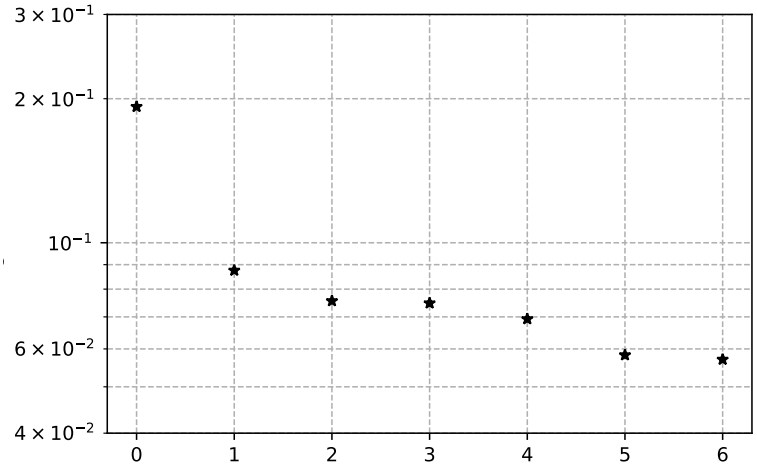

Figure 5.35: Singular values of the interaction matrix with the optimized spatial modulation vector.

5.4.5 Spatial modulation control method closed-loop

Figure 5.36 (a) plots the PIC measurements outputs during a closed-loop time sequence of 80 s. The intensity measurement outputs are minimized and the PIC telecom output s_0 (output 5) is maximized. A zoom on the first 30 points of the closed-loop is plotted in Figure 5.36 (b). The spatial modulation control method closes the loop in 5 iterations of the integrator control loop and is stable.
The measurement outputs do not reach 0 even if the modulus of the complex amplitude at the PIC inputs are uniform. This is due to the specificity of the arithmetic architecture with phase-only correction. Indeed, after the first two couplers (corresponding to outputs 8 and 1), the other couplers receive unbalanced modulus (see Section 1.4.2). However, the first two couplers receive uniform amplitudes. Thus, both outputs 1 and 8 should reach 0. It is the case for output 8 but not for output 1. It means that the coupler associated with output 1 is unbalanced or the injection losses are not identical on inputs 7 and 8.

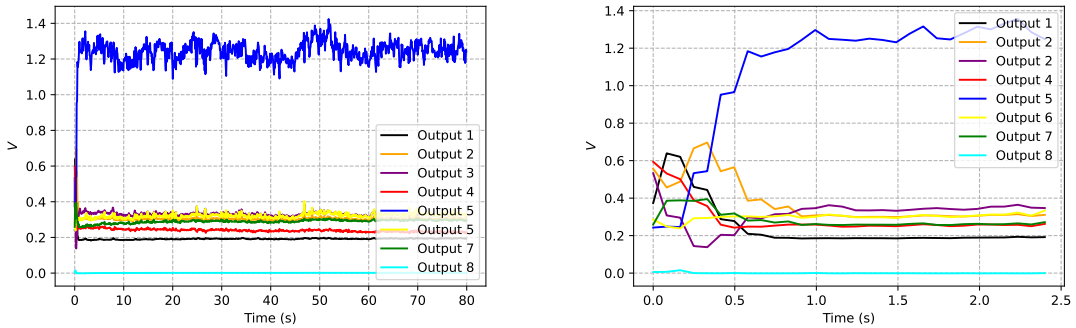

(a) (b)

Figure 5.36: (a): PIC output intensities measured in closed-loop with the spatial modulation control method. 1000 points sampled at 12.5 Hz. (b): zoom on the first 30 points.

To analyze the closed-loop performances with the spatial modulation control method, we discuss below the measurement of the rejection transfer function of the control loop.

5.4.6 Rejection transfer function

This section discusses the closed-loop Rejection Transfer Function (RTF) measurement to analyze the closed-loop performances.

To measure the RTF, a known perturbation obtained from a white noise distribution filtered by f^{-1}, is added to the computed phase correction at 6.25 Hz in equation 5.5. The perturbation PSD is plotted in Figure 5.37.
To measure the resulting perturbations in the photodiode measurements space, the differential measurements on output 5, are saved at 6.25 Hz with the integrator gain set to 0, meaning no corrections are applied (open-loop).
Then, to measure the residual perturbations in closed-loop, the differential measurements, Δs are saved at 6.25 Hz with the integrator gain set to 0.5 (closed-loop).
The RTF is computed as:

$$FTR = \left| \frac{DSP_{closed-loop}}{DSP_{open-loop}} \right| \tag{5.8}$$

However, the perturbations induced by thermal drift are too slow to be considered stationary over one typical measurement period.

If the thermal drift perturbation PSD were unchanged between open-loop measurements and closed-loop measurements, we could estimate the RTF by dividing the PSD of the closed-loop differential measurements by PSD of the open-loop differential measurements. To check the thermal drift PSD variation between two sequences of measurements, the closed-loop measurement is flanked with two open-loop measurements, one before closed-loop and one after closed-loop.

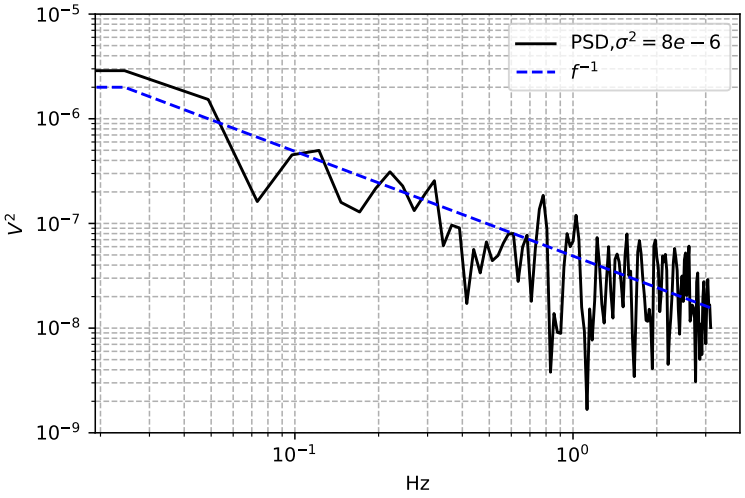

Figure 5.37: PSD of the white noise distribution filtered in f^{-1} used as a perturbation in the voltages space.

The differential measurements, Δs, measured in the open-loop before and after the closed-loop, are plotted respectively in red and orange in Figure 5.38. The black curve corresponds to the PSD of the differential measurements measured in closed-loop.
The PSDs of the differential measurements, measured before and after the closed-loop are not superimposed (red and orange curves). Even if their shape is similar, the differential measurements PSD measured in the open-loop after the closed-loop has more energy than the one measured before the closed-loop. The thermal drift perturbations were stronger after the closed-loop than before. Thus, the PSD of the thermal drifts during closed-loop measurements differs from those measured before and after the closed-loop, impairing the computations of the RTF.

Figure 5.39 compares the RTF computed with the differential measurements measured in the open-loop before the closed-loop (red curve), the RTF computed with the differential measurements measured in the open-loop after the closed-loop (orange curve), and the RTF computed with the PSD from the average differential measurements measured in the open-loop before and after the closed-loop (blue curve).

We observe a cutoff frequency at -3 dB around 1 Hz. However, there are uncertainties due to non-stationary thermal drift. To be more confident about the closed-loop properties obtained with the RTF, the computation time frame rate delays could be estimated by fitting the measured RTF with models. To overcome the thermal drifts issue, the closed-loop properties could be studied by measuring the RTF in the numerical simulation. Another solution could be performing measurements over period long enough to reach stationary thermal drift.

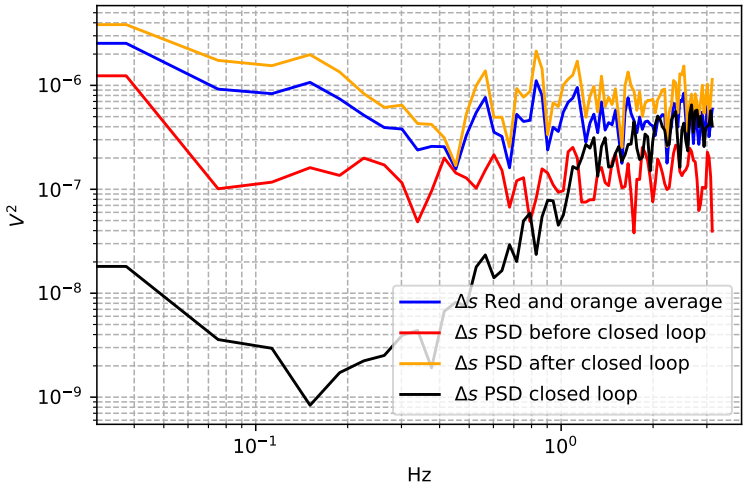

Figure 5.38: The red curve corresponds to the PSD of the differential measurements measured before the closed-loop. The orange curve corresponds to the PSD of the differential measurements measured after the closed-loop. The blue curve corresponds to the average of the PSD of the differential measurements measured after and before closed-loop. The black curve corresponds to the PSD of the differential measurements measured during the closed-loop.

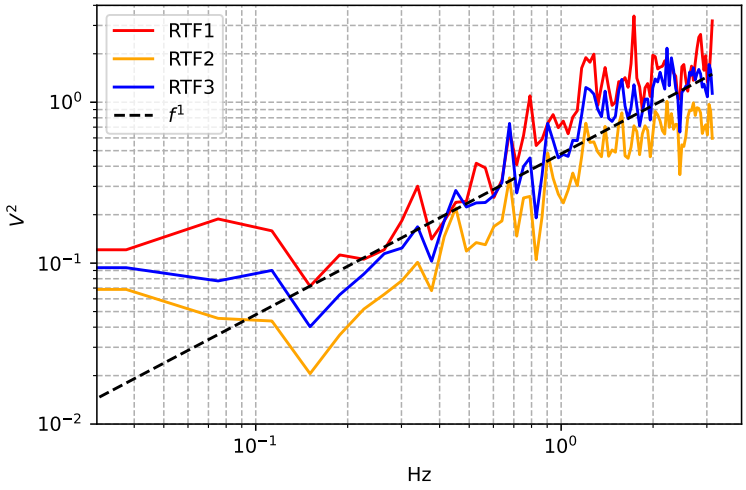

Figure 5.39: RTF computed considering the differential measurements measured: before the closed-loop measurements in red, after the closed-loop measurements in orange, and with average of both in blue.

5.4.7 Illustration of the gain brought by spatial modulation

This section aims to compare the spatial modulation control method performances with classic sequential modulation (temporal modulation) method and with SPGD and ASPGD.

Sequential modulation corresponds to encoding the modulation in time. It is equivalent to frequency modulation, but it is easier to implement in our experimental setup.
Sequential modulation, frequency modulation, SPGD and ASPGD control methods were

presented and developed in Section 1.5.1.2.1. They are quickly resumed below with the description of their parameters for the closed-loop comparison.

5.4.7.1 Sequential modulation (temporal modulation)

In sequential modulation, the modulation is encoded in time, meaning the four PIC stages are modulated and controlled sequentially one by one.
The modulation amplitude is set to 0.2 rad for the modulated signals on the photodiodes to be higher than the noise level. The corrections are applied sequentially on each stage with the integrator controller running at 6.25 Hz. The sequential modulation control method digital timing diagram is depicted in Figure 5.40.
Figure 5.41 depicts the LiNbO3-PIC schema with its four stages. One iteration of the control loop with sequential modulation is the following:

1. Phase differences $\delta\varphi_1$ and $\delta\varphi_7$ are modulated, and measurement outputs 8 and 1 are used to compute the differential measurements. From these measurements, correction phases are applied on phase differences $\delta\varphi_1$ and $\delta\varphi_7$ to correct the first stage of the PIC. It takes 160 ms to correct the first stage.

2. Then, Phase differences $\delta\varphi_2$ and $\delta\varphi_6$ are modulated, and measurement outputs 7 and 2 are used to compute the differential measurements. From these measurements, correction phases are applied on phase differences $\delta\varphi_2$ and $\delta\varphi_6$ to correct the second stage of the PIC. It takes 160 ms to correct the second stage.

3. Then, Phase differences $\delta\varphi_3$ and $\delta\varphi_5$ are modulated, and measurement outputs 6 and 3 are used to compute the differential measurements. From these measurements, correction phases are applied on phase differences $\delta\varphi_3$ and $\delta\varphi_5$ to correct the third stage of the PIC. It takes 160 ms to correct the third stage.

4. Then, Phase difference $\delta\varphi_4$ is modulated, and measurement output 4 is used to compute the differential measurements. From these measurements, correction phases are applied on phase difference $\delta\varphi_4$ to correct the fourth stage of the PIC. It takes 160 ms to correct the fourth stage.

Finally, due to the sequential modulation, the PIC stages are controlled one by one instead of all simultaneously, as with our spatial modulation control method. Thus, it takes four times more time, 640 ms, to control the PIC with sequential modulation than with spatial modulation control method, which takes 160 ms. Thus, the closed-loop runs at only 1.56 Hz with the sequential modulation control method, which is four times less than our spatial modulation control method, which runs at 6.25 Hz.

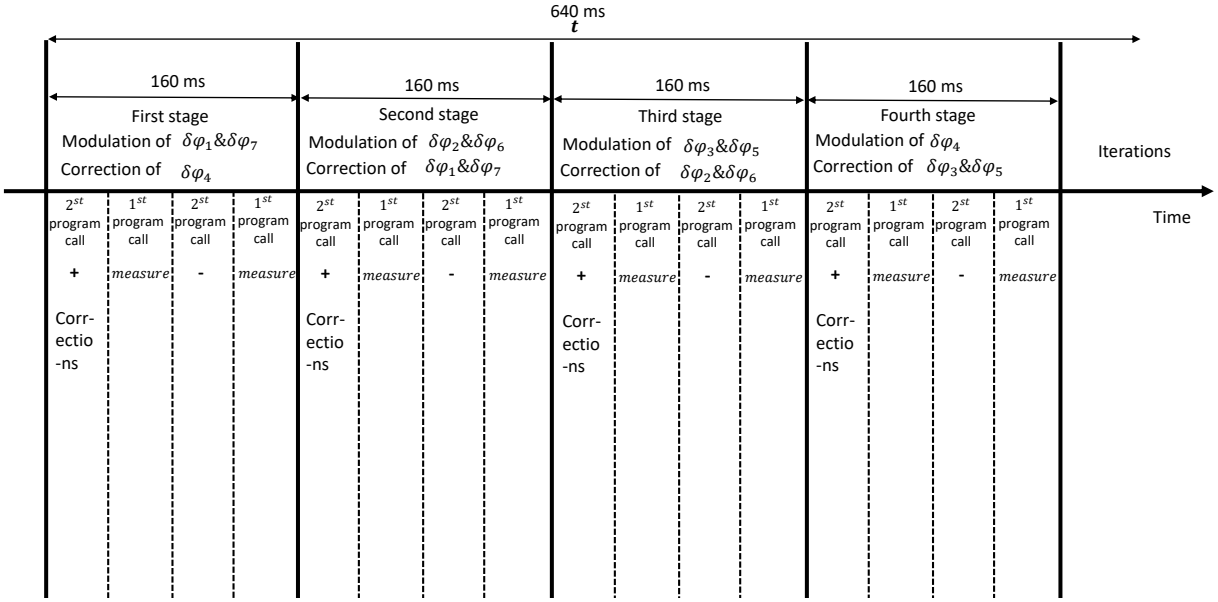

Figure 5.40: Sequential modulation (temporal modulation) digital timing diagram.

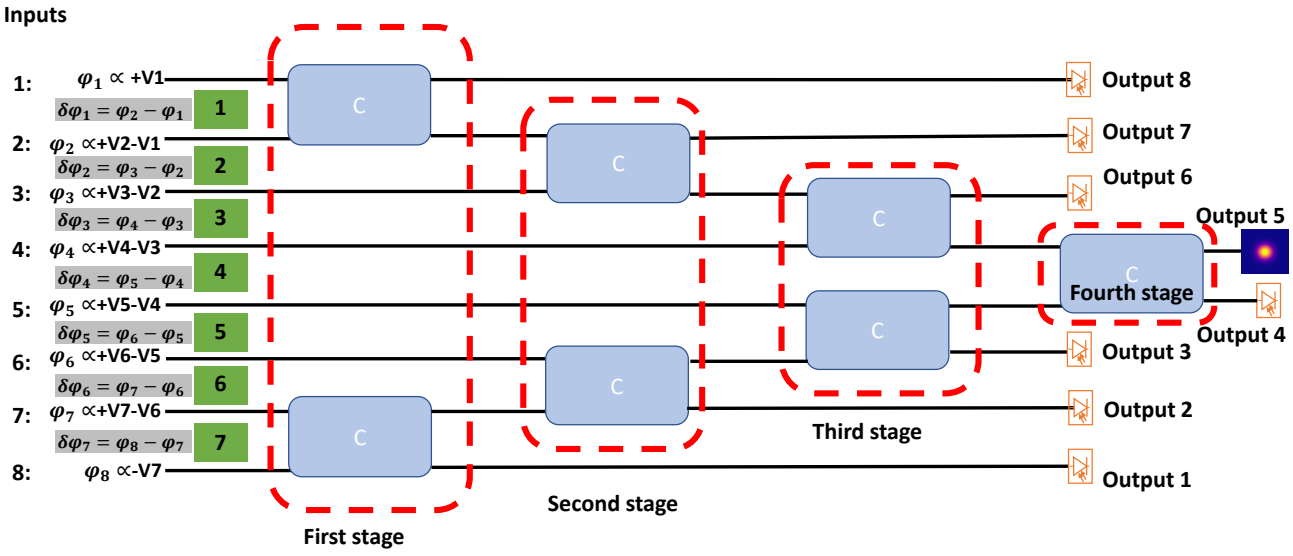

Figure 5.41: LiNbO3-PIC schema with its four stages.

5.4.7.2 SPGD

The SPGD algorithm (see Section 1.5.1.2.1, paragraph MISO stochastic coding) is implemented with a modulation set to 0.2 rad of amplitude. The SPGD gain, g is set to 2. The loop is implemented using output 5 as intensity measurement to be maximized.

The SPGD closed-loop runs at 6.25 Hz as the spatial coding of the modulation control method. Its digital timing diagram is the same as the one of the spatial modulation control method presented in Figure 5.24 but with a stochastic modulation coding instead of a spatial modulation.

5.4.7.3 ASPGD

The ASPGD algorithm is based on the classic SPGD, but it integrates adaptive learning rates based on first and second-order moments of the estimated gradient [133, 60].
The algorithm procedure is the one from [133, 60] and is summarized as follows:

Algorithm 2 ASPGD

initiate:
$\alpha \leftarrow \alpha$
$\beta_1 \leftarrow \beta_1$
$\beta_2 \leftarrow \beta_2$
$\epsilon \leftarrow \epsilon$
$\boldsymbol{m_0} \leftarrow \mathbf{0}$
$\boldsymbol{v_0} \leftarrow \mathbf{0}$
$t \leftarrow 0$
for $t = 0$, Until break **do**
  $t \leftarrow t + 1$
  $\boldsymbol{g_t} \leftarrow \boldsymbol{\nabla s_{0,t}(\varphi_t)}$
  $\boldsymbol{m_t} \leftarrow \beta_1 \boldsymbol{m_{t-1}} + (1 - \beta 1)\boldsymbol{\nabla s_{0,t}(\varphi_t)}$
  $\boldsymbol{v_t} \leftarrow \beta_2 \boldsymbol{v_{t-1}} + (1 - \beta_2)\boldsymbol{\nabla s_{0,t}(\varphi_t)}^2$
  $\boldsymbol{\hat{m}_t} \leftarrow \frac{\boldsymbol{m_t}}{1-\beta_1^t}$
  $\boldsymbol{\hat{v}_t} \leftarrow \frac{\boldsymbol{v_t}}{1-\beta_2^t}$
  $\boldsymbol{\varphi_t} \leftarrow \boldsymbol{\varphi_{t-1}} - \alpha \frac{\boldsymbol{\hat{m}_t}}{\sqrt{\boldsymbol{\hat{v}_t}}+\epsilon}$
end for

with α the gain step size set to 2 as in the SPGD, β_1 the exponential decay rate of first-order moment set to 0.9, β_2 the exponential decay rate of second-order moment set to 0.999 and $\boldsymbol{\nabla s_{0,t}(\varphi_t)}$ output 5 gradient measure as with SPGD algorithm. The parameter ϵ is set to 10^{-8}. The ASPGD parameters, except the gain step size, are the ones given in [133].

5.4.7.4 Closed-loop convergences

Closed-loop output 5 is plotted in Figure 5.42 (a) for the different control methods presented above. The signal variances in closed-loop are 0.0012 V^2 both for spatial and temporal modulation, 0.0035 V^2 for ASPGD and 0.0027 V^2 for SPGD. In closed-loop, spatial and temporal modulation outperform ASPGD and SPGD. These methods could be compared using their RTF, but they could not be measured due to a lack of time.

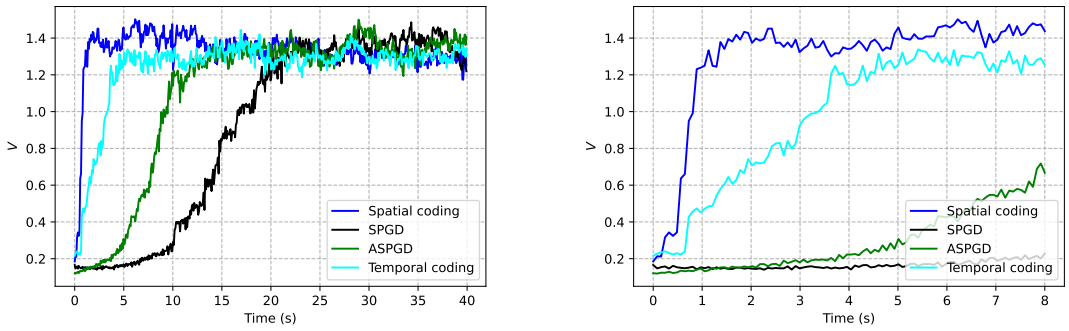

(a) (b)

Figure 5.42: (a): Output number 5 in closed-loop. Spatial modulation control method in blue, SPGD in black, ASPGD in green and sequential modulation in cyan. (b): Zoom on the first 16 s.

Figure 5.42 (b) presents a zoom on the first 16 s.
The ASPGD converges faster than the SPGD due to its adaptive step-size gain. Spatial and temporal modulation outperforms the two stochastic methods.
The temporal modulation closed-loop runs at a frequency four times slower than the spatial modulation method (due to stage-by-stage sequential modulation). This difference can be seen when closing the loop. The rising time at 90% is 0.8 s for spatial modulation and 3.5 s for temporal modulation. Thus, the temporal modulation takes approximately four times longer to converge than the spatial modulation.

However, comparing the performances of these four methods has some limitations.
First, as we have seen for the RTF computation, the thermal drift conditions differ between the different closed-loops. Thus, comparing different control algorithms on closed-loop that are not under the same perturbation conditions is limited.
Then, for the SPGD and ASPGD methods, one closed-loop realization does not represent the method behaviour as their optimization directions are stochastic. A realist comparison should be performed on hundreds of closed-loop realizations.
Finally, the SPGD and ASPGD loop parameters are difficult to adjust. The parameters used here may not be optimal, and other parameters may present much better performances.

5.4.8 LiNbO3-PIC closed-loop implementation conclusion

In conclusion, a closed-loop experiment has been performed on the LiNbO3-PIC. The measurement of the curvature tensor was not possible due to the slow loop frequency and non-stationary thermal drift. The loop was closed with a spatial modulation vector optimized from a curvature tensor measured with a numerical model of a perfect LiNbO3-PIC architecture allowing for a well-conditioned interaction matrix. A first temporal characterization of the loop was performed by measuring RTF. This characterization is not perfect due to non-stationary perturbation and difficulties in estimating the precise temporal timing in the loop. Finally, the gain brought by the spatial modulation control method has been illustrated by comparing its performances to sequential modulation and stochastic modulation. The spatial modulation control method outperformed the other methods and converges four times faster than the sequential modulation control method (due to the presence of four stages in the PIC). Finally, limitations in comparison between those methods have been discussed due to non-stationary perturbations and non-optimized setting parameters.

5.5 Conclusion

The aim of this chapter was to assess the difficulties of implementing the spatial modulation control method on a real PIC with all its imperfections. For this, two PICs were at my disposal, a 32-input SOI-PIC for phase and amplitude correction and a 8 inputs LiNbO3-PIC. Both were characterized. Both PICs present too many losses to be suitable for atmospheric effects mitigation. Possible improvements to reduce the SOI-PIC losses were discussed, and indications for future low losses PIC suitable for atmospheric effects mitigation were given. The SOI-PIC having been received too late in the thesis, the implementation of the spatial modulation control method was realized on the LiNbO3-PIC. This enabled us to highlight difficulties in measuring the PIC curvature tensor. Finally, the spatial modulation control method was implemented using a curvature tensor measured with a perfect numerical model of the PIC. The spatial modulation control method used with the optimized spatial modulation vector allows the closing of the loop and is stable. Its performances were compared to other control methods based on modulations. The spatial modulation control method allows the loop to be closed 4 times faster (corresponding to the number of stages in the PIC) than the temporal modulation control method.

General conclusion and perspectives

General conclusion

This manuscript focuses on the analysis of the ultimate performances of an integrated-AO to mitigate atmospheric turbulence effects, based on the development of an original control method for photonic integrated circuit architecture dedicated to coherent combination. The application framework I focus on in this manuscript is for LEO satellite-to-ground downlink.

As developed in Chapter 1, the two main constraints limiting integrated-AO performances are the PIC internal losses and classic sensorless modulation-based control method limited bandwidth.

To reduce the PIC internal losses, based on a careful analysis of the statistical properties of the fields to be combined, I have proposed a phase-only correction PIC architecture that allows the reduction of internal losses in dB by a factor of two. Indeed, in Chapter 2, I studied the statistics of the complex amplitudes at the input of the PIC with regard to the spatial demultiplexer choice and atmospheric turbulence strength. Four cases were derived: homogeneous and heterogeneous intensity distributions at the PIC input with both Rayleigh or Log-normal distributions. I showed that in most cases, the average loss induced by phase-only correction PIC (compared to phase and amplitude correction) is equal to or lower than 1 dB, thus highlighting the interest in phase-only correction PIC. In Chapter 5, using the characterization of a 32-input SOI PIC, I developed and discussed the sizing of a realistic PIC to reach optimal performances with phase-only correction.

To determine the PIC required correction frequency, in Chapter 2, I developed an analytical expression of the temporal decorrelation of the complex amplitudes at the PIC input. The expression I obtained, function of the turbulence strength and the spatial demultiplexer projection mode, may be used to quantify the temporal error in the error budget of the control loop. Using this analytical expression applied in the case of the LEO satellite downlink presented in Appendix B, a correction frequency of 10 kHz is required for the temporal error to be negligible.

To overcome the bandwidth constraint of classic sensorless control methods, in Chapter 3, I implemented an original control method (on a phase-only correction PIC) using a modulation spatial coding based on Rinaldi's sensorless method [7]. It allows the use of the PIC as a wavefront sensor through a reconstruction matrix to estimate residual phases in one spatial modulation period. The reconstruction matrix is obtained by a least square inversion of a direct model assuming additive Gaussian decorrelated noise. An upper bound of a norm of 1 rad for the spatial modulation vector was determined to stay in the linear range of the direct model. This approach possesses a poor linearity range but should behave as a hill-climbing algorithm outside its linear regime. I then analyzed the noise propagation of this method. To minimize the noise propagation, the amplitude of the spatial modulation must be set at its maximum value while remaining in the linear

regime of the direct model. At constant norm, I develop a method to determine the spatial coding of the modulation, allowing the minimization of additive Gaussian decorrelated and uniform noise. With the chosen architecture, I showed that the optimized spatial coding allows to reach the fundamental limits of photon noise propagation for WFS.

I developed the elements for the sizing of an integrated-AO with analytical expressions of the different error terms in the error budget. In Chapter 4, I proposed a general method for the sizing of an integrated-AO with the evaluation of the different error terms impacting the power coupled in the telecom output. However, the direct model is based on three hypotheses: the turbulence is frozen during a spatial modulation period, the phase shifters are set so that s_0 is near its maximum, and the modulus of the complex amplitudes at the PIC inputs are supposed to be constant and uniform. Such hypotheses are not satisfied in realistic atmospheric conditions. The impacts of the limited linear range of the direct model, the modulation noise and fluctuations of the complex amplitude are difficult to evaluate analytically. Thus, I developed an end-to-end simulation to evaluate close-loop performances of an integrated-AO with a perfect lossless PIC using the spatial modulation control method in realistic atmospheric turbulence conditions. The spatial modulation control method allows to close the loop as a hill-climbing algorithm, confirming the discussion about the method's behaviour out of the linearity range. The usefulness of the optimized spatial coding is demonstrated by closed-loop comparison with non-optimized spatial coding. The main limitation in the close-loop performances with the spatial modulation control method is induced by fluctuations of the modulus of the complex amplitudes at the input of the PIC. To overcome this issue, I proposed a modification of the PIC architecture to add photometric measurements to measure such fluctuations at the PIC inputs. With photometric measurements, I showed that the spatial modulation control method reaches the same performance as the theoretical phase-only correction expression.

After analyzing the performances of the spatial modulation control method in realistic atmospheric turbulence conditions but with a perfect lossless PIC and validating the gain brought by this original control method, I studied its implementation on an experimental 8-input PIC in LiNbO3 in Chapter 5. I highlighted the difficulties of measuring the PIC curvature tensor in the presence of thermal drift between the PIC input fibres. To overcome this issue, I use the curvature tensor of a numerical perfect model of the PIC to build the interaction matrix. I showed that the spatial modulation control method used with the optimized spatial modulation vector allows the closing of the loop and is stable on an experimental PIC. Finally, the spatial modulation control method allows to close the loop 4 times faster than the sequential modulation, which is the number of stages to control in the PIC.

Short term perspectives

I implemented and validated the spatial modulation control method only in the specific case of PIC as integrated-DM. However, I have established the calculus of the interaction matrix with the formalism of the SMID. Thus, the spatial modulation control method could be applied to all types of systems the SMID formalism can describe. A PIC is a mechanically robust and stable SMID, and it appears to be a gentle case for the spatial modulation control method. A study should be performed to analyze the performance of the spatial modulation control method compared to other kinds of SMID. Rinaldi's work to apply it on a DM [7] is a first step to the generalization of the spatial modulation control method in the general case of SMID.

In the case of MZI-based PIC, the internal phase shifters of MZI cannot be moved to

the PIC input, and the formalism I developed for SMID and used to establish the interaction matrix is not applicable in this case. However, I discussed the spatial modulation control method application to MZI-based PIC for phase and amplitude correction with a Taylor expansion to establish the interaction matrix. Thus, a study on the potential application of the spatial modulation control method to MZI-based PIC needs to be performed. Intuitively, one of the significant difficulties for its implementation to MZI-based PIC is that the curvature tensor of the PIC will change with the MZI internal phase shifters setting. However, as we have seen in the case of phase-only correction, the PIC curvature tensor depends on the modulus of the complex amplitudes at the PIC input, implying modifications of the PIC curvature tensor with the modulus fluctuations. Still, in such a case I demonstrated that the spatial modulation control method allows to close the loop and is stable. In closed-loop the evolution of the PIC input modulus will imply the evolution of the setting of the internal phase shifters of the PIC. Thus, even with the PIC curvature tensor evolving with the MZI internal phase shifters setting, the spatial modulation control method should be applicable in the case of MZI-based PIC with the use of an interaction matrix for phase correction (external MZI phase shifters control) and another one for amplitude correction (internal MZI phase shifters control). A complete analysis should be performed to validate this assumption.

To establish the reconstruction matrix by inversion of the interaction matrix of the direct model, I used a least square estimation supposing additive Gaussian decorrelated and uniform noise, which is a strong hypothesis. Thus, more robust estimators, such as maximum a posteriori could be investigated as well as predictive control.

The use of deep learning control methods should allow to learn the non-linearities between the intensity measurements and the perturbation phases. A comparison between the performances obtained with the spatial modulation control method and the one obtained with deep learning methods must be performed to evaluate the potential gain brought by deep learning methods.

Medium and long term perspectives

Concerning the ultimate performances of integrated-AO, I studied separately closed-loop performances in realistic atmospheric turbulence conditions (numerical experiment) and the spatial modulation control method implementation on experimental PIC. Thus, a RTC must be developed to validate experimentally the implementation and the control of an integrated-AO with the spatial modulation control method with different realistic atmospheric turbulence conditions with an in-lab demonstration.

To reach integrated-AO ultimate performances, it is necessary to reduce its losses. For this, size mode adaptation between the spatial demultiplexer and the PIC must be investigated, as well as the development of PIC architectures with reduced internal losses, as I proposed in this thesis.

Integrated-AO is a promising solution for applications to LEO satellite downlinks but also for horizontal links especially in strong perturbation conditions with intensity fluctuations. The gain brought by integrated-AO for horizontal links must be compared to the gain brought by passive methods.

Finally, an integrated-AO with reduced internal losses must be realized to perform

on-sky experimental validation of this mitigation method.

APPENDIX A

MZI coherent combination

As shown in Figure A.1, setting the external phase-shifter to obtain a $\frac{\pi}{2}$ phase difference between the two input complex amplitude (step 2) allows, after the first coupler interference, to obtain two complex amplitude with equal modulus (step 3). Thus, the internal phase-shifter can be set to obtain one output with an intensity equal to the MZI inputs intensity and the other one with zeros (steps 4 and 5).

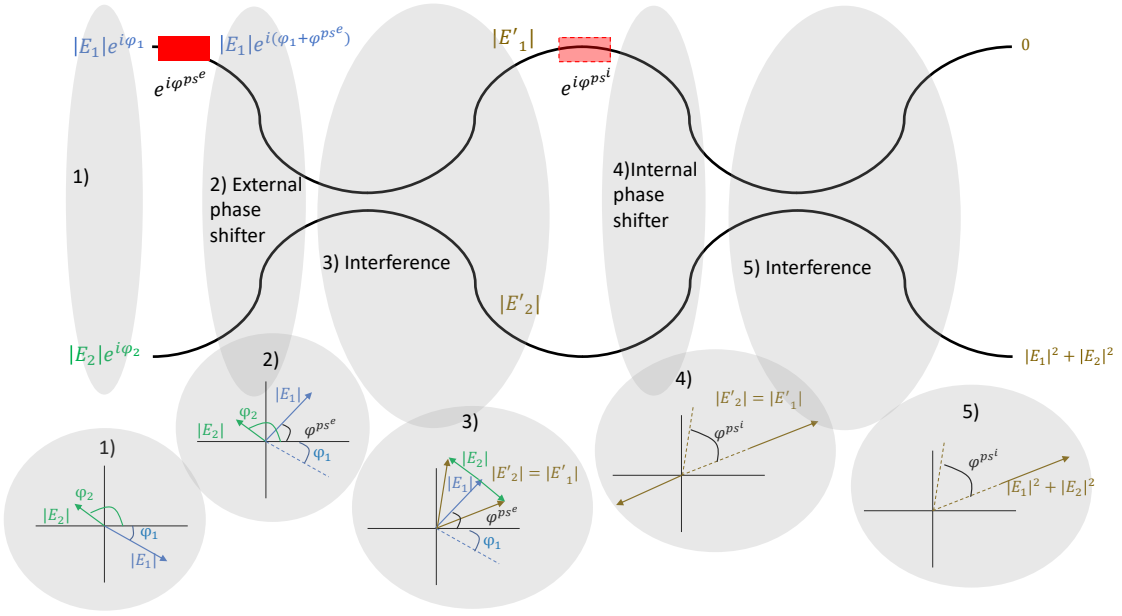

Figure A.1: MZI for phase and amplitude correction.

APPENDIX B

LEO satellite downlink scenario

The parameters of the LEO satellite downlink scenario used as an application case in this thesis are described below:

- Satellite altitude, $h_{sat} = 550$ km,
- satellite elevation (above the horizon), $\theta_{sat} = 30°$,
- satellite distance from OGS, $D_{sat} = 1100\ km$,
- satellite velocity, $V_{sat} = 7.5\ km.s^{-1}$,
- OGS telescope diameter, $D_{pup} = 50\ cm$,
- Bufton wind profile, $v_{ground} = 10\ m.s^{-1}$, $v_T = 20\ m.s^{-1}$,
- Hufnagel-Valley C_n^2 profile with tropopause altitude layer at $h_T = 12450\ m$ with scale layer, $L_T = 4800\ m$,
- Fried parameter: $r_0 = 10\ cm$ at $1.5\ \mu m$,
- Rytov variance: $\sigma_\chi^2 = 0.085$ at $1.5\ \mu m$,
- $\frac{D_{pup}}{r_0} = 5$.

The scenario is defined by the parameters characterizing the geometry of the beam between the satellite and the ground station, the optical propagation through atmospheric turbulence, and the diameter of the receiving telescope. We, choose the case of a satellite moving in the plane perpendicular to the plane of incidence of the beam on the telescope, and we consider the case where the elevation of the receiving satellite-telescope axis is $\theta_{sat} = 30°$. The C_n^2 profile is a Hufnagel-Valley profile representative of an average daytime site, which leads to propagation conditions with a Fried parameter $r_0 = 0.1\ m$, and a Rytov variance $\sigma_\chi^2 = 0,085$. The wind profile is a Bufton profile. Considering the satellite apparent trajectory, the natural wind is negligible compared to the apparent wind except for the first few hundred meters before the ground station: the mean wind velocity is $v_{moy} = 125\ m.s^{-1}$.
This scenario makes it possible to reveal field disturbances that are sufficiently complex to test the performance of a control loop while having the advantage of moderate complexity in terms of numerical modelling.

APPENDIX C

A Silicon Photonic 32-Input Coherent Combiner for Turbulence Mitigation in Free Space Optics Links

A Silicon Photonic 32-Input Coherent Combiner for Turbulence Mitigation in Free Space Optics Links

Lorenzo De Marinis[1,*], Peter Seigo Kincaid[1], Yann Lucas[2], Lea Krafft[2], Vincent Michau[2], Matteo Cherchi[3,+], Mikko Karppinen[3], and Giampiero Contestabile[1]

[1]Scuola Superiore Sant'Anna, Pisa, 56124, Italy
[2]DOTA, ONERA, Université de Paris-Saclay 92320, Châtillon, France
[3]VTT Technical Research Centre of Finland, Espoo 02044, Finland
[*]lorenzo.demarinis@santannapisa.it
[+]Now with Xanadu Quantum Technologies Inc., Toronto, Canada

ABSTRACT

A photonic integrated circuit (PIC) for the coherent combination of 32 input optical signals into a single output fiber is reported. The PIC was fabricated using a low-loss thick silicon-on-insulator (SOI) process and packaged with 32 input and 1 output fibers. The basic building block is a 2x2 Mach-Zehnder interferometer (MZI) with an external (to the MZI branches) and an internal thermal phase shifter, and a bandwidth in excess of 80 kHz. The PIC monolithically integrates 31 MZIs and 31 germanium photodetectors, and is suitable in principle for turbulence mitigation in LEO-ground and horizontal free space optics links. Improvements to the device for the coherent combination of 64 inputs and for the reduction of insertion losses are also discussed.

Introduction

Free space optical communications (FSO) have been the subject of active development for several decades. FSO links offer the potential for data rates currently inaccessible with radio frequencies, with experimental systems able to sustain terabits/s data rates over km distances[1]. Generally speaking, in all situations where laying optical fibers is either too expensive or not feasible, FSO can provide a viable solution[2], and is expected to play a crucial role as one of the technologies enabling 5G/6G[3] and satellite communications[4], including quantum links[5]. Furthermore, the short wavelength allows beams of high directivity which therefore limits possible interference problems and reduces the power required for transmission. The choice of the fiber optics C-band and the coupling of the free space beam to a single mode fiber (SMF) allow the use of existing fiber optic communication technologies and systems, thereby limiting deployment costs. However, the propagation of the beam through turbulent atmosphere is detrimental to the SMF coupling efficiency. Adaptive optics is envisaged for turbulence mitigation in future optical ground stations dedicated to ground-satellite links (GEO or LEO) to maximize the detected signal allowing throughputs of 10 to 100 Gbps per channel[6–9], some demonstrations of horizontal optical links have also been carried out[10,11], with a transmission capacity exceeding 1 Tbps[12].

Classic adaptive optics methods for turbulence mitigation require a deformable mirror and a wavefront sensor, with relatively large footprint. Furthermore, wavefront sensors are well suited to astronomical observation and to optical links close to the zenith, but are sensitive to the strong scintillation encountered when the beams propagate in the lower atmosphere over distances greater than a few kilometers[13]. An alternative solution based on modal decomposition and subsequent guided wave coherent combination was proposed for SMF coupling[14]; Fig 1 illustrates the principle in the case of a satellite to ground FSO link with beam propagation through a turbulent atmosphere. Here, the distorted field is first decomposed into N guided waves via a spatial demultiplexer, which are then added coherently within a photonic circuit whose phase shifters correct the fluctuations in the complex amplitudes of the guided waves in real time. In this scheme, the phase shifters are controlled in a closed-loop, with the correction to be applied estimated from the output signals by adding a rapid, low amplitude modulation to the phase shifter control signals[15–17]. Finally, the constructively recombined output of the photonic circuit is coupled to an output SMF. Performing the coherent combination with bulk fiber components is impractical because of large size, the requirement of matched optical paths and for mechanical stability issues. For these reasons, the use of Photonic Integrated Circuits (PIC) was proposed[14], which offer small footprint, mechanical and thermal stability, and low mismatch between optical paths[18–20]. This solution allows to overcome both the disadvantages of the large footprint and the susceptibility to strong scintillation associated with classic adaptive optics assemblies. An example of a photonic circuit architecture for the coherent addition of guided waves is presented in Fig. 2.

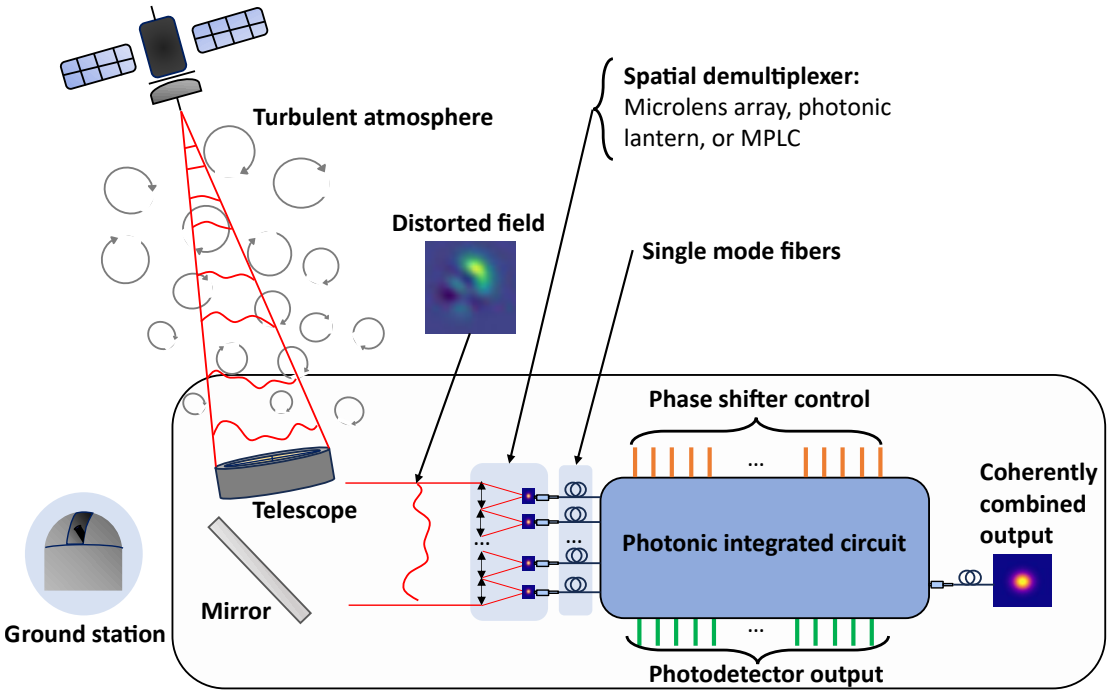

Figure 1. Satellite-to-ground FSO communication with distorted fields, modal decomposition followed by PIC coherent combination after FSO beam reception by the ground station telescope.

The practical specifications of coherent combiners may be deduced as a first approximation from that of the equivalent classic adaptive optics system. The performance depends firstly on the number of spatial modes, i.e., the number of actuators in the deformable mirror or the number of guided waves in the spatial multiplexer. The closed-loop correction frequency also plays an important role for both devices; when using a PIC, aside from the correction signal, an additional low amplitude tone must be applied to the phase shifters, with its relative frequency as high as possible to avoid any interference with the control signal. According to N. Védrenne[21], a few dozen actuators would be required for AO dedicated to LEO-ground links, with the number increasing to 100-200 for GEO-ground links; a correction frequency of between 2 and 10 kHz would be required for LEO-ground links due to the movement of the satellite, this is 10 times lower for GEO-ground links. Finally, the main interest of the correction lies in the increase in power of the collected signal, hence the losses in the component must be minimized. For comparison, the typical optical losses of classic adaptive optics systems are of the order of 5 dB, due to the presence of a few dozen optical surfaces in the beam path and SMF coupling.

In the literature, previous coherent combination schemes were demonstrated with up to 16 inputs on a single PIC fabricated with SOI[18–20], and up to 32 effective inputs by combining four 8 input PICs[22]. Recently, the fabrication of a 45 input PIC for turbulence mitigation was reported, but without integrating the photodetectors[23]. In this paper, we report the design, fabrication, and characterization of an integrated coherent combiner suitable for 32 inputs/modes. As the scalability and footprint of the device is governed by losses and integration density, we fabricated the PIC using the low-loss silicon thick SOI platform available at VTT Finland[24]. The 32 input configuration with phase shifter bandwidth in excess of 50 kHz, is suitable in principle for correcting the effects of atmospheric turbulence on any LEO-ground link. Indeed, these parameters are close to those of the AOptix R3.1 classic adaptive optics element used as part of the ORCA (Optical RF Communications Adjunct)[25]. The fabricated chip demonstrated a bandwidth larger than 80 kHz, with phase shifters able to provide more than 6π of phase shift correction. The integrated germanium photodetectors exhibited a responsivity of 0.8 A/W, a dark current < 2 nA, and a bandwidth > 2 GHz with zero bias applied. The remainder of the paper is organized as follows. First, we discuss the features of photonic integration platforms and outline their shortcomings for the development of coherent combiners. We then report the design, fabrication and packaging of the coherent combiner. In the device characterization section, we report the main characterization measurements of the PIC and its building blocks: phase shifters, Mach-Zehnder interferometers, photodetectors, and I/O losses. This is followed by a discussion section on our findings and prospected devices based on the same technology, exploring their applications in realistic FSO link. Finally, we summarise the work in the conclusions.

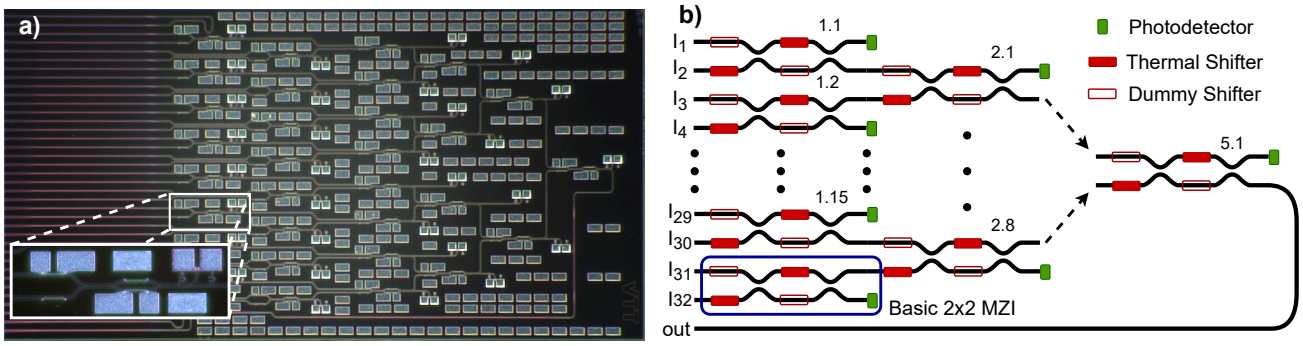

Figure 2. a) Photo of the as-fabricated Thick SOI chip with a magnification of the basic MZI; b) scheme of the coherent combiner architecture

Coherent Combiner for Free Space Optics

There are several photonic integration platforms suitable for the manufacturing of coherent combiners. Each one with its own characteristics, strengths, and limitations. However, the need of scaling the structure towards a high number of inputs poses a stringent requirement in terms of compactness: the larger the number of inputs, the larger the number of combining elements (MZIs) to be integrated and thus the associated device footprint. This renders a fabrication with the Indium Phosphide technology unpractical, due to the large bending radius and typical attainable yields[26]. The emerging lithium niobate on insulator technology (LNOI) platform provides very low losses and medium-short bending radius ($\leq$100 µm). However, its lack of maturity poses limits to practical usage: just one company in the world currently offers wafer-scale fabrication, furthermore LNOI phase shifters notoriously suffer from DC drifts, it lacks integrated PDs, and the optical I/O with fiber arrays has low yield and high losses. The Silicon Nitride platform offers a more robust process, with low coupling and propagation losses, and the possibility to hybridly integrate photodetectors. However, the scaling of structures in silicon nitride is hindered by the high bending radius of the waveguides, and the large power consumption (and related thermal crosstalk) of the thermal phase controllers.

Conversely, silicon photonics meets all the requirements as it offers compact structures (µm bends) and integrated detectors, while providing high yields with a robust process which inherited the maturity of the CMOS technology[27]. Among the various silicon platforms, the thick SOI process available at VTT was ideal for fabricating the coherent combiner demonstrator. This fabrication platform is based on 3 µm thick waveguides where the optical field modes are almost completely confined in the silicon core. This gives small propagation losses ($\sim$0.1 dB/cm in the C-band), low polarization dependency, and dense integration thanks to Euler bends that can provide an effective banding radius as small as 1.3 µm[24]. Optical I/O is facilitated by the horizontal taperings of waveguides on chip, from 3 µm to 12 µm. The tapers work as spot-size converters to improve the coupling to SMFs. In addition, VTT offers an SOI optical waveguide interposer chip as a vertical spot-size converter to further increase the coupling efficiency between fiber arrays and the SOI PIC[24]. Using the optical interposer, approximately 1.5-2 dB I/O coupling losses are possible, depending on the detailed structure of the I/O facet. Moreover, the available integrated germanium photodiodes have a low dark current and a responsivity of $\approx$ 0.8 A/W.

When scaling structures that rely on thermo-optic phase shifters, assuring a high thermal isolation is of paramount importance for correct functionality. However, high integration density with close structures often leads to poor thermal isolation with an evident footprint-isolation trade-off to be made. Nonetheless, the VTT process tackles this issue: the thermal phase shifters are made of doped silicon implanted close to the optical waveguides for high efficiency, with isolation trenches that prevent thermal cross-talk between close structures. The heaters have a power consumption associated with a π shift in phase (P_π) lower than 40 mW, and a bandwidth of several tens of kHz, making them suitable for the turbulence mitigation application. Moreover, the heaters allow for several π of phase shift (on the order of 5-6π before failure), a feature needed to reduce the fading induced by an abrupt 2π phase shift from the adaptive optics correction algorithm, which occurs when the upper limit in phase shift is reached.

Leveraging the features of the thick-SOI process, we were able to design an integrated coherent combiner with 32-inputs. The combination is performed with a binary tree architecture, where 2×2 MZIs are used to coherently combine lightwave pairs[28]. Figure 2a reports a photo of the naked fabricated PIC, with the enclosed close up displaying the basic 2×2 MZI element. The MZI structure consists of two inputs, one of which has a thermal phase shifter (the "external" shifter), a 2×2 3-dB multimode interferometer (MMI) which splits evenly to two internal branches, one with another phase shifter (the "internal"

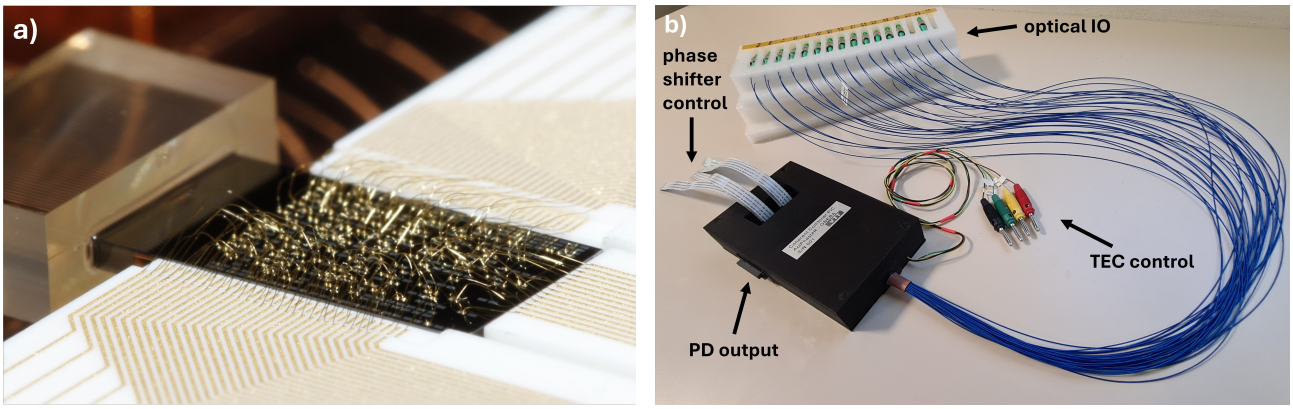

Figure 3. a) Photo of the PIC undergoing packaging after wire bonding to an electrical interposer and fixing the optical IO to a fiber array; b) Finished package with optical IO coupled to SMF fibers, thermo-electric control (coloured cables) and DC IO ports for thermal shifter control and photodiode output.

shifter). Another MMI follows with one output coupled to a monitor photodiode (PD), and the other which feeds into the next MZI or, in the case of the last MZI, to the output port. The external phase shifter sets the correct relative phase between the two incoming lightwaves such that the power in both internal branches is equal, the internal phase shifter then directs all optical power to the correct exit. The power at the exit of each MZI may be optimised using a routine which minimises the power at the monitor PDs by opportune control of the two phase shifters. The MMI should be well balanced for a MZI to be able to combine channels with different phase and amplitude. Futhermore, optical cross talk needs to be minimal for the modulation based control algorithm not to fail. Figure 2b shows the equivalent schematic of the whole structure, highlighting the basic 2×2 MZIs with a blue rectangle; to ensure maximally balanced paths within the MZIs, some non-connected, or "dummy", phase shifters were placed. The MZIs are numbered in an ascending fashion following columns and rows, e.g., MZI 1.15 is the 15^{th} from the top of the PIC in the first column and MZI 3.1 is the topmost of the third column. 32 polarization maintaining single mode fibers (SMFs) are edge-coupled to the side of the chip to provide the optical I/O, the inputs feed into the first row of MZIs (1.1-1.16). The optical connections within (and between) the MZIs are strip waveguides with a height of 3 µm and a width of 1.875 µm, which ensure high mode confinement and small bending radius, but in which higher order modes are supported. To remove any optical power coupled to higher order modes, input lightwaves passes through a 2 mm long section of straight rib waveguides, before coupling to the MZIs. This section can be made significantly shorter, but has been kept as long as possible considering the footprint of our chip with minimal optical losses associated with the thick SOI waveguides. The silicon chip contains a total of 31 MZIs, 62 thermal shifters, and 31 PDs, within a footprint of 10×5 mm^2.

The chip was packaged by VTT, the electrical pads were wire bonded to a ceramic electrical interposer, and then to a PCB, and it was enclosed with a thermoelectric cooler (TEC) element in an aluminium case to allow thermal dissipation. For technical issues, it was not possible to include the optical interposer in the packaged prototype device. This because of small positioning error of the lane etching step which defines the optical I/O facet of the PIC. This error prevented the attachment of the interposer chip close enough to the waveguide facet for efficient optical coupling. Figure 3a shows the chip after wirebonding and attachment of the optical fiber array, figure 3b shows the fully-packaged chip. The coloured DC cable connections are for piloting the TEC, on the case the laterally placed DC connectors are for the monitor photodiodes, and the central DC connectors are for MZI control.

Device Characterization

The packaged chip was characterised with an external cavity tunable laser, individually coupled to the optical inputs. The MZIs were driven with a custom digital to analog converter (DAC), whose output ranges between 0 and 32 V. The output port was connected to a PD for analysis. The temperature of the TEC was set to 20 °C unless otherwise specified. Information about the equipment used, the experimental setup and additional characterizations may be found in the supplementary information.

A first set of measurements was carried out to assess the optical loss of the whole structure: the laser at 1550 nm was coupled to each input and the power at the output port was optimised by opportune control of the MZIs (See Supplementary Fig. 1). The wavelength was then swept from 1500 nm to 1600 nm in order to analyse the wavelength dependence of the device. The results are reported in the graph of figure 4a, where the insertion loss (IL) is reported as a function of the input port and

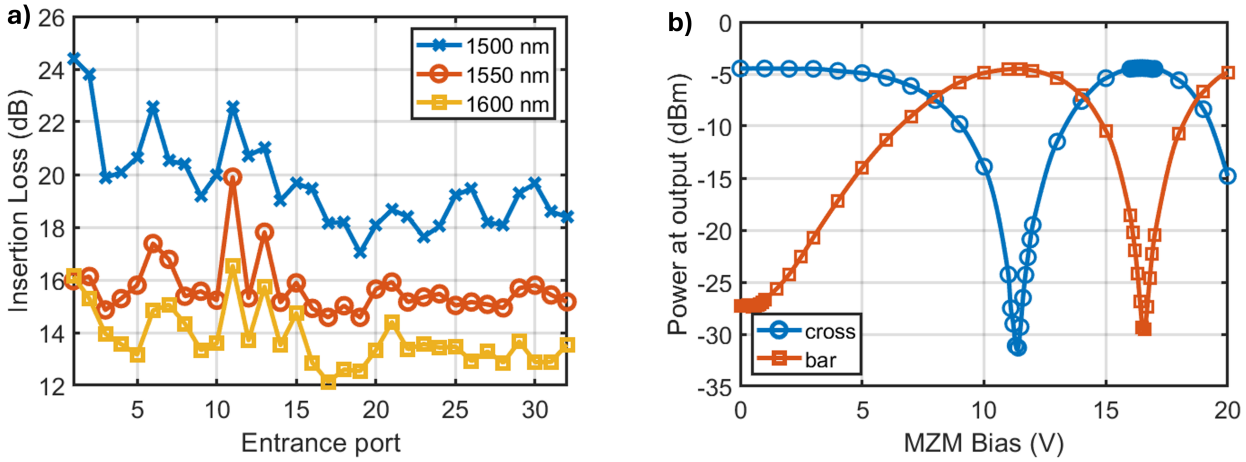

Figure 4. a) Total insertion loss as a function of different inputs and wavelengths. b) Measured interference of MZI 1.1 for bar and cross port when the external laser is coupled at inputs 2 and 1 respectively.

wavelength. The IL is maximal for 1500 nm, and minimal at 1600 nm with average values across the ports of 19.7 dB and 13.8 dB, respectively. At the typical optical communication wavelength, 1550 nm, the mean IL value is 15.7 dB with a standard deviation of 1.1 dB. Despite the considerable size of the chip, the majority of the optical losses arise from the optical I/O and not from routing, as the former contributes around 5 dB/interface of loss and the latter introduces approximately ∼0.1 dB/cm at 1550 nm. The remaining 5.7 dB of losses are introduced by the interferometers, of which there are 5 for each input-output path, resulting in an average IL of ∼1.1 dB/MZI. The fact that losses decrease at higher wavelengths suggests that the MMIs are not at the correct working point at 1550 nm, likely as a result of a wider-than-designed central section.

A second set of measurements was carried out to evaluate the performance of the MZIs in terms of extinction ratio (ER), average power for a π shift in the thermal tuners (P_π), thermal crosstalk, and phase shifter bandwidth. Figure 4b reports the interference fringes of MZI 1.1 as a function of applied bias voltage for its bar and cross port. 10 dBm of laser-light at 1550 nm was coupled individually to input 1 (cross) and input 2 (bar), and the consecutive MZIs were set to route all power to the output port. By sweeping the internal phase shifter voltage between 0 and 20 V, we evaluated an ER of 26.9 dB and 25.0 dB for the cross and bar states, respectively. The extinction ratio of all the MZIs in cross state was measured in a similar fashion, with an average value of 28.3 dB and a standard deviation of 2.4 dB. The performance of the MZIs is worse than expected by design: the IL should be lower, around 0.5 dB, and the ER should be around 40 dB. The π shift power was then derived by evaluating the bias voltage corresponding to the minimum and maximum transmission and considering the resistance of each phase shifter. The average P_π was measured to be 34.1 mW, with a standard deviation of 8.5 mW allowing for a total phase shift of more than 6π before failure. The P_π values in PICs usually have a low variance as they depend on the heater resistance, which in our case should have been 1 kΩ. Typically the P_π of similar phase shifters is close to 25 mW[24]. Here the excess and varying contact resistance of the heaters, with an average value of 4.1 kΩ and a standard deviation of 1.1 kΩ, and thus power dissipation, was due to the use of the contact metallization process optimized for the PDs. This single metal process was used for the whole chip, while optimized multi-metallization steps should be considered in the future. The list of all measured resistances can be found in the supplementary material.

The bandwidth of the phase shifters is limited by the delay between the time the voltage signal is applied and when thermal equilibrium is reached. To characterise this limit the phase shifters were driven with a square wave signal, with a frequency of around 1 kHz and peak to peak amplitude equal to V_π, the voltage required to change the phase by π, producing an optical signal that goes from maximum to minimum at the output port. Before the measurements, we derived the bandwidth of our DAC, which was >300 kHz. The setup for this measurement is depicted in Supplementary Fig. 3. Before the fabrication of the circuit, the thermal phase shifters were numerically evaluated with Lumerical HEAT and CHARGE to predict the V_π step response time. Figure 5a represents the simulation setup, composed of the thick-silicon slab waveguide, passivation silica, the electrical vias, a 100 µm thermal shifter that runs parallel to the waveguide, and below, a buried oxide layer. A conductive and thermal transient simulation was performed to evaluate the rise and fall times when V_π is applied to the electrical vias. Figure 5b represents the thermal distribution at equilibrium when the heater is driven with V_π. The numerical analysis predicted a rise time of 7.81 µs (128 kHz) and a fall time of 9.03 µs (110 kHz). Figure 5c compares the fall and rise signals, converted

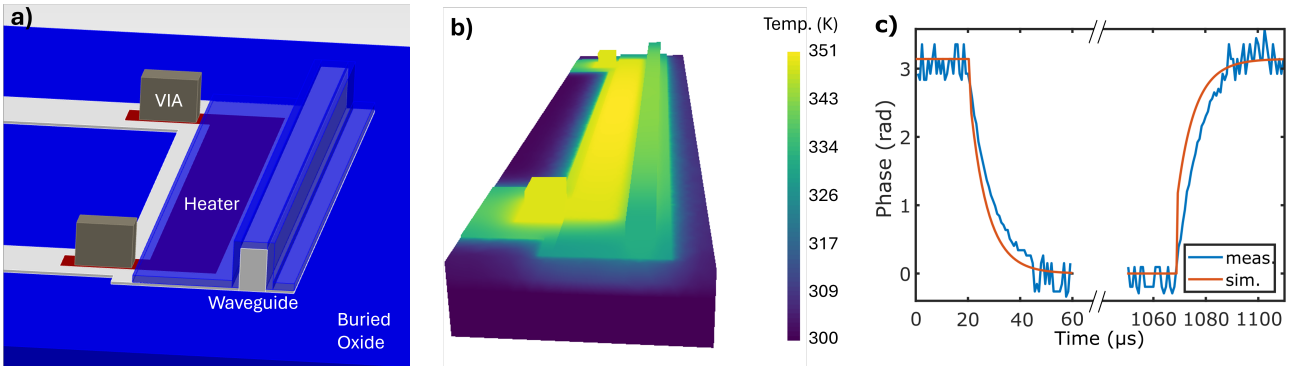

Figure 5. a) Lumerical HEAT and CHARGE simulation setup for the implanted heater response; b) thermal distribution in steady state when a V_π is applied to the shifter; c) comparison between the rise and fall signals for simulated and measured results.

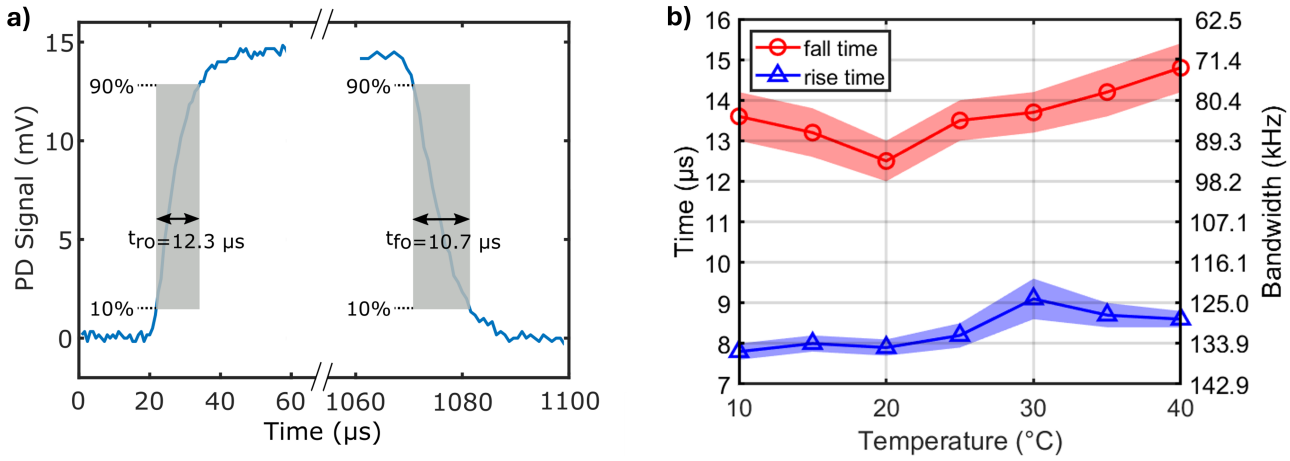

Figure 6. a) Signal at PIC output during phase shifter modulation to show how rise time, t_{fo}, and fall time, t_{ro}, are calculated. b) Rise time, fall time and associated limits in bandwidth of MZI 1.1 as a function of temperature with shaded region representing ± 1 standard deviation.

in relative phase shift, between the simulation and the experimental acquisition from the photodiode under actuation of the internal shifter of MZI 4.1.

Figure 6a illustrates how the rise and fall times are calculated for MZI 4.1. The symbols, t_{ro} and t_{fo}, correspond to the optical rise and fall times respectively. Since the MZI is being driven in cross state, t_{fo} corresponds to when the phase shifter is heating (rise time) and t_{ro} when the phase shifter is not activated and the device is returning to room temperature (fall time). In this instance, t_{ro}=1.23 $\times$ 10^{-5} s and t_{fo}=1.07$\times$ 10^{-5} s corresponding to respective limits in bandwidth of 81 kHz and 94 kHz. Four phase shifters were characterised in this way, the mean values of rise and fall time were calculated over several modulation cycles, resulting to be 12.4 μs (80.6 kHz) and 9.4 μs (106 kHz), respectively.

Since the thermalisation time is dependent on the temperature of the PIC, for MZI 1.1, a characterization was performed in a range of temperatures from 10 °C to 40 °C, to simulate the operation of the PIC in different environmental conditions. Figure 6b reports the results of this investigation, showing a notable increase in the fall time, as expected from the reduced temperature gradient, when the heater is switched off. These phase shifters are fast enough to use in a coherent combination context, for which a 50 kHz modulation at small amplitude ($\leq$ 1 radians) was proposed[29]. The thermal cross talk effect between the internal shifter of MZI 1.1 and the surrounding phase shifters was investigated by coupling light into port 1, setting the voltage at the internal shifter such that the power at the output port was at a minima (more sensitive to changes in temperature), and measuring the output power for both 0 V and 20 V applied to the closest surrounding phase shifters (corresponding to >2π

phase change). The maximum observed change in output power resulting from the cross talk was 2.1 dB corresponding to a change in phase of 0.074 radians, when the external phase shifter of MZI 1.1 was heated, it was less than 0.3 dB (0.031 radians) for all other cases. The very low thermal crosstalk is ensured by the deep trenches around the heater and waveguides of the VTT Silicon process[24].

Temp (°C)	Dark Current (nA)		
	0V	-1V	-2V
10	1.9	496.4	714.1
15	1.6	633.4	906.0
20	1.5	791.8	1125.5
25	1.6	1004.6	1426.0
30	1.5	1258.3	1788.2
35	1.7	1553.0	2236.1
40	1.7	1932.2	2794.7

(a)

Photodiode	Bandwidth (GHz)				
	0.0V	-0.5V	-1.0V	-1.5V	-2.0V
1.1	2.6	9.1	11.8	13.3	14.1
2.1	2.6	7.5	10.2	11.8	13.2
4.2	4.4	8.6	11.8	13.3	14.2
1.16	2.1	7.5	11.8	13.6	15.0

(b)

Table 1. a) Dark currents for photodiode 2.3 as a function of bias and temperature and bias. b) 3 dB bandwidth for different photodiodes as a function of bias.

A final set of measurements was carried out to assess the germanium photodiode performance in terms of dark current, responsivity, and optical bandwidth. Without any optical input, the dark current was measured as a function of bias for three different photodiodes (1.7, 1.16, 2.3), the average values at 0 V, 1 V and 2 V of negative bias are 1.1 ± 0.3 nA, 764 ± 74 nA and 1096 ± 128 nA respectively. For photodiode 2.3, the dark current was also measured as a function of both bias and temperature with results reported in table 1a, when negative bias was applied there was around four times as much dark current at a temperature of 40 °C compared to 10 °C. The responsivity of the photodiodes was estimated ≈ 0.8 A/W in DC by monitoring the output current when 10 dBm power of laser was injected, considering the coupling and propagation losses. The measurement of the 3 dB bandwidth of the monitor PDs could not be performed using the packaged PIC, as these were wirebonded to DC connectors. The PDs were characterised on a naked chip fabricated in the same run and wafer at a probe station. The laser was coupled to a external modulator with >25 GHz bandwidth, whose output was divided by a 3-dB splitter with one branch leading to a 50 GHz PD with a known bandwidth response, and the other to a SMF fiber which was edge coupled to the optical inputs on the chip. A microwave vector network analyzer was used with the output port coupled to the modulator input port, one receiver port was connected to the known PD and the other to a RF probe used to contact the PDs on the chip. This setup is represented in Supplementary Fig. 4. Different negative biases were supplied with a bias-tee at the RF probe, with the DC port connected to a source measure unit. With this configuration we subtracted the response of the known PD branch from the S_{21} response of the device under test, to compensate for the response of the RF equipment common to both outputs. The S_{21} frequency response of the known PD itself and the RF tip were then removed, and with a separate characterization, a correction was applied for the difference in output signal paths (only one had a bias-tee). With this method, the 3 dB bandwidths at differing negative bias were characterised for 4 photodiodes selected in different areas of the PIC; Table 1b reports these results. An example of a typical PD response, in this case for PD 2.1, as a function of applied negative bias is shown in Fig. 7, where the dashed horizontal line corresponds to -3 dB. The germanium photodetectors showed a large bandwidth increase by applying the first 0.5 V of negative bias, (from 2.6 to 7.5 GHz for PD 2.1), with a less pronounced improvement as the negative bias was increased. As the monitor photodiodes for the adaptive optics algorithm read signals at some tens of kHz, zero bias may be used as it provides sufficient bandwidth and a very low dark current (on the order of few nA), that would otherwise increase significantly.

Discussion

The device thermal phase shifters surpassed the target bandwidth of 50 kHz, while providing a sufficient number of π shifts ($> 6\pi$) to be used with an appropriate control algorithm in real time. The main shortcoming which prevents the use of the presented coherent combiner in realistic applications resides in the losses, which resulted much higher than expected, as discussed in the previous section. The main contribution resides in the optical I/O, accounting for 5 dB per facet, with the MZIs also contributing, whose constituent MMI were fabricated wider than designed, leading to an overall average loss of 15.7 dB at 1550 nm. However, the losses can be considerably reduced in future fabrications through the addition of the optical interposer chip inserted between the SMFs and the PIC, which lowers the coupling losses to 1.5 dB per facet. Moreover, the current VTT process has waveguides with improved smoothness thanks to a hydrogen-annealing step, thus reducing the propagation losses

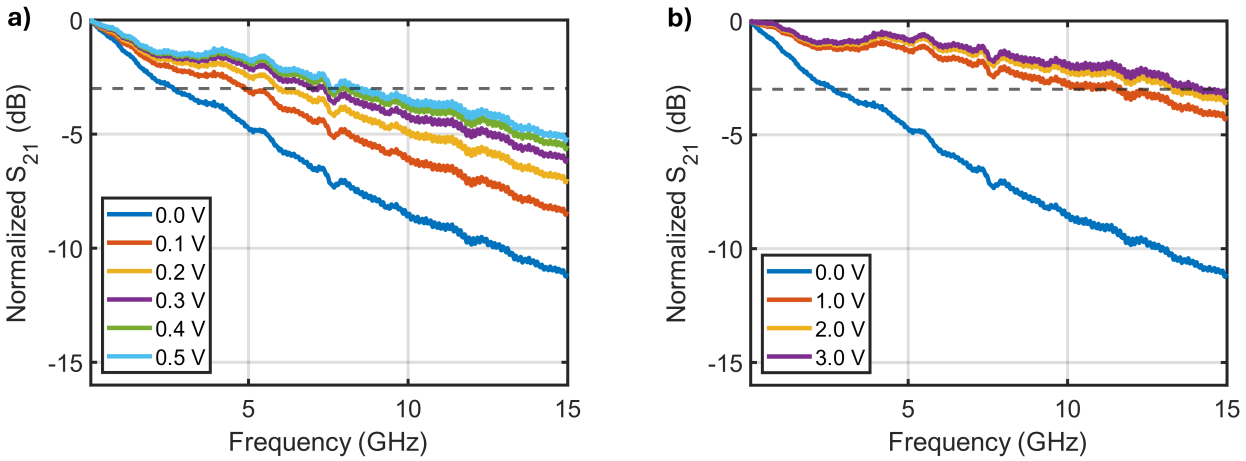

Figure 7. Normalized S_{21} response of photodiode 2.1 for a range in reverse bias a) 0.0 V - 0.5 V b) 0.0 V - 3.0 V. The horizontal grey dashed line corresponds to -3 dB.

with a demonstrated value of just 0.027 dB/cm, a more than threefold improvement with respect to the previous value of 0.1 dB/cm[30]. Finally, the IL of each MZI can be lowered to $\leq$0.5 dB/MZI with a correct fabrication of the constituent MMIs[24]. With this performance, the same chip with 32 inputs would have a total loss of 5.5 dB, accounting for 2 optical I/O and 5 MZI encountered by each path, and disregarding propagation losses. In the case of a 64-input device, the losses increase by 0.5 dB as there is one additional MZI in all input-output paths.

Aside from improvements in the losses, the PIC power consumption can be decreased considerably: the thermal phase shifter contact resistance should be lower, granting a $P_\pi \leq 25$ mW, instead of the 34.1 mW found with the current chip. Moreover, the heater thermal isolation can be further improved by removing the silicon substrate underneath the heater, leading to a P_π on the order of 1 mW[24]. Table 2 reports a comparison between our work and other coherent combiner PICs from the literature. In the last row, we have reported the prospective performance of a 32/64-input coherent combiner according to the latest demonstrated performance of the VTT process and introduction of an interposer, as discussed above. We omitted the work of Melloni et al.[20] for the lack of information reported about the PIC (which has 16 inputs with integrated photodetectors). The table reports number of supported modes (inputs), footprint, whether the PIC has integrated PDs, average total loss, phase shifter rise/fall time, P_π, and MZI IL. Although our chip has the highest optical losses at telecom wavelength, it demonstrated good performance in terms of MZI IL, phase shifter rise/fall time, and the best in term of power consumption. The prospective device would have the lowest losses even with a 64 input configuration, while also improving the power consumption. As discussed by L. Rinaldi[31], a 32-input chip would be suitable for medium-small turbulence, as in horizontal links and LEO satellites close to the zenith, while a device with 64 inputs would also allow the mitigation of strong turbulence conditions, as for LEO satellites close to the horizon.

PIC Combiner	Billaud *et al.*[19]	Billault *et al.*[18]	Billaud *et al.*[23]	This work	Prospective
# inputs	8	15	45	32	32 / 64
Platform	SOI	SOI	SOI	Thick SOI	Thick SOI
Footprint (cm^2)	$\approx$ 1	NA	NA	0.5	0.5 / 1.0
Integrated PDs	Yes	Yes	No	Yes	Yes
Avg losses (dB)	9.8 @ 1590 nm	7-11 @ 1535 nm	9 dB	15.7 @ 1550 nm	5.5 / 6.0
Rise time (µs)	10	$\approx$ 25	5.1	12.4	$\approx$10
Fall time (µs)	7.6	$\approx$ 25	NA	9.4	$\approx$10
P_π (mW)	<40	NA	NA	34.1	$\leq$25
MZI IL (dB)	$\approx$ 1	0.6	NA	1.1	$\leq$0.5

Table 2. Comparison of coherent combiners on PICs from literature with the presented work and a prospective device.

To further reduce the losses, the combiner architecture can be changed to enable phase-only correction of the decomposed modes[29]. This can be easily done by substituting the MZIs in the binary tree architecture with 3-dB (50/50) 2×2 directional couplers, or equivalently MMIs. Here, the phase control is implemented by two thermal tuners at the inputs of each element,

while the feedback for the control loop is collected by a PD at each coupler output. For the VTT process, the MMI IL is ≤ 0.2 dB instead of the ≈ 0.5 dB for an MZI[24], so accounting for 1.5 dB per I/O interface, a 32-input coherent combiner would have an overall loss of 4 dB, and a 64-input combiner would have 4.2 dB of loss, where propagation losses are neglected as extremely low (0.027 dB/cm with hydrogen-annealing). However, a phase-only correction of the input modes is equivalent to the MZI scheme only if the modes have the same amplitude. In a realistic scenario, the amplitudes can be modelled as independent random variables following a Rayleigh distribution. For this reason, as discussed by L. Rinaldi[31], for a phase-only device a higher number of modes is required to obtain an equivalent correction: around 25 for medium-small turbulence, and more than a hundred for strong turbulence. These numbers can be reduced to 16 and 64 respectively, if a tip-tilt correction is implemented in the receiving chain before mode decomposition[31].

Conclusions

Free space optical links enable wireless communication at high data rates, and are envisaged as a key component of future communication systems, spanning 5G/6G, quantum links, and satellite communications. However, atmospheric turbulence introduces distortions to the beam which limits the effective use of FSO in horizontal and satellite links.

Here, we have reported the design, fabrication, and characterization of an integrated coherent optical combiner for turbulence mitigation in free space optical links. The PIC was fabricated with the Thick SOI open platform offered by VTT, featuring 32 inputs and containing 31 integrated MZIs and photodetectors. The phase shifters were found to have a bandwidth of 81 kHz, an average P_π of 34.1 mW, and are able to shift the phase by more than 6π, meeting the requirements for turbulence correction in horizontal and LEO-to-ground links. Due to fabrication problems, the chip losses were much higher than expected, with an average value of 15.7 dB at a wavelength of 1550 nm. This is the main shortcoming preventing its use in real scenarios.

Nonetheless, by leveraging an optical interposer and the reduced losses offered by the new VTT process, a prospective device with the same number of inputs would reduce the losses to just 5.5 dB. For a 64 input device, the losses would increase to 6 dB, lower than any fabricated PIC combiner in literature. These numbers can be further reduced to 4 dB and 4.2 dB respectively if the device were to implement a phase-only correction.

References

1. Poliak, J., Calvo, R. M. & Rein, F. Demonstration of 1.72 tbit/s optical data transmission under worst-case turbulence conditions for ground-to-geostationary satellite communications. *IEEE Commun. Lett.* **22**, 1818–1821, DOI: 10.1109/LCOMM.2018.2847628 (2018).
2. Al-Gailani, S. A. *et al.* A survey of free space optics (fso) communication systems, links, and networks. *IEEE Access* **9**, 7353–7373, DOI: 10.1109/ACCESS.2020.3048049 (2021).
3. Dang, S., Amin, O., Shihada, B. & Alouini, M.-S. What should 6g be? *Nat. Electron.* **3**, 20–29, DOI: 10.1038/s41928-019-0355-6 (2020).
4. Toyoshima, M. Recent trends in space laser communications for small satellites and constellations. *J. Light. Technol.* **39**, 693–699 (2021).
5. Liao, S.-K. *et al.* Satellite-to-ground quantum key distribution. *Nature* **549**, 43–47 (2017).
6. Fischer, E. *et al.* ESA Optical Ground Station Upgrade with Adaptive Optics for High Data Rate Satellite-to-Ground Links-Test Results. In *2019 IEEE International Conference on Space Optical Systems and Applications (ICSOS)*, 1–6, DOI: 10.1109/ICSOS45490.2019.8978974 (2019).
7. Kolev, D. *et al.* Status Update on Laser Communication Activities in NICT. In *2022 IEEE International Conference on Space Optical Systems and Applications (ICSOS)*, 36–39, DOI: 10.1109/ICSOS53063.2022.9749741 (IEEE, Kyoto City, Japan, 2022).
8. Roberts, L. C. *et al.* Performance of the adaptive optics system for Laser Communications Relay Demonstration's Ground Station 1. *Appl. Opt.* **62**, G26, DOI: 10.1364/AO.486752 (2023).
9. Petit, C. *et al.* Onera's optical ground station for Geo Feeder links FEELINGS: in lab testing and on sky implementation. In *2023 IEEE International Conference on Space Optical Systems and Applications (ICSOS)*, 193–197, DOI: 10.1109/ICSOS59710.2023.10490280 (IEEE, Vancouver, BC, Canada, 2023).
10. Stotts, L. B. *et al.* Optical communications in atmospheric turbulence. In *Free-Space Laser Communications IX*, vol. 7464, 21–37, DOI: 10.1117/12.831231 (SPIE, 2009).
11. Li, M., Gao, W. & Cvijetic, M. Slant-path coherent free space optical communications over the maritime and terrestrial atmospheres with the use of adaptive optics for beam wavefront correction. *Appl. Opt., AO* **56**, 284–297, DOI: 10.1364/AO.56.000284 (2017).

12. Ciaramella, E. *et al.* 1.28 terabit/s (32x40 gbit/s) wdm transmission system for free space optical communications. *IEEE J. Sel. Areas Commun.* **27**, 1639–1645 (2009).

13. Primmerman, C. A. *et al.* Atmospheric-compensation experiments in strong-scintillation conditions. *Appl. Opt., AO* **34**, 2081–2088, DOI: 10.1364/AO.34.002081 (1995).

14. Schwartz, N. *Précompensation des effets de la turbulence par optique adaptative: application aux liaisons optiques en espace libre*. Ph.D. thesis, Université Nice Sophia Antipolis (2009).

15. O'Meara, T. R. The multidither principle in adaptive optics. *J. Opt. Soc. Am., JOSA* **67**, 306–315, DOI: 10.1364/JOSA.67.000306 (1977).

16. Shay, T. M. *et al.* First experimental demonstration of self-synchronous phase locking of an optical array. *Opt. Express, OE* **14**, 12015–12021, DOI: 10.1364/OE.14.012015 (2006).

17. Ma, Y. *et al.* Coherent beam combination with single frequency dithering technique. *Opt. Lett., OL* **35**, 1308–1310, DOI: 10.1364/OL.35.001308 (2010).

18. Billault, V. *et al.* Free space optical communication receiver based on a spatial demultiplexer and a photonic integrated coherent combining circuit. *Opt. Express* **29**, 33134–33143 (2021).

19. Billaud, A. *et al.* Turbulence mitigation via multi-plane light conversion and coherent optical combination on a 200 m and a 10 km link. In *2022 IEEE International Conference on Space Optical Systems and Applications (ICSOS)*, 85–92 (IEEE, 2022).

20. Melloni, A. *et al.* Programmable photonics for free space optics communications and computing. In *2023 IEEE Photonics Conference (IPC)*, 1–2 (IEEE, 2023).

21. Védrenne, N., Conan, J.-M., Petit, C. & Michau, V. Adaptive optics for high data rate satellite to ground laser link. In *Free-Space Laser Communication and Atmospheric Propagation XXVIII*, vol. 9739, 119–128, DOI: 10.1117/12.2218213 (SPIE, 2016).

22. Michel, T. *et al.* 100 Gbps and 45-mode multi-plane-light-conversion-based turbulence mitigation for free space optical communication. In Hemmati, H. & Robinson, B. S. (eds.) *Free-Space Laser Communications XXXV*, vol. 12413, 1241310, DOI: 10.1117/12.2654642. International Society for Optics and Photonics (SPIE, 2023).

23. Billaud, A. *et al.* TILBA-ATMO: a 45-mode MPLC-based turbulence mitigation solution for optical ground stations for direct-to-earth LEO-to-ground laser communications. In Hemmati, H. & Robinson, B. S. (eds.) *Free-Space Laser Communications XXXVI*, vol. 12877, 128771D, DOI: 10.1117/12.3003673. International Society for Optics and Photonics (SPIE, 2024).

24. Aalto, T. *et al.* Open-access 3-μm soi waveguide platform for dense photonic integrated circuits. *IEEE J. Sel. Top. Quantum Electron.* **25**, 1–9 (2019).

25. Young, D. W., Hurt, H. H., Sluz, J. E. & Juarez, J. C. Development and demonstration of laser communications systems. *Johns Hopkins APL Tech. Dig.* **33**, 122–136 (2015).

26. De Marinis, L., Andriolli, N. & Contestabile, G. Analysis of integration technologies for high-speed analog neuromorphic photonics. *IEEE J. Sel. Top. Quantum Electron.* **29**, 1–9, DOI: 10.1109/JSTQE.2023.3273784 (2023).

27. Siew, S. Y. *et al.* Review of silicon photonics technology and platform development. *J. Light. Technol.* **39**, 4374–4389 (2021).

28. Miller, D. A. B. Self-aligning universal beam coupler. *Opt. Express* **21**, 6360–6370, DOI: 10.1364/OE.21.006360 (2013).

29. Lucas, Y., Michau, V. & Meimon, S. Spatial diversity control law for demultiplexer and active photonic integrated circuits for atmospheric effect mitigation. In *Free-Space Laser Communications XXXVI*, vol. 12877, 220–236 (SPIE, 2024).

30. Marin, Y. E., Bera, A., Cherchi, M. & Aalto, T. Ultra-high-q racetrack resonators on thick soi platform through hydrogen annealing smoothing. *J. Light. Technol.* **41**, 3642–3648 (2023).

31. Rinaldi, L. *Mitigation of atmospheric turbulence effects on optical links by integrated optics.* Doctoral thesis, Université Paris-Saclay (2022).

Acknowledgements

The authors would like to thank Dr. L. Rinaldi for fruitful discussions about his work on atmospheric turbulence mitigation. This work was partially supported by the EU Horizon 2020 Programme through the Actphast 4R Project under Grant Agreement n° 779472. The authors acknowledge several of VTT's experts in Si photonics fabrication and PIC packaging for implementing

the prototype device. VTT's Si photonics activities are part of the Research Council of Finland Flagship Programme, Photonics Research and Innovation (PREIN), decision number 346545.

Author contributions statement

Conceptualization V.M. and G.C.; methodology L.D.M., V.M., G.C., and L.K.; circuit design and simulation L.D.M.; chip fabrication and packaging M.C. and M.K.; photonic chip characterization L.D.M., Y.L. and P.S.K.; data analysis, L.D.M., Y.L. and P.S.K.; writing—original draft preparation, L.D.M., V.M. and P.S.K.; supervision, G.C.; funding acquisition, G.C., V.M., M.C.; All authors contributed to the writing and review of the manuscript.

Competing interests

The authors declare no competing interests.

APPENDIX D

Calculus of the interaction matrix for the spatial modulation control method

With the notations given in Section 3.3.1, the general expression of an intensity measurement of the PIC for $j \in (1, N-1)$ is (see Section 1.5.1.1):

$$s_j = \sum_k |c^f_{j,k}|^2 |a_k|^2 + 2 \sum_k \sum_{l>k} |c^f_{j,k}||c^f_{j,l}||a_k||a_l| cos\left((\varphi_{a_k} - \varphi_{a_l}) + (\varphi^{ps}_k - \varphi^{ps}_l) + (\varphi^f_{j,k} - \varphi^f_{j,l})\right). \tag{D.1}$$

And the general expression of s_0 is:

$$s_0 = \sum_k |c^f_{0,k}|^2 |a_k|^2 + 2 \sum_k \sum_{l>k} |c^f_{0,k}||c^f_{0,l}||a_k||a_l| cos\left((\varphi_{a_k} - \varphi_{a_l}) + (\varphi^{ps}_k - \varphi^{ps}_l) + (\varphi^f_{0,k} - \varphi^f_{0,l})\right). \tag{D.2}$$

s_0 is maximum for:

$$(\varphi_{a_k} - \varphi_{a_l}) + (\varphi^{ps}_k - \varphi^{ps}_l) + (\varphi^f_{0,k} - \varphi^f_{0,l}) = 2n\pi,\ \forall (k,l) \in (0, N-1), \text{ and, } n \in \mathbb{N}. \tag{D.3}$$

Using expressions D.1 and D.3, when (s_j) for $j \in (1, N-1)$ are minimums we have the relation:

$$\varphi^f_{0,l} - \varphi^f_{0,k} + \varphi^f_{j,k} - \varphi^f_{j,l} = (2n+1)\pi,\ \forall (k,l) \in (0, N-1), \text{ and, } n \in \mathbb{N}. \tag{D.4}$$

By applying the spatial modulation as a positive step dither it comes:

$$\begin{aligned} s^+_j = &\sum_k |c^f_{j,k}|^2 |a_k|^2 \\ &+ 2 \sum_k \sum_{l>k} |c^f_{j,k}||c^f_{j,l}||a_k||a_l| cos\left((\varphi_{a_k} - \varphi_{a_l}) + (\varphi^{ps}_k - \varphi^{ps}_l) + (\delta\varphi^m_k - \delta\varphi^m_l) + (\varphi^f_{j,k} - \varphi^f_{j,l})\right). \end{aligned} \tag{D.5}$$

By applying the spatial modulation as a negative step dither and with hypothesis 1, it comes:

$$s_j^- = \sum_k |c_{j,k}^f|^2 |a_k|^2 + 2\sum_k \sum_{l>k} |c_{j,k}^f||c_{j,l}^f||a_k||a_l| cos\left((\varphi_{a_k} - \varphi_{a_l}) + (\varphi_k^{ps} - \varphi_l^{ps}) + (-\delta\varphi_k^m + \delta\varphi_l^m) + (\varphi_{j,k}^f - \varphi_{j,l}^f)\right). \tag{D.6}$$

Now we use hypothesis 2 by considering that the phase shifters are set to maximize s_0 using relations D.3 and D.4 and that s_0 is drifted from its maximum by the residual phase vector (φ_k) of small amplitude. Expressions D.5 and D.6 become:

$$s_j^+ = \sum_k |c_{j,k}^f|^2 |a_k|^2 + 2\sum_k \sum_{l>k} |c_{j,k}^f||c_{j,l}^f||a_k||a_l| cos\left((\delta\varphi_k^m - \delta\varphi_l^m) + (\varphi_k - \varphi_l) + \pi\right), \tag{D.7}$$

and

$$s_j^- = \sum_k |c_{j,k}^f|^2 |a_k|^2 + 2\sum_k \sum_{l>k} |c_{j,k}^f||c_{j,l}^f||a_k||a_l| cos\left((-\delta\varphi_k^m + \delta\varphi_l^m) + (\varphi_k - \varphi_l) + \pi\right). \tag{D.8}$$

Using the trigonometric identity $cos(\theta + \pi) = -cos(\theta)$ and expanding the cos term around 0 with a quadratic model it comes:

$$s_j^+ = \sum_k |c_{j,k}^f|^2 |a_k|^2 - 2\sum_k \sum_{l>k} |c_{j,k}^f||c_{j,l}^f||a_k||a_l| \left(1 - \frac{\left((\varphi_k - \varphi_l) + (\delta\varphi_k^m - \delta\varphi_l^m)\right)^2}{2}\right), \tag{D.9}$$

and

$$s_j^- = \sum_k |c_{j,k}^f|^2 |a_k|^2 - 2\sum_k \sum_{l>k} |c_{j,k}^f||c_{j,l}^f||a_k||a_l| \left(1 - \frac{\left((\varphi_k - \varphi_l) - (\delta\varphi_k^m - \delta\varphi_l^m)\right)^2}{2}\right). \tag{D.10}$$

Then taking the differential measurement with expressions D.9 and D.10 it comes:

$$\Delta s_j = 4\sum_k \sum_{l>k} |c_{j,k}^f||c_{j,l}^f||a_k||a_l| (\delta\varphi_k^m - \delta\varphi_l^m)(\varphi_k - \varphi_l). \tag{D.11}$$

The terms $|c_{j,k}^f||c_{j,l}^f||a_k||a_l|$ correspond to the curvatures of the quadratic model when (s_j) are near their minimums.

We define the three dimension curvature tensor $\boldsymbol{E}$ such as:

$$E_{k,l,j} = \begin{cases} 4|c_{j,k}^f||c_{j,l}^f||a_k||a_l| & \text{if } l > k \\ 0 & \text{otherwise} \end{cases}, \tag{D.12}$$

with j corresponding to the PIC output numbering and k, l corresponding to the phase shifters numbering such as the j^{th} matrix in $\boldsymbol{E}$ is a triangular matrix.

The j^{th} differential measurement writes:

$$\begin{aligned}\Delta s_j &= \sum_k \sum_l E_{k,l,j}(\delta\varphi_k - \delta\varphi_l)(\varphi_k - \varphi_l) \\ &= \sum_k \sum_l E_{k,l,j}(\delta\varphi_k - \delta\varphi_l)\varphi_k - \sum_k \sum_l E_{k,l,j}(\delta\varphi_k - \delta\varphi_l)\varphi_l \\ &= \sum_k \sum_l \left(\underbrace{E_{k,l,j} + E^t_{k,l,j}}_{H_{k,l,j}} \right) (\delta\varphi_k - \delta\varphi_l)\varphi_k\end{aligned} , \tag{D.13}$$

with $\boldsymbol{H} = \boldsymbol{E} + \boldsymbol{E}^t$ the tensor in which the matrix corresponding to the j^{th} output measurement is the sum of the j^{th} matrix in $\boldsymbol{E}$ with its transpose.

By sorting the terms of the sum and defining the three dimensional PIC curvature tensor $\boldsymbol{T} = (T_{k,l,j})$ as:

$$T_{k,l,j} = \begin{cases} -4|c^f_{j,k}||c^f_{j,l}||a_k||a_l| & \text{if } k \neq l \\ \sum_{n\neq k} 4|c^f_{j,k}||c^f_{j,n}||a_k||a_n| & \text{if } k = l \end{cases} , \tag{D.14}$$

the differential measurements can be rewritten:

$$\Delta s_j = \sum_k \sum_l T_{k,l,j}\delta\varphi^m_l\varphi_k \,. \tag{D.15}$$

The PIC curvature tensor depends on the modulus of the complex amplitudes of the PIC input guided waves. Using hypothesis 3, i.e. supposing that (a_k) are constant for all k we obtain the linear relation:

$$\begin{aligned}\boldsymbol{\Delta s} &= (\boldsymbol{\delta\varphi^m})^t \,.\boldsymbol{T}.\boldsymbol{\varphi} \\ &= \boldsymbol{M_{int}}.\boldsymbol{\varphi}\end{aligned} , \tag{D.16}$$

with the interaction matrix $\boldsymbol{M_{int}} = (\boldsymbol{\delta\varphi^m})^t \,.\boldsymbol{T}$, so that the j^{th} line in $\boldsymbol{M_{int}}$ corresponds to the product between $(\boldsymbol{\delta\varphi^m})^t$ (the transpose of $\boldsymbol{\delta\varphi^m}$) and the j^{th} matrix of the curvature tensor $\boldsymbol{T}$. The j^{th} matrix of the curvature tensor $\boldsymbol{T}$ corresponds to the curvature of the j^{th} intensity measurements with respect to the phase shifters measured near the minimum. Indeed by taking the second order derivative of Expression D.1 near its minimum it comes:

$$\begin{aligned}\left.\frac{\partial^2 s_j}{\partial\varphi^{ps}_p\partial\varphi^{ps}_q}\right|_{min} &= -2|c^f_{j,p}||c^f_{j,q}||a_p||a_q| \text{ if } p \neq q \text{ and,} \\ \left.\frac{\partial^2 s_j}{\partial\varphi^{ps^2}_p}\right|_{min} &= \sum_{q\neq p} 2|c^f_{j,p}||c^f_{j,q}||a_p||a_q|\end{aligned} \tag{D.17}$$

APPENDIX E

Noise propagation of sequential modulation

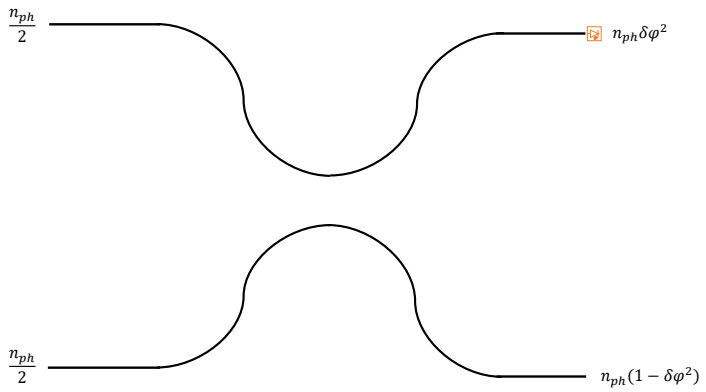

Figure E.1: Notation for photon noise propagation calculus.

Let $N_{ph} = \frac{n_{ph}}{2}$ be the number of photons per input and per cycle of modulation. The interferometric signal measurement is:

$$s = \frac{A}{2}(1 - cos(\varphi))\,, \tag{E.1}$$

At its maximum intensity the interferometric signal is $s = 2n_{ph}$. It cames $A = 2n_{ph}$. The differential measurement is express as:

$$\Delta s = A\delta\varphi \times \varphi\,, \tag{E.2}$$

The estimated phase is:

$$\hat{\varphi} = \frac{\Delta s}{A\delta\varphi}\,, \tag{E.3}$$

The mean quadratic error of phase error can be written:

$$< |\hat{\varphi}|^2 >= \frac{\sigma_b^2}{A^2\delta\varphi^2}\,, \tag{E.4}$$

The photon noise variance σ_b^2 is equal to two times the number of photons used for the measurements during one modulation: $\sigma_b^2 = 2 \times n_{ph}\delta\varphi^2$. It comes:

$$\begin{aligned} < |\hat{\varphi}|^2 > &= \frac{2 \times n_{ph}\delta\varphi^2}{4n_{ph}^2\delta\varphi^2} \\ &= \frac{1}{2n_{ph}} \\ &= \frac{1}{4N_{ph}} \end{aligned} \quad , \tag{E.5}$$

Bibliography

[1] Noah Schwartz. "Précompensation des effets de la turbulence par optique adaptative: application aux liaisons optiques en espace libre". PhD thesis. Université Nice Sophia Antipolis, 2009.

[2] A Melloni et al. "Programmable photonics for free space optics communications and computing". In: *2023 IEEE Photonics Conference (IPC)*. IEEE. 2023, pp. 1–2.

[3] Vincent Billault et al. "Free space optical communication receiver based on a spatial demultiplexer and a photonic integrated coherent combining circuit". en. In: *Optics Express* 29.21 (Oct. 2021), p. 33134. ISSN: 1094-4087. DOI: 10.1364/OE.433087. URL: https://www.osapublishing.org/abstract.cfm?URI=oe-29-21-33134 (visited on 10/21/2021).

[4] Antonin Billaud et al. "Turbulence Mitigation via Multi-Plane Light Conversion and Coherent Optical Combination on a 200 m and a 10 km Link". In: *2022 IEEE International Conference on Space Optical Systems and Applications (ICSOS)*. Mar. 2022, pp. 85–92. DOI: 10.1109/ICSOS53063.2022.9749710.

[5] Antonin Billaud et al. "TILBA-ATMO: a 45-mode MPLC-based turbulence mitigation solution for optical ground stations for direct-to-earth LEO-to-ground laser communications". In: *Free-Space Laser Communications XXXVI*. Vol. 12877. SPIE. 2024, p. 128771D.

[6] Luca Rinaldi. "Mitigation of atmospheric turbulence effects on optical links by integrated optics". PhD thesis. Université Paris-Saclay, 2022.

[7] Luca Rinaldi et al. "Sensorless adaptive optics for optical communications". en. In: *Free-Space Laser Communications XXXIII*. Ed. by Hamid Hemmati and Don M. Boroson. Online Only, United States: SPIE, Mar. 2021, p. 26. ISBN: 978-1-5106-4191-4 978-1-5106-4192-1. DOI: 10.1117/12.2582942. URL: https://www.spiedigitallibrary.org/conference-proceedings-of-spie/11678/2582942/Sensorless-adaptive-optics-for-optical-communications/10.1117/12.2582942.full (visited on 10/21/2021).

[8] Mohammad Ali Khalighi and Murat Uysal. "Survey on Free Space Optical Communication: A Communication Theory Perspective". en. In: *IEEE Communications Surveys & Tutorials* 16.4 (2014), pp. 2231–2258. ISSN: 1553-877X, 2373-745X. DOI: 10.1109/COMST.2014.2329501. URL: https://ieeexplore.ieee.org/document/6844864/ (visited on 10/21/2021).

[9] Hemani Kaushal and Georges Kaddoum. "Optical Communication in Space: Challenges and Mitigation Techniques". en. In: *IEEE Communications Surveys & Tutorials* 19.1 (2017). arXiv: 1705.10630, pp. 57–96. ISSN: 1553-877X. DOI: 10.1109/COMST.2016.2603518. URL: http://arxiv.org/abs/1705.10630 (visited on 03/25/2022).

[10] W Dan Williams et al. "RF and optical communications: A comparison of high data rate returns from deep space in the 2020 timeframe". In: *12th Ka and Broadband Communications Conference*. E-15723. 2007.

[11] Abu Jahid, Mohammed H Alsharif, and Trevor J Hall. "A contemporary survey on free space optical communication: Potentials, technical challenges, recent advances and research direction". In: *Journal of network and computer applications* 200 (2022), p. 103311.

[12] Juan C Juarez et al. "Testing of a compact 10-Gbps Lasercomm system at Trident Warrior 2017". In: *Free-Space Laser Communication and Atmospheric Propagation XXX*. Vol. 10524. SPIE. 2018, pp. 104–112.

[13] Guray Acar et al. "HydRON Vision: preparation towards a flight demonstration". In: *International Conference on Space Optics—ICSO 2022*. Vol. 12777. SPIE. 2023, pp. 1656–1673.

[14] Harald Hauschildt et al. "HydRON: High throughput optical network". In: *Free-Space Laser Communications XXXII*. Vol. 11272. SPIE. 2020, pp. 57–67.

[15] Malcolm W. Wright et al. "Adaptive optics correction into single mode fiber for a low Earth orbiting space to ground optical communication link using the OPALS downlink". en. In: *Optics Express* 23.26 (Dec. 2015), p. 33705. ISSN: 1094-4087. DOI: 10.1364/OE.23.033705. URL: https://opg.optica.org/abstract.cfm?URI=oe-23-26-33705 (visited on 03/14/2022).

[16] Thomas Weyrauch et al. "Fiber coupling with adaptive optics for free-space optical communication". en. In: ed. by David G. Voelz and Jennifer C. Ricklin. San Diego, CA, Jan. 2002, pp. 177–184. DOI: 10.1117/12.453227. URL: http://proceedings.spiedigitallibrary.org/proceeding.aspx?articleid=893647 (visited on 10/22/2021).

[17] Yamaç Dikmelik and Frederic M Davidson. "Fiber-coupling efficiency for free-space optical communication through atmospheric turbulence". en. In: (), p. 7.

[18] Nicolas Védrenne et al. "Turbulence effects on bi-directional ground-to-satellite laser communication systems". In: *Proc. Int. Conf. Sp. Opt. Syst. Appl.* Vol. 12. 2012.

[19] Alexander Mikhailovich Obukhov et al. "Structure of the temperature field in a turbulent flow". In: *Izv. Akad. Nauk SSSR, Ser. Geogr. Geofiz* 13.1 (1949), pp. 58–69.

[20] Valerian Ilich Tatarski. *Wave propagation in a turbulent medium*. Courier Dover Publications, 2016.

[21] Joseph W Goodman. *Statistical optics*. John Wiley & Sons, 2015.

[22] Nicolas Védrenne et al. "Propagation optique et correction en forte turbulence". fr. In: (), p. 293.

[23] George C Valley. "Isoplanatic degradation of tilt correction and short-term imaging systems". In: *Applied Optics* 19.4 (1980), pp. 574–577.

[24] A-R Camboulives et al. "Statistical and temporal irradiance fluctuations modeling for a ground-to-geostationary satellite optical link". In: *Applied optics* 57.4 (2018), pp. 709–721.

[25] Geoffrey Ingram Taylor. "The spectrum of turbulence". In: *Proceedings of the Royal Society of London. Series A-Mathematical and Physical Sciences* 164.919 (1938), pp. 476–490.

[26] Jack L Bufton. “Comparison of vertical profile turbulence structure with stellar observations”. In: *Applied optics* 12.8 (1973), pp. 1785–1793.

[27] J Strohbehn and S Clifford. “Polarization and angle-of-arrival fluctuations for a plane wave propagated through a turbulent medium”. In: *IEEE Transactions on Antennas and Propagation* 15.3 (1967), pp. 416–421.

[28] Olga Korotkova and Emil Wolf. “Changes in the state of polarization of a random electromagnetic beam on propagation”. In: *Optics communications* 246.1-3 (2005), pp. 35–43.

[29] Roddier. “The effects of atmospheric turbulence in optical astronomy”. In: *Progress in optics*. Vol. 19. Elsevier, 1981, pp. 281–376.

[30] Robert W Lee and Jeffrey C Harp. “Weak scattering in random media, with applications to remote probing”. In: *Proceedings of the IEEE* 57.4 (1969), pp. 375–406.

[31] Stanley M Flatté, Guang-Yu Wang, and Jan Martin. “Irradiance variance of optical waves through atmospheric turbulence by numerical simulation and comparison with experiment”. In: *JOSA A* 10.11 (1993), pp. 2363–2370.

[32] Ronald L Fante. “Electromagnetic beam propagation in turbulent media”. In: *Proceedings of the IEEE* 63.12 (1975), pp. 1669–1692.

[33] John Christopher Dainty. *Laser speckle and related phenomena*. Vol. 9. Springer science & business Media, 2013.

[34] Stuart Shaklan and Francois Roddier. “Coupling starlight into single-mode fiber optics”. en. In: *Applied Optics* 27.11 (June 1988), p. 2334. ISSN: 0003-6935, 1539-4522. DOI: 10.1364/AO.27.002334. URL: https://www.osapublishing.org/abstract.cfm?URI=ao-27-11-2334 (visited on 10/21/2021).

[35] Cyril Ruilier and Frédéric Cassaing. “Coupling of large telescopes and single-mode waveguides: application to stellar interferometry”. en. In: *Journal of the Optical Society of America A* 18.1 (Jan. 2001), p. 143. ISSN: 1084-7529, 1520-8532. DOI: 10.1364/JOSAA.18.000143. URL: https://www.osapublishing.org/abstract.cfm?URI=josaa-18-1-143 (visited on 11/18/2021).

[36] S Mohammad Navidpour, Murat Uysal, and Mohsen Kavehrad. “BER performance of free-space optical transmission with spatial diversity”. In: *IEEE Transactions on wireless communications* 6.8 (2007), pp. 2813–2819.

[37] V Xarcha et al. “Wavelength diversity/or free space optical systems: performance evaluation over log normal turbulence channels”. In: *2012 19th International Conference on Microwaves, Radar & Wireless Communications*. Vol. 2. IEEE. 2012, pp. 678–683.

[38] Fang Xu et al. “Channel coding and time-diversity for optical wireless links”. In: *Optics express* 17.2 (2009), pp. 872–887.

[39] Nicholas J Rattenbury et al. “Update on the German and Australasian Optical Ground Station Networks”. In: *arXiv preprint arXiv:2402.13282* (2024).

[40] Robert T Schwarz et al. “Optical Ground Station for Free-Space Optical Communication Research and Experimentation”. In: *Photonic Networks; 24th ITG-Symposium*. VDE. 2023, pp. 1–4.

[41] Horace W Babcock. “The possibility of compensating astronomical seeing”. In: *Publications of the Astronomical Society of the Pacific* 65.386 (1953), pp. 229–236.

[42] G Rousset et al. “First diffraction-limited astronomical images with adaptive optics”. In: *Astronomy and Astrophysics (ISSN 0004-6361), vol. 230, no. 2, April 1990, p. L29-L32. Research supported by the European Southern Observatory, Ministere de la Recherche et de la Technologie, Ministere de l'Education Nationale, INSU, DRET, and Ministere de la Defense.* 230 (1990), pp. L29–L32.

[43] Vincent Michau and Cyril Petit. “Optique adaptative-Principe et applications”. In: *Les Techniques de l'Ingenieur* (2021), E6290.

[44] Charles A. Primmerman et al. “Atmospheric-compensation experiments in strong-scintillation conditions”. en. In: *Applied Optics* 34.12 (Apr. 1995), p. 2081. ISSN: 0003-6935, 1539-4522. DOI: 10.1364/AO.34.002081. URL: https://www.osapublishing.org/abstract.cfm?URI=ao-34-12-2081 (visited on 11/18/2021).

[45] Jeffrey D Barchers, David L Fried, and Donald J Link. “Evaluation of the performance of Hartmann sensors in strong scintillation”. In: *Applied optics* 41.6 (2002), pp. 1012–1021.

[46] CB Lim et al. “Single-mode fiber coupling for satellite-to-ground telecommunication links corrected by adaptive optics”. In: *SF2A-2018: Proceedings of the Annual meeting of the French Society of Astronomy and Astrophysics*. 2018, p. Di.

[47] Curt M Schieler et al. “On-orbit demonstration of 200-Gbps laser communication downlink from the TBIRD CubeSat”. In: *Free-Space Laser Communications XXXV*. Vol. 12413. SPIE. 2023, p. 1241302.

[48] David J Israel et al. “Early results from NASA's laser communications relay demonstration (LCRD) experiment program”. In: *Free-Space Laser Communications XXXV*. Vol. 12413. SPIE. 2023, pp. 10–24.

[49] Karen Saucke et al. “The Tesat transportable adaptive optical ground station”. In: *Free-Space Laser Communication and Atmospheric Propagation XXVIII*. Vol. 9739. SPIE. 2016, pp. 37–47.

[50] Karen Saucke et al. “The TESAT transportable adaptive optical ground station and the operational experiences”. In: *International Conference on Space Optics—ICSO 2016*. Vol. 10562. SPIE. 2017, pp. 1033–1056.

[51] Frank Heine et al. “The European data relay system and Alphasat to T-AOGS space to ground links, status, and achievements in 2017”. In: *Free-Space Laser Communication and Atmospheric Propagation XXX*. Vol. 10524. SPIE. 2018, pp. 236–241.

[52] E Fischer et al. “Adaptive optics upgrades for laser communications to the ESA optical ground station”. In: *International Conference on Space Optics—ICSO 2020*. Vol. 11852. SPIE. 2021, pp. 971–980.

[53] Klaus Kudielka et al. “Optical feeder link demonstrations between the ESA Optical Ground Station and Alphasat”. In: *2023 IEEE International Conference on Space Optical Systems and Applications (ICSOS)*. IEEE. 2023, pp. 64–68.

[54] Johannes Prell et al. “Optical Ground Station Oberpfaffenhofen Next Generation: first satellite link tests with 80 cm telescope and AO system”. In: *2023 IEEE International Conference on Space Optical Systems and Applications (ICSOS)*. IEEE. 2023, pp. 42–48.

[55] Cyril Petit et al. “Onera's optical ground station for Geo Feeder links FEELINGS: in lab testing and on sky implementation”. In: *2023 IEEE International Conference on Space Optical Systems and Applications (ICSOS)*. IEEE. 2023, pp. 193–197.

[56] Geraldine Artaud et al. “FrOGS: French Optical Ground Station for space laser applications”. In: *2023 IEEE International Conference on Space Optical Systems and Applications (ICSOS)*. IEEE. 2023, pp. 182–188.

[57] Noelia Martinez et al. “AO-enhanced quantum communications with the ANU Optical Ground Station”. In: *International Conference on Space Optics—ICSO 2022*. Vol. 12777. SPIE. 2023, pp. 2813–2824.

[58] Ondrej Cierny. “Sensorless Wavefront Correction Algorithms for Free-Space Optical Communications”. en. In: ().

[59] Martin J. Booth. “Wavefront sensorless adaptive optics for large aberrations”. en. In: *Optics Letters* 32.1 (Jan. 2007), p. 5. ISSN: 0146-9592, 1539-4794. DOI: 10.1364/OL.32.000005. URL: https://opg.optica.org/abstract.cfm?URI=ol-32-1-5 (visited on 07/21/2022).

[60] Qintao Hu et al. “Adaptive stochastic parallel gradient descent approach for efficient fiber coupling”. In: *Optics Express* 28.9 (2020), pp. 13141–13154.

[61] T. R. O’Meara. “The multidither principle in adaptive optics”. en. In: *Journal of the Optical Society of America* 67.3 (Mar. 1977), p. 306. ISSN: 0030-3941. DOI: 10.1364/JOSA.67.000306. URL: https://www.osapublishing.org/abstract.cfm?URI=josa-67-3-306 (visited on 12/01/2021).

[62] Feiling Wang. “Control of deformable mirror with light-intensity measurements through single-mode fiber”. In: *Applied Optics* 49.31 (2010), G60–G66.

[63] M. A. Vorontsov, G. W. Carhart, and J. C. Ricklin. “Adaptive phase-distortion correction based on parallel gradient-descent optimization”. en. In: *Optics Letters* 22.12 (June 1997), p. 907. ISSN: 0146-9592, 1539-4794. DOI: 10.1364/OL.22.000907. URL: https://www.osapublishing.org/abstract.cfm?URI=ol-22-12-907 (visited on 10/21/2021).

[64] Nicolas K Fontaine et al. “Photonic lanterns, 3-d waveguides, multiplane light conversion, and other components that enable space-division multiplexing”. In: *Proceedings of the IEEE* 110.11 (2022), pp. 1821–1834.

[65] Mikhail A. Vorontsov and Svetlana L. Lachinova. “Laser beam projection with adaptive array of fiber collimators I Basic considerations for analysis”. en. In: *Journal of the Optical Society of America A* 25.8 (Aug. 2008), p. 1949. ISSN: 1084-7529, 1520-8532. DOI: 10.1364/JOSAA.25.001949. URL: https://opg.optica.org/abstract.cfm?URI=josaa-25-8-1949 (visited on 03/09/2022).

[66] Hongxiang Chang et al. “First experimental demonstration of coherent beam combining of more than 100 beams”. In: *Photonics Research* 8.12 (2020), pp. 1943–1948.

[67] Ernst-Georg Neumann. *Single-mode fibers: fundamentals*. Vol. 57. Springer, 2013, pp. 167–193.

[68] IDIL compagny. “2D fiber array / Bundles and Fiber assemblies IDIL compagny”. In: (Visited 04/28/2024).

[69] amsTECHNOLOGIES. “Fiberguide industries”. In: (Visited 04/28/2024).

[70] Elsa Huby et al. “First, a fibered aperture masking instrument-i. first on-sky test results”. In: *Astronomy & Astrophysics* 541 (2012), A55.

[71] Sergio G Leon-Saval et al. “Mode-selective photonic lanterns for space-division multiplexing”. In: *Optics express* 22.1 (2014), pp. 1036–1044.

[72] John J Davenport et al. “Photonic lanterns: a practical guide to filament tapering”. In: *Optical Materials Express* 11.8 (2021), pp. 2639–2649.

[73] Barnaby R. M. Norris et al. “An all-photonic focal-plane wavefront sensor”. en. In: *Nature Communications* 11.1 (Dec. 2020), p. 5335. ISSN: 2041-1723. DOI: 10.1038/s41467-020-19117-w. URL: https://www.nature.com/articles/s41467-020-19117-w (visited on 12/01/2021).

[74] Daniel Cruz-Delgado et al. “Photonic lantern tip/tilt detector for adaptive optics systems”. en. In: *Optics Letters* 46.13 (July 2021), p. 3292. ISSN: 0146-9592, 1539-4794. DOI: 10.1364/OL.430761. URL: https://www.osapublishing.org/abstract.cfm?URI=ol-46-13-3292 (visited on 10/21/2021).

[75] Guillaume Labroille et al. “Efficient and mode selective spatial mode multiplexer based on multi-plane light conversion”. en. In: *Optics Express* 22.13 (June 2014), p. 15599. ISSN: 1094-4087. DOI: 10.1364/OE.22.015599. URL: https://opg.optica.org/oe/abstract.cfm?uri=oe-22-13-15599 (visited on 03/10/2022).

[76] Pauline Boucher. “Spatial mode multiplexing: from fundamental concepts to applications”. en. In: (), p. 213.

[77] Tatsuhiko Watanabe et al. “Coherent few mode demultiplexer realized as a 2D grating coupler array in silicon”. en. In: (), p. 11.

[78] Karel Van Acoleyen, Hendrik Rogier, and Roel Baets. “Two-dimensional optical phased array antenna on silicon-on-insulator”. In: *Optics express* 18.13 (2010), pp. 13655–13660.

[79] Günther Roelkens et al. “Grating-based optical fiber interfaces for silicon-on-insulator photonic integrated circuits”. In: *IEEE Journal of Selected topics in quantum Electronics* 17.3 (2010), pp. 571–580.

[80] Maziyar Milanizadeh et al. “Multibeam Free Space Optics Receiver Enabled by a Programmable Photonic Mesh”. en. In: (), p. 9.

[81] David A. B. Miller. “Self-aligning universal beam coupler”. en. In: *Optics Express* 21.5 (Mar. 2013), p. 6360. ISSN: 1094-4087. DOI: 10.1364/OE.21.006360. URL: https://opg.optica.org/abstract.cfm?URI=oe-21-5-6360 (visited on 08/30/2022).

[82] Andrea Annoni. “Unscrambling light—automatically undoing strong mixing between modes”. en. In: (), p. 10.

[83] SeyedMohammad SeyedinNavadeh et al. “Determining the optimal communication channels of arbitrary optical systems using integrated photonic processors”. In: *Nature Photonics* 18.2 (2024), pp. 149–155.

[84] Maziyar Milanizadeh et al. “Multibeam free space optics receiver enabled by a programmable photonic mesh”. In: *arXiv preprint arXiv:2112.13644* (2021).

[85] Kassem Saab. “Optique adaptative pour les télécommunications optiques”. PhD thesis. Paris Sciences et Lettres (ComUE), 2017.

[86] Thomas M. Shay. “Theory of electronically phased coherent beam combination without a reference beam”. en. In: *Optics Express* 14.25 (2006), p. 12188. ISSN: 1094-4087. DOI: 10.1364/OE.14.012188. URL: https://opg.optica.org/oe/abstract.cfm?uri=oe-14-25-12188 (visited on 11/04/2022).

[87] Adrian Azarian et al. “Orthogonal coding methods for increasing the number of multiplexed channels in coherent beam combining”. In: *Applied Optics* 53.8 (2014), pp. 1493–1502.

[88] D.N. Loizos, P.P. Sotiriadis, and G. Cauwenberghs. "A Robust Continuous-Time Multi-Dithering Technique for Laser Communications using Adaptive Optics". en. In: *2006 IEEE International Symposium on Circuits and Systems*. Island of Kos, Greece: IEEE, 2006, pp. 3626–3629. ISBN: 978-0-7803-9389-9. DOI: 10.1109/ISCAS.2006.1693412. URL: http://ieeexplore.ieee.org/document/1693412/ (visited on 12/01/2021).

[89] Francesco Zanetto et al. "Dithering-based real-time control of cascaded silicon photonic devices by means of non-invasive detectors". en. In: *IET Optoelectronics* 15.2 (2021). _eprint: https://onlinelibrary.wiley.com/doi/pdf/10.1049/ote2.12019, pp. 111–120. ISSN: 1751-8776. DOI: 10.1049/ote2.12019. URL: https://onlinelibrary.wiley.com/doi/abs/10.1049/ote2.12019 (visited on 07/28/2022).

[90] Hee Kyung Ahn and Hong Jin Kong. "Cascaded multi-dithering theory for coherent beam combining of multiplexed beam elements". en. In: *Optics Express* 23.9 (May 2015), p. 12407. ISSN: 1094-4087. DOI: 10.1364/OE.23.012407. URL: https://opg.optica.org/abstract.cfm?URI=oe-23-9-12407 (visited on 10/25/2022).

[91] Yanxing Ma et al. "Coherent beam combination with single frequency dithering technique". EN. In: *Optics Letters* 35.9 (May 2010). Publisher: Optica Publishing Group, pp. 1308–1310. ISSN: 1539-4794. DOI: 10.1364/OL.35.001308. URL: https://opg.optica.org/ol/abstract.cfm?uri=ol-35-9-1308 (visited on 10/25/2022).

[92] Yanxing Ma et al. "Active phase locking of fiber amplifiers using sine–cosine single-frequency dithering technique". en. In: *Applied Optics* 50.19 (July 2011), p. 3330. ISSN: 0003-6935, 1539-4522. DOI: 10.1364/AO.50.003330. URL: https://opg.optica.org/abstract.cfm?URI=ao-50-19-3330 (visited on 11/04/2022).

[93] M. A. Vorontsov and V. P. Sivokon. "Stochastic parallel-gradient-descent technique for high-resolution wave-front phase-distortion correction". EN. In: *JOSA A* 15.10 (Oct. 1998). Publisher: Optica Publishing Group, pp. 2745–2758. ISSN: 1520-8532. DOI: 10.1364/JOSAA.15.002745. URL: https://opg.optica.org/josaa/abstract.cfm?uri=josaa-15-10-2745 (visited on 08/25/2023).

[94] Hui Zhao et al. "Nesterov-accelerated adaptive momentum estimation-based wavefront distortion correction algorithm". EN. In: *Applied Optics* 60.24 (Aug. 2021). Publisher: Optica Publishing Group, pp. 7177–7185. ISSN: 2155-3165. DOI: 10.1364/AO.428465. URL: https://opg.optica.org/ao/abstract.cfm?uri=ao-60-24-7177 (visited on 07/21/2022).

[95] Jiaxun Li et al. "A Novel SPGD Algorithm for Wavefront Sensorless Adaptive Optics System". In: *IEEE Photonics Journal* 15.4 (Aug. 2023). Conference Name: IEEE Photonics Journal, pp. 1–9. ISSN: 1943-0655. DOI: 10.1109/JPHOT.2023.3285871.

[96] John A Nelder and Roger Mead. "A simplex method for function minimization". In: *The computer journal* 7.4 (1965), pp. 308–313.

[97] T. R. O'Meara. "Stability of an N-loop ensemble-reference phase control system". EN. In: *JOSA* 67.3 (Mar. 1977). Publisher: Optica Publishing Group, pp. 315–318. DOI: 10.1364/JOSA.67.000315. URL: https://opg.optica.org/josa/abstract.cfm?uri=josa-67-3-315 (visited on 10/27/2022).

[98] Min Jiang et al. "Coherent beam combining of fiber lasers using a CDMA-based single-frequency dithering technique". In: *Applied Optics* 56.15 (2017), pp. 4255–4260.

[99] Mikhail A Vorontsov et al. “Adaptive imaging system for phase-distorted extended source and multiple-distance objects”. In: *Applied Optics* 36.15 (1997), pp. 3319–3328.

[100] Ryan C Lawrence et al. “Thermal-blooming compensation using target-in-the-loop techniques”. In: *Target-in-the-Loop: Atmospheric Tracking, Imaging, and Compensation II*. Vol. 5895. SPIE. 2005, pp. 110–123.

[101] Jan E Kansky et al. “Beam control of a 2D polarization maintaining fiber optic phased array with high-fiber count”. In: *Advanced Wavefront Control: Methods, Devices, and Applications IV*. Vol. 6306. SPIE. 2006, pp. 135–145.

[102] Mikhail A. Vorontsov. “Decoupled stochastic parallel gradient descent optimization for adaptive optics: integrated approach for wave-front sensor information fusion”. en. In: *Journal of the Optical Society of America A* 19.2 (Feb. 2002), p. 356. ISSN: 1084-7529, 1520-8532. DOI: 10.1364/JOSAA.19.000356. URL: https://opg.optica.org/abstract.cfm?URI=josaa-19-2-356 (visited on 07/21/2022).

[103] B. Pou et al. “Adaptive optics control with multi-agent model-free reinforcement learning”. en. In: *Optics Express* 30.2 (Jan. 2022), p. 2991. ISSN: 1094-4087. DOI: 10.1364/OE.444099. URL: https://www.osapublishing.org/abstract.cfm?URI=oe-30-2-2991 (visited on 01/17/2022).

[104] Alison P Wong et al. “Machine learning for wavefront sensing”. In: *Adaptive Optics Systems VIII*. Vol. 12185. SPIE. 2022, pp. 791–809.

[105] Yohei Nishizaki et al. “Deep learning wavefront sensing”. In: *Optics express* 27.1 (2019), pp. 240–251.

[106] Qinghua Tian et al. “DNN-based aberration correction in a wavefront sensorless adaptive optics system”. en. In: *Optics Express* 27.8 (Apr. 2019), p. 10765. ISSN: 1094-4087. DOI: 10.1364/OE.27.010765. URL: https://www.osapublishing.org/abstract.cfm?URI=oe-27-8-10765 (visited on 10/21/2021).

[107] Maksym Shpakovych et al. “Experimental phase control of a 100 laser beam array with quasi-reinforcement learning of a neural network in an error reduction loop”. en. In: *Optics Express* 29.8 (Apr. 2021), p. 12307. ISSN: 1094-4087. DOI: 10.1364/OE.419232. URL: https://www.osapublishing.org/abstract.cfm?URI=oe-29-8-12307 (visited on 10/21/2021).

[108] Alison P. Wong et al. “Predictive control for adaptive optics using neural networks”. en. In: *Journal of Astronomical Telescopes, Instruments, and Systems* 7.01 (Feb. 2021). ISSN: 2329-4124. DOI: 10.1117/1.JATIS.7.1.019001. URL: https://www.spiedigitallibrary.org/journals/Journal-of-Astronomical-Telescopes-Instruments-and-Systems/volume-7/issue-01/019001/Predictive-control-for-adaptive-optics-using-neural-networks/10.1117/1.JATIS.7.1.019001.full (visited on 12/01/2021).

[109] David A. B. Miller. “Perfect optics with imperfect components”. EN. In: *Optica* 2.8 (Aug. 2015). Publisher: Optica Publishing Group, pp. 747–750. ISSN: 2334-2536. DOI: 10.1364/OPTICA.2.000747. URL: https://opg.optica.org/optica/abstract.cfm?uri=optica-2-8-747 (visited on 07/27/2022).

[110] S. Y. Siew et al. “Review of Silicon Photonics Technology and Platform Development”. In: *Journal of Lightwave Technology* 39.13 (July 2021). Conference Name: Journal of Lightwave Technology, pp. 4374–4389. ISSN: 1558-2213. DOI: 10.1109/JLT.2021.3066203.

[111] Timo Aalto et al. "Open-Access 3-μm SOI Waveguide Platform for Dense Photonic Integrated Circuits". In: *IEEE Journal of Selected Topics in Quantum Electronics* 25.5 (Sept. 2019). Conference Name: IEEE Journal of Selected Topics in Quantum Electronics, pp. 1–9. ISSN: 1558-4542. DOI: 10.1109/JSTQE.2019.2908551.

[112] AG Rickman, GT Reed, and Fereydoon Namavar. "Silicon-on-insulator optical rib waveguide loss and mode characteristics". In: *Journal of Lightwave Technology* 12.10 (1994), pp. 1771–1776.

[113] Daoxin Dai and Sailing He. "Analysis of characteristics of bent rib waveguides". In: *JOSA A* 21.1 (2004), pp. 113–121.

[114] Tatsurou Hiraki et al. "Heterogeneously integrated iii–v/si mos capacitor mach–zehnder modulator". In: *Nature Photonics* 11.8 (2017), pp. 482–485.

[115] Chao Xiang, Warren Jin, and John E. Bowers. "Silicon nitride passive and active photonic integrated circuits: trends and prospects". en. In: *Photonics Research* 10.6 (June 2022), A82. ISSN: 2327-9125. DOI: 10.1364/PRJ.452936. URL: https://opg.optica.org/abstract.cfm?URI=prj-10-6-A82 (visited on 08/23/2023).

[116] Maziyar Milanizadeh et al. "Canceling Thermal Cross-Talk Effects in Photonic Integrated Circuits". In: *Journal of Lightwave Technology* 37.4 (Feb. 2019). Conference Name: Journal of Lightwave Technology, pp. 1325–1332. ISSN: 1558-2213. DOI: 10.1109/JLT.2019.2892512.

[117] Mark Dong et al. "High-speed programmable photonic circuits in a cryogenically compatible, visible–near-infrared 200 mm CMOS architecture". en. In: *Nature Photonics* 16.1 (Jan. 2022). Number: 1 Publisher: Nature Publishing Group, pp. 59–65. ISSN: 1749-4893. DOI: 10.1038/s41566-021-00903-x. URL: https://www.nature.com/articles/s41566-021-00903-x (visited on 10/13/2022).

[118] David AB Miller. "Photonic chips embrace piezo-optomechanics". In: *Nature Photonics* 16.1 (2022), pp. 10–11.

[119] Nadège Courjal et al. "Lithium niobate optical waveguides and microwaveguides". In: *Emerging waveguide technology* (2018), p. 155.

[120] Jintian Lin et al. "Advances in on-chip photonic devices based on lithium niobate on insulator". EN. In: *Photonics Research* 8.12 (Dec. 2020). Publisher: Optica Publishing Group, pp. 1910–1936. ISSN: 2327-9125. DOI: 10.1364/PRJ.395305. URL: https://opg.optica.org/prj/abstract.cfm?uri=prj-8-12-1910 (visited on 07/04/2023).

[121] Nadège Courjal et al. "Microsystèmes intégrés en niobate de lithium". fr. In: *Photoniques* 98 (Sept. 2019), pp. 34–38. ISSN: 1629-4475, 2269-8418. DOI: 10.1051/photon/20199834. URL: https://www.photoniques.com/10.1051/photon/20199834 (visited on 10/21/2021).

[122] Di Zhu et al. "Integrated photonics on thin-film lithium niobate". In: *Advances in Optics and Photonics* 13.2 (2021), pp. 242–352.

[123] Huangpu Han, Lutong Cai, and Hui Hu. "Optical and structural properties of single-crystal lithium niobate thin film". In: *Optical Materials* 42 (2015), pp. 47–51.

[124] Weike Zhao et al. "High-Performance Mode-Multiplexing Device with Anisotropic Lithium-Niobate-on-Insulator Waveguides". In: *Laser & Photonics Reviews* 17.5 (2023), p. 2200774.

[125] Gorazd Poberaj et al. "Lithium niobate on insulator (LNOI) for micro-photonic devices". In: *Laser & photonics reviews* 6.4 (2012), pp. 488–503.

[126] Guanyu Chen et al. “Advances in lithium niobate photonics: development status and perspectives”. In: *Advanced Photonics* 4.3 (2022), pp. 034003–034003.

[127] Rongbo Wu et al. “Fabrication of a multifunctional photonic integrated chip on lithium niobate on insulator using femtosecond laser-assisted chemomechanical polish”. In: *Optics Letters* 44.19 (2019), pp. 4698–4701.

[128] Anaëlle Maho et al. “Robust atmospheric FSO communication receiver based on the coherent combination of spatial modes: an experimental evaluation”. In: *2022 IEEE International Conference on Space Optical Systems and Applications (ICSOS)*. Mar. 2022, pp. 164–167. DOI: 10.1109/ICSOS53063.2022.9749704.

[129] Domitille Schanne et al. “Turbulence mitigated optical ground station for LEO-to-ground optical communication in project Keraunos”. In: *Free-Space Laser Communications XXXVI*. Vol. 12877. SPIE. 2024, 128771E.

[130] Momen Diab et al. “Experimental demonstration of photonic phase correctors based on grating coupler arrays and thermo-optic shifters”. In: *arXiv preprint arXiv:2408.07735* (2024).

[131] Antonin Billaud et al. “Optimal Coherent Beam Combining Based on Multi-Plane Light Conversion for High Throughput Optical Feeder Links”. en. In: *2019 IEEE International Conference on Space Optical Systems and Applications (ICSOS)*. Portland, OR, USA: IEEE, Oct. 2019, pp. 1–5. ISBN: 978-1-72810-500-0. DOI: 10.1109/ICSOS45490.2019.8978969. URL: https://ieeexplore.ieee.org/document/8978969/ (visited on 03/14/2022).

[132] Jan R. Magnus. “On Differentiating Eigenvalues and Eigenvectors”. en. In: *Econometric Theory* 1.2 (Aug. 1985). Publisher: Cambridge University Press, pp. 179–191. ISSN: 1469-4360, 0266-4666. DOI: 10.1017/S0266466600011129. URL: https://www.cambridge.org/core/journals/econometric-theory/article/on-differentiating-eigenvalues-and-eigenvectors/E44CD3EAE5CB211F6D79DDA9B7609EEE (visited on 09/28/2023).

[133] Diederik P. Kingma and Jimmy Ba. “Adam: A Method for Stochastic Optimization”. en. In: *arXiv:1412.6980 [cs]* (Jan. 2017). arXiv: 1412.6980. URL: http://arxiv.org/abs/1412.6980 (visited on 12/06/2021).

[134] C Paterson. “Towards practical wavefront sensing at the fundamental information limit”. en. In: *Journal of Physics: Conference Series* 139 (Nov. 2008), p. 012021. ISSN: 1742-6596. DOI: 10.1088/1742-6596/139/1/012021. URL: https://iopscience.iop.org/article/10.1088/1742-6596/139/1/012021 (visited on 11/02/2023).

[135] Sebastiaan Y. Haffert, Jared R. Males, and Olivier Guyon. *Reaching the fundamental sensitivity limit of wavefront sensing on arbitrary apertures with the Phase Induced Amplitude Apodized Zernike Wavefront Sensor (PIAA-ZWFS)*. en. Number: arXiv:2310.10889 arXiv:2310.10889 [astro-ph, physics:physics]. Oct. 2023. URL: http://arxiv.org/abs/2310.10889 (visited on 11/02/2023).

[136] Francesco Morichetti et al. “Non-Invasive On-Chip Light Observation by Contactless Waveguide Conductivity Monitoring”. In: *IEEE Journal of Selected Topics in Quantum Electronics* 20.4 (July 2014). Conference Name: IEEE Journal of Selected Topics in Quantum Electronics, pp. 292–301. ISSN: 1558-4542. DOI: 10.1109/JSTQE.2014.2300046.

[137] Monsef Zaboub et al. “Fabrication of polymer microlenses on single mode optical fibers for light coupling”. In: *Optics Communications* 366 (2016), pp. 122–126.

[138] Djamila Bouaziz et al. “Direct imaging of a photonic jet at shaped fiber tips”. In: *Optics Letters* 46.20 (2021), pp. 5125–5128.

[139] Lorenzo De Marinis et al. “A Silicon Photonic 32-Input Coherent Combiner for Turbulence Mitigation in Free Space Optics Links”. In: *arXiv preprint arXiv:2406.02076* (2024).

[140] Yisbel E Marin et al. “Ultra-High-Q Racetrack Resonators on Thick SOI Platform Through Hydrogen Annealing Smoothing”. In: *Journal of Lightwave Technology* 41.11 (2023), pp. 3642–3648.

[141] Serge Meimon, Cyril Petit, and Thierry Fusco. “Optimized calibration strategy for high order adaptive optics systems in closed-loop: the slope-oriented Hadamard actuation”. In: *Optics express* 23.21 (2015), pp. 27134–27144.

[142] S Oberti et al. “Large DM AO systems: synthetic IM or calibration on sky?” In: *Advances in Adaptive Optics II*. Vol. 6272. SPIE. 2006, pp. 652–663.

université PARIS-SACLAY

ÉCOLE DOCTORALE
Ondes et matière (EDOM)

Titre: Optique adaptative intégrée pour l'atténuation des effets de la turbulence atmosphérique sur les liaisons optiques

Mots clés: Communications optiques en espace libre, Turbulence atmosphérique, Circuit photonique intégré, Optique adaptative

Résumé: Avec un besoin croissant de communication en espace libre, les transmissions radiofréquences deviennent saturées et les liaisons optiques représentent une solution prometteuse. A la réception, l'injection du signal optique dans une fibre optique monomode (FOM) permet un débit élevé en utilisant les composants déjà développés pour les communications fibrées. Cette injection peut être fortement perturbée par les effets de la turbulence pour des liens à travers l'atmosphère. Pour s'affranchir de ces effets, l'optique adaptative (OA) est couramment utilisée. Une approche alternative, appelée ici OA-intégrée, a été récemment proposée. Elle est basée sur un démultiplexeur spatial (DS) suivi d'un circuit photonique intégré (PIC) assurant l'injection dans la FOM après combinaison cohérente. L'OA-intégrée pourrait représenter une solution compacte et robuste s'appliquant aussi aux fortes perturbations. Sa mise en œuvre nécessite toutefois la réalisation d'un PIC complexe, avec des pertes minimales et des déphaseurs rapides pour un contrôle en temps réel. Or les PIC actuels ne répondent pas à ces besoins. Les PIC en Niobate de Lithium (NL) autorisent des déphaseurs avec une bande passante élevée mais pas une architecture complexe, alors que la technologie Silicium (SI) permet des architectures complexes mais des déphaseurs relativement lents. Par ailleurs, les pertes sont encore élevées avec les deux technologies. Cette thèse porte sur l'analyse des performances ultimes d'une OA-intégrée en présence de turbulence atmosphérique, basée sur le développement d'une méthode de contrôle originale pour l'architecture de PIC dédiés à la combinaison cohérente. Premièrement j'ai caractérisé les propriétés des signaux à combiner. Une analyse des propriétés statistiques des amplitudes complexes en sortie du DS m'a conduit à proposer une architecture simplifiée basée sur une correction de phase suivie d'une combinaison cohérente statique présentant moins de pertes. Une telle architecture réduisant significativement les pertes dans le PIC, je l'ai retenue dans la suite de ma thèse. J'ai établi une expression analytique du temps de décorrélation des amplitudes complexes en sortie du DS. En appliquant cette expression au cas d'une liaison satellite-sol, j'ai mis en évidence que la bande passante typique des déphaseurs des PIC en SI est limitée pour permettre un contrôle classique par modulation dans le cas d'un grand nombre d'entrées. Pour surmonter cette contrainte, j'ai proposé une méthode de contrôle originale basée sur une modulation spatiale. Avec cette méthode, le PIC peut être vu comme un analyseur de surface d'onde (ASO) qui permet d'estimer les phases résiduelles en une seule période de modulation. J'ai analysé le comportement de cette méthode en présence de bruit de mesure et j'ai optimisé la forme de la modulation spatiale vis-à-vis de ce critère. Le codage optimal permet à cette méthode d'atteindre la limite fondamentale de la propagation du bruit de photons des analyseurs de surface d'onde. Sur la base des conclusions précédentes (correction phase seule, temps de décorrélation, codage spatial optimisé), j'ai défini les principaux paramètres d'une OA-intégrée dédiée à une liaison satellite-sol. J'ai réalisé une expérience numérique et démontré que cette méthode de contrôle permet la fermeture de la boucle et est stable en présence de bruit de mesure représentatif de conditions réalistes. J'ai également proposé une architecture légèrement modifiée pour simplifier la loi de contrôle. Finalement, pour montrer que cette méthode de contrôle originale est applicable à un PIC réel présentant des imperfections, je l'ai mise en œuvre expérimentalement avec un PIC en NL que j'ai préalablement caractérisé. J'ai mis en évidence son intérêt en comparant ses performances à celles de méthodes de modulation classique. Enfin, j'ai utilisé la caractérisation d'un PIC en SI, à laquelle j'ai participé, pour définir un futur PIC avec des performances optimales.

université PARIS-SACLAY

ÉCOLE DOCTORALE
Ondes et matière (EDOM)

Title: Integrated adaptive optics for atmospheric turbulence effects mitigation on optical links

Keywords: Free-space optical communications, Atmospheric turbulence, Photonic integrated circuit, Adaptive optics

Abstract: Optical links offer a promising solution to lighten saturated radio-frequency transmissions with the growing need for free-space communications. At the receiver end, the injection into a Single-Mode Fibre (SMF) allows high-data-rate and the use of components already developed for fibre communications. In the case of links through the atmosphere, turbulence effects on the optical wave severely degrade the SMF coupling. A method to mitigate these effects is Adaptive Optics (AO). An alternative technique has been recently proposed. This solution, referred to here as integrated-AO, is based on a spatial demultiplexer followed by a Photonic Integrated Circuit (PIC) that ensures the SMF injection after coherent combination. Integrated-AO could represent a compact and robust promising solution also enabling correction in strong perturbation regimes. However, its implementation faces an important issue: the realization of a complex PIC with minimum losses and phase shifters bandwidth high enough for real-time control. Indeed, PICs allowing for phase shifters with sufficient bandwidth, such as Lithium Niobate PICs, do not allow complex architecture and possess limiting losses. PICs in Silicon, allow for complex architecture but also possess limiting losses and permit phase shifters with limited bandwidth in our application case. It is therefore essential to take the best advantage of the available technologies. This thesis focuses on the analysis of the ultimate performances of an integrated-AO in the presence of atmospheric turbulence, based on the development of an original control method for photonic integrated circuit architecture dedicated to coherent combination. In a first step, to determine the properties of the signals to be combined after the spatial demultiplexer, I analyzed the statistical properties of its output complex amplitudes. It highlighted the interest in a simplified architecture that presents fewer losses based on a phase correction followed by a static coherent combination. I retained such an architecture in my thesis. Moreover, I established an analytical expression of the decorrelation time of the complex amplitudes at the spatial demultiplexer output. A numerical application of a representative satellite-to-ground link allows me to highlight that typical phase shifters of Silicon PICs present limited bandwidth to apply classic modulation-based control methods for the real-time control of PICs with a high number of inputs. To overcome the constraints on phase shifters bandwidth, I implemented an original control method based on a spatial coding. This method allowed me to use the PIC as a wavefront sensor to estimate residual phases after one modulation period. I analyzed its behavior in the presence of measurement noises and optimized the spatial coding with respect to this criterion. With the optimized coding, this method reaches the fundamental photon noise propagation of wavefront sensors. Based on the previous conclusions (phase-only architecture, decorrelation time, optimized spatial coding), I defined the main parameters of an integrated-AO dedicated to satellite-to-ground link. I carried out a numerical experiment demonstrating that this original control method can close the loop and is stable with respect to measurement noises in realistic conditions. I then proposed a slightly modified architecture to simplify the control law. Finally, to demonstrate that this original control method can close the loop and is stable on an experimental PIC with all its imperfections, I implemented it to control the phase shifters of a Lithium Niobate PIC that I characterized beforehand. I validated its usefulness by comparing its closed-loop performances with classic modulation-based control methods. In a last step, I used the characterization of a Silicon PIC, in which I participated, to define the sizing and architecture for realizing a future PIC with optimal performances.